Modélisation multi-échelle des composites tissés à matrice thermoplastique, comportement cyclique et dépendance au temps

Francis Praud

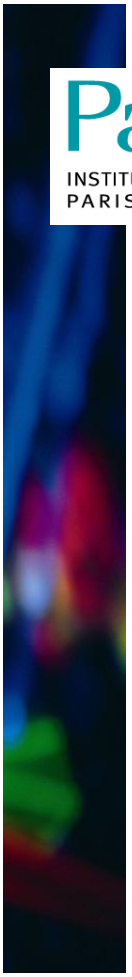

ParisTech
INSTITUT DES SCIENCES ET TECHNOLOGIES
PARIS INSTITUTE OF TECHNOLOGY

ARTS ET MÉTIERS ParisTech

2018-ENAM-0018

École Doctorale n° 432: Science des Métiers de l'ingénieur

Doctorat ParisTech

T H È S E

pour obtenir le grade de docteur délivré par

l'École Nationale Supérieure d'Arts et Métiers

Spécialité "Mécanique-Matériaux"

Présentée et soutenue publiquement par

Francis Praud

le 19 04 2018

Multi-scale modelling of thermoplastic-based woven composites, cyclic and time-dependent behaviour

Directeur de thèse: **Fodil Meraghni**
Co-encadrement de la thèse: **George Chatzigeorgiou**

Jury

Andreas Menzel, Professeur, Technische Universität Dortmund	Président
Laurent Gornet, Maître de conférence (HDR), GeM, École Centrale de Nantes	Rapporteur
Christian Hochard, Professeur, Laboratoire de Mécanique et d'Acoustique de Marseille	Rapporteur
George Chatzigeorgiou, CR1, CNRS, Arts et Métiers ParisTech - Metz	Examinateur
Benoit Delattre, Docteur, PSA	Examinateur
Fodil Meraghni, Professeur, Arts et Métiers ParisTech - Metz	Examinateur
Jérôme Bikard, Docteur, Solvay	Invité
Yves Chemisky, Maître de conférence (HDR), Arts et Métiers ParisTech - Metz	Invité
Mamadou Abdoul Mbacké, Docteur, IRT Jules Verne	Invité

T H È S E

Arts et Métiers ParisTech - Centre de Metz
Laboratoire d'Étude des Microstructures et de Mécanique des Matériaux (LEM3)

"Learn from yesterday, live for today, hope for tomorrow. The important thing is not to stop questioning."

Albert Einstein

Contents

List of Figures

List of Tables

Acknowledgements

I would like to express my sincere gratitude to **Prof. Fodil Mergahni**, my thesis director and main supervisor, for his guidance and support, and for providing me with numerous opportunities for professional growth and development. His enthusiasm and friendly attitude made my stay among his research team a wonderful experience. His patience, availability and flexible supervising time have been the driving force in my ability to complete this PhD thesis. I extend particular thanks to **Dr. George Chatzigeorgiou** and **Dr. Yves Chemisky** for their excellent support, advices and encouragement during all the course of my PhD. Their doors were always open for me. The enriching and constructive interactions we had together hugely contributed to the achievement of this work. and undoubtedly allowed me to grow as a research scientist.

I also thank **Prof. Andreas Menzel** from *Technische Universität Dortmund* for being the president of my PhD thesis committee. I would like to express my gratitude to the reporters, **Dr. Laurent Gornet** from *École Centrale de Nantes* and **Prof. Christian Hochard** from *Laboratoire de Mécanique et d'Acoustique de Marseille*, for their comments and reports. An appreciation also goes to **Dr. Benoit Delattre** from *PSA*, **Dr. Jérôme Bikard** from *Solvay* and **Dr. Mamadou Abdoul Mbacké** from *IRT Jules Verne* for accepting the invitation to attend my thesis defence, but also their valuable and constructive comments all along the COPERSIM Fatigue project.

The financial support of *IRT Jules Verne* through the COPERSIM Fatigue project is gratefully acknowledged along with the industrial partners that took part of it: *Solvay*, *Plastic Omnium*, *PSA* and *Renault*. In this context, I would like to thank **Dr. Tanguy Moro** and **Gaëlle Guyader** from *IRT Jules Verne* for the organization and the management. Additional thanks are also addressed to **Dr. Benjamin Surowiec** from *Plastic Omnium*, **Dr. Nicolas Feld** formerly from *PSA* and **Dr. Jean-François Vittori** from *Renault*. I sincerely appreciated their insightful remarks and advices during the COPERSIM Fatigue project.

I would like to thank **Laurent Peltier** for his valuable help and assistance for the experimental works, as well as **Boris Piotrowski** and **Sylvain Pagura** for the IT support. I also thank all my friends and colleagues for their kindness and keeping me entertained during my time at the *LEM3* laboratory: **Pascal Pomarede**, **Clément Nony-Davadie**, **El-Hadi Tikarrouchine**, **Kevin Bonnay**, **Nadia Achour**, **Nicolas Despringre**, **Francis Adzima**, **Peng Wang**, **Dimitris Chatziathanasiou**, **Dimitris Anagnostou**, **Marie Fischer**, **Wafa Elmay**, **Paul Didier**, **Paul Lohmuller**, **Mathilde Barral**, **Nada Miqoi**, **Nadine Bourgeois**, **Pierre Charbonnier**, **Patrick Moll**, **Gaël Lecoz**, **Pascal Laheurte**, **Jean-Sébastien Lecompte**, **Julien Favre**, **Dominique Vincent**, and countless others with whom I shared great moments.

Finally, I express my sincere gratefulness to all my family and especially my mother **Chantal Altmeyer** who has always been supporting and encouraging me in all my achievements.

Notation

Symbols:

- Scalars: a, b... A, B... α, β...
- Vectors: $\boldsymbol{a}$, $\boldsymbol{b}$...
- 2^{nd} order tensors: $\boldsymbol{A}$, $\boldsymbol{B}$... $\boldsymbol{\alpha}$, $\boldsymbol{\beta}$...
- 4^{th} order tensors: $\mathbb{A}$, $\mathbb{B}$...
- Quantities with undefined order: $\mathcal{A}$, $\mathcal{B}$...

2^{nd} and 4^{th} order identity tensors:

$$(\boldsymbol{I})_{ij} = \delta_{ij} \qquad (\mathbb{I})_{ijkl} = \frac{1}{2}(\delta_{ik}\delta_{jl} + \delta_{il}\delta_{jk}) \qquad \text{where} \quad \delta_{ij} = \begin{cases} 1 & \text{if} \quad i = j \\ 0 & \text{if} \quad i \neq j \end{cases}$$

Tensorial products:

- Single contracted products:

$$\boldsymbol{a} \cdot \boldsymbol{b} = a_i b_i \qquad (\boldsymbol{A} \cdot \boldsymbol{b})_i = A_{ij} b_j \qquad (\boldsymbol{A} \cdot \boldsymbol{B})_{ij} = A_{ik} B_{kj}$$

- Twice contracted products:

$$\boldsymbol{A} : \boldsymbol{B} = A_{ij} B_{ij} \qquad (\mathbb{A} : \boldsymbol{B})_{ij} = A_{ijkl} B_{kl} \qquad (\mathbb{A} : \mathbb{B})_{ijkl} = A_{ijmn} B_{mnkl}$$

- Dyadic products:

$$(\boldsymbol{a} \otimes \boldsymbol{b})_{ij} = a_i b_j \qquad (\boldsymbol{A} \otimes \boldsymbol{B})_{ijkl} = A_{ij} B_{kl} \qquad (\boldsymbol{A} \overline{\otimes} \boldsymbol{B})_{ijkl} = A_{ik} B_{jl} \qquad (\boldsymbol{A} \underline{\otimes} \boldsymbol{B})_{ijkl} = A_{il} B_{jk}$$

– Undefined order scalar product:

$$\mathcal{A} * \mathcal{B} = \begin{cases} \mathcal{A} \times \mathcal{B} & \text{if } \mathcal{A} \text{ and } \mathcal{B} \text{ are scalars} \\ \mathcal{A} \cdot \mathcal{B} & \text{if } \mathcal{A} \text{ and } \mathcal{B} \text{ are vectors} \\ \mathcal{A} : \mathcal{B} & \text{if } \mathcal{A} \text{ and } \mathcal{B} \text{ are } 2^{nd} \text{ order tensors} \end{cases}$$

Tensorial operators:

– Transpose:

$$(\boldsymbol{A}^T)_{ij} = A_{ji} \qquad (\mathbb{A}^T)_{ijkl} = A_{klij}$$

– Trace of a 2^{nd} order tensor:

$$\mathrm{tr}(\boldsymbol{A}) = A_{ii}$$

– Inverse of a 2^{nd} order tensor:

$$\boldsymbol{A}^{-1} \qquad \text{such as} \qquad \boldsymbol{A} \cdot \boldsymbol{A}^{-1} = \boldsymbol{A}^{-1} \cdot \boldsymbol{A} = \boldsymbol{I} \qquad \text{(as long as } \boldsymbol{A} \text{ is invertible)}$$

– Inverse of a 4^{th} order tensor that has the minor symmetries ($A_{ijkl} = A_{jikl} = A_{ijlk}$):

$$\mathbb{A}^{-1} \qquad \text{such as} \qquad \mathbb{A} : \mathbb{A}^{-1} = \mathbb{A}^{-1} : \mathbb{A} = \mathbb{I} \qquad \text{(as long as } \mathbb{A} \text{ is invertible)}$$

Differential operators:

– Gradient:

$$\left(\mathbf{grad}_{\boldsymbol{x}}(a)\right)_i = \frac{\partial a}{\partial x_i} \qquad \left(\mathbf{Grad}_{\boldsymbol{x}}(\boldsymbol{a})\right)_{ij} = \frac{\partial a_i}{\partial x_j}$$

– Divergence:

$$\mathrm{div}_{\boldsymbol{x}}(\boldsymbol{a}) = \frac{\partial a_i}{\partial x_i} \qquad \left(\mathbf{div}_{\boldsymbol{x}}(\boldsymbol{A})\right)_i = \frac{\partial A_{ij}}{\partial x_j}$$

– Rate:

$$\dot{\mathcal{A}} = \frac{d\mathcal{A}}{dt}$$

Positive and negative part of a scalar:

$$\langle a \rangle_+ = \begin{cases} a & \text{if } a \geq 0 \\ 0 & \text{if } a < 0 \end{cases} \qquad \langle a \rangle_- = \begin{cases} a & \text{if } a \leq 0 \\ 0 & \text{if } a > 0 \end{cases}$$

Voigt notation:

As usual in continuum mechanics, the symmetric 2^{nd} order tensors ($A_{ij} = A_{ji}$) and the 4^{th} order tensors having at least the minor symmetries ($A_{ijkl} = A_{jikl} = A_{ijlk}$) can be considered with reduced orders according to the Voigt notation for simplifying the calculations. In this manuscript the following Voigt notation is adopted.

When symmetric, a 2^{nd} order tensor has only 6 independent components and can be written under the form of a 6×1 vector. The "stress-type" and "strain-type" 2^{nd} order tensors, respectively denoted by $\boldsymbol{\sigma}$ and $\boldsymbol{\varepsilon}$, are expressed in Voigt notation as follows:

$$\boldsymbol{\sigma} = \begin{pmatrix} \sigma_{11} & \sigma_{12} & \sigma_{13} \\ & \sigma_{22} & \sigma_{23} \\ \text{sym.} & & \sigma_{33} \end{pmatrix} \xrightarrow[\text{Voigt not.}]{} \boldsymbol{\sigma} = \begin{Bmatrix} \sigma_{11} \\ \sigma_{22} \\ \sigma_{33} \\ \sigma_{12} \\ \sigma_{13} \\ \sigma_{23} \end{Bmatrix},$$

$$\boldsymbol{\varepsilon} = \begin{pmatrix} \varepsilon_{11} & \varepsilon_{12} & \varepsilon_{13} \\ & \varepsilon_{22} & \varepsilon_{23} \\ \text{sym.} & & \varepsilon_{33} \end{pmatrix} \xrightarrow[\text{Voigt not.}]{} \boldsymbol{\varepsilon} = \begin{Bmatrix} \varepsilon_{11} \\ \varepsilon_{22} \\ \varepsilon_{33} \\ 2\varepsilon_{12} \\ 2\varepsilon_{13} \\ 2\varepsilon_{23} \end{Bmatrix}.$$

Using this formalism, the twice contracted product between a "stress-type" and a "strain-type" quantity can be written as a scalar product of two vectors:

$$\boldsymbol{\sigma} : \boldsymbol{\varepsilon} \xrightarrow[\text{Voigt not.}]{} \begin{Bmatrix} \sigma_{11} \\ \sigma_{22} \\ \sigma_{33} \\ \sigma_{12} \\ \sigma_{13} \\ \sigma_{23} \end{Bmatrix}^T \times \begin{Bmatrix} \varepsilon_{11} \\ \varepsilon_{22} \\ \varepsilon_{33} \\ 2\varepsilon_{12} \\ 2\varepsilon_{13} \\ 2\varepsilon_{23} \end{Bmatrix}.$$

However, some precautions must be taken when dealing with the twice contracted product of two 2^{nd} order tensors of the same type. In order to be well consistent with the the tensorial calculation, the following expressions are proposed to express the twice contracted product between two "stress-type" or between two "strain-type" quantities:

$$\boldsymbol{\sigma'} : \boldsymbol{\sigma} \xrightarrow[\text{Voigt not.}]{} \begin{Bmatrix} \sigma'_{11} \\ \sigma'_{22} \\ \sigma'_{33} \\ \sigma'_{12} \\ \sigma'_{13} \\ \sigma'_{23} \end{Bmatrix}^T \times \begin{pmatrix} 1 & 0 & 0 & 0 & 0 & 0 \\ & 1 & 0 & 0 & 0 & 0 \\ & & 1 & 0 & 0 & 0 \\ & & & 2 & 0 & 0 \\ & & & & 2 & 0 \\ \text{sym.} & & & & & 2 \end{pmatrix} \times \begin{Bmatrix} \sigma_{11} \\ \sigma_{22} \\ \sigma_{33} \\ \sigma_{12} \\ \sigma_{13} \\ \sigma_{23} \end{Bmatrix},$$

$$\boldsymbol{\varepsilon'} : \boldsymbol{\varepsilon} \xrightarrow[\text{Voigt not.}]{} \begin{Bmatrix} \varepsilon'_{11} \\ \varepsilon'_{22} \\ \varepsilon'_{33} \\ 2\varepsilon'_{12} \\ 2\varepsilon'_{13} \\ 2\varepsilon'_{23} \end{Bmatrix}^T \times \begin{pmatrix} 1 & 0 & 0 & 0 & 0 & 0 \\ & 1 & 0 & 0 & 0 & 0 \\ & & 1 & 0 & 0 & 0 \\ & & & \frac{1}{2} & 0 & 0 \\ & & & & \frac{1}{2} & 0 \\ \text{sym.} & & & & & \frac{1}{2} \end{pmatrix} \times \begin{Bmatrix} \varepsilon_{11} \\ \varepsilon_{22} \\ \varepsilon_{33} \\ 2\varepsilon_{12} \\ 2\varepsilon_{13} \\ 2\varepsilon_{23} \end{Bmatrix}.$$

A 4^{th} order tensor with the minor symmetries has only 36 independent components and can be written under the form of a 6×6 matrix. There are four types of 4^{th} order tensors: the "stiffness-type", the "compliance-type", the "stress-to-stress-type" and the "strain-to-strain-type". They are respectively denoted in this section by $\mathbb{C}$, $\mathbb{S}$, $\mathbb{B}$ and $\mathbb{A}$.

A "stiffness-type" tensor results from the dyadic product of two "stress-type" tensors. The twice contracted product of a "stiffness-type" 4^{th} order tensor with a "strain-type" 2^{nd} order tensor returns a "stress-type" quantity. Written with the help of the Voigt notation, this gives:

$$\mathbb{C} = \boldsymbol{\sigma'} \otimes \boldsymbol{\sigma''} \xrightarrow[\text{Voigt not.}]{} \mathbb{C} = \begin{pmatrix} C_{1111} & C_{1122} & C_{1133} & C_{1112} & C_{1113} & C_{1123} \\ C_{2211} & C_{2222} & C_{2233} & C_{2212} & C_{2213} & C_{2223} \\ C_{3311} & C_{3322} & C_{3333} & C_{3312} & C_{3313} & C_{3323} \\ C_{1211} & C_{1222} & C_{1233} & C_{1212} & C_{1213} & C_{1223} \\ C_{1311} & C_{1322} & C_{1333} & C_{1312} & C_{1313} & C_{1323} \\ C_{2311} & C_{2322} & C_{2333} & C_{2312} & C_{2313} & C_{2323} \end{pmatrix},$$

with $C_{ijkl} = \sigma'_{ij}\sigma''_{kl}$.

$$\boldsymbol{\sigma} = \mathbb{C} : \boldsymbol{\varepsilon} \xrightarrow[\text{Voigt not.}]{} \begin{Bmatrix} \sigma_{11} \\ \sigma_{22} \\ \sigma_{33} \\ \sigma_{12} \\ \sigma_{13} \\ \sigma_{23} \end{Bmatrix} = \begin{pmatrix} C_{1111} & C_{1122} & C_{1133} & C_{1112} & C_{1113} & C_{1123} \\ C_{2211} & C_{2222} & C_{2233} & C_{2212} & C_{2213} & C_{2223} \\ C_{3311} & C_{3322} & C_{3333} & C_{3312} & C_{3313} & C_{3323} \\ C_{1211} & C_{1222} & C_{1233} & C_{1212} & C_{1213} & C_{1223} \\ C_{1311} & C_{1322} & C_{1333} & C_{1312} & C_{1313} & C_{1323} \\ C_{2311} & C_{2322} & C_{2333} & C_{2312} & C_{2313} & C_{2323} \end{pmatrix} \times \begin{Bmatrix} \varepsilon_{11} \\ \varepsilon_{22} \\ \varepsilon_{33} \\ 2\varepsilon_{12} \\ 2\varepsilon_{13} \\ 2\varepsilon_{23} \end{Bmatrix}.$$

A "compliance-type" tensor results from the dyadic product of two "strain-type" tensors. The twice contracted product of a "compliance-type" 4^{th} order tensor with a "stress-type" 2^{nd} order tensor returns a "strain-type" quantity. Written with the help of the Voigt notation, this gives:

$$\mathbb{S} = \boldsymbol{\varepsilon'} \otimes \boldsymbol{\varepsilon''} \xrightarrow[\text{Voigt not.}]{} \mathbb{S} = \begin{pmatrix} S_{1111} & S_{1122} & S_{1133} & 2S_{1112} & 2S_{1113} & 2S_{1123} \\ S_{2211} & S_{2222} & S_{2233} & 2S_{2212} & 2S_{2213} & 2S_{2223} \\ S_{3311} & S_{3322} & S_{3333} & 2S_{3312} & 2S_{3313} & 2S_{3323} \\ 2S_{1211} & 2S_{1222} & 2S_{1233} & 4S_{1212} & 4S_{1213} & 4S_{1223} \\ 2S_{1311} & 2S_{1322} & 2S_{1333} & 4S_{1312} & 4S_{1313} & 4S_{1323} \\ 2S_{2311} & 2S_{2322} & 2S_{2333} & 4S_{2312} & 4S_{2313} & 4S_{2323} \end{pmatrix},$$

with $S_{ijkl} = \varepsilon'_{ij}\varepsilon''_{kl}$.

$$\boldsymbol{\varepsilon} = \mathbb{S} : \boldsymbol{\sigma} \xrightarrow[\text{Voigt not.}]{} \begin{Bmatrix} \varepsilon_{11} \\ \varepsilon_{22} \\ \varepsilon_{33} \\ 2\varepsilon_{12} \\ 2\varepsilon_{13} \\ 2\varepsilon_{23} \end{Bmatrix} = \begin{pmatrix} S_{1111} & S_{1122} & S_{1133} & 2S_{1112} & 2S_{1113} & 2S_{1123} \\ S_{2211} & S_{2222} & S_{2233} & 2S_{2212} & 2S_{2213} & 2S_{2223} \\ S_{3311} & S_{3322} & S_{3333} & 2S_{3312} & 2S_{3313} & 2S_{3323} \\ 2S_{1211} & 2S_{1222} & 2S_{1233} & 4S_{1212} & 4S_{1213} & 4S_{1223} \\ 2S_{1311} & 2S_{1322} & 2S_{1333} & 4S_{1312} & 4S_{1313} & 4S_{1323} \\ 2S_{2311} & 2S_{2322} & 2S_{2333} & 4S_{2312} & 4S_{2313} & 4S_{2323} \end{pmatrix} \times \begin{Bmatrix} \sigma_{11} \\ \sigma_{22} \\ \sigma_{33} \\ \sigma_{12} \\ \sigma_{13} \\ \sigma_{23} \end{Bmatrix}.$$

A "stress-to-stress-type" tensor results from the dyadic product of a "stress-type" with a "strain-type" tensor. The twice contracted product of a "stress-to-stress-type" 4^{th} order tensor with a "stress-type" 2^{nd} order tensor returns a "stress-type" quantity. Written with the help of the Voigt notation, this gives:

$$\mathbb{B} = \boldsymbol{\sigma'} \otimes \boldsymbol{\varepsilon'} \xrightarrow[\text{Voigt not.}]{} \mathbb{B} = \begin{pmatrix} B_{1111} & B_{1122} & B_{1133} & 2B_{1112} & 2B_{1113} & 2B_{1123} \\ B_{2211} & B_{2222} & B_{2233} & 2B_{2212} & 2B_{2213} & 2B_{2223} \\ B_{3311} & B_{3322} & B_{3333} & 2B_{3312} & 2B_{3313} & 2B_{3323} \\ B_{1211} & B_{1222} & B_{1233} & 2B_{1212} & 2B_{1213} & 2B_{1223} \\ B_{1311} & B_{1322} & B_{1333} & 2B_{1312} & 2B_{1313} & 2B_{1323} \\ B_{2311} & B_{2322} & B_{2333} & 2B_{2312} & 2B_{2313} & 2B_{2323} \end{pmatrix},$$

with $B_{ijkl} = \sigma'_{ij}\varepsilon'_{kl}$.

$$\boldsymbol{\sigma''} = \mathbb{B} : \boldsymbol{\sigma} \xrightarrow[\text{Voigt not.}]{} \begin{Bmatrix} \sigma''_{11} \\ \sigma''_{22} \\ \sigma''_{33} \\ \sigma''_{12} \\ \sigma''_{13} \\ \sigma''_{23} \end{Bmatrix} = \begin{pmatrix} B_{1111} & B_{1122} & B_{1133} & 2B_{1112} & 2B_{1113} & 2B_{1123} \\ B_{2211} & B_{2222} & B_{2233} & 2B_{2212} & 2B_{2213} & 2B_{2223} \\ B_{3311} & B_{3322} & B_{3333} & 2B_{3312} & 2B_{3313} & 2B_{3323} \\ B_{1211} & B_{1222} & B_{1233} & 2B_{1212} & 2B_{1213} & 2B_{1223} \\ B_{1311} & B_{1322} & B_{1333} & 2B_{1312} & 2B_{1313} & 2B_{1323} \\ B_{2311} & B_{2322} & B_{2333} & 2B_{2312} & 2B_{2313} & 2B_{2323} \end{pmatrix} \times \begin{Bmatrix} \sigma_{11} \\ \sigma_{22} \\ \sigma_{33} \\ \sigma_{12} \\ \sigma_{13} \\ \sigma_{23} \end{Bmatrix}.$$

A "strain-to-strain-type" tensor results from the dyadic product of a "strain-type" with a "stress-type" tensor. The twice contracted product of a "strain-to-strain-type" 4^{th} order tensor with a "strain-type" 2^{nd} order tensor returns a "strain-type" quantity. Written with the help of the Voigt notation, this gives:

$$\mathbb{A} = \boldsymbol{\varepsilon'} \otimes \boldsymbol{\sigma'} \xrightarrow[\text{Voigt not.}]{} \mathbb{A} = \begin{pmatrix} A_{1111} & A_{1122} & A_{1133} & A_{1112} & A_{1113} & A_{1123} \\ A_{2211} & A_{2222} & A_{2233} & A_{2212} & A_{2213} & A_{2223} \\ A_{3311} & A_{3322} & A_{3333} & A_{3312} & A_{3313} & A_{3323} \\ 2A_{1211} & 2A_{1222} & 2A_{1233} & 2A_{1212} & 2A_{1213} & 2A_{1223} \\ 2A_{1311} & 2A_{1322} & 2A_{1333} & 2A_{1312} & 2A_{1313} & 2A_{1323} \\ 2A_{2311} & 2A_{2322} & 2A_{2333} & 2A_{2312} & 2A_{2313} & 2A_{2323} \end{pmatrix},$$

with $A_{ijkl} = \varepsilon'_{ij}\sigma'_{kl}$.

$$\boldsymbol{\varepsilon''} = \mathbb{A} : \boldsymbol{\varepsilon} \xrightarrow[\text{Voigt not.}]{} \begin{Bmatrix} \varepsilon''_{11} \\ \varepsilon''_{22} \\ \varepsilon''_{33} \\ 2\varepsilon''_{12} \\ 2\varepsilon''_{13} \\ 2\varepsilon''_{23} \end{Bmatrix} = \begin{pmatrix} A_{1111} & A_{1122} & A_{1133} & A_{1112} & A_{1113} & A_{1123} \\ A_{2211} & A_{2222} & A_{2233} & A_{2212} & A_{2213} & A_{2223} \\ A_{3311} & A_{3322} & A_{3333} & A_{3312} & A_{3313} & A_{3323} \\ 2A_{1211} & 2A_{1222} & 2A_{1233} & 2A_{1212} & 2A_{1213} & 2A_{1223} \\ 2A_{1311} & 2A_{1322} & 2A_{1333} & 2A_{1312} & 2A_{1313} & 2A_{1323} \\ 2A_{2311} & 2A_{2322} & 2A_{2333} & 2A_{2312} & 2A_{2313} & 2A_{2323} \end{pmatrix} \times \begin{Bmatrix} \varepsilon_{11} \\ \varepsilon_{22} \\ \varepsilon_{33} \\ 2\varepsilon_{12} \\ 2\varepsilon_{13} \\ 2\varepsilon_{23} \end{Bmatrix}.$$

Note that, with the Voigt notation, the inverse of a "stiffness-type" tensor returns a "compliance-like" tensor and reciprocally, the inverse of a "compliance-like" tensor returns a "stiffness-like" tensor. The inverse of a "stress-to-stress" or a "strain-to-strain" tensor gives a tensor of the same type.

Additionally, the 2^{nd} and 4^{th} order identity tensors are given in Voigt notation by:

$$\boldsymbol{I} = \begin{Bmatrix} 1 \\ 1 \\ 1 \\ 0 \\ 0 \\ 0 \end{Bmatrix}, \qquad \mathbb{I} = \begin{pmatrix} 1 & 0 & 0 & 0 & 0 & 0 \\ & 1 & 0 & 0 & 0 & 0 \\ & & 1 & 0 & 0 & 0 \\ & & & 1 & 0 & 0 \\ & & & & 1 & 0 \\ \text{sym.} & & & & & 1 \end{pmatrix}$$

General Introduction

Contents

1 Motivations and context

A composite is a material constructed from two or more constituents with significantly different physical properties which, when combined, produce a new material with characteristics unavailable from its individual components. The constituents remain separate and distinct within the composite material. A vast majority of composites especially in automotive industry, are made of a polymer matrix and fibres (or reinforcement). The matrix surrounds and supports the fibres by maintaining their positions. The fibres impart their stiffness and strength properties to mechanically enhance the matrix, which is usually lighter than the reinforcement. This produces materials that are particularly suitable for structural applications. They have very interesting properties in terms of stiffness and/or strength, while being relatively light when compared to traditional materials like metals.

For several decades, composite materials, due to their remarkable properties, have been extensively utilized in many industries, such as aeronautic or automotive, where designing lightweight structures becomes an objective of prime importance. This increasing utilization is achieved with strong requirements in terms of performance, strength and durability. In the automotive industry, thermoplastic-based composites appear to be an interesting alternative to classical metallic materials. Indeed, besides their lightweight and good mechanical properties, this type of composites can be easily and rapidly manufactured for a reduced cost. Today, thermoplastic-based composites are mainly utilized for moderately loaded structural components (i.e. bumpers). However, the actual economic and ecological requirements lead the manufacturers to consider composite materials also for highly loaded components that were classically made of metals until now.

The wide-scale use of thermoplastic-based composites in structural applications has been hampered by the lack of predictive simulation tools, especially for failure and lifetime estimation. Unlike classical materials, the fatigue of thermoplastic-based composites still remains a major scientific issue and the current prediction tools do not take into account all the specificities that exist in such materials. Among them, it can be mentioned: the damage mechanisms coupled to the rheology of the matrix, the anisotropy, and the effects related to the microstructure, which play a key role in the initiation and evolution of these phenomena.

2 Scope of the thesis

This thesis is part of the innovative COPERSIM Fatigue project (COmposite PERformance SIMulation), which aims at structuring the modelling and simulation tools towards the durability prediction of composite components. It involves a consortium with the following industrial and academic partners: *IRT Jules Verne* (project management leader), *PSA*, *Renault*, *Solvay*, and *Plastic-Omnium* and *Arts et Métiers ParisTech* (scientific leader). The aim of this project is the development of an integrated multi-scale modelling approach for failure analyses and lifetime estimations of composite structures for automotive applications. To achieve these objectives, it is essential to fully understand and predict the cyclic and time-dependent behaviour of thermoplastic-based composites through the description of the local damage mechanisms and deformation processes. This is the scope of the present thesis, where the attention will be focused on the case of thermoplastic-based woven composites.

In this thesis, a multi-scale model established from the concept of periodic homogeniz-

ation is utilized to describe the cyclic and time-dependent response of thermoplastic-based woven composites. In the proposed approach, the macroscopic response of the composite is determined from a FE simulation of the unit cell representative of the microstructure, where the local constitutive laws of the components are integrated (matrix and the yarns). The local behaviour of the thermoplastic matrix is described by a phenomenological multi-mechanisms constitutive model accounting for viscoelasticity, viscoplasticity and ductile damage. For the yarns, a hybrid micromechanical-phenomenological constitutive model is utilized to describe the local behaviour of the yarns. The latter considers anisotropic damage and anelasticity induced by the presence of a diffuse micro-crack network inside the yarns. Besides describing the cyclic and time-dependent response of thermoplastic-based woven composites, the multi-scale model is employed to understand the local damage mechanisms and deformation processes, and to analyse their influence on the macroscopic response of the composite. In parallel to the modelling efforts, experimental works are also carried out on both the studied composite and the unfilled matrix in order to feed and to validate the fully integrated multi-scale modelling approach.

It is important to mention that the proposed multi-scale modelling approach is entirely modular, as it results from the assembly of several sub-models and from the geometric definition of the microstructure. Thus, if a composite with another composition and/or another periodic microstructure is to be studied, then the present multi-scale approach is still valid and only the ingredients should change.

This thesis is structured as follows:

- In Chapter I, a comprehensive framework of multi-scale modelling based on the concept of periodic homogenization is presented and applied to the case of woven composites. The approach establishes a proper transition between the macroscopic and microscopic scales, enabling to simulate the macroscopic response of a composite through the integration of the local constitutive equations of each individual component (the matrix and the yarns).

- In Chapter II, a phenomenological multi-mechanisms constitutive model is proposed to describe the mechanical behaviour of thermoplastic polymers and is intended to be used as matrix phase in the multi-scale modelling approach for the woven composite. The constitutive equations lie within the framework of thermodynamics and account for viscoelasticity, viscoplasticity and ductile damage. The developed model is identified for the polyamide 6-6 through a suitable experimental program as well as a stepwise strategy.

- In Chapter III, a hybrid micromechanical-phenomenological constitutive model is proposed to predict the mechanical behaviour of unidirectional composites and is intended to be used as yarn phase in the multi-scale modelling approach for the woven composite. The constitutive equations are formulated within the framework of thermodynamics and account for anisotropic damage and anelasticity induced by the presence of a diffuse micro-crack network. The representation of damage is achieved through a micromechanical description of a micro-cracked Representative Volume Element (RVE).

- In Chapter IV, a multi-scale model for woven composites is established from the homogenization scheme described in Chapter I, in which the local constitutive models

of the matrix and the yarns presented in Chapters II and III, respectively, are introduced. This multi-scale model is employed to capture the cyclic and time-dependent macroscopic response of the studied composites.

3 Studied composite

The composite material studied in this work is supplied by *Solvay* under the denomination *Evolite*. As shown in Figure 1, this composite is made of a polyamide 6-6 matrix and a E-glass balanced 2-2 twill weave woven reinforcement (650 g.m^{-2}). Such a weaving pattern is obtained by passing a weft yarn over two warp yarns and then under two warp yarns and so on, with an offset, between rows to create the characteristic diagonal pattern. The material is manufactured by thermocompression process and, after impregnation, has a fibre volume fraction of 50%. It is provided under the form of plates with the following stacking sequences: $[0^o]_4$, $[\pm 15^o]_s$, $[\pm 30^o]_s$ and $[\pm 45^o]_s$. The thickness of the individual layers is about 0.5 mm, making a total thickness of 2 mm for the plates.

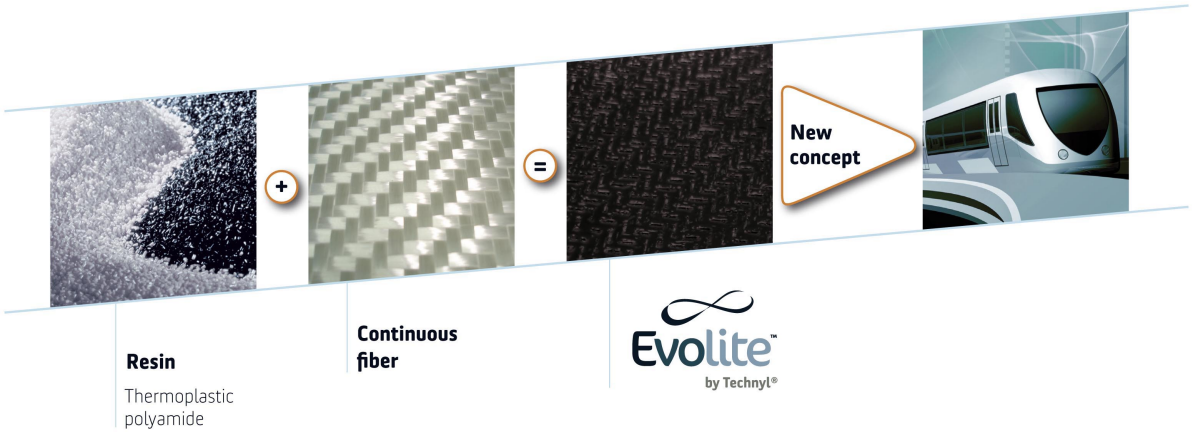

Figure 1: Studied composite material: *Evolite* by *Solvay*.

Chapter I

Multi-scale modelling of woven composites using periodic homogenization

Contents

The content of this chapter was discussed in various conference proceedings [164, 166, 184].

1 Introduction

Homogenization and multi-scale analyses of heterogeneous materials in which the components exhibit non-linear mechanical responses, such as thermoplastic-based woven composites, is nowadays at the centre of the research attentions. Among all the existing theories, two of them appear to be particularly attractive for this purpose, as they can easily account for many types of constitute laws and microstructures (including woven reinforcements):

- The mean-field approaches [172] based on the Eshelby solution [59] such as the micromechanical scheme of Mori-Tanaka [137, 16], the self-consistent method [77, 141] or the method proposed by Ponte Castañeda and Willis [161]. These theories usually deal with randomly distributed ellipsoidal inclusions as inhomogeneities and can also account for an eventual coating [17, 19]. Particularly adapted to the cases of short and long fibres reinforced composites, woven composites may be eventually considered if the yarns undulation is neglected, or by discretizing the wavy yarns into smaller segments and replacing them with an equivalent system of ellipsoids [1]. While initially developed for linear elasticity or thermoelasticity [158], these methods can be extended to the case of non-linear behaviours through an incremental formulation [66, 96, 49, 29, 157, 159, 160, 41, 27, 196, 134, 45, 90, 195, 2, 33]. In such analyses, the local instantaneous stiffness (tangent operator) of each phase is used to compute the stress-strain localisations and the resultant overall instantaneous response of the composite. While these methods are based on semi-analytical solutions with fast computations, they unfortunately keep a limited accuracy and must be used with caution, especially when the matrix phase exhibits a non-linear response [96]. This inaccuracy is mainly caused by the local fields in the matrix that are considered in an average way. This is likely not to give good enough estimates when the non-linearity is matrix-dominated. However, it should be noted that more accurate solutions are sometimes obtained via specific enhancements [49, 29, 157, 196, 195]. Another issue regarding the Eshelby-based mean-field methods is the lack of energetic consistency between the macroscopic and microscopic works (non-respect of the Hill-Mandel condition). This issue is illustrated by the absence of major symmetry on the macroscopic elasticity tensor estimated from Mori-Tanaka or self-consistent for certain configurations of multiple inhomogeneities with different shapes [18].

- The periodic homogenization [173, 181, 133], by opposition to the mean-field theories, is a full-field approach that is particularly suitable for composites with periodic microstructure such as woven composites. Fundamentally, periodic homogenization provides a rigorous framework allowing to properly define the concept of homogenized behaviour [30]. Moreover, this framework is independent of the choice of the local constitutive laws of the constituents [34]. Due to its periodicity, the RVE is represented by the smallest repeating element, commonly referred as the unit cell, on which well-defined boundary conditions are applied. Except for particular cases, the resolution of such a problem requires the use of numerical techniques, mostly the finite element method, that may lead to important computational costs. The geometry of the unit cell is then represented through a finite element mesh integrating the local constitutive equations of each sub-domain. Thereby, the obtained solutions

generally show good accuracy, depending on the mesh discretization, and are well energetically consistent, as it is proven that the Hill-Mandel condition holds when dealing with periodic homogenization. This last point is very important, because it allows to extend this approach to fully-coupled thermomechanical analyses [32, 22, 33].

From the above discussion, the theories of periodic homogenization are the most suitable to the case of woven composites. This chapter presents a comprehensive framework of multi-scale modelling based on the concept of periodic homogenization [173, 181, 133] that lies within the small strain assumption at isothermal conditions. The approach establishes a proper transition between the macroscopic and microscopic scales. The macroscopic response of a composite with a periodic microstructure is then obtained through the simulation of its unit cell, integrating the local constitutive laws of each individual component. From a practical point of view, specific boundary conditions are used to control the unit cell with the help of additional degrees of freedom that are directly linked to the macroscopic strains and stresses [112, 113, 114]. Proceeding this way then allows to apply any state of macroscopic strain, stress or even mixed stress-strain on the unit cell. A novel extension of this method is also proposed, permitting to control the unit cell with any type of off-axis loading paths, while keeping a unit cell defined in its coordinate system.

In order to apply the framework of periodic homogenization to the case of woven composites, it is necessary to provide a geometric representation of the unit cell along with its associated finite element mesh. In this purpose, many works have been already undertaken [116, 117, 188, 118, 177, 40, 115] , leading to the development of several dedicated tools. Among these tools, the *TexGen* platform [115], an open source and free software developed at the University of Nottingham, shows very interesting capabilities in generating finite element unit cells of any woven patterns. That is why it is utilized in this work.

This chapter is structured as follows: In Section 2, a general framework of multi-scale modelling based on the concept of periodic homogenization [173, 181, 133] is presented. The latter includes both theoretical and practical aspects of the approach. Section 3 is devoted to the geometrical and finite element representation of unit cells for woven composites via the software *TexGen* [115]. Section 4 presents applicative examples dealing with linear elasticity like the assessments of the homogenized stiffness properties of a woven composite. Note that non-linear applications will be treated in Chapter IV, once the local constitutive laws will have been introduced in Chapters II and III. To finish, Section 5 summarizes the main conclusions related to this chapter.

2 Periodic homogenization

2.1 Theoretical framework

2.1.1 Scale separation

A periodic medium is defined by a unit cell that is representative of the microstructure. If the dimensions of the unit cell are small enough compared to the dimensions of the macroscopic media, then a scale separation can be assumed and two scales are considered:

- A macroscopic scale defined by the macroscopic (or global) coordinates denoted by $\overline{\boldsymbol{x}}$.
- A microscopic scale defined by the microscopic (or local) coordinates denoted by $\boldsymbol{x}$.

The assumption of scale separation ($\overline{\boldsymbol{x}} >> \boldsymbol{x}$) allows to consider the unit cell as a macroscopic material point. Thus, at the macroscopic scale, the heterogeneous medium is replaced by an equivalent homogenized medium, which has an equivalent macroscopic response in an average sense (Figure I.1).

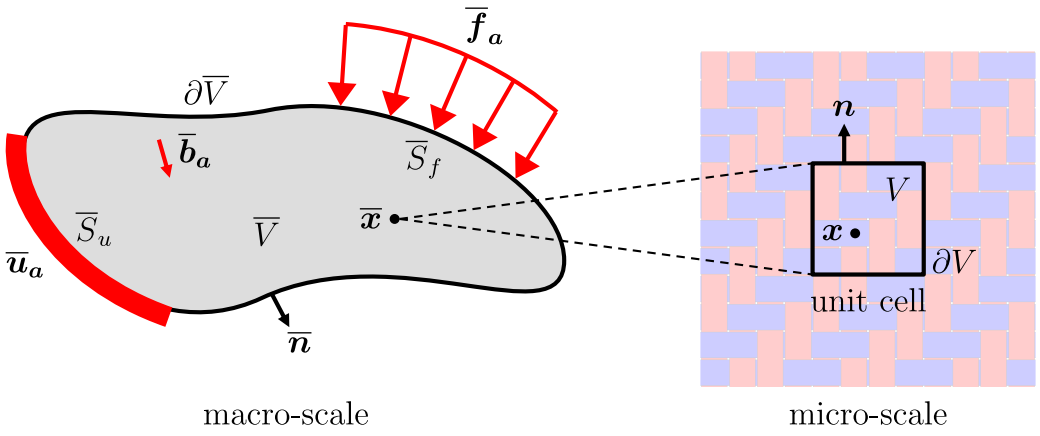

Figure I.1: Schematic representation of a heterogeneous material with a periodic microstructure by considering a scale separation.

Under quasi-static conditions (the inertia effects are considered negligible), the motion of any macroscopic and microscopic material point $\overline{M}(\overline{\boldsymbol{x}})$ and $M(\overline{\boldsymbol{x}}, \boldsymbol{x})$, respectively, is governed by the macro-scale and micro-scale equations given in Table I.1.

Equations	Macro-scale $\forall \overline{\boldsymbol{x}} \in \overline{V}, \forall t$	Micro-scale $\forall \overline{\boldsymbol{x}} \in \overline{V}, \forall \boldsymbol{x} \in V, \forall t$
Equilibrium	$\mathbf{div}_{\overline{\boldsymbol{x}}}(\overline{\boldsymbol{\sigma}}) + \overline{\boldsymbol{b}}_a = \boldsymbol{0}$	$\mathbf{div}_{\boldsymbol{x}}(\boldsymbol{\sigma}) = \boldsymbol{0}$
Kinematics	$\overline{\boldsymbol{\varepsilon}} = \frac{1}{2}\left(\mathbf{Grad}_{\overline{\boldsymbol{x}}}(\overline{\boldsymbol{u}}) + \mathbf{Grad}^T_{\overline{\boldsymbol{x}}}(\overline{\boldsymbol{u}})\right)$	$\boldsymbol{\varepsilon} = \frac{1}{2}\left(\mathbf{Grad}_{\boldsymbol{x}}(\boldsymbol{u}) + \mathbf{Grad}^T_{\boldsymbol{x}}(\boldsymbol{u})\right)$
Constitutive law	$\overline{\boldsymbol{\sigma}} = \overline{\boldsymbol{F}}(\overline{\boldsymbol{\varepsilon}})$	$\boldsymbol{\sigma} = \boldsymbol{F}(\boldsymbol{x}, \boldsymbol{\varepsilon})$
Mechanical work	$\overline{W} = \overline{\boldsymbol{\sigma}} : \overline{\boldsymbol{\varepsilon}}$	$W = \boldsymbol{\sigma} : \boldsymbol{\varepsilon}$

Table I.1: Macro-scale and micro-scale equations.

The macroscopic problem is defined by the macro-scale equations in the left part of Table I.1 along with macroscopic boundary conditions, as illustrated on Figure I.1:

$$\begin{cases} \overline{\boldsymbol{u}}(\overline{\boldsymbol{x}},t) = \overline{\boldsymbol{u}}_{\boldsymbol{a}}(\overline{\boldsymbol{x}},t) & \forall \overline{\boldsymbol{x}} \in \overline{S}_u \subset \partial\overline{V} \\ \overline{\boldsymbol{\sigma}}(\overline{\boldsymbol{x}},t)\cdot\overline{\boldsymbol{n}}(\overline{\boldsymbol{x}}) = \overline{\boldsymbol{f}}_{\boldsymbol{a}}(\overline{\boldsymbol{x}},t) & \forall \overline{\boldsymbol{x}} \in \overline{S}_f \subset \partial\overline{V} \qquad \text{with} \quad \overline{S}_u \cap \overline{S}_f = \varnothing, \\ \overline{\boldsymbol{\sigma}}(\overline{\boldsymbol{x}},t)\cdot\overline{\boldsymbol{n}}(\overline{\boldsymbol{x}}) = \boldsymbol{0} & \forall \overline{\boldsymbol{x}} \in \partial\overline{V} \setminus (\overline{S}_u \cup \overline{S}_f) \end{cases} \tag{I.1}$$

where $\overline{\boldsymbol{n}}$ stands for the outgoing normal of each macroscopic point on the border of the macroscopic medium ($\forall \overline{\boldsymbol{x}} \in \partial\overline{V}$). $\overline{\boldsymbol{u}}_{\boldsymbol{a}}$ represents the applied displacements on $\overline{S}_u$ and $\overline{\boldsymbol{f}}_{\boldsymbol{a}}$ the applied forces (force per unit of surface) on $\overline{S}_f$. In Table I.1, $\overline{\boldsymbol{b}}_{\boldsymbol{a}}$ is an eventual macroscopic body force (force per unit of volume) applied on $\overline{V}$. Note that $\overline{\boldsymbol{b}}_{\boldsymbol{a}}$ does not have any microscopic counterpart as a direct consequence of the scale separation assumption [141].

The microscopic problem, also called the unit cell problem, is defined by the micro-scale equations in the right part of Table I.1 while considering the periodicity conditions. The latter will be described in Section 2.1.3.

The homogenization consists in defining the global constitutive behaviour, described by the operator $\overline{\boldsymbol{F}}$ (see the left part of Table I.1), from the known local behaviours, defined by the operator $\boldsymbol{F}$ (see the right part of Table I.1) and the geometrical characteristics of the various constituents in the unit cell. The local constitutive equations may be non-linear, time-dependent (viscoelasticity, viscoplasticity...) and involve internal state variables, according to the framework of thermodynamics [67, 68, 69, 109, 33] that is briefly described in Appendix B.

2.1.2 Connection between scales

In order to link the micro-scale with the macro-scale equations, a connection between scales is required. To do so, as it is usual in homogenization, the macroscopic stress and strain fields are identified through volume averaging of their microscopic counterparts over the unit cell [78, 141, 172]. Moreover, from the divergence theorem, it can be demonstrated that the stress and strain averages within a unit cell are also connected to the traction and displacement vectors applied on its boundaries:

$$\overline{\boldsymbol{\sigma}}(\overline{\boldsymbol{x}},t) = \frac{1}{V}\int_V \boldsymbol{\sigma}(\overline{\boldsymbol{x}},\boldsymbol{x},t)\ dV = \frac{1}{V}\int_{\partial V} \boldsymbol{\sigma}(\overline{\boldsymbol{x}},\boldsymbol{x},t)\cdot\boldsymbol{n}(\boldsymbol{x})\otimes\boldsymbol{x}\ dS, \tag{I.2}$$

$$\overline{\boldsymbol{\varepsilon}}(\overline{\boldsymbol{x}},t) = \frac{1}{V}\int_V \boldsymbol{\varepsilon}(\overline{\boldsymbol{x}},\boldsymbol{x},t)\ dV = \frac{1}{2V}\int_{\partial V} \Big(\boldsymbol{u}(\overline{\boldsymbol{x}},\boldsymbol{x},t)\otimes\boldsymbol{n}(\boldsymbol{x}) + \boldsymbol{n}(\boldsymbol{x})\otimes\boldsymbol{u}(\overline{\boldsymbol{x}},\boldsymbol{x},t)\Big)\ dS, \tag{I.3}$$

where $\boldsymbol{n}$ stands for the outgoing normal defined on each point of the unit cell borders ($\forall \boldsymbol{x} \in \partial V$). In addition, it is worth mentioning that, according to the Hill-Mandel postulate [141], the macroscopic mechanical work is equal to the volume average of its microscopic field within the unit cell:

$$\overline{W}(\overline{\boldsymbol{x}},t) = \frac{1}{V}\int_V W(\overline{\boldsymbol{x}},\boldsymbol{x},t)\ dV. \tag{I.4}$$

If the latter condition is verified, a connection between scales can be also ensured for certain thermodynamical quantities (see Table B.1 in Section 2 in Appendix B). Indeed, if the

local stress-strain relationships are established from the derivation of a state potential, then the existence of a macro state potential can be demonstrated [141]. Accordingly, for the Helmholtz and Gibbs potentials, this respectively gives:

$$\overline{\psi}(\overline{\boldsymbol{x}},t)=\frac{1}{\overline{\rho}V}\int_V \rho\psi(\overline{\boldsymbol{x}},\boldsymbol{x},t)\ \ dV \qquad \text{such that} \qquad \boldsymbol{\sigma}=\rho\frac{\partial\psi}{\partial\boldsymbol{\varepsilon}} \quad \text{and} \quad \overline{\boldsymbol{\sigma}}=\overline{\rho}\frac{\partial\overline{\psi}}{\partial\overline{\boldsymbol{\varepsilon}}}, \tag{I.5}$$

$$\overline{\psi}^*(\overline{\boldsymbol{x}},t)=\frac{1}{\overline{\rho}V}\int_V \rho\psi^*(\overline{\boldsymbol{x}},\boldsymbol{x},t)\ \ dV \qquad \text{such that} \qquad \boldsymbol{\varepsilon}=-\rho\frac{\partial\psi^*}{\partial\boldsymbol{\sigma}} \quad \text{and} \quad \overline{\boldsymbol{\varepsilon}}=-\overline{\rho}\frac{\partial\overline{\psi}^*}{\partial\overline{\boldsymbol{\sigma}}}, \tag{I.6}$$

where $\overline{\rho}$ stands for the macroscopic density [1]. Therewith, by assuming isothermal conditions and integrating the Claussius-Duhem inequality (see Table B.1 in Section 2 in Appendix B) over the volume of the unit cell [32], the macroscopic dissipation respectively becomes for the Helmholtz and Gibbs potentials:

$$\dot{\overline{\Phi}}(\overline{\boldsymbol{x}},t)=\frac{1}{V}\int_V \dot{\Phi}(\overline{\boldsymbol{x}},\boldsymbol{x},t)\ \ dV=\dot{\overline{W}}_{\varepsilon}(\overline{\boldsymbol{x}},t)-\dot{\overline{\rho\psi}}(\overline{\boldsymbol{x}},t)\geq 0, \tag{I.7}$$

$$\dot{\overline{\Phi}}(\overline{\boldsymbol{x}},t)=\frac{1}{V}\int_V \dot{\Phi}(\overline{\boldsymbol{x}},\boldsymbol{x},t)\ \ dV=-\dot{\overline{W}}_{\sigma}(\overline{\boldsymbol{x}},t)-\dot{\overline{\rho\psi}}^*(\overline{\boldsymbol{x}},t)\geq 0. \tag{I.8}$$

2.1.3 Periodicity

The assumption of periodicity [181] implies that, within the unit cell, the displacement vector $\boldsymbol{u}$ of any microscopic material point $M(\overline{\boldsymbol{x}},\boldsymbol{x})$ can be written under the following additive form:

$$\boldsymbol{u}(\overline{\boldsymbol{x}},\boldsymbol{x},t)=\overline{\boldsymbol{\varepsilon}}(\overline{\boldsymbol{x}},t)\cdot\boldsymbol{x}+\boldsymbol{u'}(\overline{\boldsymbol{x}},\boldsymbol{x},t)+\boldsymbol{u_0}(\overline{\boldsymbol{x}},t). \tag{I.9}$$

As illustrated in Figure I.2, the first term stands for the affine part of the local displacement field that is directly related to the macroscopic strain $\overline{\boldsymbol{\varepsilon}}$, while the second term $\boldsymbol{u'}$ represents a periodic fluctuation within the unit cell. The last term $\boldsymbol{u_0}$ depicts a rigid body motion that comes out from the macroscopic problem and consequently does not depend on the microscopic problem.

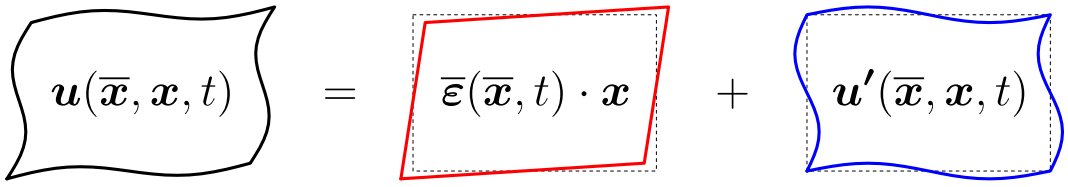

Figure I.2: Definition of the displacement field within the unit cell as the sum of an affine part and a periodic fluctuation. The part related to the rigid body motion is purposely omitted as this term is independent from the microscopic scale.

Note that, as $\boldsymbol{u'}$ is periodic, it takes the same value on each pair of opposite points $\boldsymbol{x}_+$ and $\boldsymbol{x}_-$ of the unit cell boundaries ($\boldsymbol{x}_+,\boldsymbol{x}_-\in\partial V$):

$$\boldsymbol{u'}(\overline{\boldsymbol{x}},\boldsymbol{x}_+,t)=\boldsymbol{u'}(\overline{\boldsymbol{x}},\boldsymbol{x}_-,t). \tag{I.10}$$

1. The macroscopic density is obtained from the volume average of its microscopic counterpart, namely: $\overline{\rho}=\frac{1}{V}\int_V \rho(\boldsymbol{x})\ \ dV$, and is considered as constant under the small strain assumption.

Substituting (I.9) into (I.10), these specific conditions can be expressed in terms of $\boldsymbol{u}$ instead of $\boldsymbol{u'}$, while involving the macroscopic strain tensor $\overline{\boldsymbol{\varepsilon}}$:

$$\boldsymbol{u}(\overline{\boldsymbol{x}}, \boldsymbol{x}_+, t) - \boldsymbol{u}(\overline{\boldsymbol{x}}, \boldsymbol{x}_-, t) = \overline{\boldsymbol{\varepsilon}}(\overline{\boldsymbol{x}}, t) \cdot (\boldsymbol{x}_+ - \boldsymbol{x}_-). \tag{I.11}$$

Through the periodicity assumption (I.9), the local strain field becomes:

$$\boldsymbol{\varepsilon}(\overline{\boldsymbol{x}}, \boldsymbol{x}, t) = \overline{\boldsymbol{\varepsilon}}(\overline{\boldsymbol{x}}, t) + \boldsymbol{\varepsilon'}(\overline{\boldsymbol{x}}, \boldsymbol{x}, t), \tag{I.12}$$

with

$$\boldsymbol{\varepsilon'}(\overline{\boldsymbol{x}}, \boldsymbol{x}, t) = \frac{1}{2}\Big(\mathbf{Grad}_{\boldsymbol{x}}\big(\boldsymbol{u'}(\overline{\boldsymbol{x}}, \boldsymbol{x}, t)\big) + \mathbf{Grad}_{\boldsymbol{x}}^{T}\big(\boldsymbol{u'}(\overline{\boldsymbol{x}}, \boldsymbol{x}, t)\big)\Big). \tag{I.13}$$

$\boldsymbol{\varepsilon'}$ represents the part of the local strain induced by $\boldsymbol{u'}$, the periodic aspect of the latter implies that:

$$\frac{1}{V}\int_V \boldsymbol{\varepsilon'}(\overline{\boldsymbol{x}}, \boldsymbol{x}, t) \;\; dV = \frac{1}{2V}\int_{\partial V} \Big(\boldsymbol{u'}(\overline{\boldsymbol{x}}, \boldsymbol{x}, t) \otimes \boldsymbol{n}(\boldsymbol{x}) + \boldsymbol{n}(\boldsymbol{x}) \otimes \boldsymbol{u'}(\overline{\boldsymbol{x}}, \boldsymbol{x}, t)\Big) \;\; dS = \mathbf{0}, \tag{I.14}$$

and thus ensures the compatibility between equations (I.9) and (I.3).

The local stress field satisfies the conditions of equilibrium within the unit cell (local equilibrium) and a proper connection with the surrounding unit cells. The second condition implies an anti-periodicity of the tractions vectors, namely $\boldsymbol{\sigma} \cdot \boldsymbol{n}$, on the unit cell borders:

$$\boldsymbol{\sigma}(\overline{\boldsymbol{x}}, \boldsymbol{x}_+, t) \cdot \boldsymbol{n}(\boldsymbol{x}_+) = -\boldsymbol{\sigma}(\overline{\boldsymbol{x}}, \boldsymbol{x}_-, t) \cdot \boldsymbol{n}(\boldsymbol{x}_-). \tag{I.15}$$

Considering the Hill lemma, obtained from the difference between the volume average of the microscopic works and the macroscopic work, along with the divergence principle, the following equality can be written:

$$\begin{aligned}
&\frac{1}{V}\int_V W(\overline{\boldsymbol{x}}, \boldsymbol{x}, t) \;\; dV - \overline{W}(\overline{\boldsymbol{x}}, t) \\
&\quad = \frac{1}{V}\int_V \boldsymbol{\sigma}(\overline{\boldsymbol{x}}, \boldsymbol{x}, t) : \boldsymbol{\varepsilon}(\overline{\boldsymbol{x}}, \boldsymbol{x}, t) \;\; dV - \overline{\boldsymbol{\sigma}}(\overline{\boldsymbol{x}}, t) : \overline{\boldsymbol{\varepsilon}}(\overline{\boldsymbol{x}}, t) \\
&\quad = \frac{1}{V}\int_{\partial V} \Big(\boldsymbol{u}(\overline{\boldsymbol{x}}, \boldsymbol{x}, t) - \overline{\boldsymbol{\varepsilon}}(\overline{\boldsymbol{x}}, t) \cdot \boldsymbol{x}\Big) \cdot \Big(\boldsymbol{\sigma}(\overline{\boldsymbol{x}}, \boldsymbol{x}, t) \cdot \boldsymbol{n}(\boldsymbol{x}) - \overline{\boldsymbol{\sigma}}(\overline{\boldsymbol{x}}, t) \cdot \boldsymbol{n}(\boldsymbol{x})\Big) \;\; dS.
\end{aligned} \tag{I.16}$$

Then, based on (I.9), the Hill lemma eventually gives:

$$\begin{aligned}
&\frac{1}{V}\int_V W(\overline{\boldsymbol{x}}, \boldsymbol{x}, t) \;\; dV - \overline{W}(\overline{\boldsymbol{x}}, t) \\
&= \frac{1}{V}\int_{\partial V} \underbrace{\Big(\boldsymbol{u'}(\overline{\boldsymbol{x}}, \boldsymbol{x}, t) + \boldsymbol{u_0}(\overline{\boldsymbol{x}}, t)\Big)}_{\boldsymbol{u'} \;\; \text{periodic}} \cdot \underbrace{\Big(\boldsymbol{\sigma}(\overline{\boldsymbol{x}}, \boldsymbol{x}, t) \cdot \boldsymbol{n}(\boldsymbol{x}) - \overline{\boldsymbol{\sigma}}(\overline{\boldsymbol{x}}, t) \cdot \boldsymbol{n}(\boldsymbol{x})\Big)}_{\boldsymbol{\sigma}\cdot\boldsymbol{n} \;\; \text{anti-periodic}} \;\; dS = 0.
\end{aligned} \tag{I.17}$$

In the above equation, due to the periodicity of $\boldsymbol{u'}$ and the anti-periodicity of $\boldsymbol{\sigma} \cdot \boldsymbol{n}$, the Hill-Mandel condition (I.4) holds.

2.1.4 Solution of the unit cell problem

Considering a strain driven approach on a single macroscopic material point $\overline{M}(\overline{\boldsymbol{x}})$, a unique solution of the displacement field $\boldsymbol{u}$ can be found (up to a rigid body motion), for a given macroscopic strain $\overline{\boldsymbol{\varepsilon}}$, by solving the micro-scale equations (see the right part of Table I.1) along with (I.11) as Dirichlet boundary conditions. Subsequently, the macroscopic stress $\overline{\boldsymbol{\sigma}}$ can be determined using equation (I.2).

Alternatively, with a stress driven approach, a unique solution of the displacement field $\boldsymbol{u}$ can be found (up to a rigid body motion) by solving the micro-scale equations (see the right part of Table I.1) in which a macroscopic stress $\overline{\boldsymbol{\sigma}}$ is applied on the unit cell with the help of (I.2) as Neumann boundary conditions. Subsequently, the macroscopic strain $\overline{\boldsymbol{\varepsilon}}$ can be determined using equation (I.3).

Finally, let's remark that the solution of the micro-scale equations (see the right part of Table I.1) obtained with the appropriate boundary conditions, namely (I.11) or (I.2), while considering the connection between the microscopic and macroscopic scales in (I.2) and (I.3), allows to define the global constitutive behaviour of the unit cell and consequently the operator $\overline{\boldsymbol{F}}$. Indeed, for a given macroscopic strain or stress loading path applied on a single macroscopic material point $\overline{M}(\overline{\boldsymbol{x}})$, the macroscopic strain or stress response can be determined through the resolution of the unit cell problem. The latter includes the geometrical characteristics of the unit cell as well as the local constitutive equations (operator $\boldsymbol{F}$).

2.1.5 Solution of the macroscopic problem

The solution of the macroscopic problem is treated as any mechanical problem at the exception that, for each macroscopic material point, the stress-strain relationship is obtained from the solution of the unit cell problem (Section 2.1.4). Consequently, as the solutions of the macroscopic and microscopic problems are interdependent, such a two-scales analysis requires to solve both problems simultaneously [61, 63, 62, 9, 182, 184, 183].

2.1.6 Homogenized stiffness properties

In the case of linear elasticity, the local constitutive law, with the help of the Voigt notation, is given by:

$$\underbrace{\begin{Bmatrix}\sigma_{11}\\ \sigma_{22}\\ \sigma_{33}\\ \sigma_{12}\\ \sigma_{13}\\ \sigma_{23}\end{Bmatrix}}_{\boldsymbol{\sigma}(\overline{\boldsymbol{x}},\boldsymbol{x},t)} = \underbrace{\begin{pmatrix} C_{1111} & C_{1122} & C_{1133} & C_{1112} & C_{1113} & C_{1123}\\ & C_{2222} & C_{2233} & C_{2212} & C_{2213} & C_{2223}\\ & & C_{3333} & C_{3312} & C_{3313} & C_{3323}\\ & & & C_{1212} & C_{1213} & C_{1223}\\ & & & & C_{1313} & C_{1323}\\ \text{sym.} & & & & & C_{2323}\end{pmatrix}}_{\mathbb{C}(\boldsymbol{x})} \times \underbrace{\begin{Bmatrix}\varepsilon_{11}\\ \varepsilon_{22}\\ \varepsilon_{33}\\ 2\varepsilon_{12}\\ 2\varepsilon_{13}\\ 2\varepsilon_{23}\end{Bmatrix}}_{\boldsymbol{\varepsilon}(\overline{\boldsymbol{x}},\boldsymbol{x},t)}, \tag{I.18}$$

or, in its inverse form:

$$\underbrace{\begin{Bmatrix}\varepsilon_{11}\\ \varepsilon_{22}\\ \varepsilon_{33}\\ 2\varepsilon_{12}\\ 2\varepsilon_{13}\\ 2\varepsilon_{23}\end{Bmatrix}}_{\boldsymbol{\varepsilon}(\overline{\boldsymbol{x}},\boldsymbol{x},t)} = \underbrace{\begin{pmatrix} S_{1111} & S_{1122} & S_{1133} & 2S_{1112} & 2S_{1113} & 2S_{1123}\\ & S_{2222} & S_{2233} & 2S_{2212} & 2S_{2213} & 2S_{2223}\\ & & S_{3333} & 2S_{3312} & 2S_{3313} & 2S_{3323}\\ & & & 4S_{1212} & 4S_{1213} & 4S_{1223}\\ & & & & 4S_{1313} & 4S_{1323}\\ \text{sym.} & & & & & 4S_{2323}\end{pmatrix}}_{\mathbb{S}(\boldsymbol{x})} \times \underbrace{\begin{Bmatrix}\sigma_{11}\\ \sigma_{22}\\ \sigma_{33}\\ \sigma_{12}\\ \sigma_{13}\\ \sigma_{23}\end{Bmatrix}}_{\boldsymbol{\sigma}(\overline{\boldsymbol{x}},\boldsymbol{x},t)}, \tag{I.19}$$

where $\mathbb{C}$ and $\mathbb{S}$ are the microscopic fourth order stiffness and compliance tensors, respectively, one being the inverse of the other:

$$\mathbb{C} = \mathbb{S}^{-1}. \tag{I.20}$$

As written in (I.18) and (I.19), the elastic stiffness and compliance tensors have necessarily the minor and major symmetries.

It can be shown that, in the same way, the global constitutive law is also linear. With the help of the Voigt notation, this gives:

$$\underbrace{\begin{Bmatrix}\overline{\sigma}_{11}\\ \overline{\sigma}_{22}\\ \overline{\sigma}_{33}\\ \overline{\sigma}_{12}\\ \overline{\sigma}_{13}\\ \overline{\sigma}_{23}\end{Bmatrix}}_{\overline{\boldsymbol{\sigma}}(\overline{\boldsymbol{x}},t)} = \underbrace{\begin{pmatrix} \overline{C}_{1111} & \overline{C}_{1122} & \overline{C}_{1133} & \overline{C}_{1112} & \overline{C}_{1113} & \overline{C}_{1123}\\ & \overline{C}_{2222} & \overline{C}_{2233} & \overline{C}_{2212} & \overline{C}_{2213} & \overline{C}_{2223}\\ & & \overline{C}_{3333} & \overline{C}_{3312} & \overline{C}_{3313} & \overline{C}_{3323}\\ & & & \overline{C}_{1212} & \overline{C}_{1213} & \overline{C}_{1223}\\ & & & & \overline{C}_{1313} & \overline{C}_{1323}\\ \text{sym.} & & & & & \overline{C}_{2323}\end{pmatrix}}_{\overline{\mathbb{C}}} \times \underbrace{\begin{Bmatrix}\overline{\varepsilon}_{11}\\ \overline{\varepsilon}_{22}\\ \overline{\varepsilon}_{33}\\ 2\overline{\varepsilon}_{12}\\ 2\overline{\varepsilon}_{13}\\ 2\overline{\varepsilon}_{23}\end{Bmatrix}}_{\overline{\boldsymbol{\varepsilon}}(\overline{\boldsymbol{x}},t)}, \tag{I.21}$$

or, in its inverse form:

$$\underbrace{\begin{Bmatrix}\overline{\varepsilon}_{11}\\ \overline{\varepsilon}_{22}\\ \overline{\varepsilon}_{33}\\ 2\overline{\varepsilon}_{12}\\ 2\overline{\varepsilon}_{13}\\ 2\overline{\varepsilon}_{23}\end{Bmatrix}}_{\overline{\boldsymbol{\varepsilon}}(\overline{\boldsymbol{x}},t)} = \underbrace{\begin{pmatrix} \overline{S}_{1111} & \overline{S}_{1122} & \overline{S}_{1133} & 2\overline{S}_{1112} & 2\overline{S}_{1113} & 2\overline{S}_{1123}\\ & \overline{S}_{2222} & \overline{S}_{2233} & 2\overline{S}_{2212} & 2\overline{S}_{2213} & 2\overline{S}_{2223}\\ & & \overline{S}_{3333} & 2\overline{S}_{3312} & 2\overline{S}_{3313} & 2\overline{S}_{3323}\\ & & & 4\overline{S}_{1212} & 4\overline{S}_{1213} & 4\overline{S}_{1223}\\ & & & & 4\overline{S}_{1313} & 4\overline{S}_{1323}\\ \text{sym.} & & & & & 4\overline{S}_{2323}\end{pmatrix}}_{\overline{\mathbb{S}}} \times \underbrace{\begin{Bmatrix}\overline{\sigma}_{11}\\ \overline{\sigma}_{22}\\ \overline{\sigma}_{33}\\ \overline{\sigma}_{12}\\ \overline{\sigma}_{13}\\ \overline{\sigma}_{23}\end{Bmatrix}}_{\overline{\boldsymbol{\sigma}}(\overline{\boldsymbol{x}},t)}, \tag{I.22}$$

where $\overline{\mathbb{C}}$ and $\overline{\mathbb{S}}$ are the macroscopic fourth order stiffness and compliance tensors, respectively.

Through a strain driven approach, the macroscopic stiffness tensor $\overline{\mathbb{C}}$ can be recovered by calculating the macroscopic stress resulting from the six unitary strain states. With the

help of the Voigt notation, the unitary strain states are written such as:

$$\begin{cases} \overline{\boldsymbol{\varepsilon}}_{(11)} = \begin{pmatrix} \overline{\varepsilon}_{11} = \delta & \overline{\varepsilon}_{22} = 0 & \overline{\varepsilon}_{33} = 0 & 2\overline{\varepsilon}_{12} = 0 & 2\overline{\varepsilon}_{13} = 0 & 2\overline{\varepsilon}_{23} = 0 \end{pmatrix}^T \\ \overline{\boldsymbol{\varepsilon}}_{(22)} = \begin{pmatrix} \overline{\varepsilon}_{11} = 0 & \overline{\varepsilon}_{22} = \delta & \overline{\varepsilon}_{33} = 0 & 2\overline{\varepsilon}_{12} = 0 & 2\overline{\varepsilon}_{13} = 0 & 2\overline{\varepsilon}_{23} = 0 \end{pmatrix}^T \\ \overline{\boldsymbol{\varepsilon}}_{(33)} = \begin{pmatrix} \overline{\varepsilon}_{11} = 0 & \overline{\varepsilon}_{22} = 0 & \overline{\varepsilon}_{33} = \delta & 2\overline{\varepsilon}_{12} = 0 & 2\overline{\varepsilon}_{13} = 0 & 2\overline{\varepsilon}_{23} = 0 \end{pmatrix}^T \\ \overline{\boldsymbol{\varepsilon}}_{(12)} = \begin{pmatrix} \overline{\varepsilon}_{11} = 0 & \overline{\varepsilon}_{22} = 0 & \overline{\varepsilon}_{33} = 0 & 2\overline{\varepsilon}_{12} = \delta & 2\overline{\varepsilon}_{13} = 0 & 2\overline{\varepsilon}_{23} = 0 \end{pmatrix}^T \\ \overline{\boldsymbol{\varepsilon}}_{(13)} = \begin{pmatrix} \overline{\varepsilon}_{11} = 0 & \overline{\varepsilon}_{22} = 0 & \overline{\varepsilon}_{33} = 0 & 2\overline{\varepsilon}_{12} = 0 & 2\overline{\varepsilon}_{13} = \delta & 2\overline{\varepsilon}_{23} = 0 \end{pmatrix}^T \\ \overline{\boldsymbol{\varepsilon}}_{(23)} = \begin{pmatrix} \overline{\varepsilon}_{11} = 0 & \overline{\varepsilon}_{22} = 0 & \overline{\varepsilon}_{33} = 0 & 2\overline{\varepsilon}_{12} = 0 & 2\overline{\varepsilon}_{13} = 0 & 2\overline{\varepsilon}_{23} = \delta \end{pmatrix}^T \end{cases}, \tag{I.23}$$

where δ is a real value (the simplest is to take $\delta = 1$). Thus, the $ijkl$ component of the macroscopic stiffness tensor is given by the ij component of the stress tensor calculated for the kl elementary strain state, divided by δ:

$$\overline{C}_{ijkl} = \begin{cases} \dfrac{\overline{\sigma}_{ij(kl)}}{\overline{\varepsilon}_{kl(kl)}} & \text{if } kl = 11, 22, 33 \\ \dfrac{\overline{\sigma}_{ij(kl)}}{2\overline{\varepsilon}_{kl(kl)}} & \text{if } kl = 12, 13, 23 \end{cases} = \frac{\overline{\sigma}_{ij(kl)}}{\delta}, \quad ij, kl = 11, 22, 33, 12, 13, 23. \tag{I.24}$$

Similarly, through a stress driven approach, the macroscopic compliance tensor $\overline{\mathbb{S}}$ can be recovered by calculating the macroscopic strain resulting from the six unitary stress states. With the help of the Voigt notation, the unitary stress states are written such as:

$$\begin{cases} \overline{\boldsymbol{\sigma}}_{(11)} = \begin{pmatrix} \overline{\sigma}_{11} = \delta & \overline{\sigma}_{22} = 0 & \overline{\sigma}_{33} = 0 & \overline{\sigma}_{12} = 0 & \overline{\sigma}_{13} = 0 & \overline{\sigma}_{23} = 0 \end{pmatrix}^T \\ \overline{\boldsymbol{\sigma}}_{(22)} = \begin{pmatrix} \overline{\sigma}_{11} = 0 & \overline{\sigma}_{22} = \delta & \overline{\sigma}_{33} = 0 & \overline{\sigma}_{12} = 0 & \overline{\sigma}_{13} = 0 & \overline{\sigma}_{23} = 0 \end{pmatrix}^T \\ \overline{\boldsymbol{\sigma}}_{(33)} = \begin{pmatrix} \overline{\sigma}_{11} = 0 & \overline{\sigma}_{22} = 0 & \overline{\sigma}_{33} = \delta & \overline{\sigma}_{12} = 0 & \overline{\sigma}_{13} = 0 & \overline{\sigma}_{23} = 0 \end{pmatrix}^T \\ \overline{\boldsymbol{\sigma}}_{(12)} = \begin{pmatrix} \overline{\sigma}_{11} = 0 & \overline{\sigma}_{22} = 0 & \overline{\sigma}_{33} = 0 & \overline{\sigma}_{12} = \delta & \overline{\sigma}_{13} = 0 & \overline{\sigma}_{23} = 0 \end{pmatrix}^T \\ \overline{\boldsymbol{\sigma}}_{(13)} = \begin{pmatrix} \overline{\sigma}_{11} = 0 & \overline{\sigma}_{22} = 0 & \overline{\sigma}_{33} = 0 & \overline{\sigma}_{12} = 0 & \overline{\sigma}_{13} = \delta & \overline{\sigma}_{23} = 0 \end{pmatrix}^T \\ \overline{\boldsymbol{\sigma}}_{(23)} = \begin{pmatrix} \overline{\sigma}_{11} = 0 & \overline{\sigma}_{22} = 0 & \overline{\sigma}_{33} = 0 & \overline{\sigma}_{12} = 0 & \overline{\sigma}_{13} = 0 & \overline{\sigma}_{23} = \delta \end{pmatrix}^T \end{cases}, \tag{I.25}$$

Thus, the $ijkl$ component of the macroscopic compliance tensor is given by the ij component of the strain tensor calculated for the kl elementary stress state, divided by δ for the tension stress states or 2δ for the shear stress states:

$$\overline{S}_{ijkl} = \begin{cases} \dfrac{\overline{\varepsilon}_{ij(kl)}}{\overline{\sigma}_{kl(kl)}} = \dfrac{\overline{\varepsilon}_{ij(kl)}}{\delta} & \text{if } kl = 11, 22, 33 \\ \dfrac{\overline{\varepsilon}_{ij(kl)}}{2\overline{\sigma}_{kl(kl)}} = \dfrac{\overline{\varepsilon}_{ij(kl)}}{2\delta} & \text{if } kl = 12, 13, 23 \end{cases}. \tag{I.26}$$

It can be shown that, when using periodic homogenization, the macroscopic compliance tensor is well equal to the inverse of the macroscopic stiffness tensor (and vice versa):

$$\overline{\mathbb{C}} = \overline{\mathbb{S}}^{-1}. \tag{I.27}$$

Thus, the strain and stress driven approaches are strictly equivalent. Moreover, as written in (I.21) and (I.22), the resulting macroscopic stiffness and compliance tensors always have the major symmetry. This is ensured by the energetic consistency between the macroscopic and microscopic works [133] demonstrated in Section 2.1.3.

For non-linear cases, when solving the macroscopic problem with an implicit resolution scheme, the identification of the instantaneous macroscopic stiffness (tangent operator) is required to achieve a fast convergence of the solution within a given time increment. Then, the instantaneous macroscopic stress-strain relationship is expressed, at each macroscopic integration point, by:

$$d\overline{\boldsymbol{\sigma}}(\overline{\boldsymbol{x}}, t) = \overline{\mathbb{C}}_{\boldsymbol{t}}(\overline{\boldsymbol{x}}, t) : d\overline{\boldsymbol{\varepsilon}}(\overline{\boldsymbol{x}}, t), \tag{I.28}$$

where $\overline{\mathbb{C}}_{\boldsymbol{t}}$ is the macroscopic tangent operator. The resolution of the macroscopic problem is performed by calling the microscopic problem for each macroscopic integration point and at each time increment. During the resolution of the microscopic problem, to achieve fast convergence, the local constitutive relationships are also written in their instantaneous forms at each microscopic integration point:

$$d\boldsymbol{\sigma}(\overline{\boldsymbol{x}}, \boldsymbol{x}, t) = \mathbb{C}_{\boldsymbol{t}}(\overline{\boldsymbol{x}}, \boldsymbol{x}, t) : d\boldsymbol{\varepsilon}(\overline{\boldsymbol{x}}, \boldsymbol{x}, t), \tag{I.29}$$

where $\mathbb{C}_{\boldsymbol{t}}$ is the microscopic tangent operator whose formulation is obtained from the linearisation of the local constitutive equations (see for example Section 3.3 in Chapter II and Section 3.3 in Chapter III). Thus, the macroscopic tangent operator $\overline{\mathbb{C}}_{\boldsymbol{t}}$ can be recovered at each time increment, in a similar manner than for the elastic case, using a unit cell in which the local instantaneous stiffness $\mathbb{C}_{\boldsymbol{t}}$ is assigned to each microscopic integration point. Note that, according to the considered local constitutive equations, the microscopic and macroscopic tangent operators do not have necessarily the major symmetry.

2.2 Finite element resolution of the unit cell problem

The concept of periodic homogenization is generally well suited with the Finite Element Method. However, its use requires specific periodic boundary conditions. This section introduces a generalized method for defining periodic boundary conditions, allowing to apply any state of macroscopic strain, stress or even mixed stress-strain on a cubic periodic finite element unit cell.

2.2.1 Control of the unit cell

Using the finite element method, it seems evident that the meshing of the unit cell must be well periodic. This means that for each border node, there must be another node at the same relative position on the opposite border. Considering a cubic unit cell, the aim of the method is to apply a macroscopic strain $\overline{\boldsymbol{\varepsilon}}$, by taking into account the periodic boundary conditions previously described in (I.11). A displacement gradient is then applied between each pair of opposite boundary nodes, respectively denoted by the indices i and j. This

gradient is directly related to the macroscopic strain tensor $\overline{\boldsymbol{\varepsilon}}$:

$$\begin{Bmatrix} u_1^i - u_1^j \\ u_2^i - u_2^j \\ u_3^i - u_3^j \end{Bmatrix} = \begin{pmatrix} \overline{\varepsilon}_{11} & \overline{\varepsilon}_{12} & \overline{\varepsilon}_{13} \\ & \overline{\varepsilon}_{22} & \overline{\varepsilon}_{23} \\ \text{sym.} & & \overline{\varepsilon}_{33} \end{pmatrix} \times \begin{Bmatrix} x_1^i - x_1^j \\ x_2^i - x_2^j \\ x_3^i - x_3^j \end{Bmatrix}. \tag{I.30}$$

In the above expression, u_1, u_2, u_3 and x_1, x_2, x_3 are the components of the displacement and position vectors, $\boldsymbol{u}$ and $\boldsymbol{x}$, respectively. The proposed method introduces the six components of the macroscopic strain tensor as additional degrees of freedom that are directly involved in the boundary conditions [112, 113, 114]. Theses additional degrees of freedom are linked to the mesh of the unit cell using kinematic constraint equations obtained from (I.30) and are thus used as "constraint drivers". From a practical point of view, the "constraint drivers" can be introduced by adding six new nodes among which only the first degree of freedom is used. The displacement of those "constraint drivers", noted u_{11}^{cd}, u_{22}^{cd}, u_{33}^{cd}, u_{12}^{cd}, u_{13}^{cd} and u_{23}^{cd}, takes the values of each component of the macroscopic strain tensor: $\overline{\varepsilon}_{11}$, $\overline{\varepsilon}_{22}$, $\overline{\varepsilon}_{33}$, $2\overline{\varepsilon}_{12}$, $2\overline{\varepsilon}_{13}$ and $2\overline{\varepsilon}_{23}$, respectively. The dual forces on the "constraint drivers", noted F_{11}^{cd}, F_{22}^{cd}, F_{33}^{cd}, F_{12}^{cd}, F_{13}^{cd} and F_{23}^{cd}, are directly related to the corresponding components of the macroscopic stress tensor: $\overline{\sigma}_{11}$, $\overline{\sigma}_{22}$, $\overline{\sigma}_{33}$, $\overline{\sigma}_{12}$, $\overline{\sigma}_{13}$ and $\overline{\sigma}_{23}$, respectively.

As an example, for the tension term 11, the previously given kinematic equation (I.30) is reduced to:

$$u_1^i - u_1^j = \overline{\varepsilon}_{11}\ \Delta x_1 \quad \Leftrightarrow \quad u_1^i - u_1^j - u_{11}^{cd}\ \Delta x_1 = 0, \tag{I.31}$$

where Δx_1 is the length of the unit cell in the x_1 direction. In the same way, Δx_2 and Δx_3 are the lengths of the unit cell in the x_2 and x_3 directions, respectively. The term $\overline{\varepsilon}_{11}\Delta x_1$ corresponds to the global displacement of the unit cell needed to represent a macroscopic strain $\overline{\varepsilon}_{11}$. On the other hand, $\overline{\sigma}_{11}\Delta x_2\Delta x_3$ corresponds to the global force needed to represent a macroscopic stress $\overline{\sigma}_{11}$. Then, if the value of $\overline{\varepsilon}_{11}$ is set as displacement in the "constraint driver" node 11 ($u_{11}^{cd} = \overline{\varepsilon}_{11}$), the computed dual force will give the product between the macroscopic stress $\overline{\sigma}_{11}$ and the volume ($F_{11}^{cd} = \overline{\sigma}_{11}\Delta x_1\Delta x_2\Delta x_3$) and vice versa (see Figure I.3).

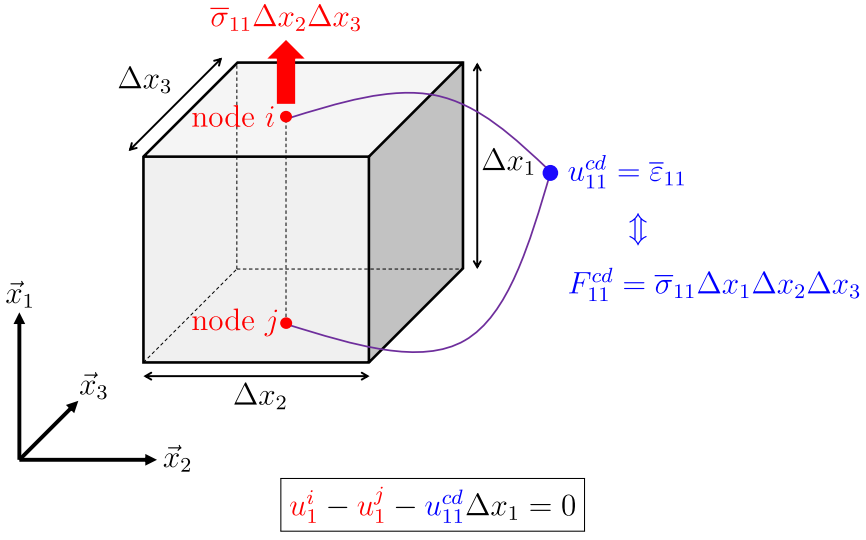

Figure I.3: Kinematic constraint equation for tension 11.

For the shearing term 12, the kinematic equation (I.30) is reduced to:

$$u_1^k - u_1^l = 2\overline{\varepsilon}_{12}\ \frac{1}{2}\Delta x_2 \quad \Leftrightarrow \quad u_1^k - u_1^l - u_{12}^{cd}\ \frac{1}{2}\Delta x_2 = 0. \tag{I.32}$$

and

$$u_2^i - u_2^j = 2\overline{\varepsilon}_{12}\,\frac{1}{2}\Delta x_1 \quad \Leftrightarrow \quad u_2^i - u_2^j - u_{12}^{cd}\,\frac{1}{2}\Delta x_1 = 0, \tag{I.33}$$

Similarly, if the value of $2\overline{\varepsilon}_{12}$ is set to the "constraint driver" node 12 ($u_{12}^{cd} = 2\overline{\varepsilon}_{12}$), then the computed dual force will directly provide the product between the macroscopic stress $\overline{\sigma}_{12}$ and the volume ($F_{12}^{cd} = \overline{\sigma}_{12}\Delta x_1\Delta x_2\Delta x_3$) and vice versa (see Figure I.4).

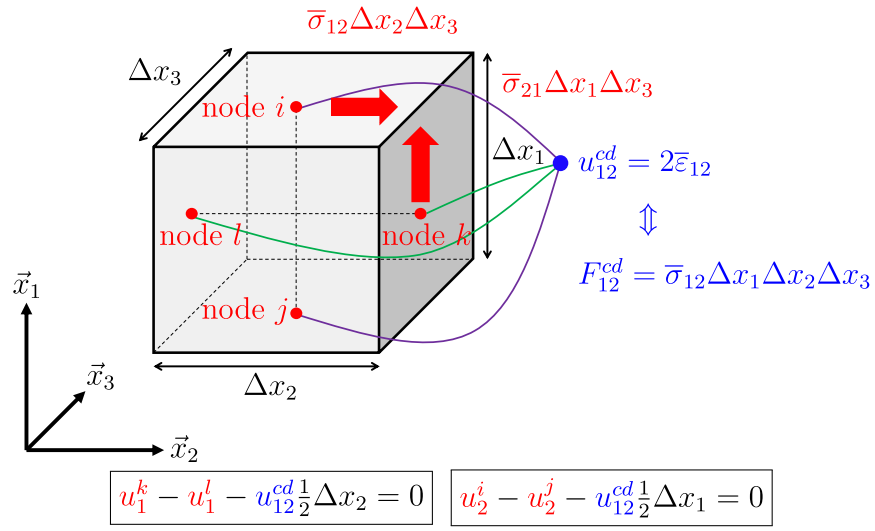

Figure I.4: Kinematic constraint equations for shear 12.

Using the six "constraint drivers" (one for each component of the macroscopic strain tensor), the approach can be generalized in three dimensions in order to apply any state of macroscopic strain or stress on the unit cell. Even mixed stress-strain states can be considered. Indeed, each "constraint driver" can be independently set either in displacement (macroscopic strain) or in force (macroscopic stress by the volume) as illustrated in Figure I.5. As previously mentioned the solution of a periodic homogenization is defined up to a rigid body motion. For this reason, a node of the model needs to be clamped in order to guarantee the uniqueness of the solution and the solvability of the finite element system.

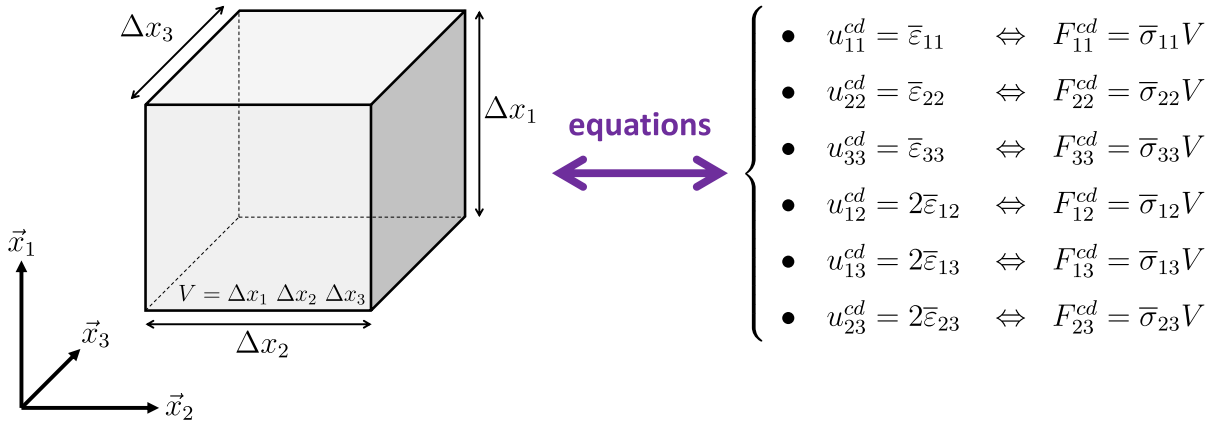

Figure I.5: Connection of the "constraint drivers" with the unit cell

The details for all the kinematic constraint equations used to connect the "constraint drivers" with the unit cell can be found in Appendix A.

2.2.2 Off-axis control of the unit cell

In some cases, it can be interesting to control the unit cell with an off-axis stress-strain state. In this purpose, as illustrated in Figure I.6, a rotation of the unit cell is considered. Thus, a 2^{nd} order tensor $\boldsymbol{T}$ expressed in the unit cell coordinate system $(\vec{x}_1, \vec{x}_2, \vec{x}_3)$ is obtained from its counterpart expressed in a reference coordinate system $(\vec{x}, \vec{y}, \vec{z})$ through the following relationships:

$$\boldsymbol{T}_{(\vec{x}_1,\vec{x}_2,\vec{x}_3)} = \boldsymbol{R} \cdot \boldsymbol{T}_{(\vec{x},\vec{y},\vec{z})} \cdot \boldsymbol{R}^T = \mathbb{Q} : \boldsymbol{T}_{(\vec{x},\vec{y},\vec{z})} \qquad \text{where} \qquad \mathbb{Q} = \boldsymbol{R} \overline{\otimes} \boldsymbol{R}. \tag{I.34}$$

As usual in mechanics, the rotational $\boldsymbol{R}$ is a 2^{nd} order orthonormal tensor such as $\boldsymbol{R} \cdot \boldsymbol{R}^{-1} = \boldsymbol{R} \cdot \boldsymbol{R}^T = \boldsymbol{I}$. Its general expression is given by:

$$\boldsymbol{R} = \begin{pmatrix} a & b & c \\ d & e & f \\ g & h & i \end{pmatrix}, \tag{I.35}$$

where the coefficients a, b, c, d, e, f, g, h and i are to be defined according to the considered rotation. As an example, for the case of a rotation around the $\vec{z}$ axis (see Figure I.6b), these coefficients are directly related to the angle of rotation θ such as $a = e = \cos(\theta)$, $b = -d = \sin(\theta)$, $i = 1$ and $c = f = g = h = 0$. Using this formalism, with the help of the Voigt notation, the relationship (I.34), written in terms of macroscopic strain, becomes:

$$\underbrace{\begin{Bmatrix} \overline{\varepsilon}_{11} \\ \overline{\varepsilon}_{22} \\ \overline{\varepsilon}_{33} \\ 2\overline{\varepsilon}_{12} \\ 2\overline{\varepsilon}_{13} \\ 2\overline{\varepsilon}_{23} \end{Bmatrix}}_{\overline{\boldsymbol{\varepsilon}}_{(\vec{x}_1,\vec{x}_2,\vec{x}_3)}} = \underbrace{\begin{pmatrix} a^2 & b^2 & c^2 & ab & ac & bc \\ d^2 & e^2 & f^2 & de & df & ef \\ g^2 & h^2 & i^2 & gh & gi & hi \\ 2ad & 2be & 2cf & bd+ae & cd+af & ce+bf \\ 2ag & 2bh & 2ci & bg+ah & cg+ai & ch+bi \\ 2dg & 2eh & 2fi & eg+dh & fg+di & fh+ei \end{pmatrix}}_{\mathbb{Q}} \times \underbrace{\begin{Bmatrix} \overline{\varepsilon}_{xx} \\ \overline{\varepsilon}_{yy} \\ \overline{\varepsilon}_{zz} \\ 2\overline{\varepsilon}_{xy} \\ 2\overline{\varepsilon}_{xz} \\ 2\overline{\varepsilon}_{yz} \end{Bmatrix}}_{\overline{\boldsymbol{\varepsilon}}_{(\vec{x},\vec{y},\vec{z})}}, \tag{I.36}$$

whereas, written in terms of macroscopic stress, this gives:

$$\underbrace{\begin{Bmatrix} \overline{\sigma}_{11} \\ \overline{\sigma}_{22} \\ \overline{\sigma}_{33} \\ \overline{\sigma}_{12} \\ \overline{\sigma}_{13} \\ \overline{\sigma}_{23} \end{Bmatrix}}_{\overline{\boldsymbol{\sigma}}_{(\vec{x}_1,\vec{x}_2,\vec{x}_3)}} = \underbrace{\begin{pmatrix} a^2 & b^2 & c^2 & 2ab & 2ac & 2bc \\ d^2 & e^2 & f^2 & 2de & 2df & 2ef \\ g^2 & h^2 & i^2 & 2gh & 2gi & 2hi \\ ad & be & cf & bd+ae & cd+af & ce+bf \\ ag & bh & ci & bg+ah & cg+ai & ch+bi \\ dg & eh & fi & eg+dh & fg+di & fh+ei \end{pmatrix}}_{\mathbb{Q}} \times \underbrace{\begin{Bmatrix} \overline{\sigma}_{xx} \\ \overline{\varepsilon}_{yy} \\ \overline{\sigma}_{zz} \\ \overline{\sigma}_{xy} \\ \overline{\sigma}_{xz} \\ \overline{\sigma}_{yz} \end{Bmatrix}}_{\overline{\boldsymbol{\sigma}}_{(\vec{x},\vec{y},\vec{z})}}, \tag{I.37}$$

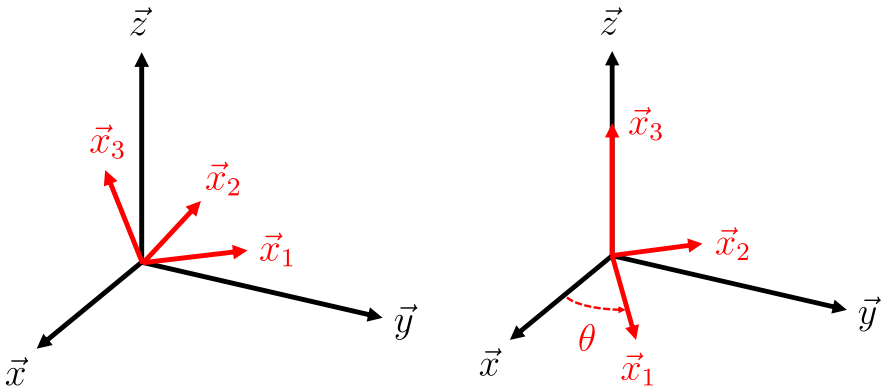

(a) General rotation (b) Rotation around the $\vec{z}$ axis

Figure I.6: Illustration of the unit cell coordinate system $(\vec{x}_1, \vec{x}_2, \vec{x}_3)$ and the reference coordinate system $(\vec{x}, \vec{y}, \vec{z})$.

The "constraint drivers" previously defined allow only to describe the macroscopic behaviour in the coordinate system of the unit cell $(\vec{x}_1, \vec{x}_2, \vec{x}_3)$. In order to consider an off axis stress-strain state, it is proposed to create six new "constraint drivers" that will represent the behaviour of the unit cell in the reference coordinate system $(\vec{x}, \vec{y}, \vec{z})$. These new "constraint drivers" are also introduced by adding six new nodes (among which only the first degree of freedom is used). Their displacements are noted u^{cd}_{xx}, u^{cd}_{yy}, u^{cd}_{zz}, u^{cd}_{xy}, u^{cd}_{xz} and u^{cd}_{yz}, and take the values of each component of the macroscopic strain tensor defined in the reference coordinate system: $\overline{\varepsilon}_{xx}$, $\overline{\varepsilon}_{yy}$, $\overline{\varepsilon}_{zz}$, $2\overline{\varepsilon}_{xy}$, $2\overline{\varepsilon}_{xz}$ and $2\overline{\varepsilon}_{yz}$, respectively. Then, as shown in Figure I.7, the link between the new constrain drivers, defining the macroscopic strain in $(\vec{x}, \vec{y}, \vec{z})$, and the previous ones, defining the macroscopic strain in $(\vec{x}_1, \vec{x}_2, \vec{x}_3)$, is ensured using a set of six new kinematic constraint equations directly obtained from (I.36):

$$\begin{cases} u^{cd}_{11} - a^2\ u^{cd}_{xx} - b^2\ u^{cd}_{yy} - c^2\ u^{cd}_{zz} - ab\ u^{cd}_{xy} - ac\ u^{cd}_{xz} - bc\ u^{cd}_{yz} = 0 \\ u^{cd}_{22} - d^2\ u^{cd}_{xx} - e^2\ u^{cd}_{yy} - f^2\ u^{cd}_{zz} - de\ u^{cd}_{xy} - df\ u^{cd}_{xz} - ef\ u^{cd}_{yz} = 0 \\ u^{cd}_{33} - g^2\ u^{cd}_{xx} - h^2\ u^{cd}_{yy} - i^2\ u^{cd}_{zz} - gh\ u^{cd}_{xy} - gi\ u^{cd}_{xz} - hi\ u^{cd}_{yz} = 0 \\ u^{cd}_{12} - 2ad\ u^{cd}_{xx} - 2be\ u^{cd}_{yy} - 2cf\ u^{cd}_{zz} - (bd+ae)\ u^{cd}_{xy} - (cd+af)\ u^{cd}_{xz} - (ce+bf)\ u^{cd}_{yz} = 0 \\ u^{cd}_{13} - 2ag\ u^{cd}_{xx} - 2bh\ u^{cd}_{yy} - 2ci\ u^{cd}_{zz} - (bg+ah)\ u^{cd}_{xy} - (cg+ai)\ u^{cd}_{xz} - (ch+bi)\ u^{cd}_{yz} = 0 \\ u^{cd}_{23} - 2dg\ u^{cd}_{xx} - 2eh\ u^{cd}_{yy} - 2fi\ u^{cd}_{zz} - (eg+dh)\ u^{cd}_{xy} - (fg+di)\ u^{cd}_{xz} - (fh+ei)\ u^{cd}_{yz} = 0 \end{cases} \tag{I.38}$$

The dual forces on these new "constraint drivers", noted F^{cd}_{xx}, F^{cd}_{yy}, F^{cd}_{zz}, F^{cd}_{xy}, F^{cd}_{xz} and F^{cd}_{yz}, directly give the product between the macroscopic stress in the reference coordinate system (the corresponding components: $\overline{\sigma}_{xx}$, $\overline{\sigma}_{yy}$, $\overline{\sigma}_{zz}$, $\overline{\sigma}_{xy}$, $\overline{\sigma}_{xz}$ and $\overline{\sigma}_{yz}$) and the volume of the unit cell (see Figure I.7).

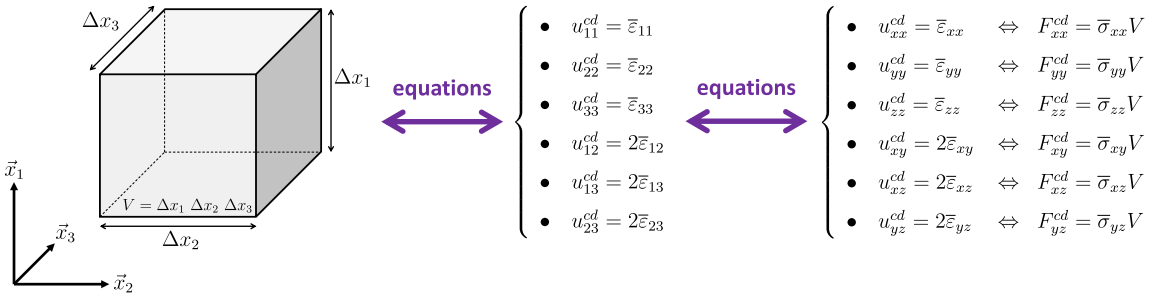

Figure I.7: Connexion between the "constraint drivers" defining the macroscopic stress-strain in the unit cell coordinate system $(\vec{x}_1, \vec{x}_2, \vec{x}_3)$ and the "constraint drivers" defining the macroscopic stress-strain in reference coordinate system $(\vec{x}, \vec{y}, \vec{z})$.

This methodology is particularly helpful because it allows to apply any complex off-axis stress-strain state on the unit cell, while the latter is always geometrically defined in its axes. This point is illustrated through an example of an off-axis tension in Section 4.2.

3 Unit cells for woven composites

As mentioned in the introductory section, in this work, the geometrical and finite element representation of woven composites unit cells are performed with the help of the software *TexGen*[2] [115], where much of the details regarding the modelling theory can be found in [177].

3.1 Geometrical representation of woven microstructures

Independently from the weaving pattern, the geometry of a woven microstructure is defined through the parameters a, b, h, l and δ. As shown in Figure I.8, a and b are the dimensions of the yarns cross section that is assumed to be elliptic, h denotes the thickness of the microstructure, l is the in plane distance between the centres of two consecutive parallel yarns and δ defines the vertical space between two perpendicular yarns. Let's remark that, in reality, the yarns are composed of numerous fibres unidirectionally oriented embedded in the matrix. With the described modelling approach, the yarns are considered as an equivalent homogeneous medium with an anisotropic constitutive behaviour that depends on a certain material orientation. The latter is defined for each yarn material point with respect to the yarns middle line. The waviness of this middle line is automatically calculated according to the considered weaving pattern (see Figure I.9) via the *TexGen* utilities [115, 177].

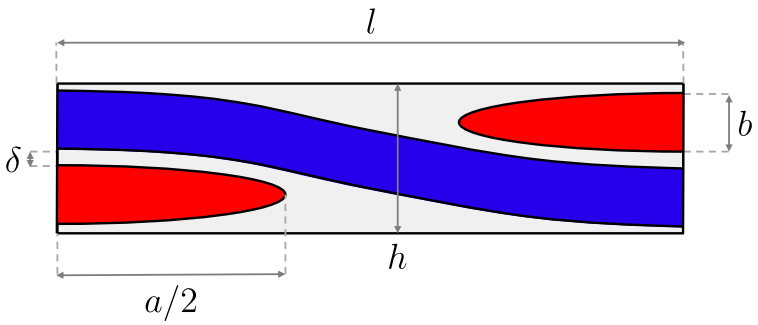

Figure I.8: Geometric definition of a woven microstructure. The grey domain represents the matrix phase, while the blue and red domains are the warp and weft yarns, respectively.

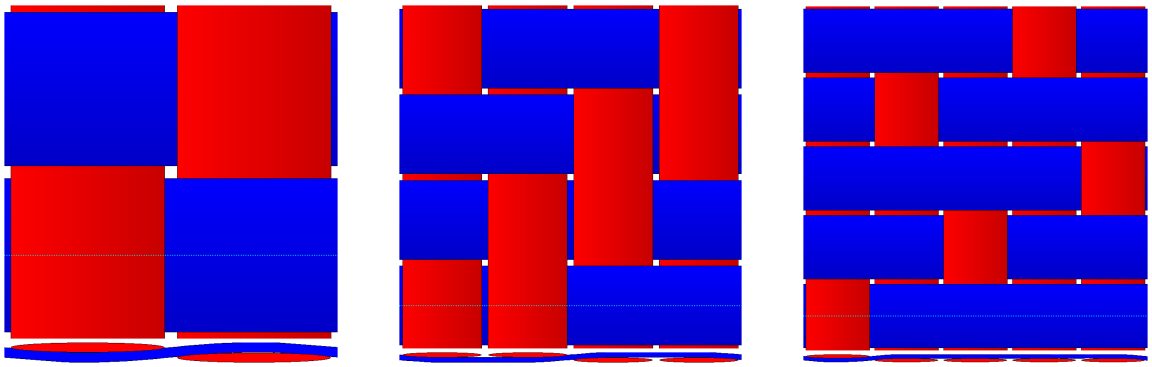

(a) Plain weave pattern (b) 2-2 Twill weave pattern (c) 5-H Satin weave pattern

Figure I.9: Examples of weaving patterns.

2. http://texgen.sourceforge.net/index.php/Main_Page

Note that, in such composites, the periodicity of the microstructure is well respected in the plane of the reinforcement, but is not always ensured in the 3^{rd} direction. Nevertheless, in this work it will be considered that the 3D periodicity stands. Thus, the RVE of the microstructure is directly defined by its unit cell that represents the smallest repeating unit element.

3.2 Finite element mesh of the unit cell

The previously described geometry is periodically meshed through the *TexGen* utilities [115, 177]. So as to illustrate this feature, the mesh of the unit cell considered for the studied composite is presented in Figure I.10. Its characteristic dimensions (see Figure I.8) are later identified in Section 2 of Chapter IV. The mesh of the unit cell contains 8522 nodes and 40060 first order tetrahedral elements (C3D4 in *ABAQUS*). Note that a spatial convergence analysis was carried out regarding the mesh refinement in order to obtain a good enough compromise between accuracy and reasonable computational cost.

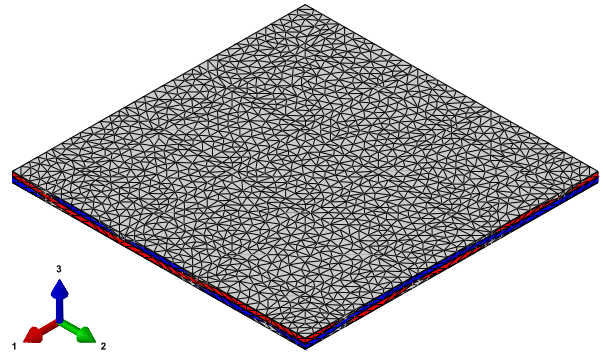

(a) Mesh of the entire unit cell

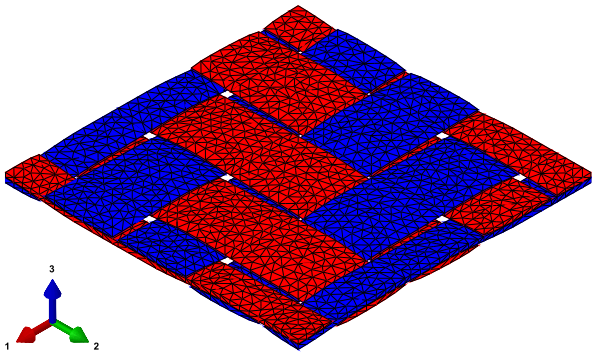

(b) Mesh of the yarns

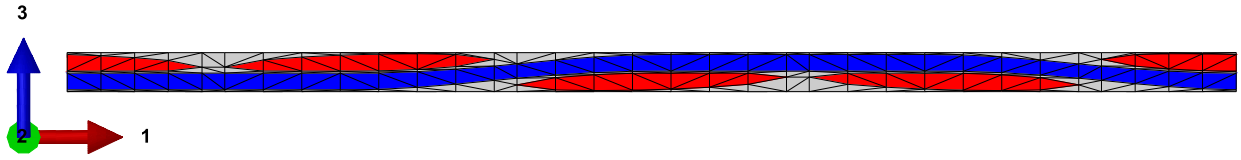

(c) Side view of the mesh

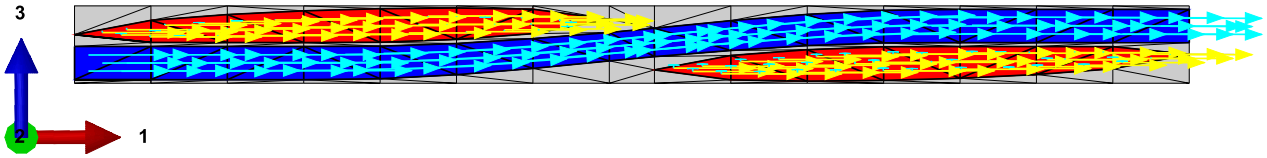

(d) Material orientations of the yarns elements: the blue and yellow arrows represent the 1^{st} and 2^{nd} axes, respectively

Figure I.10: Finite element mesh of the unit cell of the studied composite. The weaving pattern is a 2-2 twill weave (see Figure I.9b). The characteristic dimensions (see Figure I.8) are identified later in Section 2 in Chapter IV. They are provided in Table IV.1.

As already mentioned, the yarns are considered as an equivalent homogeneous medium with an anisotropic behaviour that depends on a certain material orientation. Thus, for each yarns element, a local material coordinate system is defined in such a way that the 1^{st} axis is always oriented along the middle line of the yarns, while the 2^{nd} axis is always parallel to the plane of the woven reinforcement, as shown in Figure I.10d.

4 Examples

In this section, applicative examples dealing with linear elasticity are proposed to illustrate the framework of periodic homogenization described in Section 2. The unit cell of the studied composite is utilized (see Figure I.10) with the following elastic properties:

Constituent	Parameter	value	unit
Matrix (isotropic)	E	2074	MPa
	ν	0.3	-
Yarns (transversely isotropic)	E_1	62615	MPa
	$E_2 = E_3$	21526	MPa
	$\nu_{12} = \nu_{13}$	0.228	-
	$\nu_{23} = \frac{E_2}{2G_{23}} - 1$	0.268	-
	$G_{12} = G_{13}$	8661	MPa
	$G_{23} = \frac{E_2}{2(1+\nu_{23})}$	8488	MPa

Table I.2: Elastic properties of the composite constituents, namely: the matrix and the yarns. These properties are identified in Section 1 of Appendix G.

4.1 Computation of the homogenized stiffness tensor

In this first example, The homogenized stiffness tensor of the whole composite is computed through the strain driven approach (see Section 2.1.6). Thus, according to the relationship (I.24), each term of the macroscopic stiffness tensor is recovered from the stresses resulting from the six unitary strain states (I.23) whose deflections are shown in Figures I.11, I.12, I.13, I.14, I.15 and I.16. With the help of the Voigt notation, this gives the following stiffness tensor:

$$\overline{\mathbb{C}} = \begin{pmatrix} 25016 & 3618 & 2171 & 0 & 0 & 0 \\ & 25016 & 2171 & 0 & 0 & 0 \\ & & 6453 & 0 & 0 & 0 \\ & & & 4551 & 0 & 0 \\ & & & & 1883 & 0 \\ \text{sym.} & & & & & 1883 \end{pmatrix} \text{ MPa.} \tag{I.39}$$

The computed macroscopic stiffness tensor shows that the homogenized behaviour can be considered as orthotropic with tetragonal symmetry [3] [186], since $\overline{C}_{1111} = \overline{C}_{2222}$, $\overline{C}_{1133} = \overline{C}_{2233}$ and $\overline{C}_{1313} = \overline{C}_{2323}$.

3. Note that the computed terms of $\overline{\mathbb{C}}$ were slightly modified so that the latter is perfectly orthotropic with tetragonal symmetry. Indeed, due to numerical approximations, a small deviation of a few MPa may be observed.

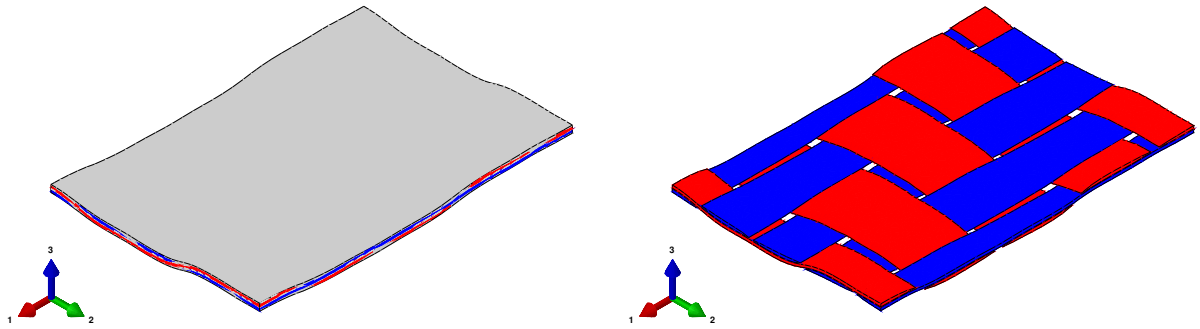

(a) Entire unit cell (b) Yarns

Figure I.11: Deflection of the unit cell for the unitary strain state $\overline{\boldsymbol{\varepsilon}}_{(11)}$.

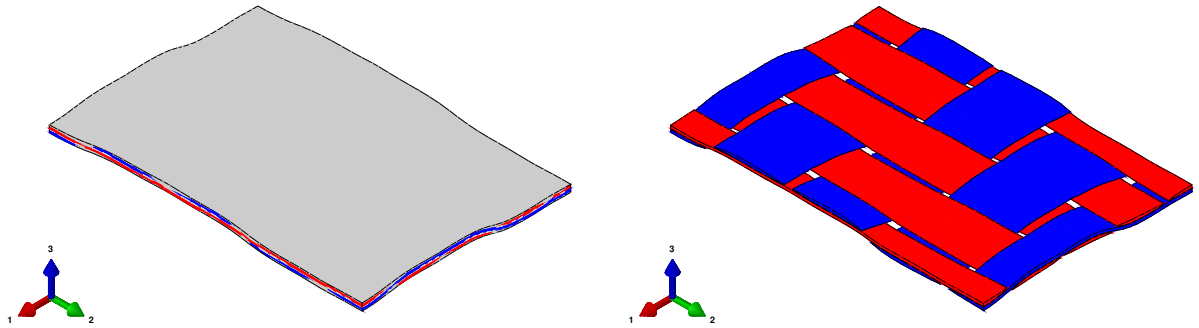

(a) Entire unit cell (b) Yarns

Figure I.12: Deflection of the unit cell for the unitary strain state $\overline{\boldsymbol{\varepsilon}}_{(22)}$.

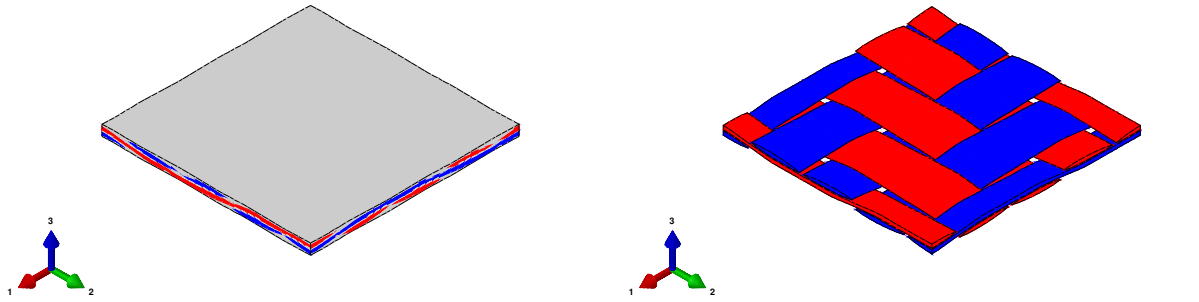

(a) Entire unit cell (b) Yarns

Figure I.13: Deflection of the unit cell for the unitary strain state $\overline{\boldsymbol{\varepsilon}}_{(33)}$.

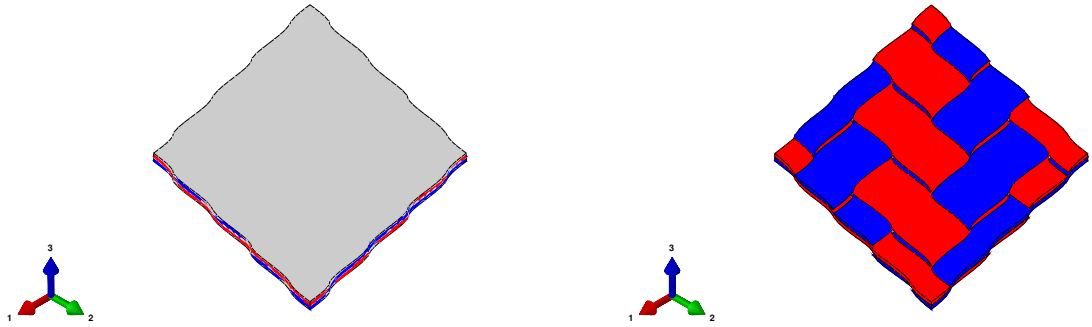

(a) Entire unit cell (b) Yarns

Figure I.14: Deflection of the unit cell for the unitary strain state $\overline{\boldsymbol{\varepsilon}}_{(12)}$.

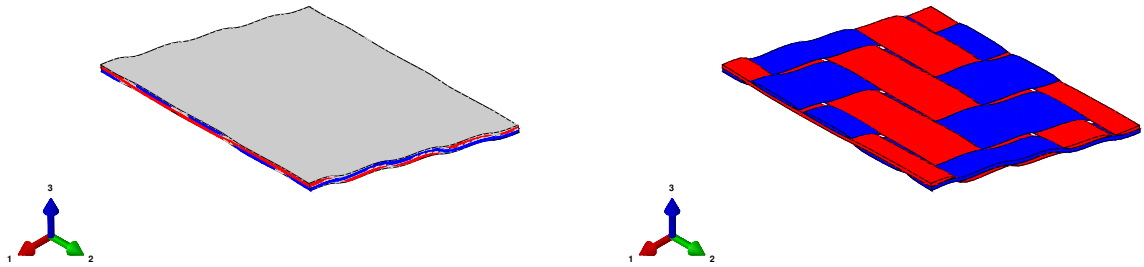

(a) Entire unit cell (b) Yarns

Figure I.15: Deflection of the unit cell for the unitary strain state $\overline{\boldsymbol{\varepsilon}}_{(13)}$.

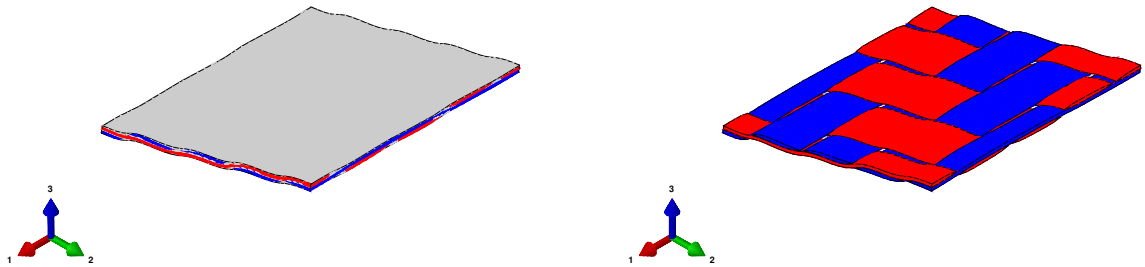

(a) Entire unit cell (b) Yarns

Figure I.16: Deflection of the unit cell for the unitary strain state $\overline{\boldsymbol{\varepsilon}}_{(23)}$.

4.2 Off-axis tension

This second example illustrates the off-axis control of the unit cell as introduced in Section 2.2.2. Thus, the case of an off-axis tension is proposed as shown in Figure I.17.

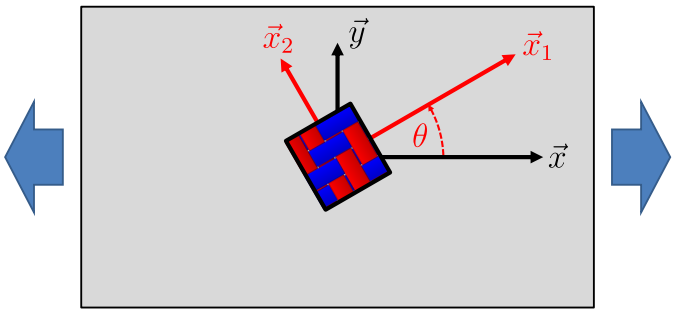

Figure I.17: Illustration of an off-axis uni-axial test.

The unit cell is defined in the coordinate system $(\vec{x}_1, \vec{x}_2, \vec{x}_3)$, itself defined with respect to the reference coordinate system $(\vec{x}, \vec{y}, \vec{z})$ by a rotation around the $\vec{z}$ axis. This rotation is quantified by an angle $\theta = 30^o$. The composite is then subjected to a uni-axial strain in the reference coordinate system, namely: $\overline{\varepsilon}_{xx} = \delta$, while being free of stress in all the other components:

$$\left\{ \begin{array}{rcl} \overline{\varepsilon}_{xx} & = & \delta \\ \overline{\varepsilon}_{yy} & = & \text{unknown} \\ \overline{\varepsilon}_{zz} & = & \text{unknown} \\ 2\overline{\varepsilon}_{xy} & = & \text{unknown} \\ 2\overline{\varepsilon}_{xz} & = & \text{unknown} \\ 2\overline{\varepsilon}_{yz} & = & \text{unknown} \end{array} \right\}, \quad \left\{ \begin{array}{rcl} \overline{\sigma}_{xx} & = & \text{unknown} \\ \overline{\sigma}_{yy} & = & 0 \\ \overline{\sigma}_{zz} & = & 0 \\ \overline{\sigma}_{xy} & = & 0 \\ \overline{\sigma}_{xz} & = & 0 \\ \overline{\sigma}_{yz} & = & 0 \end{array} \right\} \quad \text{MPa.} \tag{I.40}$$

After computation, the unknown values of the macroscopic strain and stress tensor in the reference coordinate system are obtained:

$$\left\{ \begin{array}{rcl} \overline{\varepsilon}_{xx} & = & 1 \\ \overline{\varepsilon}_{yy} & = & -0.4378 \\ \overline{\varepsilon}_{zz} & = & -0.1882 \\ 2\overline{\varepsilon}_{xy} & = & -0.4175 \\ 2\overline{\varepsilon}_{xz} & = & 0.0000 \\ 2\overline{\varepsilon}_{yz} & = & 0.0000 \end{array} \right\} \times \delta, \quad \left\{ \begin{array}{rcl} \overline{\sigma}_{xx} & = & 15284 \\ \overline{\sigma}_{yy} & = & 0 \\ \overline{\sigma}_{zz} & = & 0 \\ \overline{\sigma}_{xy} & = & 0 \\ \overline{\sigma}_{xz} & = & 0 \\ \overline{\sigma}_{yz} & = & 0 \end{array} \right\} \times \delta \quad \text{MPa.} \tag{I.41}$$

The associated deflection of the unit cell is shown in Figure I.18. Expressed in the coordinate system of the unit cell $(\vec{x}_1, \vec{x}_2, \vec{x}_3)$, with the help of (I.36) and (I.37), the macroscopic strain and stress respectively become:

$$\left\{ \begin{array}{rcl} \overline{\varepsilon}_{11} & = & 0.4598 \\ \overline{\varepsilon}_{22} & = & 0.1024 \\ \overline{\varepsilon}_{33} & = & -0.1882 \\ 2\overline{\varepsilon}_{12} & = & -1.4539 \\ 2\overline{\varepsilon}_{13} & = & 0.0000 \\ 2\overline{\varepsilon}_{23} & = & 0.0000 \end{array} \right\} \times \delta, \quad \left\{ \begin{array}{rcl} \overline{\sigma}_{11} & = & 11463 \\ \overline{\sigma}_{22} & = & 3821 \\ \overline{\sigma}_{33} & = & 0 \\ \overline{\sigma}_{12} & = & -6618 \\ \overline{\sigma}_{13} & = & 0 \\ \overline{\sigma}_{23} & = & 0 \end{array} \right\} \times \delta \quad \text{MPa.} \tag{I.42}$$

Thus, it can be remarked that the obtained values are well consistent with the macroscopic stiffness tensor previously computed in (I.39).

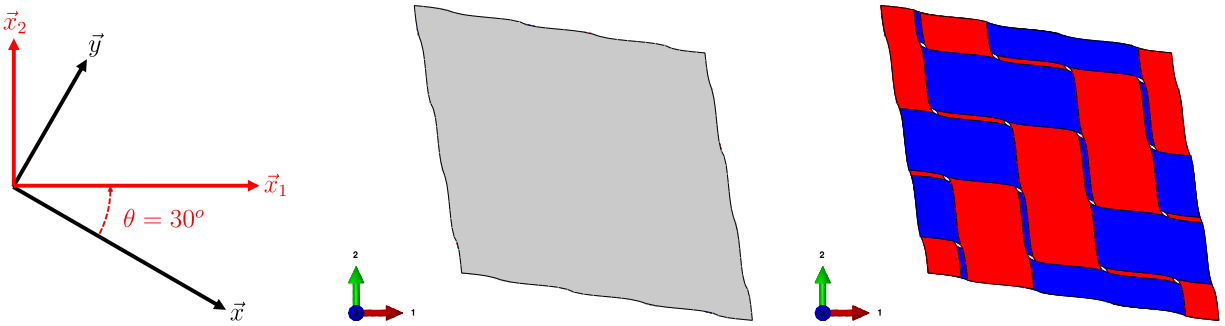

(a) Reference and unit cell coordinate systems, $(\vec{x}, \vec{y}, \vec{z})$ and $(\vec{x}_1, \vec{x}_2, \vec{x}_3)$, respectively.

(b) Entire unit cell

(c) Yarns

Figure I.18: Deflection of the unit cell under an off-axis tension.

5 Conclusions

In this chapter, a general framework of multi-scale modelling based on the concept of periodic homogenization has been introduced and applied to the particular case of woven composites through the use of the dedicated tool *TexGen*. A new method is proposed to perform off-axis control of the unit cell, while the latter remains geometrically defined in its axes. Although only applications dealing with linear elasticity are treated in this chapter, the proposed framework is independent from the local constitutive equations, thus it can be easily utilized with complex non-linear behaviours. For this purpose, specific constitutive models will be developed in Chapters II and III for the matrix and the yarns, respectively, and will be applied together with the unit cell geometrical characteristics to study the composite non-linear response under cyclic loading conditions, in Chapter IV.

Chapter II

Phenomenological multi-mechanisms constitutive modelling for thermoplastic matrices

Contents

The content of the present chapter was the scope of a peer-reviewed paper entitled **"Phenomenological multi-mechanisms constitutive modelling for thermoplastic polymers, implicit implementation and experimental validation"** published in *Mechanics of Materials* [163].

1 Introduction

Thermoplastics and more especially semi-crystalline polymers are well known to exhibit a mechanical time-dependent (or rate-dependent) behaviour combining both solid and fluid properties. They also appear to be sensitive to the environmental conditions, namely relative humidity and temperature [102, 7, 6, 121, 122, 120, 123]. Investigations showed that these materials are also subjected to stiffness reduction during loading caused by the existence of damage mechanisms related to the initiation, the growth and the coalescence of micro defects [47].

The growing interest for this type of materials, especially for automotive applications, has contributed to many modelling efforts aiming at capturing the complex behaviour of thermoplastics or thermoplastic-based composites. Among the existing models, those based on phenomenological approaches account for one or several dissipative mechanisms. Indeed, to capture the overall behaviour of polymers or polymeric composites, some authors refer to the theories of viscoelasticity [174, 136, 86, 138], viscoplasticity [56, 57, 3, 52, 50, 51, 54, 55], coupled viscoelasticity and viscoplasticity [53, 135, 189, 197, 198], damage [143, 144] or even both coupled viscoelasticity, viscoplasticity and damage [101, 99, 89, 187, 103, 200]. Some other models integrate aspects related to physics of polymers, such as the molecular chains network reorganization [126] or the partial phase transformation between crystalline and amorphous phases [146, 147]. Other works [8] have introduced conformational rearrangement as mechanisms behind yielding and plasticity of glassy polymers. More recent studies [190] consider the deformation of glassy polymers through the evolution of the free volume and shear transformation zones during the generation of plastic strain. Despite their efficiency, the latter type of constitutive models requires physical data that can be difficult to measure experimentally or to control during the manufacturing process. Thermodynamically-based phenomenological models are more suitable since they require material parameters that can be identified from conventional mechanical tests. Indeed, the phenomenological approaches focus only on the overall description of the material behaviour, using internal state variables. For polymers, the deformation and degradation mechanisms are generally time-dependent. These phenomena are introduced through anelastic strain and stiffness reduction, along with their related dissipation. When acting simultaneously, these dissipative mechanisms can be modelled together using coupled formulations.

With regard to viscoelasticity, two main modelling approaches can be used, namely: the hereditary integral [135, 89] or the differential form. The hereditary integral representation is based on the concept of relaxation or creep functions that need to be integrated through the whole time history to establish the stress-strain relationship. The main interest of the integral form is that the viscoelastic mechanism can be modelled through a single strain state variable. However, its practical use is generally adopted for the case of isotropic viscoelasticity and an extension to non-isotropic media is not straightforward. In addition, the fully coupled thermomechanical behaviour cannot be easily integrated within the integral formalism, since such coupling effects require derivative operations of the thermodynamic potentials that may be complicated within a formulation involving time integral. On the

other hand, the differential representation is based on the assembly of rheological elements that store or dissipate energy, namely: springs and dash-pots respectively. Such a description may involve a certain number of strain state variables in order to capture properly the complete viscoelastic response. The main advantage of this formalism is that it permits an explicit splitting of the various energetic terms of the thermodynamic potentials. It also offers more flexibilities for the integration of additional effects such as thermally activated mechanisms [197, 198] or anisotropy.

Concerning damage, several approaches can be found in the literature. In some of them, the effect of damage is introduced through a micromechanical representation based on a physical definition of a damaged representative volume element that accounts for material micro-discontinuities [71, 165]. For semi-crystalline polymers such a description requires a deep knowledge of the involved degradation mechanisms at the macromolecular chains scale [47] and also a proper modelling theory. This task is neither straightforward nor feasible due to the fact that the definition of a continuum medium does not stand at this scale. Alternatively, damage can also be taken into account in a purely phenomenological manner, where only its effect on the overall material response is considered, namely: the stiffness reduction. For this purpose, the Continuum Damage Mechanics (CDM) theories are particularly adapted. Therefore, the damage is introduced with the help of one or several internal state variables [109, 110] and is hence considered as a continuum quantity describing the state of the material at the scale of interest.

In this chapter, a constitutive model accounting for viscoelasticity, viscoplasticity and ductile damage is proposed. It is formulated within a proper thermodynamical framework and is applied to predict the deformation of semi-crystalline polymers under the small strain assumption. It is well established that such materials are time and temperature-dependent [8]. The temperature may play a significant role due to the self-heating phenomenon arising from dissipative mechanisms, especially upon cyclic loading [13, 14, 15, 198]. With the present model, it is important to mention that only the time-dependency is accounted for, while the material is assumed to stay under isothermal conditions. The formulation of the proposed model is partially inspired by the works of [89, 88], especially regarding the integration of viscoplasticity and damage. Nevertheless, the main difference lies within the viscoelastic contribution. In [89, 88], the latter is described through the Prony series (several Maxwell branches in parallel) with the help of an integral representation. In the present work, the viscoelasticity is described from a series of Kelvin-Voigt branches, considering a differential representation. Despite the fact that both approaches have a different formalism[1], it should be mentioned that they are both equivalent in terms of global response, including both creep and relaxation effects. The choice of the adopted formalism, namely: series of Kelvin-Voigt branches with a differential representation, is motivated by its flexibilities regarding a potential extension to fully-coupled thermomechanical analyses and/or the integration of anisotropic effects, as previously mentioned.

The constitutive model proposed in this chapter will be used as matrix phase for the whole woven composite through the multi-scale approach previously introduced in Chapter

1. Their practical difference is the following: Prony series (several Maxwell branches in parallel) imply an additive decomposition of the stress as proposed by several authors, among them [135, 89]. Indeed, the sum of the stresses in each single Maxwell branch provides the total stress, while all the Maxwell branches share the same strain. On the other hand, a multiple Kelvin Voigt (several Kelvin-Voigt branches in series) implies an additive decomposition of the strain. Each Kelvin-Voigt branch has its own viscoelastic strain, while all branches share the same stress.

I. Let's recall that another constitutive model will be proposed for the yarn phase in Chapter III, before presenting the whole multi-scale model for thermoplastic-based woven composites in Chapter IV.

This chapter is structured as follows: In Section 2, the constitutive equations and the thermodynamics framework of the proposed model are presented. Section 4 focuses on the experimental procedure and the identification strategy of the model parameters for the polyamide 6-6, as well as its experimental validation under various loading conditions. Section 5 illustrates the model's capabilities through examples of simulations (including a 3D FE analysis) highlighting the time-dependent response of the material as well as its dissipative behaviour, especially under cyclic loading. To finish, Section 6 summarizes the main conclusions related to this chapter.

In this chapter, the operators $\mathrm{hyd}(\boldsymbol{\sigma})$ and $\mathbf{Dev}(\boldsymbol{\sigma})$ designate the hydrostatic pressure and the deviatoric part of a stress tensor $\boldsymbol{\sigma}$, respectively, whereas $\mathrm{eq}(\boldsymbol{\sigma})$ is the equivalent Von Mises stress:

$$\mathrm{hyd}(\boldsymbol{\sigma}) = \frac{1}{3}\mathrm{tr}(\boldsymbol{\sigma}), \tag{II.1}$$

$$\mathbf{Dev}(\boldsymbol{\sigma}) = \boldsymbol{\sigma} - \mathrm{hyd}(\boldsymbol{\sigma})\boldsymbol{I}, \tag{II.2}$$

$$\mathrm{eq}(\boldsymbol{\sigma}) = \sqrt{\frac{3}{2}\Big(\mathbf{Dev}(\boldsymbol{\sigma}) : \mathbf{Dev}(\boldsymbol{\sigma})\Big)}. \tag{II.3}$$

2 Constitutive equations and thermodynamical framework

The objective of this section is to present the formulation of a thermodynamically based phenomenological model accounting for viscoelasticity, viscoplasticity and ductile damage in semi-crystalline polymers. The proposed model is represented by the rheological scheme given in Figure II.1a. It is composed of several elements positioned in series, which are detailed below. The damage is introduced through the CDM theories based on the well-known principle of effective stress [109, 110]. First introduced in the uni-axial case, a similar formalism can be easily applied in 3D if damage is regarded as an isotropic phenomenon. Thus, the definition of the effective stress tensor, that has been adopted here, is simply given by:

$$\widetilde{\boldsymbol{\sigma}} = \frac{\boldsymbol{\sigma}}{1-D}, \tag{II.4}$$

where D is the damage variable expressed as a scalar quantity. Actually, even if the material is assumed to be initially isotropic, the overall response may exhibit anisotropic effects induced by damage that are governed by the directions of the principal stresses. Examples of extensions to 3D damage induced anisotropy can be found in the literature [28, 58, 110, 44, 43]. Nevertheless, such a description requires quantification through further experimental data highlighting the behaviour in the other directions or from experiments where the material is subjected to multi-axial loading conditions. In the absence of these data, the simplest assumption remains the case of isotropic damage.

The rheological model consists of the following elements:

- One single linear spring subjected to an elastic strain $\boldsymbol{\varepsilon_e}$.
- N viscoelastic Kelvin-Voigt branches, consisting of a linear spring and a linear dash-pot assembled in parallel (Figure II.1b). Each Kelvin-Voigt branch i is subjected to a viscoelastic strain $\boldsymbol{\varepsilon_{v_i}}$. From a conceptual point of view, a single linear Kelvin-Voigt branch offers interesting capabilities, capturing the creep and relaxation effects, but only within a particular range of time. Considering several Kelvin-Voigt branches allow to account for similar effects within an extended range of time [149].
- One viscoplastic branch, consisting of a frictional element, a non-linear spring and a non-linear dash-pot both assembled in parallel (Figure II.1c). This branch is subjected to a viscoplastic strain $\boldsymbol{\varepsilon_p}$ that is only generated if the equivalent effective stress eq($\widetilde{\boldsymbol{\sigma}}$) exceeds a certain threshold.

The assembly in series of all those elements implies an additive decomposition of the total strain $\boldsymbol{\varepsilon}$:

$$\boldsymbol{\varepsilon} = \boldsymbol{\varepsilon_e} + \sum_{i=1}^{N} \boldsymbol{\varepsilon_{v_i}} + \boldsymbol{\varepsilon_p}, \tag{II.5}$$

while all the branches act on the same effective stress $\widetilde{\boldsymbol{\sigma}}$. Nevertheless, the viscoplastic branch is assumed to be only sensitive to deviatoric part of $\widetilde{\boldsymbol{\sigma}}$ through the effective equivalent stress eq($\widetilde{\boldsymbol{\sigma}}$). The duality between stress and strain implies the existence of an effective equivalent viscoplastic strain denoted by the scalar variable r. The latter is connected to the viscoplastic strain tensor $\boldsymbol{\varepsilon_p}$ through the evolution laws. It is worth noticing that,

in the proposed model, the damage is assumed to be "ductile" as it only evolves when the viscoplastic strain is being generated, making those two mechanisms directly coupled [108, 110, 89].

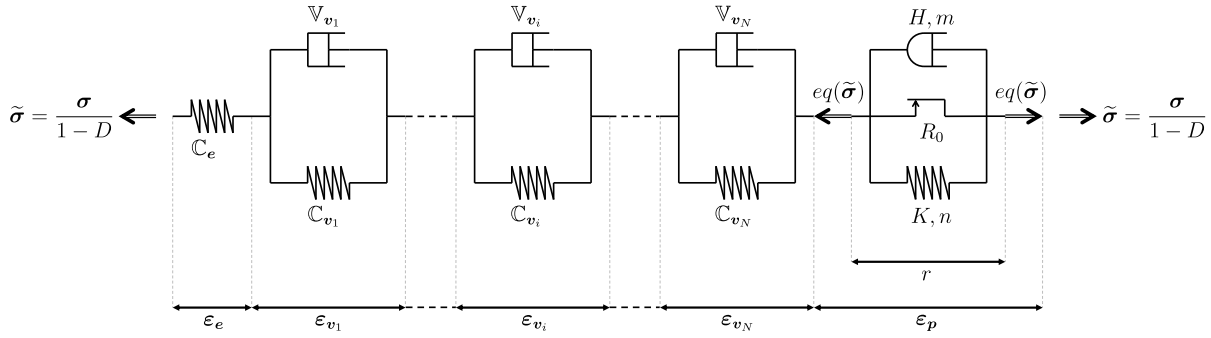

(a) Complete rheological scheme

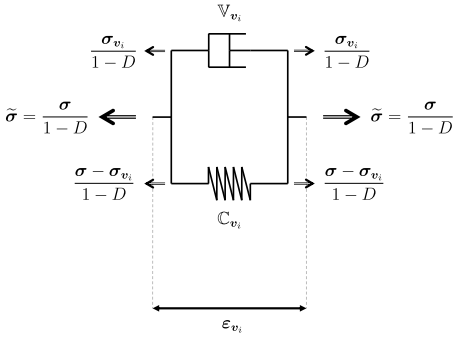

(b) Single Kelvin-Voigt branch

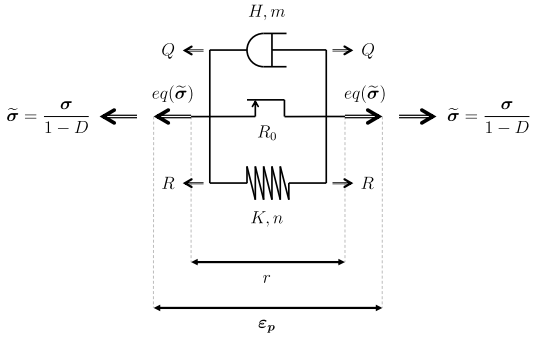

(c) Viscoplastic branch

Figure II.1: Rheological scheme of the proposed model.

Finally, the observable state variable of the proposed model is $\boldsymbol{\varepsilon}$, while the internal state variables are $\boldsymbol{\varepsilon_{v_i}}$, $\boldsymbol{\varepsilon_p}$, r and D. The elastic strain $\boldsymbol{\varepsilon_e}$ is not considered as a state variable but, for convenience, is expressed by the difference between the total strain and both the viscoelastic and viscoplastic strains.

2.1 State laws

The proposed model is formulated within the framework of thermodynamics [67, 68, 69, 109, 33] , which is briefly described in Appendix B. Accordingly, the material state laws are based on a state potential, the Helmholtz free energy in the present case, that depends on the state variables previously mentioned. This potential is written as the sum of the stored energy functions of the single spring ψ_e, each Kelvin-Voigt branch ψ_{v_i} and the viscoplastic branch ψ_p:

$$\psi(\boldsymbol{\varepsilon}, \boldsymbol{\varepsilon_{v_i}}, \boldsymbol{\varepsilon_p}, r, D) = \psi_e(\boldsymbol{\varepsilon}, \boldsymbol{\varepsilon_{v_i}}, \boldsymbol{\varepsilon_p}, D) + \sum_{i=1}^{N} \psi_{v_i}(\boldsymbol{\varepsilon_{v_i}}, D) + \psi_p(r), \tag{II.6}$$

with

$$\rho\psi_e = \frac{1}{2}\left(\boldsymbol{\varepsilon} - \sum_{i=1}^{N} \boldsymbol{\varepsilon_{v_i}} - \boldsymbol{\varepsilon_p}\right) : (1-D)\mathbb{C}_{\boldsymbol{e}} : \left(\boldsymbol{\varepsilon} - \sum_{i=1}^{N} \boldsymbol{\varepsilon_{v_i}} - \boldsymbol{\varepsilon_p}\right), \tag{II.7}$$

$$\rho\psi_{v_i} = \frac{1}{2}\boldsymbol{\varepsilon_{v_i}} : (1-D)\mathbb{C}_{\boldsymbol{v_i}} : \boldsymbol{\varepsilon_{v_i}}, \tag{II.8}$$

$$\rho\psi_p = \int_0^r R(\xi)\ \ d\xi. \tag{II.9}$$

The associated variables, namely $\boldsymbol{\sigma}$, $-\boldsymbol{\sigma}_{\boldsymbol{v}_i}$, $-\boldsymbol{\sigma}$, R and $-Y$ are obtained from the derivation of the potential with respect to the state variables $\boldsymbol{\varepsilon}$, $\boldsymbol{\varepsilon}_{\boldsymbol{v}_i}$, $\boldsymbol{\varepsilon}_{\boldsymbol{p}}$, r and D, respectively:

$$\boldsymbol{\sigma} = \rho\frac{\partial\psi}{\partial\boldsymbol{\varepsilon}} = (1-D)\mathbb{C}_{\boldsymbol{e}} : \left(\boldsymbol{\varepsilon} - \sum_{i=1}^{N}\boldsymbol{\varepsilon}_{\boldsymbol{v}_i} - \boldsymbol{\varepsilon}_{\boldsymbol{p}}\right), \tag{II.10}$$

$$-\boldsymbol{\sigma}_{\boldsymbol{v}_i} = \rho\frac{\partial\psi}{\partial\boldsymbol{\varepsilon}_{\boldsymbol{v}_i}} = (1-D)\mathbb{C}_{\boldsymbol{v}_i} : \boldsymbol{\varepsilon}_{\boldsymbol{v}_i} - \boldsymbol{\sigma}, \tag{II.11}$$

$$-\boldsymbol{\sigma} = \rho\frac{\partial\psi}{\partial\boldsymbol{\varepsilon}_{\boldsymbol{p}}}, \tag{II.12}$$

$$R(r) = \rho\frac{\partial\psi}{\partial r}, \tag{II.13}$$

$$-Y = \rho\frac{\partial\psi}{\partial D} = -Y_e - \sum_{i=1}^{N} Y_{v_i}. \tag{II.14}$$

$\mathbb{C}_{\boldsymbol{e}}$ and $\mathbb{C}_{\boldsymbol{v}_i}$ denote the initial fourth order stiffness tensors of the single spring and the spring of the i^{th} Kelvin-Voigt branch, respectively. These tensors are classically formulated for bulk isotropic materials and are defined by the Young modulus E_e or E_{v_i}, respectively, as well as the Poisson ratio ν that is assumed to be the same in each stiffness tensor. The viscous stress $\boldsymbol{\sigma}_{\boldsymbol{v}_i}$ and the difference between $\boldsymbol{\sigma}$ and $\boldsymbol{\sigma}_{\boldsymbol{v}_i}$ respectively represent the stress acting on the linear dash-pot and spring of the i_{th} Kelvin-Voigt branch (Figure II.1b). The hardening function $R(r)$ stands for the effective equivalent stress acting on the non-linear spring of the viscoplastic branch (Figure II.1c). $R(r)$ must be an increasing function defined positive and null at $r = 0$. In this model, $R(r)$ is chosen under the form of a power law:

$$R(r) = Kr^n, \tag{II.15}$$

where K and n are material parameters. The total energy density release Y is written as the sum of the energy density releases associated with the single spring and each Kelvin-Voigt branch, Y_e and Y_{v_i} respectively, as expressed in (II.14). These quantities can be formulated either in terms of strain:

$$-Y_e = \rho\frac{\partial\psi_e}{\partial D} = -\frac{1}{2}\left(\boldsymbol{\varepsilon} - \sum_{i=1}^{N}\boldsymbol{\varepsilon}_{\boldsymbol{v}_i} - \boldsymbol{\varepsilon}_{\boldsymbol{p}}\right) : \mathbb{C}_{\boldsymbol{e}} : \left(\boldsymbol{\varepsilon} - \sum_{i=1}^{N}\boldsymbol{\varepsilon}_{\boldsymbol{v}_i} - \boldsymbol{\varepsilon}_{\boldsymbol{p}}\right), \tag{II.16}$$

$$-Y_{v_i} = \rho\frac{\partial\psi_{v_i}}{\partial D} = -\frac{1}{2}\boldsymbol{\varepsilon}_{\boldsymbol{v}_i} : \mathbb{C}_{\boldsymbol{v}_i} : \boldsymbol{\varepsilon}_{\boldsymbol{v}_i}, \tag{II.17}$$

or, by introducing (II.10) into (II.16) and (II.11) into (II.17), in terms of stress:

$$-Y_e = -\frac{\mathrm{eq}(\boldsymbol{\sigma})^2}{2E_e(1-D)^2}T_e(\boldsymbol{\sigma}), \tag{II.18}$$

$$-Y_{v_i} = -\frac{\mathrm{eq}(\boldsymbol{\sigma}-\boldsymbol{\sigma}_{\boldsymbol{v}_i})^2}{2E_{v_i}(1-D)^2}T_{v_i}(\boldsymbol{\sigma},\boldsymbol{\sigma}_{\boldsymbol{v}_i}), \tag{II.19}$$

where T_e ans T_{v_i} are the stress triaxiality functions of the single spring and the i^{th} Kelvin-Voigt branch, respectively:

$$T_e(\boldsymbol{\sigma}) = \frac{2}{3}(1+\nu) + 3(1-2\nu)\left[\frac{\mathrm{hyd}(\boldsymbol{\sigma})}{\mathrm{eq}(\boldsymbol{\sigma})}\right]^2, \tag{II.20}$$

$$T_{v_i}(\boldsymbol{\sigma}, \boldsymbol{\sigma}_{\boldsymbol{v}_i}) = \frac{2}{3}(1+\nu) + 3(1-2\nu)\left[\frac{\mathrm{hyd}(\boldsymbol{\sigma}-\boldsymbol{\sigma}_{\boldsymbol{v}_i})}{\mathrm{eq}(\boldsymbol{\sigma}-\boldsymbol{\sigma}_{\boldsymbol{v}_i})}\right]^2. \tag{II.21}$$

It is worth noticing that, under uni-axial stress conditions, T_e and T_{v_i} are equal to 1.

The state and associated variables of the proposed model are summarised in Table II.1.

State variables		Associated variables
Observable	internal	-
$\boldsymbol{\varepsilon}$		$\boldsymbol{\sigma}$
	$\boldsymbol{\varepsilon}_{\boldsymbol{v}_i}$	$-\boldsymbol{\sigma}_{\boldsymbol{v}_i}$
	$\boldsymbol{\varepsilon}_{\boldsymbol{p}}$	$-\boldsymbol{\sigma}$
	r	R
	D	$-Y$

Table II.1: State and associated variables of the proposed model.

2.2 Evolution laws

The second law of thermodynamics implies that the mechanical dissipation has to be always positive or null through the Clausius-Duhem inequality (see Section 1.3 in Appendix B). Considering isothermal conditions (see Section 2 in Appendix B), the rate of the dissipated energy Φ is expressed by the difference between the rate of the strain energy W_ε and the rate of the stored energy $\rho\psi$, in which equations (II.10), (II.11), (II.12), (II.13) and (II.14) are substituted:

$$\begin{aligned}
\dot{\Phi} &= \dot{W}_\varepsilon - \rho\dot{\psi} \geq 0 \\
&= \boldsymbol{\sigma} : \dot{\boldsymbol{\varepsilon}} - \rho\left(\frac{\partial\psi}{\partial\boldsymbol{\varepsilon}} : \dot{\boldsymbol{\varepsilon}} + \sum_{i=1}^{N}\frac{\partial\psi}{\partial\boldsymbol{\varepsilon}_{\boldsymbol{v}_i}} : \dot{\boldsymbol{\varepsilon}}_{\boldsymbol{v}_i} + \frac{\partial\psi}{\partial\boldsymbol{\varepsilon}_{\boldsymbol{p}}} : \dot{\boldsymbol{\varepsilon}}_{\boldsymbol{p}} + \frac{\partial\psi}{\partial r}\dot{r} + \frac{\partial\psi}{\partial D}\dot{D}\right) \geq 0 \\
&= \sum_{i=1}^{N}\boldsymbol{\sigma}_{\boldsymbol{v}_i} : \dot{\boldsymbol{\varepsilon}}_{\boldsymbol{v}_i} + \boldsymbol{\sigma} : \dot{\boldsymbol{\varepsilon}}_{\boldsymbol{p}} - R\dot{r} + Y\dot{D} \geq 0.
\end{aligned} \tag{II.22}$$

In order to satisfy the above inequality, the evolution laws expressing the rate of the internal state variables must be derived from a convex dual dissipation potential or a convex indicative function of the associated variables, in which the state variables themselves may act as parameters (see Section 1.5 in Appendix B).

2.2.1 Evolution laws for viscoelasticity

The evolution of each viscoelastic strain $\boldsymbol{\varepsilon}_{\boldsymbol{v}_i}$ is governed by a dual dissipation potential written as the sum of the sub-potentials of the linear dash-pot of each Kelvin-Voigt branch:

$$\varphi^*(\boldsymbol{\sigma}_{\boldsymbol{v}_i}; D) = \sum_{i=1}^{N} \varphi^*_{v_i}(\boldsymbol{\sigma}_{\boldsymbol{v}_i}; D), \tag{II.23}$$

where

$$\varphi^*_{v_i}(\boldsymbol{\sigma}_{\boldsymbol{v}_i}; D) = \frac{1}{2}\boldsymbol{\sigma}_{\boldsymbol{v}_i} : \frac{\mathbb{V}^{-1}_{\boldsymbol{v}_i}}{1-D} : \boldsymbol{\sigma}_{\boldsymbol{v}_i}. \tag{II.24}$$

Then, the evolution of each viscoelastic strain $\boldsymbol{\varepsilon}_{\boldsymbol{v}_i}$ is obtained from the derivation of the pseudo-potential φ^* with respect to its associated variable $\boldsymbol{\sigma}_{\boldsymbol{v}_i}$:

$$\dot{\boldsymbol{\varepsilon}}_{\boldsymbol{v}_i} = \frac{\partial \varphi^*}{\partial \boldsymbol{\sigma}_{\boldsymbol{v}_i}} = \frac{\partial \varphi^*_{v_i}}{\partial \boldsymbol{\sigma}_{\boldsymbol{v}_i}} = \frac{\mathbb{V}^{-1}_{\boldsymbol{v}_i}}{1-D} : \boldsymbol{\sigma}_{\boldsymbol{v}_i}. \tag{II.25}$$

The introduction of (II.11) into (II.25) finally allows to express the effective stress as a function of $\boldsymbol{\varepsilon}_{\boldsymbol{v}_i}$ and its rate:

$$\frac{\boldsymbol{\sigma}}{1-D} = \mathbb{C}_{\boldsymbol{v}_i} : \boldsymbol{\varepsilon}_{\boldsymbol{v}_i} + \mathbb{V}_{\boldsymbol{v}_i} : \dot{\boldsymbol{\varepsilon}}_{\boldsymbol{v}_i}, \tag{II.26}$$

where $\mathbb{V}_{\boldsymbol{v}_i}$ denotes the viscosity tensor of the linear dash-pot of the i^{th} Kelvin-Voigt branch. As for the stiffness tensors, each viscosity tensor is classically formulated for bulk isotropic materials and is defined by a viscosity η_{v_i} and the Poisson ratio ν. The latter is assumed to be the same in each stiffness and viscosity tensor. It is noted that the viscosity is introduced only in the dissipation potential and not in the Helmholtz free energy. This is always the case when viscoelasticity is described in differential form. In integral formulations, the viscocity is integrated directly in the Helmholtz free energy [89].

Within such a differential relationship (II.26), a characteristic time can be clearly identified for each Kelvin-Voigt branch by observing its creep response. Indeed, if a sudden constant effective stress $\widetilde{\boldsymbol{\sigma}}_{\mathbf{0}}$ is applied on a single Kelvin-Voigt branch at a time t_0 (Figure II.2a), then it can be shown [149] that the strain response is approaching exponentially in time the strain of the pure elastic material $\boldsymbol{\varepsilon}^{\infty}_{\boldsymbol{v}_i}$ (Figure II.2b):

$$\boldsymbol{\varepsilon}_{\boldsymbol{v}_i}(t) = \boldsymbol{\varepsilon}^{\infty}_{\boldsymbol{v}_i}\left(1 - \exp\left(-\frac{t-t_0}{\tau_{v_i}}\right)\right) \qquad \text{where} \qquad \boldsymbol{\varepsilon}^{\infty}_{\boldsymbol{v}_i} = \mathbb{C}^{-1}_{\boldsymbol{v}_i} : \widetilde{\boldsymbol{\sigma}}_{\mathbf{0}}. \tag{II.27}$$

In the above equation, τ_{v_i} is the characteristic time given by:

$$\tau_{v_i}\mathbb{I} = \mathbb{C}^{-1}_{\boldsymbol{v}_i} : \mathbb{V}_{\boldsymbol{v}_i} \qquad \text{or} \qquad \tau_{v_i} = \frac{\eta_{v_i}}{E_{v_i}}. \tag{II.28}$$

From a mathematical point of view, τ_{v_i} corresponds to the time needed to reach 63% of the pure elastic strain $\boldsymbol{\varepsilon}^{\infty}_{\boldsymbol{v}_i}$ (Figure II.2b), as $1 - \exp(-1) = 0.63$. Basically, the characteristic time provides an information about which range of time a Kelvin-Voigt branch is expected to move.

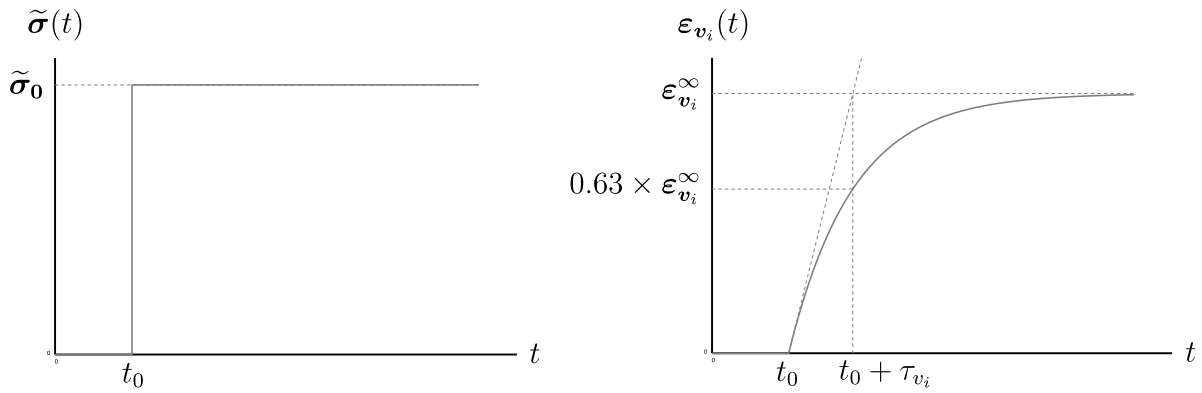

(a) Application of a sudden constant effective stress

(b) Strain response

Figure II.2: Illustration of the creep response of a single Kelvin-Voigt branch.

Considering any type of loading conditions as being a continuous succession of creep stage, the Boltzmann superposition principle [149] allows to express the evolution of each viscoelastic strain $\boldsymbol{\varepsilon}_{\boldsymbol{v}_i}$ from an integral representation that involves the whole history of the effective stress:

$$\boldsymbol{\varepsilon}_{\boldsymbol{v}_i}(t) = \int_{-\infty}^{t} \mathbb{C}_{\boldsymbol{v}_i}^{-1} \left(1 - \exp\left(-\frac{t-\xi}{\tau_{v_i}} \right) \right) : \frac{d\widetilde{\boldsymbol{\sigma}}(\xi)}{d\xi} \; d\xi. \tag{II.29}$$

Thus, the relations governing each viscoelastic strain can be expressed either under the differential formalism (II.26) or under the integral one (II.29). Both representations have advantages and drawbacks as previously discussed in the introductory section (Section 1). The integral formulation in (II.29) along with the relationships (II.27) and (II.28) are only valid if the stiffness and viscosity tensors $\mathbb{C}_{\boldsymbol{v}_i}$ and $\mathbb{V}_{\boldsymbol{v}_i}$, respectively, are defined as isotropic with the same Poisson ratio. However, it is worth noticing that the differential form (II.26) provides more freedom regarding the expressions of $\mathbb{C}_{\boldsymbol{v}_i}$ and $\mathbb{V}_{\boldsymbol{v}_i}$. With this formalism, anisotropy can be integrated in a straightforward manner. In this work, it is recalled that the differential representation (II.26) has been adopted.

2.2.2 Evolution laws for coupled viscoplasticity and damage

As previously mentioned, viscoplasticity and damage are considered to be coupled phenomena [108, 110, 89]. Such a connection requires a non-associative mechanism. Consequently, the evolution of r, $\boldsymbol{\varepsilon}_p$ and D cannot be obtained from a dual dissipation potential. However, the evolution laws are expressed by the normality of a an indicative function given by:

$$F(\boldsymbol{\sigma}, R, Y; D) = f(\boldsymbol{\sigma}, R; D) + f_D(Y; D). \tag{II.30}$$

In the above equation, $f(\boldsymbol{\sigma}, R; D)$ is the yield criterion function that is expressed in the effective stress space in order to account for the coupling between damage and viscoplasticity:

$$f(\boldsymbol{\sigma}, R; D) = \frac{\mathrm{eq}(\boldsymbol{\sigma})}{1-D} - R - R_0, \tag{II.31}$$

where R_0 is the yield threshold. In (II.30), The damage contribution $f_D(Y; D)$ is given by:

$$f_D(Y; D) = \frac{S}{(\beta+1)(1-D)} \left(\frac{Y}{S} \right)^{\beta+1}, \tag{II.32}$$

where S and β are material parameters. Then, as previously mentioned, the evolution of r, $\boldsymbol{\varepsilon_p}$ and D are given by the normality of the indicative function $F(\boldsymbol{\sigma}, R, Y; D)$, introducing a viscoplastic-damage multiplier λ ($\dot{\lambda} \geq 0$):

$$\dot{r} = -\frac{\partial F}{\partial R}\dot{\lambda} = -\frac{\partial f}{\partial R}\dot{\lambda} = \dot{\lambda}, \tag{II.33}$$

$$\dot{\boldsymbol{\varepsilon}}_{\boldsymbol{p}} = \frac{\partial F}{\partial \boldsymbol{\sigma}}\dot{\lambda} = \frac{\partial f}{\partial \boldsymbol{\sigma}}\dot{\lambda} = \frac{3}{2}\frac{\mathbf{Dev}(\boldsymbol{\sigma})}{\mathrm{eq}(\boldsymbol{\sigma})}\frac{\dot{\lambda}}{1-D}, \tag{II.34}$$

$$\dot{D} = \frac{\partial F}{\partial Y}\dot{\lambda} = \frac{\partial f_D}{\partial Y}\dot{\lambda} = \left(\frac{Y}{S}\right)^{\beta}\frac{\dot{\lambda}}{1-D}. \tag{II.35}$$

The introduction of (II.33) into (II.34) and (II.35) allows to express the evolution of $\boldsymbol{\varepsilon_p}$ and D under the form of flow equations:

$$\dot{\boldsymbol{\varepsilon}}_{\boldsymbol{p}} = \frac{\boldsymbol{\Lambda}(\boldsymbol{\sigma})}{1-D}\dot{r}, \qquad \dot{D} = \frac{\Omega(Y)}{1-D}\dot{r}, \tag{II.36}$$

where $\boldsymbol{\Lambda}(\boldsymbol{\sigma})$ and $\Omega(Y)$ are given by:

$$\boldsymbol{\Lambda}(\boldsymbol{\sigma}) = \frac{3}{2}\frac{\mathbf{Dev}(\boldsymbol{\sigma})}{\mathrm{eq}(\boldsymbol{\sigma})}, \qquad \Omega(Y) = \left(\frac{Y}{S}\right)^{\beta}. \tag{II.37}$$

Note that, for semi-crystalline polymers the damage growth appears to be relatively fast at the beginning of a loading stage and gradually decreases as the loading continues [47]. In order to account for this experimentally observed tendency, the parameter β in (II.32) and (II.37) must be negative. When β is positive the inverse trend is obtained (slow initiation and faster subsequent growth), which is frequently observed in metals [89].

The evolution of the multiplier $\dot{\lambda} = \dot{r}$ is activated ($\dot{r} > 0$) only if the criterion function f becomes positive. In order to account for the visoplasticity, a rate dependency is introduced by considering that the positive part of f is equal to the effective equivalent stress acting on the non-linear dash-pot of the viscoplastic branch (Figure II.1c). This stress is connected to the rate of r through the function $Q(\dot{r})$. This finally gives a relationship between the effective equivalent stress, the variable r and its rate:

$$\Big\langle \underbrace{\frac{\mathrm{eq}(\boldsymbol{\sigma})}{1-D} - R(r) - R_0}_{f} \Big\rangle_+ = Q(\dot{r}). \tag{II.38}$$

The function $Q(\dot{r})$ must be increasing, positive and null at $\dot{r} = 0$. In this model, this function is chosen under the form of a power law:

$$Q(\dot{r}) = H\dot{r}^m, \tag{II.39}$$

where H and m are material parameters. It is worth noticing that r can only increase ($\dot{r} > 0$ if $f > 0$) or remain constant ($\dot{r} = 0$ if $f < 0$). Consequently, the part of the stored energy related to the viscoplastic branch ψ_p written in (II.9), appears to be irrecoverable, as it cannot return back to zero.

2.3 Summary of the constitutive equations

In summary, the proposed model can be described by the set of constitutive equations given above in Table II.2.

Observable state variable	Associated variable (state law)	
$\boldsymbol{\varepsilon}$	$\boldsymbol{\sigma} = \rho\dfrac{\partial\psi}{\partial\boldsymbol{\varepsilon}} = (1-D)\mathbb{C}_{\boldsymbol{e}} : \left(\boldsymbol{\varepsilon} - \sum_{i=1}^{N}\boldsymbol{\varepsilon}_{\boldsymbol{v}_i} - \boldsymbol{\varepsilon}_{\boldsymbol{p}}\right)$	
Internal state variables	Associated variables (state laws)	Evolution laws
$\boldsymbol{\varepsilon}_{\boldsymbol{v}_i}$	$-\boldsymbol{\sigma}_{\boldsymbol{v}_i} = \rho\dfrac{\partial\psi}{\partial\boldsymbol{\varepsilon}_{\boldsymbol{v}_i}} = (1-D)\mathbb{C}_{\boldsymbol{v}_i} : \boldsymbol{\varepsilon}_{\boldsymbol{v}_i} - \boldsymbol{\sigma}$	$\dot{\boldsymbol{\varepsilon}}_{\boldsymbol{v}_i} = \dfrac{\partial\varphi^*}{\partial\boldsymbol{\sigma}_{\boldsymbol{v}_i}} = \dfrac{\mathbb{V}_{\boldsymbol{v}_i}^{-1}}{1-D} : \boldsymbol{\sigma}_{\boldsymbol{v}_i}$
$\boldsymbol{\varepsilon}_{\boldsymbol{p}}$	$-\boldsymbol{\sigma} = \rho\dfrac{\partial\psi}{\partial\boldsymbol{\varepsilon}_{\boldsymbol{p}}}$	$\dot{\boldsymbol{\varepsilon}}_{\boldsymbol{p}} = \dfrac{\partial F}{\partial\boldsymbol{\sigma}}\dot{\lambda} = \dfrac{\boldsymbol{\Lambda}(\boldsymbol{\sigma})}{1-D}\dot{r}$
r	$R = \rho\dfrac{\partial\psi}{\partial r} = R(r)$	$\dot{r} = -\dfrac{\partial F}{\partial R}\dot{\lambda} = \dot{\lambda}$
D	$-Y = \rho\dfrac{\partial\psi}{\partial D}$	$\dot{D} = \dfrac{\partial F}{\partial Y}\dot{\lambda} = \dfrac{\Omega(Y)}{1-D}\dot{r}$
Multiplier	Criterion	Active ($\dot{\lambda} > 0$) if $f > 0$
$\lambda = r$	$f = \dfrac{\mathrm{eq}(\boldsymbol{\sigma})}{1-D} - R(r) - R_0$	$\langle f \rangle_+ = Q(\dot{r})$

Table II.2: Summary of the constitutive equations.

3 Numerical implementation: Backward Euler time implicit algorithm

The proposed constitutive model is implemented into the FE solver *ABAQUS/Standard* through a User MATerial subroutine (UMAT). The latter is based on the "convex cutting plane" form of the "return mapping algorithm" [179, 145, 178], which is described in this section for this model.

Let's recall that a FE solver, like *ABAQUS/Standard*, employs a backward Euler (or time-implicit) integration scheme. Accordingly, the value of a given quantity x is computed from the previous time increment n to the current one $n+1$ such that $x^{(n+1)} = x^{(n)} + \Delta x^{(n+1)}$. Such a relationship is usually solved through an iterative scheme. Thus, the current value of the quantity x is corrected for each iteration k by: $x^{(n+1)(k+1)} = x^{(n+1)(k)} + \delta x^{(n+1)(k)}$ or $\Delta x^{(n+1)(k+1)} = \Delta x^{(n+1)(k)} + \delta x^{(n+1)(k)}$ until $x^{(n+1)}$ converges.

The implementation of a constitutive model in such a FE solver is usually ensured by a User MATarial subroutine (UMAT). When the analysis is completed at the time increment n, the FE solver provides, for each integration point, all the state variables at the time increment n along with the increment of total strain $\Delta\boldsymbol{\varepsilon}^{(n+1)}$. From these data, the role of the UMAT subroutine is to compute: i) the stress and the state variables at the time increment $n+1$, and ii) the tangent operator $\mathbb{C}_{\boldsymbol{t}}$ that is necessary to achieve a fast convergence for the next FE calculation.

3.1 Residuals

When considering the backward Euler time-implicit method, it is convenient to write the equations governing the evolutions of the state variables under the form of residual functions that must satisfy a nullity condition. In the case of the proposed model, the evolution law of each viscoelastic strain $\boldsymbol{\varepsilon}_{\boldsymbol{v}_i}$ (II.26) is written under the form of a tensorial function $\boldsymbol{\phi}_{\boldsymbol{v}_i}$ that must always remain null as the viscoelasticity is always active:

$$\boldsymbol{\phi}_{\boldsymbol{v}_i}(\boldsymbol{\sigma}, \boldsymbol{\varepsilon}_{\boldsymbol{v}_i}, \dot{\boldsymbol{\varepsilon}}_{\boldsymbol{v}_i}, D) = \dot{\boldsymbol{\varepsilon}}_{\boldsymbol{v}_i} - \mathbb{V}_{\boldsymbol{v}_i}^{-1} : \left(\frac{\boldsymbol{\sigma}}{1-D} - \mathbb{C}_{\boldsymbol{v}_i} : \boldsymbol{\varepsilon}_{\boldsymbol{v}_i} \right) = \mathbf{0}. \tag{II.40}$$

In the same principle, the evolution law governing viscoplasticity and damage through the variable r (II.38) is written under the form of a scalar function ϕ_r that must remain null as long as f is positive:

$$\phi_r(\boldsymbol{\sigma}, r, \dot{r}, D) = \dot{r} - Q^{-1}\Bigg(\underbrace{\frac{\mathrm{eq}(\boldsymbol{\sigma})}{1-D} - R(r) - R_0}_{f>0} \Bigg) = 0. \tag{II.41}$$

$Q^{-1}(f)$ is the inverse function of $Q(\dot{r})$ that is defined in (II.39). Moreover, the proposed implementation is based on the "convex cutting plane" form of the "return mapping algorithm" [179, 145, 178], which does not require to integrate the flow equations (II.36) as residual functions.

The implicit implementation of the proposed model requires to linearise the above residuals, as well as the stress. The details of these calculations are provided in Appendix D.

3.2 Computation of the stress

3.2.1 Stress prediction

In order to initiate the computation of the stress, the internal state variables are assumed not to evolve at first ($\Delta\boldsymbol{\varepsilon_{v_i}}^{(n+1)(k=0)} = \mathbf{0}$, $\Delta r^{(n+1)(k=0)} = 0$, $\Delta\boldsymbol{\varepsilon_p}^{(n+1)(k=0)} = \mathbf{0}$ and $\Delta D^{(n+1)(k=0)} = 0$), while the total strain at the end of the increment is given by $\boldsymbol{\varepsilon}^{(n+1)} = \boldsymbol{\varepsilon}^{(n)} + \Delta\boldsymbol{\varepsilon}^{(n+1)}$. Therefore, the stress is predicted along with the residuals $\boldsymbol{\phi_{v_i}}$. At the end of this step, the nullity of the residuals $\boldsymbol{\phi_{v_i}}$ cannot be respected, then the stress must be corrected in order to satisfy this condition. It is the role of the next step so-called the "viscoelastic stress correction/prediction".

3.2.2 Viscoelastic stress correction/prediction

During the "viscoelastic stress correction/prediction", only the viscoelastic strains $\boldsymbol{\varepsilon_{v_i}}$ evolve, while the other internal state variables are still assumed to be unchanged, as it is not known yet whether the viscoplasticity and damage are active or not. Consequently: $\delta r^{(n+1)(k)} = 0$, $\delta\boldsymbol{\varepsilon_p}^{(n+1)(k)} = \mathbf{0}$ and $\delta D^{(n+1)(k)} = 0$. The "visoelastic stress correction/prediction" consists in returning the residuals $\boldsymbol{\phi_{v_i}}$ back to zero by developing only the viscoelastic strains $\boldsymbol{\varepsilon_{v_i}}$, while the total strain does not evolve: $\delta\boldsymbol{\varepsilon}^{(n+1)(k)} = \mathbf{0}$. Accordingly, the viscoelastic strains $\boldsymbol{\varepsilon_{v_i}}$ are updated at each iteration k by:

$$\boldsymbol{\varepsilon}_{\boldsymbol{v}_i}^{(n+1)(k+1)} = \boldsymbol{\varepsilon}_{\boldsymbol{v}_i}^{(n+1)(k)} + \delta\boldsymbol{\varepsilon}_{\boldsymbol{v}_i}^{(n+1)(k)}, \tag{II.42}$$

where all the $\delta\boldsymbol{\varepsilon}_{\boldsymbol{v}_i}^{(n+1)(k)}$ are obtained from the nullity condition of all the residuals $\boldsymbol{\phi_{v_i}}$:

$$\boldsymbol{\phi}_{\boldsymbol{v}_i}^{(n+1)(k)} + \delta\boldsymbol{\phi}_{\boldsymbol{v}_i}^{(n+1)(k)} = \mathbf{0}. \tag{II.43}$$

In the above equation, all the $\delta\boldsymbol{\phi}_{\boldsymbol{v}_i}^{(n+1)(k)}$ are expressed by linearisation. After proper calculation (D.2), this gives (all the quantities are taken at the increment $^{(n+1)(k)}$):

$$\delta\boldsymbol{\phi_{v_i}} = \mathbb{A}_{\boldsymbol{v_i\sigma}} : \delta\boldsymbol{\sigma} + \mathbb{A}_{\boldsymbol{v_iv_i}} : \delta\boldsymbol{\varepsilon_{v_i}}. \tag{II.44}$$

In the same manner (D.4), $\delta\boldsymbol{\sigma}$ is written as:

$$\delta\boldsymbol{\sigma} = \sum_{j=1}^{N} \mathbb{B}_{\boldsymbol{\sigma v}_j} : \delta\boldsymbol{\varepsilon}_{\boldsymbol{v}_j}. \tag{II.45}$$

By introducing (II.45) into (II.44), while considering (II.43), the unknown values of $\delta\boldsymbol{\varepsilon_{v_i}}$ are computed from the known residuals $\boldsymbol{\phi_{v_i}}$ through the construction of the following "viscoelastic corrector system":

$$\begin{Bmatrix} \delta\boldsymbol{\varepsilon}_{\boldsymbol{v}_1} \\ \delta\boldsymbol{\varepsilon}_{\boldsymbol{v}_2} \\ \delta\boldsymbol{\varepsilon}_{\boldsymbol{v}_3} \\ \vdots \\ \delta\boldsymbol{\varepsilon}_{\boldsymbol{v}_N} \end{Bmatrix} = \begin{pmatrix} \mathbb{L}^*_{\boldsymbol{v}_1\boldsymbol{v}_1} & \mathbb{L}^*_{\boldsymbol{v}_1\boldsymbol{v}_2} & \mathbb{L}^*_{\boldsymbol{v}_1\boldsymbol{v}_3} & \dots & \mathbb{L}^*_{\boldsymbol{v}_1\boldsymbol{v}_N} \\ \mathbb{L}^*_{\boldsymbol{v}_2\boldsymbol{v}_1} & \mathbb{L}^*_{\boldsymbol{v}_2\boldsymbol{v}_2} & \mathbb{L}^*_{\boldsymbol{v}_2\boldsymbol{v}_3} & \dots & \mathbb{L}^*_{\boldsymbol{v}_2\boldsymbol{v}_N} \\ \mathbb{L}^*_{\boldsymbol{v}_3\boldsymbol{v}_1} & \mathbb{L}^*_{\boldsymbol{v}_3\boldsymbol{v}_2} & \mathbb{L}^*_{\boldsymbol{v}_3\boldsymbol{v}_3} & \dots & \mathbb{L}^*_{\boldsymbol{v}_3\boldsymbol{v}_N} \\ \vdots & \vdots & \vdots & \ddots & \vdots \\ \mathbb{L}^*_{\boldsymbol{v}_N\boldsymbol{v}_1} & \mathbb{L}^*_{\boldsymbol{v}_N\boldsymbol{v}_2} & \mathbb{L}^*_{\boldsymbol{v}_N\boldsymbol{v}_3} & \dots & \mathbb{L}^*_{\boldsymbol{v}_N\boldsymbol{v}_N} \end{pmatrix} \times \begin{Bmatrix} -\boldsymbol{\phi}_{\boldsymbol{v}_1} \\ -\boldsymbol{\phi}_{\boldsymbol{v}_2} \\ -\boldsymbol{\phi}_{\boldsymbol{v}_3} \\ \vdots \\ -\boldsymbol{\phi}_{\boldsymbol{v}_N} \end{Bmatrix}, \tag{II.46}$$

with

$$\begin{pmatrix} \mathbb{L}^*_{\boldsymbol{v}_1\boldsymbol{v}_1} & \mathbb{L}^*_{\boldsymbol{v}_1\boldsymbol{v}_2} & \mathbb{L}^*_{\boldsymbol{v}_1\boldsymbol{v}_3} & \cdots & \mathbb{L}^*_{\boldsymbol{v}_1\boldsymbol{v}_N} \\ \mathbb{L}^*_{\boldsymbol{v}_2\boldsymbol{v}_1} & \mathbb{L}^*_{\boldsymbol{v}_2\boldsymbol{v}_2} & \mathbb{L}^*_{\boldsymbol{v}_2\boldsymbol{v}_3} & \cdots & \mathbb{L}^*_{\boldsymbol{v}_2\boldsymbol{v}_N} \\ \mathbb{L}^*_{\boldsymbol{v}_3\boldsymbol{v}_1} & \mathbb{L}^*_{\boldsymbol{v}_3\boldsymbol{v}_2} & \mathbb{L}^*_{\boldsymbol{v}_3\boldsymbol{v}_3} & \cdots & \mathbb{L}^*_{\boldsymbol{v}_3\boldsymbol{v}_N} \\ \vdots & \vdots & \vdots & \ddots & \vdots \\ \mathbb{L}^*_{\boldsymbol{v}_N\boldsymbol{v}_1} & \mathbb{L}^*_{\boldsymbol{v}_N\boldsymbol{v}_2} & \mathbb{L}^*_{\boldsymbol{v}_N\boldsymbol{v}_3} & \cdots & \mathbb{L}^*_{\boldsymbol{v}_N\boldsymbol{v}_N} \end{pmatrix} = \begin{pmatrix} \mathbb{K}_{\boldsymbol{v}_1\boldsymbol{v}_1} & \mathbb{K}_{\boldsymbol{v}_1\boldsymbol{v}_2} & \mathbb{K}_{\boldsymbol{v}_1\boldsymbol{v}_3} & \cdots & \mathbb{K}_{\boldsymbol{v}_1\boldsymbol{v}_N} \\ \mathbb{K}_{\boldsymbol{v}_2\boldsymbol{v}_1} & \mathbb{K}_{\boldsymbol{v}_2\boldsymbol{v}_2} & \mathbb{K}_{\boldsymbol{v}_2\boldsymbol{v}_3} & \cdots & \mathbb{K}_{\boldsymbol{v}_2\boldsymbol{v}_N} \\ \mathbb{K}_{\boldsymbol{v}_3\boldsymbol{v}_1} & \mathbb{K}_{\boldsymbol{v}_3\boldsymbol{v}_2} & \mathbb{K}_{\boldsymbol{v}_3\boldsymbol{v}_3} & \cdots & \mathbb{K}_{\boldsymbol{v}_3\boldsymbol{v}_N} \\ \vdots & \vdots & \vdots & \ddots & \vdots \\ \mathbb{K}_{\boldsymbol{v}_N\boldsymbol{v}_1} & \mathbb{K}_{\boldsymbol{v}_N\boldsymbol{v}_2} & \mathbb{K}_{\boldsymbol{v}_N\boldsymbol{v}_3} & \cdots & \mathbb{K}_{\boldsymbol{v}_N\boldsymbol{v}_N} \end{pmatrix}^{-1}, \tag{II.47}$$

where

$$\mathbb{K}_{\boldsymbol{v}_i\boldsymbol{v}_j} = \begin{cases} \mathbb{A}_{\boldsymbol{v}_i\boldsymbol{\sigma}} : \mathbb{B}_{\boldsymbol{\sigma}\boldsymbol{v}_j} + \mathbb{A}_{\boldsymbol{v}_i\boldsymbol{v}_i} & \text{if } i = j \\ \mathbb{A}_{\boldsymbol{v}_i\boldsymbol{\sigma}} : \mathbb{B}_{\boldsymbol{\sigma}\boldsymbol{v}_j} & \text{if } i \neq j \end{cases}. \tag{II.48}$$

Once the viscoelastic strains are updated, the stress and the residuals $\boldsymbol{\phi}_{\boldsymbol{v}_i}$ are reassessed through the relationships (II.10) and (II.40), respectively. This correction procedure is iteratively repeated (k loop) until the convergence is reached [2], namely when $|\boldsymbol{\phi}_{\boldsymbol{v}_i}^{(n+1)(k+1)}| \leq \mathbf{0} + \boldsymbol{\delta}$.

At the end of this step, the criterion function f is checked in order to identify whether the viscoplasticity and the damage are active or not:

- If $f^{(n+1)(k+1)} \leq 0$, then the viscoplasticity and the damage are not active and the stress does not need to be corrected any more.

- If $f^{(n+1)(k+1)} > 0$, then the viscoplasticity and the damage are active. In the present state, the nullity of ϕ_r cannot be respected, then the stress must be corrected once more, in order to satisfy the nullity condition of all the residuals $\boldsymbol{\phi}_{\boldsymbol{v}_i}$ and ϕ_r at the same time. It is the role of the final step, so-called the "full stress correction".

3.2.3 Full stress correction

The "full stress correction" consists in returning all the residuals $\boldsymbol{\phi}_{\boldsymbol{v}_i}$ and ϕ_r back to zero by developing all the internal state variables, while the total strain does not evolve: $\delta\boldsymbol{\varepsilon}^{(n+1)(k)} = \mathbf{0}$. Accordingly, all the internal state variables are updated at each iteration k by:

$$\boldsymbol{\varepsilon}_{\boldsymbol{v}_i}^{(n+1)(k+1)} = \boldsymbol{\varepsilon}_{\boldsymbol{v}_i}^{(n+1)(k)} + \delta\boldsymbol{\varepsilon}_{\boldsymbol{v}_i}^{(n+1)(k)}, \tag{II.49}$$

$$\boldsymbol{\varepsilon}_{\boldsymbol{p}}^{(n+1)(k+1)} = \boldsymbol{\varepsilon}_{\boldsymbol{p}}^{(n+1)(k)} + \delta\boldsymbol{\varepsilon}_{\boldsymbol{p}}^{(n+1)(k)}, \tag{II.50}$$

$$r^{(n+1)(k+1)} = r^{(n+1)(k)} + \delta r^{(n+1)(k)}, \tag{II.51}$$

and

$$D^{(n+1)(k+1)} = D^{(n+1)(k)} + \delta D^{(n+1)(k)}, \tag{II.52}$$

where all the $\delta\boldsymbol{\varepsilon}_{\boldsymbol{v}_i}^{(n+1)(k)}$ and $\delta r^{(n+1)(k)}$ are obtained from the nullity condition of all the residuals $\boldsymbol{\phi}_{\boldsymbol{v}_i}$ and ϕ_r:

$$\begin{cases} \boldsymbol{\phi}_{\boldsymbol{v}_i}^{(n+1)(k)} + \delta\boldsymbol{\phi}_{\boldsymbol{v}_i}^{(n+1)(k)} = \mathbf{0} \\ \\ \phi_r^{(n+1)(k)} + \delta\phi_r^{(n+1)(k)} = 0 \end{cases}. \tag{II.53}$$

2. Normally, as the differential equations governing the viscoelasticity are linear, it can be shown that only one correction is sufficient to reach the convergence. However, this scheme can also be applied to non-linear viscoelasticity where several corrections would be likely required.

In the above equation, all the $\delta\boldsymbol{\phi}_{\boldsymbol{v}_i}^{(n+1)(k)}$ and $\delta\phi_r^{(n+1)(k)}$ are expressed by linearisation. After proper calculation (D.2 and D.3), this gives (all the quantities are taken at the increment $^{(n+1)(k)}$):

$$\begin{cases} \delta\boldsymbol{\phi}_{\boldsymbol{v}_i} = \mathbb{A}_{\boldsymbol{v}_i\boldsymbol{\sigma}} : \delta\boldsymbol{\sigma} + \mathbb{A}_{\boldsymbol{v}_i\boldsymbol{v}_i} : \delta\boldsymbol{\varepsilon}_{\boldsymbol{v}_i} + \boldsymbol{A}_{\boldsymbol{v}_i\boldsymbol{r}}\delta r \\ \\ \delta\phi_r = \boldsymbol{A}_{\boldsymbol{r}\boldsymbol{\sigma}} : \delta\boldsymbol{\sigma} + A_{rr}\delta r \end{cases}. \tag{II.54}$$

In the same manner (D.4), $\delta\boldsymbol{\sigma}$ is written as:

$$\delta\boldsymbol{\sigma} = \sum_{j=1}^{N} \mathbb{B}_{\boldsymbol{\sigma}\boldsymbol{v}_j} : \delta\boldsymbol{\varepsilon}_{\boldsymbol{v}_j} + \boldsymbol{B}_{\boldsymbol{\sigma}\boldsymbol{r}}\delta r. \tag{II.55}$$

By introducing (II.55) into (II.54) while considering (II.53), the unknown values of $\delta\boldsymbol{\varepsilon}_{\boldsymbol{v}_i}$ and δr are computed from the known residuals $\boldsymbol{\phi}_{\boldsymbol{v}_i}$ and ϕ_r through the construction of the following "full corrector system":

$$\begin{Bmatrix} \delta\boldsymbol{\varepsilon}_{\boldsymbol{v}_1} \\ \delta\boldsymbol{\varepsilon}_{\boldsymbol{v}_2} \\ \delta\boldsymbol{\varepsilon}_{\boldsymbol{v}_3} \\ \vdots \\ \delta\boldsymbol{\varepsilon}_{\boldsymbol{v}_N} \\ \delta r \end{Bmatrix} = \begin{pmatrix} \mathbb{L}_{\boldsymbol{v}_1\boldsymbol{v}_1} & \mathbb{L}_{\boldsymbol{v}_1\boldsymbol{v}_2} & \mathbb{L}_{\boldsymbol{v}_1\boldsymbol{v}_3} & \dots & \mathbb{L}_{\boldsymbol{v}_1\boldsymbol{v}_N} & \boldsymbol{L}_{\boldsymbol{v}_1\boldsymbol{r}} \\ \mathbb{L}_{\boldsymbol{v}_2\boldsymbol{v}_1} & \mathbb{L}_{\boldsymbol{v}_2\boldsymbol{v}_2} & \mathbb{L}_{\boldsymbol{v}_2\boldsymbol{v}_3} & \dots & \mathbb{L}_{\boldsymbol{v}_2\boldsymbol{v}_N} & \boldsymbol{L}_{\boldsymbol{v}_2\boldsymbol{r}} \\ \mathbb{L}_{\boldsymbol{v}_3\boldsymbol{v}_1} & \mathbb{L}_{\boldsymbol{v}_3\boldsymbol{v}_2} & \mathbb{L}_{\boldsymbol{v}_3\boldsymbol{v}_3} & \dots & \mathbb{L}_{\boldsymbol{v}_3\boldsymbol{v}_N} & \boldsymbol{L}_{\boldsymbol{v}_3\boldsymbol{r}} \\ \vdots & \vdots & \vdots & \ddots & \vdots & \vdots \\ \mathbb{L}_{\boldsymbol{v}_N\boldsymbol{v}_1} & \mathbb{L}_{\boldsymbol{v}_N\boldsymbol{v}_2} & \mathbb{L}_{\boldsymbol{v}_N\boldsymbol{v}_3} & \dots & \mathbb{L}_{\boldsymbol{v}_N\boldsymbol{v}_N} & \boldsymbol{L}_{\boldsymbol{v}_N\boldsymbol{r}} \\ \boldsymbol{L}_{\boldsymbol{r}\boldsymbol{v}_1} & \boldsymbol{L}_{\boldsymbol{r}\boldsymbol{v}_2} & \boldsymbol{L}_{\boldsymbol{r}\boldsymbol{v}_3} & \dots & \boldsymbol{L}_{\boldsymbol{r}\boldsymbol{v}_N} & L_{rr} \end{pmatrix} \times \begin{Bmatrix} -\boldsymbol{\phi}_{\boldsymbol{v}_1} \\ -\boldsymbol{\phi}_{\boldsymbol{v}_2} \\ -\boldsymbol{\phi}_{\boldsymbol{v}_3} \\ \vdots \\ -\boldsymbol{\phi}_{\boldsymbol{v}_N} \\ -\phi_r \end{Bmatrix}, \tag{II.56}$$

with

$$\begin{pmatrix} \mathbb{L}_{\boldsymbol{v}_1\boldsymbol{v}_1} & \mathbb{L}_{\boldsymbol{v}_1\boldsymbol{v}_2} & \mathbb{L}_{\boldsymbol{v}_1\boldsymbol{v}_3} & \dots & \mathbb{L}_{\boldsymbol{v}_1\boldsymbol{v}_N} & \boldsymbol{L}_{\boldsymbol{v}_1\boldsymbol{r}} \\ \mathbb{L}_{\boldsymbol{v}_2\boldsymbol{v}_1} & \mathbb{L}_{\boldsymbol{v}_2\boldsymbol{v}_2} & \mathbb{L}_{\boldsymbol{v}_2\boldsymbol{v}_3} & \dots & \mathbb{L}_{\boldsymbol{v}_2\boldsymbol{v}_N} & \boldsymbol{L}_{\boldsymbol{v}_2\boldsymbol{r}} \\ \mathbb{L}_{\boldsymbol{v}_3\boldsymbol{v}_1} & \mathbb{L}_{\boldsymbol{v}_3\boldsymbol{v}_2} & \mathbb{L}_{\boldsymbol{v}_3\boldsymbol{v}_3} & \dots & \mathbb{L}_{\boldsymbol{v}_3\boldsymbol{v}_N} & \boldsymbol{L}_{\boldsymbol{v}_3\boldsymbol{r}} \\ \vdots & \vdots & \vdots & \ddots & \vdots & \vdots \\ \mathbb{L}_{\boldsymbol{v}_N\boldsymbol{v}_1} & \mathbb{L}_{\boldsymbol{v}_N\boldsymbol{v}_2} & \mathbb{L}_{\boldsymbol{v}_N\boldsymbol{v}_3} & \dots & \mathbb{L}_{\boldsymbol{v}_N\boldsymbol{v}_N} & \boldsymbol{L}_{\boldsymbol{v}_N\boldsymbol{r}} \\ \boldsymbol{L}_{\boldsymbol{r}\boldsymbol{v}_1} & \boldsymbol{L}_{\boldsymbol{r}\boldsymbol{v}_2} & \boldsymbol{L}_{\boldsymbol{r}\boldsymbol{v}_3} & \dots & \boldsymbol{L}_{\boldsymbol{r}\boldsymbol{v}_N} & L_{rr} \end{pmatrix} = \begin{pmatrix} \mathbb{K}_{\boldsymbol{v}_1\boldsymbol{v}_1} & \mathbb{K}_{\boldsymbol{v}_1\boldsymbol{v}_2} & \mathbb{K}_{\boldsymbol{v}_1\boldsymbol{v}_3} & \dots & \mathbb{K}_{\boldsymbol{v}_1\boldsymbol{v}_N} & \boldsymbol{K}_{\boldsymbol{v}_1\boldsymbol{r}} \\ \mathbb{K}_{\boldsymbol{v}_2\boldsymbol{v}_1} & \mathbb{K}_{\boldsymbol{v}_2\boldsymbol{v}_2} & \mathbb{K}_{\boldsymbol{v}_2\boldsymbol{v}_3} & \dots & \mathbb{K}_{\boldsymbol{v}_2\boldsymbol{v}_N} & \boldsymbol{K}_{\boldsymbol{v}_2\boldsymbol{r}} \\ \mathbb{K}_{\boldsymbol{v}_3\boldsymbol{v}_1} & \mathbb{K}_{\boldsymbol{v}_3\boldsymbol{v}_2} & \mathbb{K}_{\boldsymbol{v}_3\boldsymbol{v}_3} & \dots & \mathbb{K}_{\boldsymbol{v}_3\boldsymbol{v}_N} & \boldsymbol{K}_{\boldsymbol{v}_3\boldsymbol{r}} \\ \vdots & \vdots & \vdots & \ddots & \vdots & \vdots \\ \mathbb{K}_{\boldsymbol{v}_N\boldsymbol{v}_1} & \mathbb{K}_{\boldsymbol{v}_N\boldsymbol{v}_2} & \mathbb{K}_{\boldsymbol{v}_N\boldsymbol{v}_3} & \dots & \mathbb{K}_{\boldsymbol{v}_N\boldsymbol{v}_N} & \boldsymbol{K}_{\boldsymbol{v}_N\boldsymbol{r}} \\ \boldsymbol{K}_{\boldsymbol{r}\boldsymbol{v}_1} & \boldsymbol{K}_{\boldsymbol{r}\boldsymbol{v}_2} & \boldsymbol{K}_{\boldsymbol{r}\boldsymbol{v}_3} & \dots & \boldsymbol{K}_{\boldsymbol{r}\boldsymbol{v}_N} & K_{rr} \end{pmatrix}^{-1}, \tag{II.57}$$

where the terms $\mathbb{K}_{\boldsymbol{v}_i\boldsymbol{v}_j}$ are provided by (II.48) and where

$$\boldsymbol{K}_{\boldsymbol{v}_i\boldsymbol{r}} = \mathbb{A}_{\boldsymbol{v}_i\boldsymbol{\sigma}} : \boldsymbol{B}_{\boldsymbol{\sigma}\boldsymbol{r}} + \boldsymbol{A}_{\boldsymbol{v}_i\boldsymbol{r}}, \qquad \boldsymbol{K}_{\boldsymbol{r}\boldsymbol{v}_j} = \boldsymbol{A}_{\boldsymbol{r}\boldsymbol{\sigma}} : \mathbb{B}_{\boldsymbol{\sigma}\boldsymbol{v}_j}, \qquad K_{rr} = \boldsymbol{A}_{\boldsymbol{r}\boldsymbol{\sigma}} : \boldsymbol{B}_{\boldsymbol{\sigma}\boldsymbol{r}} + A_{rr}. \tag{II.58}$$

Furthermore, according to the "convex cutting plane" method[3], $\delta\boldsymbol{\varepsilon}_{\boldsymbol{p}}^{(n+1)(k)}$ and $\delta D^{(n+1)(k)}$, are directly linked to $\delta r^{(n+1)(k)}$ by:

$$\delta\boldsymbol{\varepsilon}_{\boldsymbol{p}}^{(n+1)(k)} = \frac{\boldsymbol{\Lambda}(\boldsymbol{\sigma}^{(n+1)(k)})}{1 - D^{(n+1)(k)}}\delta r^{(n+1)(k)}, \quad \delta D^{(n+1)(k)} = \frac{\Omega(Y^{(n+1)(k)})}{1 - D^{(n+1)(k)}}\delta r^{(n+1)(k)}. \tag{II.59}$$

Once the internal state variables are updated, the stress and the residuals $\boldsymbol{\phi}_{\boldsymbol{v}_i}$ and ϕ_r are re-assessed through the relationships (II.10), (II.40) and (II.41), respectively. This correction procedure is iteratively repeated (k loop) until the convergence is reached, namely when $|\boldsymbol{\phi}_{\boldsymbol{v}_i}^{(n+1)(k+1)}| \leq \mathbf{0} + \boldsymbol{\delta}$ and $|\phi_r^{(n+1)(k+1)}| \leq 0 + \delta$.

3. Note that, according to the "convex cutting plane" method [179, 145, 178], the flow equations (II.36) are explicitly integrated within the correction procedure. This is why in (II.59) the flows $\frac{\boldsymbol{\Lambda}(\boldsymbol{\sigma})}{1-D}$ and $\frac{\Omega(Y)}{1-D}$ are calculated from the previously updated state (taken at the increment $^{(n+1)(k)}$). Nevertheless, it is worth pointing out that the time integration remains implicit. Despite this simplification, the "convex cutting plane" method provides a good accuracy compared to other schemes, while involving less computational cost [171, 170, 83].

3.3 Tangent operator

Besides the computation of the stress, the global finite element solver also requires the tangent operator $\mathbb{C}_{\boldsymbol{t}}$, which defines the current rate in the variation of stress with the variation of total strain. As previously mentioned, the proposed implementation is based on the "convex cutting plane" form of the "return mapping algorithm", which utilizes the continuum tangent operator [178]. The formulation of the latter is obtained by identifying a linear relationship between $d\boldsymbol{\sigma}$ and $d\boldsymbol{\varepsilon}$ through a continuum description. To do so, the stress-strain relationship is written in differential form and the evolution equations are substituted.

With the proposed model, two configurations of tangent operator are to be taken into account, namely: the "viscoelastic tangent operator" and the "full tangent operator".

3.3.1 Viscoelastic tangent operator

If the "return mapping algorithm" stops at the "viscoelastic stress correction/prediction", then only the viscoelasticity is active. In this case, the stress-strain relationship (II.10) is written in differential form. After proper calculation (D.4), this gives:

$$d\boldsymbol{\sigma} = \mathbb{B}_{\boldsymbol{\sigma\varepsilon}} : d\boldsymbol{\varepsilon} + \sum_{j=1}^{N} \mathbb{B}_{\boldsymbol{\sigma v}_j} : d\boldsymbol{\varepsilon}_{\boldsymbol{v}_j}. \tag{II.60}$$

The fact that the viscoelasticity is always active implies that $d\boldsymbol{\phi}_{\boldsymbol{v}_i} = \mathbf{0}$. Written in differential form (D.2), this condition becomes:

$$d\boldsymbol{\phi}_{\boldsymbol{v}_i} = \mathbb{A}_{\boldsymbol{v}_i\boldsymbol{\sigma}} : d\boldsymbol{\sigma} + \mathbb{A}_{\boldsymbol{v}_i\boldsymbol{v}_i} : d\boldsymbol{\varepsilon}_{\boldsymbol{v}_i} = \mathbf{0}. \tag{II.61}$$

By introducing (II.60) into (II.61), a linear relationship can be identified between each $d\boldsymbol{\varepsilon}_{\boldsymbol{v}_j}$ and $d\boldsymbol{\varepsilon}$:

$$d\boldsymbol{\varepsilon}_{\boldsymbol{v}_j} = \mathbb{X}^*_{\boldsymbol{v}_j\boldsymbol{\varepsilon}} : d\boldsymbol{\varepsilon} \qquad \text{where} \qquad \mathbb{X}^*_{\boldsymbol{v}_j\boldsymbol{\varepsilon}} = -\sum_{i=1}^{N} \mathbb{L}^*_{\boldsymbol{v}_j\boldsymbol{v}_i} : \mathbb{A}_{\boldsymbol{v}_i\boldsymbol{\sigma}} : \mathbb{B}_{\boldsymbol{\sigma\varepsilon}}. \tag{II.62}$$

Finally, the substitution of (II.62) into (II.60) leads to the formulation of the "viscoelastic tangent operator":

$$d\boldsymbol{\sigma} = \mathbb{C}_{\boldsymbol{t}} : d\boldsymbol{\varepsilon} \qquad \text{where} \qquad \mathbb{C}_{\boldsymbol{t}} = \mathbb{B}_{\boldsymbol{\sigma\varepsilon}} + \sum_{j=1}^{N} \mathbb{B}_{\boldsymbol{\sigma v}_j} : \mathbb{X}^*_{\boldsymbol{v}_j\boldsymbol{\varepsilon}}. \tag{II.63}$$

3.3.2 Full tangent operator

If the "return mapping algorithm" passes to the "full stress correction", then both viscoelasticity, viscoplasticity and damage are active. In this case, the stress-strain relationship (II.10) is written in differential form. After proper calculation (D.4), this gives:

$$d\boldsymbol{\sigma} = \mathbb{B}_{\boldsymbol{\sigma\varepsilon}} : d\boldsymbol{\varepsilon} + \sum_{j=1}^{N} \mathbb{B}_{\boldsymbol{\sigma v}_j} : d\boldsymbol{\varepsilon}_{\boldsymbol{v}_j} + \boldsymbol{B}_{\boldsymbol{\sigma r}} dr. \tag{II.64}$$

The fact that both viscoelasticity, viscoplasticity and damage are active implies that $d\boldsymbol{\phi}_{\boldsymbol{v}_i} = \mathbf{0}$ and $d\phi_r = 0$. Written in differential form (D.2 and D.3), these conditions become:

$$\begin{cases} d\boldsymbol{\phi}_{\boldsymbol{v}_i} = \mathbb{A}_{\boldsymbol{v}_i\boldsymbol{\sigma}} : d\boldsymbol{\sigma} + \mathbb{A}_{\boldsymbol{v}_i\boldsymbol{v}_i} : d\boldsymbol{\varepsilon}_{\boldsymbol{v}_i} + \boldsymbol{A}_{\boldsymbol{v}_i\boldsymbol{r}} dr = \mathbf{0} \\ d\phi_r = \boldsymbol{A}_{\boldsymbol{r}\boldsymbol{\sigma}} : d\boldsymbol{\sigma} + A_{rr} dr = 0 \end{cases}. \tag{II.65}$$

By introducing (II.64) into (II.65), a linear relationship can be identified between each $d\boldsymbol{\varepsilon}_{\boldsymbol{v}_j}$ and $d\boldsymbol{\varepsilon}$, and between dr and $d\boldsymbol{\varepsilon}$:

$$\begin{cases} d\boldsymbol{\varepsilon}_{\boldsymbol{v}_j} = \mathbb{X}_{\boldsymbol{v}_j\boldsymbol{\varepsilon}} : d\boldsymbol{\varepsilon} \qquad \text{where} \qquad \mathbb{X}_{\boldsymbol{v}_j\boldsymbol{\varepsilon}} = -\sum_{i=1}^{N} \mathbb{L}_{\boldsymbol{v}_j\boldsymbol{v}_i} : \mathbb{A}_{\boldsymbol{v}_i\boldsymbol{\sigma}} : \mathbb{B}_{\boldsymbol{\sigma}\boldsymbol{\varepsilon}} - \boldsymbol{L}_{\boldsymbol{v}_j\boldsymbol{r}} \otimes \boldsymbol{A}_{\boldsymbol{r}\boldsymbol{\sigma}} : \mathbb{B}_{\boldsymbol{\sigma}\boldsymbol{\varepsilon}} \\ dr = \boldsymbol{X}_{\boldsymbol{r}\boldsymbol{\varepsilon}} : d\boldsymbol{\varepsilon} \qquad \text{where} \qquad \boldsymbol{X}_{\boldsymbol{r}\boldsymbol{\varepsilon}} = -\sum_{i=1}^{N} \boldsymbol{L}_{\boldsymbol{r}\boldsymbol{v}_i} : \mathbb{A}_{\boldsymbol{v}_i\boldsymbol{\sigma}} : \mathbb{B}_{\boldsymbol{\sigma}\boldsymbol{\varepsilon}} - L_{rr}\boldsymbol{A}_{\boldsymbol{r}\boldsymbol{\sigma}} : \mathbb{B}_{\boldsymbol{\sigma}\boldsymbol{\varepsilon}} \end{cases} . \tag{II.66}$$

Finally, the substitution of (II.66) into (II.64) leads to the formulation of the "full tangent operator":

$$d\boldsymbol{\sigma} = \mathbb{C}_{\boldsymbol{t}} : d\boldsymbol{\varepsilon} \qquad \text{where} \qquad \mathbb{C}_{\boldsymbol{t}} = \mathbb{B}_{\boldsymbol{\sigma}\boldsymbol{\varepsilon}} + \sum_{j=1}^{N} \mathbb{B}_{\boldsymbol{\sigma}\boldsymbol{v}_j} : \mathbb{X}_{\boldsymbol{v}_j\boldsymbol{\varepsilon}} + \boldsymbol{B}_{\boldsymbol{\sigma}\boldsymbol{r}} \otimes \boldsymbol{X}_{\boldsymbol{r}\boldsymbol{\varepsilon}}. \tag{II.67}$$

4 Experimental identification, strategy and validation

4.1 Experimental procedure and testing

In this section, it is proposed to apply the previously formulated constitutive model to describe the behaviour of the polyamide 6-6. This type of material is well known to be highly sensitive to the environmental conditions [102, 7, 6, 121, 122, 120, 123], especially the relative humidity (RH) and the temperature (T). In the present case, the following environmental conditions were considered: $RH = 50\%$ and $T = 23^oC$ (room temperature). For all the experiments, uni-axial tests were carried out on ISO527-2-1A tensile specimens (see Figure II.3). A particular attention has been paid concerning the RH conditioning prior to performing the mechanical testing. The specimens were placed in a oven with an air containing 50% of relative humidity at the temperature of 70^oC until the equilibrium in water concentration was reached within the material. This was checked by regularly weighting the samples until their mass does not evolve any more. Next, the specimens were placed in a sealed bag before testing. The tensile tests were performed with a servo-hydraulic tensile machine at room temperature. During the tests, the axial strain ε_{11} is locally measured by means of an extensometer (see Figure II.4a), while the axial stress σ_{11} is monitored by a load cell.

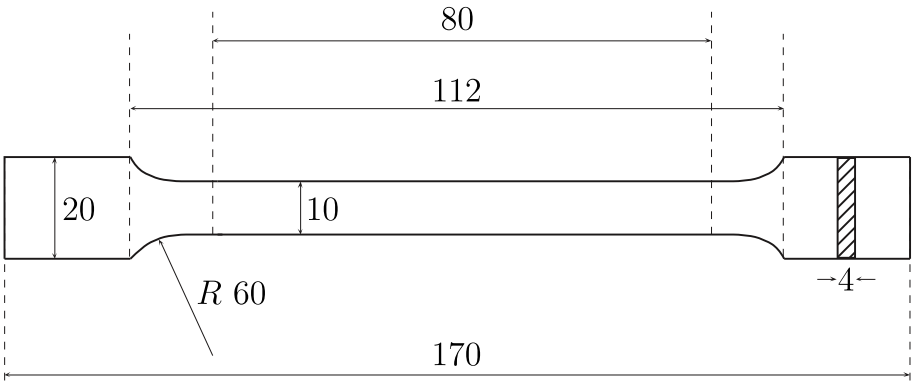

Figure II.3: ISO527-2-1A tensile specimen (dimensions in mm).

In order to properly identify and validate the model, an experimental program involving the following types of tests is proposed:

- Monotonic tests:
  The material is subjected to a relatively high level of strain, about 0.08, followed by an unloading stage up to zero stress. These tests are performed at different strain rates, namely: 8.0×10^{-4}, 8.0×10^{-3} and 8.0×10^{-2} s^{-1}. This test configuration emphasizes the global rate effect related to the viscoelasticity and viscoplasticity. In addition, the unloading stage highlights the apparent stiffness reduction due to damage.

- Creep and strain recovery tests:
  The material is first loaded in 5 s up to a certain level of stress, namely: 30, 40 and 50 MPa. This stress is then held for 300 s before being released in 5 s. Finally, the material is left free of stress for another 300 s. This test configuration mainly emphasizes the creep effects caused by the viscoplasticity and the viscoelasticity acting under long periods of time. Moreover, the strain recovery stage (when the material is kept under zero stress) enables to distinguish the part of the total strain that is recoverable

(viscoelastic) and the part that is irrecoverable (viscoplastic).

– Stress-controlled cyclic tests:
The material is subjected to a triangular stress signal oscillating between a top and a bottom stress level at a frequency of 1 Hz during 100 s, i.e. 100 cycles. Three top stress levels: 30, 40 and 50 MPa, are considered, while the bottom stress level is always the same: 5 MPa. This test configuration brings out the accumulation of damage and strain occurring through a long period of time. Moreover, at each cycle, the hysteresis loops highlight the viscoelasticity acting under short periods of time.

For the stress-controlled cyclic tests, as complementary data, thermal measurements were carried out by means of an IR thermal camera, as shown in Figure II.4a. Indeed, as mentioned in Section 1, it is well established that thermoplastic polymers may exhibit a significant elevation of temperature, especially upon cyclic loading [13, 14, 15, 198], due to the self-heating phenomenon arising from the dissipative mechanisms (see Section 1.6 in Appendix B).

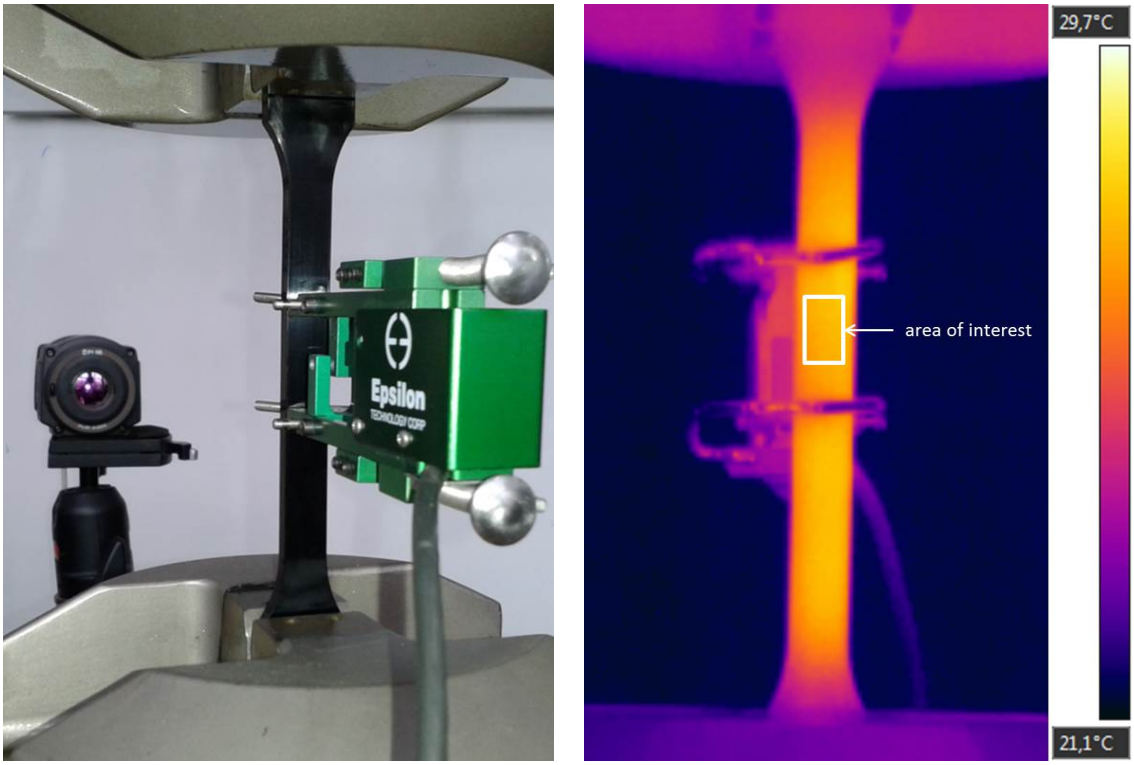

(a) Experimental setup

(b) Measurment of the average temperature within the aera of interest

Figure II.4: Thermomechanical testing.

It is important to recall that the proposed constitutive model assumes isothermal conditions. Neither the temperature effect on the mechanical properties, nor the heat induced by the mechanical work are accounted for. Nevertheless, a simple way to evaluate if a the self-heating is likely to occur is to integrate the mechanical dissipation $\dot{\Phi}$ as a heat source in an uncoupled thermal analysis (see Appendix C). This provides an estimation of the temperature elevation caused the mechanical dissipation that can be compared to the one experimentally observed. Assuming uniform thermomechanical fields in the area of interest,

the heat equation can be reduced to its "0D" formalism (see Section 1 in Appendix C). This gives:

$$\rho c\left(\dot{T}(t)+\frac{T(t)-T_{\infty}}{\tau}\right)=\dot{\Phi}(t), \tag{II.68}$$

where ρ and c stand for the material density and the specific heat capacity, respectively. The characteristic time τ quantifies the local heat losses which are assumed to be proportional to the difference between the current temperature of the material $T(t)$ and the its equilibrium temperature T_{∞} (room temperature). The thermal data utilized in this chapter are listed in Table II.3. The "0D" heat equation (II.68) is then solved independently from the mechanical problem with the help of a time-implicit algorithm (see Section 2 in Appendix C).

Feature	Parameter	value	unit
Density	ρ	1.120×10^{-9}	$\mathrm{T.mm^{-3}}$
Specific heat capacity	c	$1.638\times10^{+9}$	$\mathrm{mJ.T^{-1}.{}^{o}C^{-1}}$
Characteristic time (heat losses)	τ	160	s

Table II.3: Parameters of the uncoupled "0D" thermal problem for polyamide 6-6 specimens. The values for the density and the specific heat capacity were taken from [13]. The characteristic time τ was evaluated for the ISO527-2-1A tensile specimens (see Figures II.3 and II.4) using the methodology proposed by [20] that is briefly presented in Section 3 in Appendix C.

4.2 Identification strategy

It is well known that parameters related to viscoelasticity can be identified from Dynamic Mechanical Analysis (DMA) by calibrating the storage and loss modulus E' and E'' on the master curve within a predefined frequency range [97]. Nevertheless, even though from a theoretical point of view, this method is very convenient, it may not provide satisfying results. Indeed, these tests are usually performed at very low stress levels, which may not bring about the same mechanisms than those considered in the proposed model. In the present work, a direct identification procedure is proposed as an alternative way.

The identification of such complex constitutive models, where several mechanisms are simultaneously involved, often requires a suitable methodology. Indeed, most of the times, it is impossible to completely isolate a single mechanism in order to identify independently its related parameters. Consequently, the identification procedure necessitates the use of reverse engineering methods. To do so, an optimization algorithm based on the Levenberg-Marquardt technique [111, 125, 131, 129] has been utilized. The aim of this method is to identify a set of parameters $\boldsymbol{p}$ by minimizing a cost function C. In the present case, this cost function is expressed by the least squares between the numerical and experimental responses, m^{num} and m^{exp}, respectively:

$$C(\boldsymbol{p})=\frac{1}{2}\sum_{k=1}^{N_p} w_k\left[m_k^{num}(\boldsymbol{p})-m_k^{exp}\right]^2, \tag{II.69}$$

where N_p is the number of measuring points and w_k a weighting term given to each of them. In the present case, the response of the material m denotes either the uni-axial stress σ_{11} if the associated test is strain-controlled (a uni-axial strain ε_{11} is applied), or the uni-axial strain ε_{11} if the associated test is stress-controlled (a uni-axial stress σ_{11} is applied).

This identification method permits, starting from an initial set of parameter, to find out a new one by satisfying a local minimum condition of the cost function C. However, the local minimum is not necessarily the global one and/or the solution may not be unique. This is why it is very important to carry out the identification from an experimental data base where all the considered mechanisms are well emphasized (see Section 4.1). It is noted that, for complicated constitutive models, this procedure cannot guarantee uniqueness of the obtained set of parameters.

For the present model, given the number of parameters involved, it is strongly advised not to directly identify all of them simultaneously. Instead, to facilitate the identification procedure, the following three-step strategy is proposed:

- Step 1:
  At low stress levels, the effects of damage and viscoplasticity can be neglected so that the material remains in the viscoelastic regime. This condition is obtained at the beginning of the "monotonic tests", from which the parameters related to the viscoelasticity are identified in a first time.

- Step 2:
  The parameters previously identified are kept constant, while the parameters related to viscoplasticity and damage are identified from the complete "monotonic tests" along with the "creep and strain recovery tests".

- Step 3:
  Starting from the previously obtained values, all the parameters are identified once more from the same tests than the previous step, adding the five first cycles of the "stress-controlled cyclic test" performed at the intermediate stress level (40 MPa). This last step mainly enables to adjust the viscoelasticity acting under short periods of time and thus to capture the hysteresis loop appearing at each cycle.

Note that, except the Poisson ratio ν, all the other parameters of the model can be identified from uni-axial stress-strain responses. Obviously, the Poisson ratio can be obtained from measurements of the transverse strain (ε_{22} or ε_{33}) in addition to the longitudinal one (ε_{11}), at a stress level low enough so that no plastic strains are generated.

4.3 Identification and validation

Using the previously described strategy, the parameters of the proposed constitutive model have been identified considering four Kelvin-Voigt branches for the viscoelastic part besides the viscoplaticity coupled to damage. The obtained parameters are listed in Table II.4. Due to the lack of data regrading the transverse strain, the standard value of 0.3 is considered for the Poisson ratio.

Mechanical feature		Parameter	value	unit
Viscoelasticity	Single spring	E_e	2731	MPa
	Kelvin-Voigt branch 1	E_{v_1}	8766	MPa
		η_{v_1}	1395	MPa.s
		$\tau_{v_1} = \frac{\eta_{v_1}}{E_{v_1}}$	0.16	s
	Kelvin-Voigt branch 2	E_{v_2}	13754	MPa
		η_{v_2}	165601	MPa.s
		$\tau_{v_2} = \frac{\eta_{v_2}}{E_{v_2}}$	12.04	s
	Kelvin-Voigt branch 3	E_{v_3}	15010	MPa
		η_{v_3}	457955	MPa.s
		$\tau_{v_3} = \frac{\eta_{v_3}}{E_{v_3}}$	30.51	s
	Kelvin-Voigt branch 4	E_{v_4}	11634	MPa
		η_{v_4}	1307516	MPa.s
		$\tau_{v_4} = \frac{\eta_{v_4}}{E_{v_4}}$	112.39	s
	Poisson ratio (standard value)	ν	0.3	-
Viscoplasticity	Yield threshold	R_0	4.86	MPa
coupled to damage	Hardening function	K	1304.33	MPa
		n	0.674	-
	Viscous stress function	H	47.35	MPa.s^m
		m	0.068	-
	Damage	S	21.607	MPa
		β	-1.105	-

Table II.4: Identified parameters for polyamide 6-6.

It is worth mentioning that, as explained in the previous section, all the monotonic and creep tests (see Figures II.5 and II.6, respectively) were utilized as identification data. Besides the previously mentioned tests, the identification data were completed by the five first cycles of the cyclic test performed at the intermediate stress level (40 MPa). This test is shown in Figures II.8. All the other experimental data, namely: the entire cyclic tests (see Figures II.7, II.8 and II.9), are kept for the validation of the model. The overall good agreement between the experimental and simulated results demonstrates the efficiency of the identification procedure as well as the model's capabilities to capture the time-dependent and cyclic response of the polyamide 6-6 with a single set of parameters.

Under monotonic loading (see Figure II.5), the stress response takes a higher amplitude when the strain rate increases. Moreover, upon unloading, an apparent stiffness reduction

can be observed. The good agreement between the model and the experiments demonstrates both viscoelastic, viscoplastic and damage mechanisms are appropriate to capture both the global rate effect and the apparent stiffness reduction.

For the creep and strain recovery tests (see Figure II.6), note that, under a constant stress level, the strain rapidly increases at first and subsequently slows down as the material continues to creep. The higher this stress level is, the strain generated during the creep stage takes bigger values. Once this stress is released, a certain amount of strain is gradually recovered over a certain time, while another part does not recover. The creep response of the material is also well described by the model. Even so, the prediction becomes less accurate for the highest stress level (50 MPa) and the damage is slightly overestimated during the creep stage.

Under cyclic loading (see Figures II.7, II.8 and II.9), the material exhibits an accumulation of strain from one cycle to another. As remarked for the creep and strain recovery tests, the higher amplitude of stress signal results in bigger strain accumulation. Its evolution is relatively fast within the first cycles and subsequently decreases once a certain number of cycles have passed. In addition, hysteresis loops can also be observed at each cycle. Once more, the simulated responses are in good agreement with the experimental data. For each stress level, the model is able to properly predict the observed accumulation of strain and damage occurring throughout the repeated cycles. In addition, the hysteresis loops appearing at each single cycle are also well represented.

From an energetic point of view, the dissipative behaviour of the model seems to be accurate as the elevations of temperature computed from the uncoupled "0D" thermal analyses (see Figures II.10, II.11 and II.12) are of the same order than the ones experimentally observed. Moreover, it can be remarked that, within the 100 cycles performed during the tests, the temperature elevation induced by the dissipative mechanisms remains relatively low (about 1.5 to 4.5 ^{o}C). Thus, the isothermal assumption can be reasonably considered as relevant in the present cases. However, it is worth noticing that the observed temperature elevations are far from any stabilized regime within 100 cycles. This means that, under a more important number of cycles, a significant temperature increase may likely occur.

In order to illustrate this point, an additional test has been carried out for the highest stress level (50 MPa) with the same frequency (1 Hz), but this time 1000 cycles are performed (instead of 100). The model is confronted to this additional test (see Figure II.13) and the elevations of temperature computed from the uncoupled "0D" thermal analyses is compared to the one experimentally observed (see Figure II.14). It can be remarked that the predicted strain response and temperature elevation are accurate as long as the latter remains limited. However, after a certain number of cycles, the temperature becomes significant enough and starts having a non-negligible effect on the material. Such temperature dependencies are not integrated within the proposed model which explains why the prediction starts deviating once a hundred of cycles have passed. The treatment of such cases requires to enhance the model with a fully-coupled thermomechanical formalism where the temperature effects would be integrated as well as the heat induced by the mechanical work.

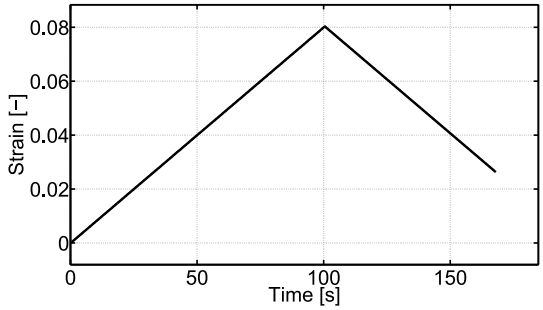

(a) Applied strain (ε_{11}) vs. time

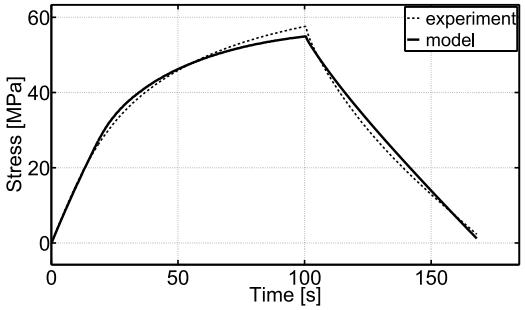

(b) Stress response (σ_{11}) vs. time

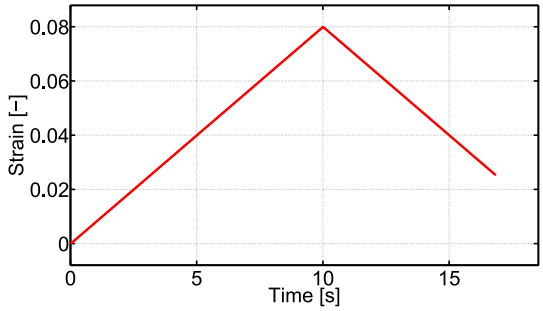

(c) Applied strain (ε_{11}) vs. time

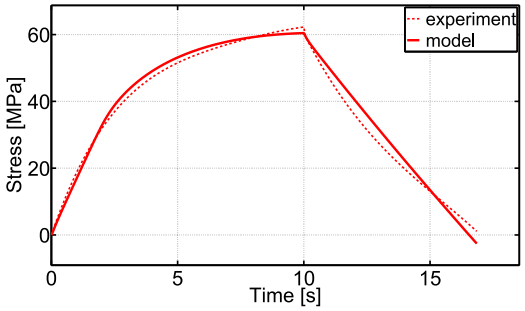

(d) Stress response (σ_{11}) vs. time

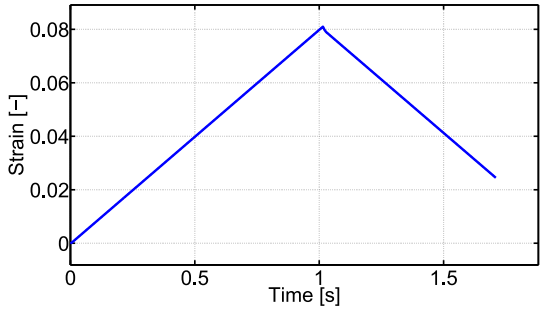

(e) Applied strain (ε_{11}) vs. time

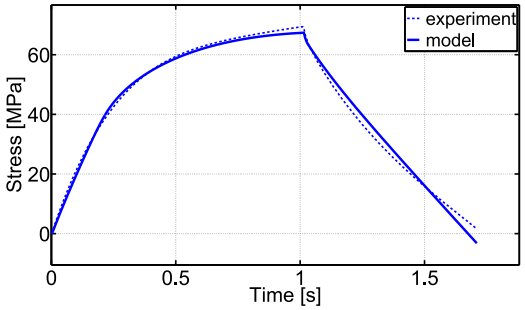

(f) Stress response (σ_{11}) vs. time

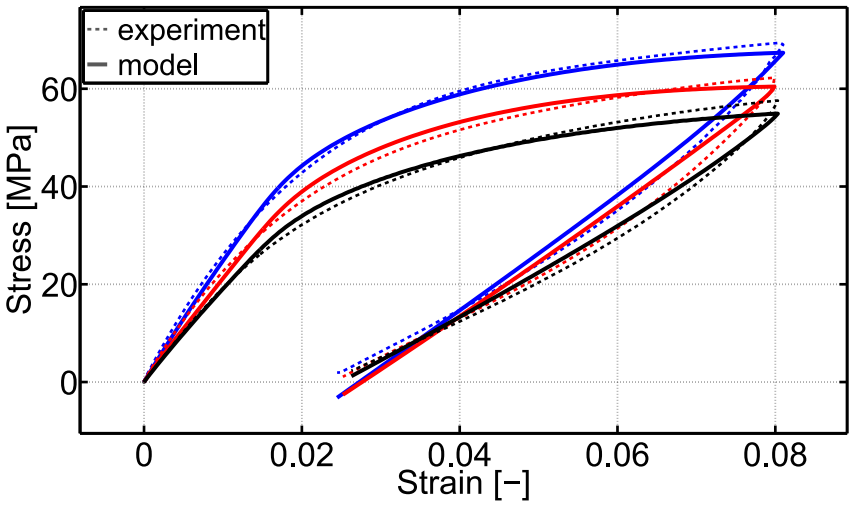

(g) Stress (σ_{11}) vs. strain (ε_{11})

Figure II.5: Monotonic tests performed at the strain rates of 8.0×10^{-4}, 8.0×10^{-3} and 8.0×10^{-2} s^{-1}, represented in black, red and blue, respectively. These data are used for the identification.

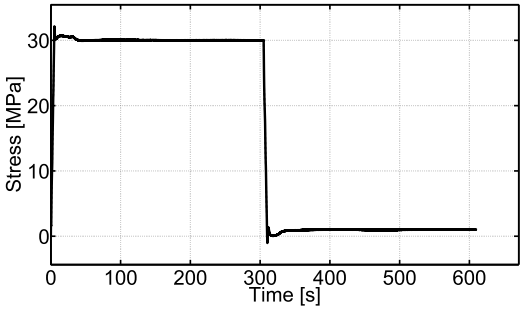

(a) Applied stress (σ_{11}) vs. time

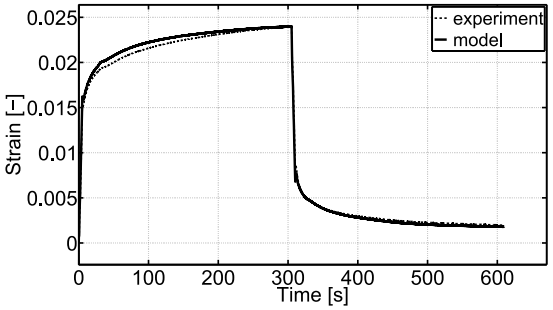

(b) Strain response (ε_{11}) vs. time

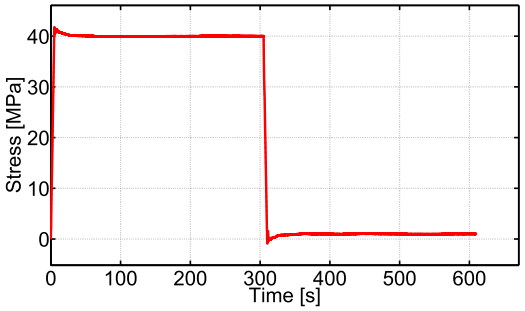

(c) Applied stress (σ_{11}) vs. time

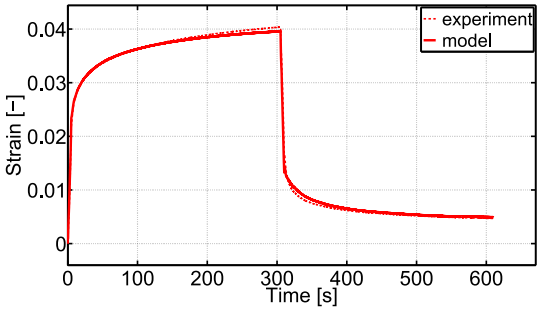

(d) Strain response (ε_{11}) vs. time

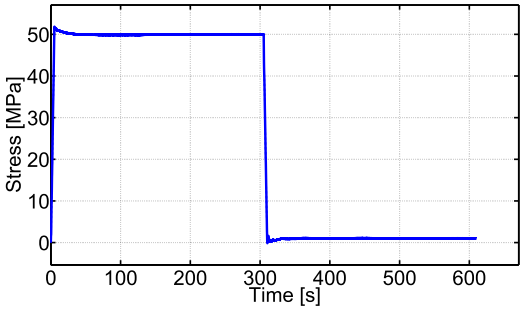

(e) Applied stress (σ_{11}) vs. time

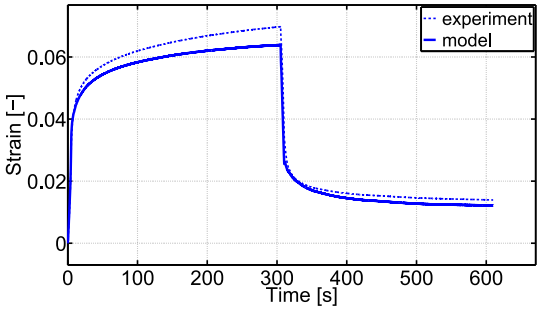

(f) Strain response (ε_{11}) vs. time

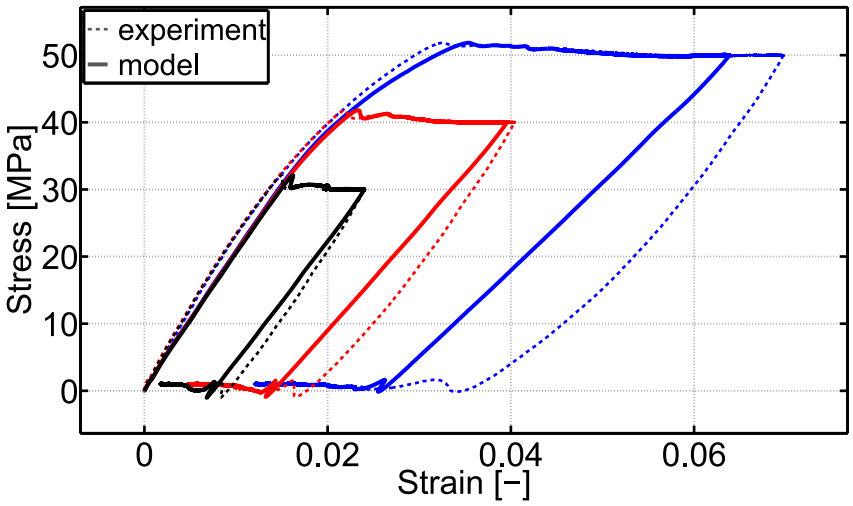

(g) Stress (σ_{11}) vs. strain (ε_{11})

Figure II.6: Creep and strain recovery tests performed at the stress level of 30, 40 and 50 MPa, represented in black, red and blue, respectively. These data are used for the identification.

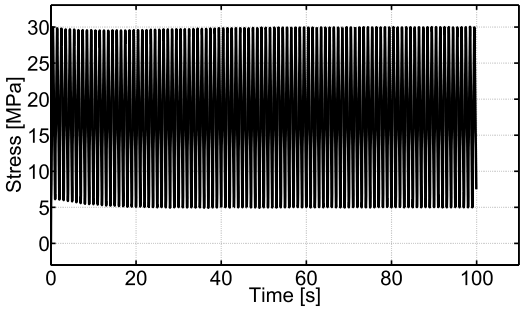

(a) Applied stress (σ_{11}) vs. time

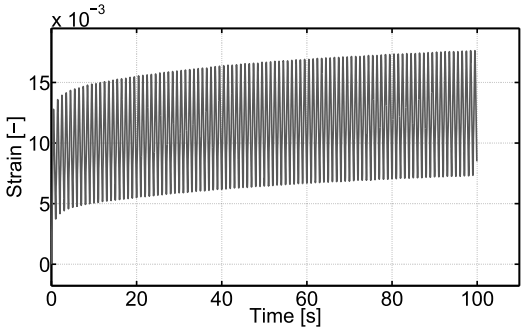

(b) Experimental strain response (ε_{11}) vs. time

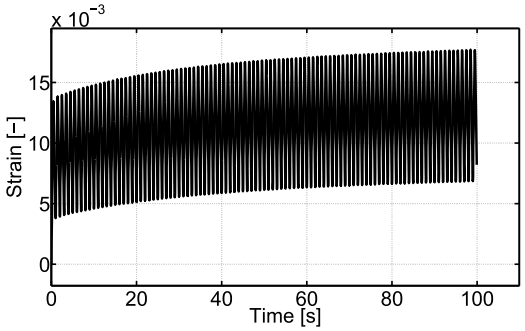

(c) Simulated strain response (ε_{11}) vs. time

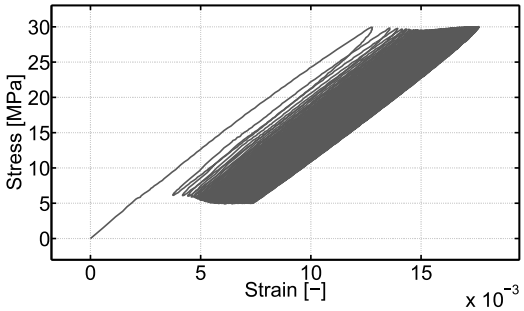

(d) Stress (σ_{11}) vs. strain (ε_{11}), experiment

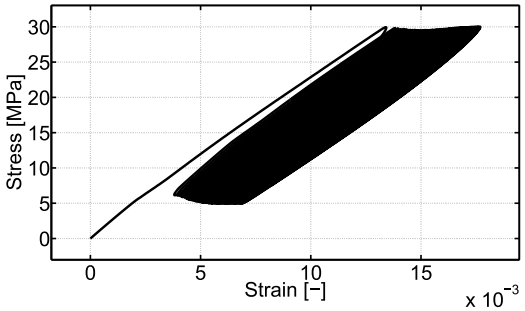

(e) Stress (σ_{11}) vs. strain (ε_{11}), simulation

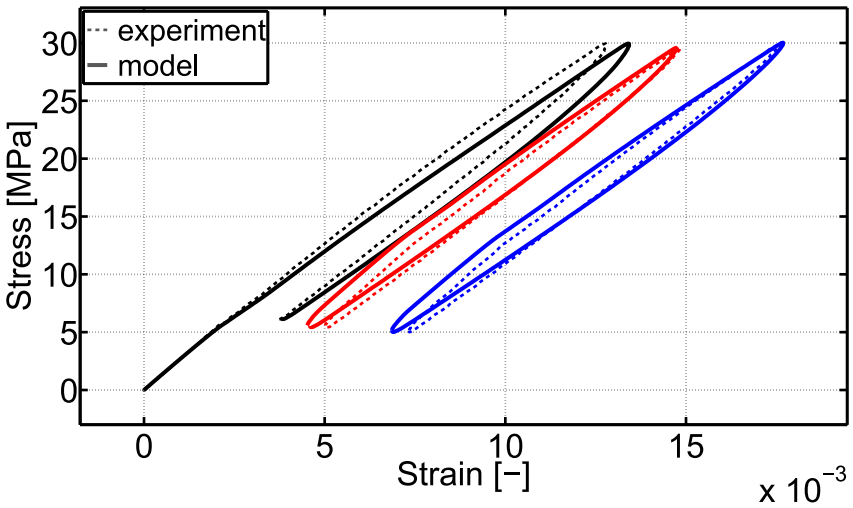

(f) Stress (σ_{11}) vs. strain (ε_{11}) for the 1^{st}, 10^{th} and the 99^{th} cycles, represented in black, red and blue, respectively

Figure II.7: Stress-controlled cyclic test: 100 cycles performed at 1 Hz with a top stress level of 30 MPa. These data are used for the validation.

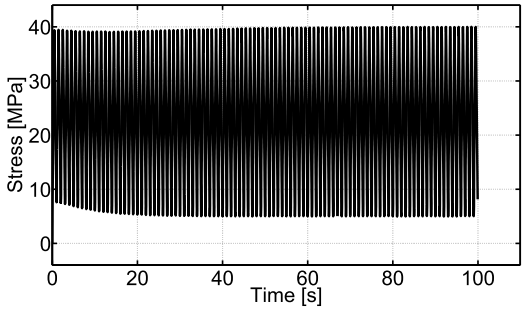

(a) Applied stress (σ_{11}) vs. time

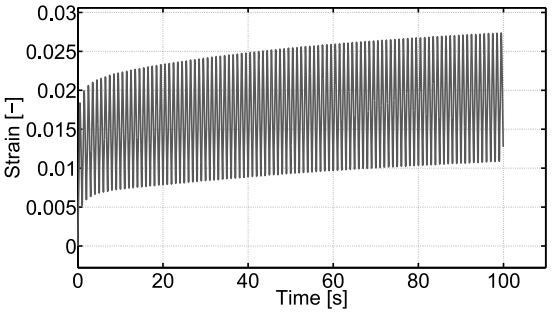

(b) Experimental strain response (ε_{11}) vs. time

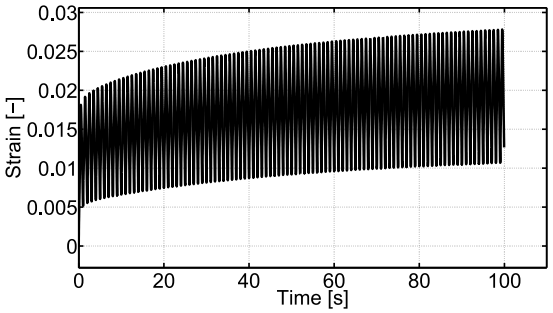

(c) Simulated strain response (ε_{11}) vs. time

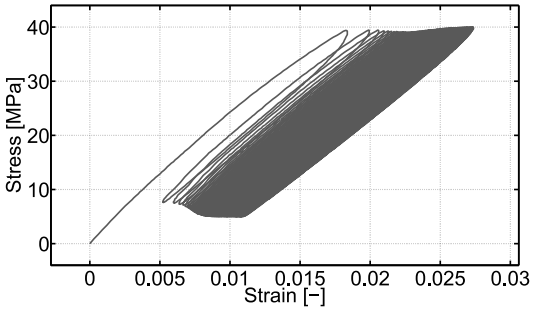

(d) Stress (σ_{11}) vs. strain (ε_{11}), experiment

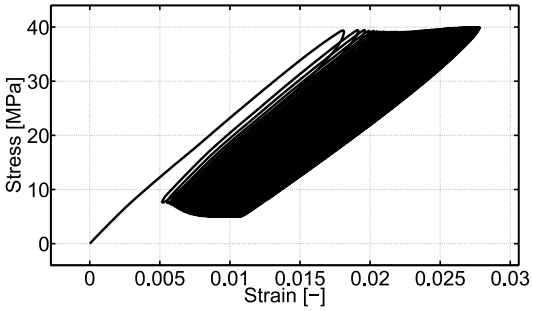

(e) Stress (σ_{11}) vs. strain (ε_{11}), simulation

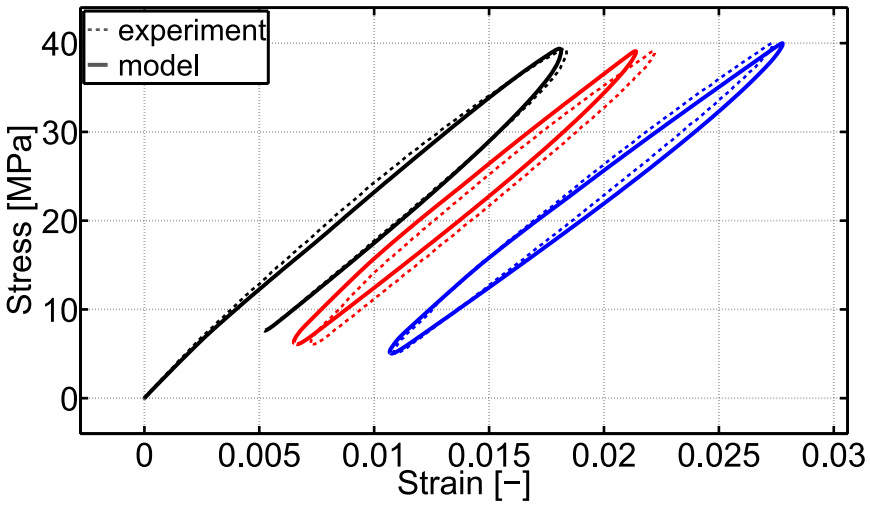

(f) Stress (σ_{11}) vs. strain (ε_{11}) for the 1^{st}, 10^{th} and the 99^{th} cycles, represented in black, red and blue, respectively

Figure II.8: Stress-controlled cyclic test: 100 cycles performed at 1 Hz with a top stress level of 40 MPa. The five first cycles are used for the identification, whereas the rest of the test is kept for the validation.

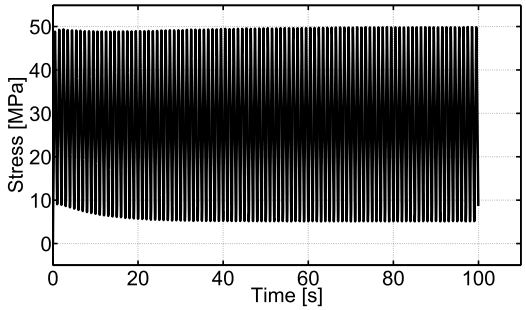

(a) Applied stress (σ_{11}) vs. time

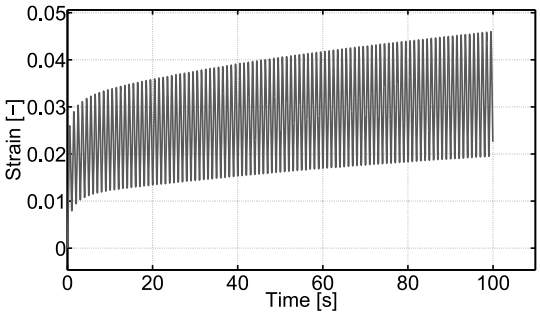

(b) Experimental strain response (ε_{11}) vs. time

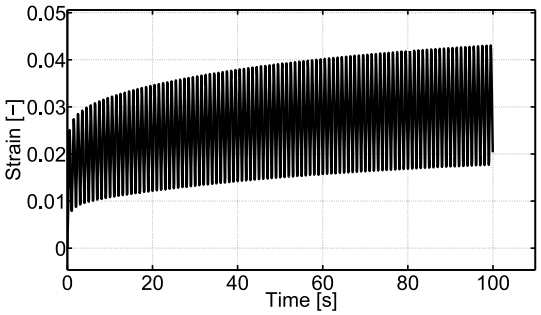

(c) Simulated strain response (ε_{11}) vs. time

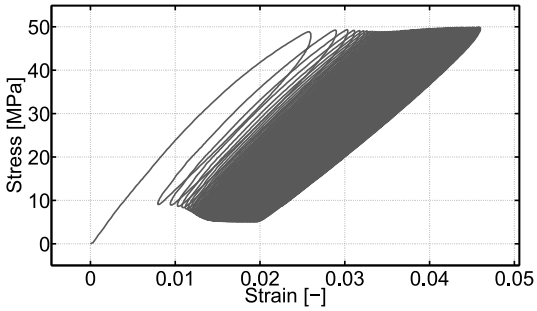

(d) Stress (σ_{11}) vs. strain (ε_{11}), experiment

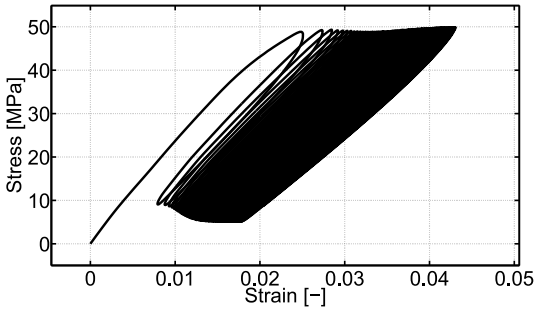

(e) Stress (σ_{11}) vs. strain (ε_{11}), simulation

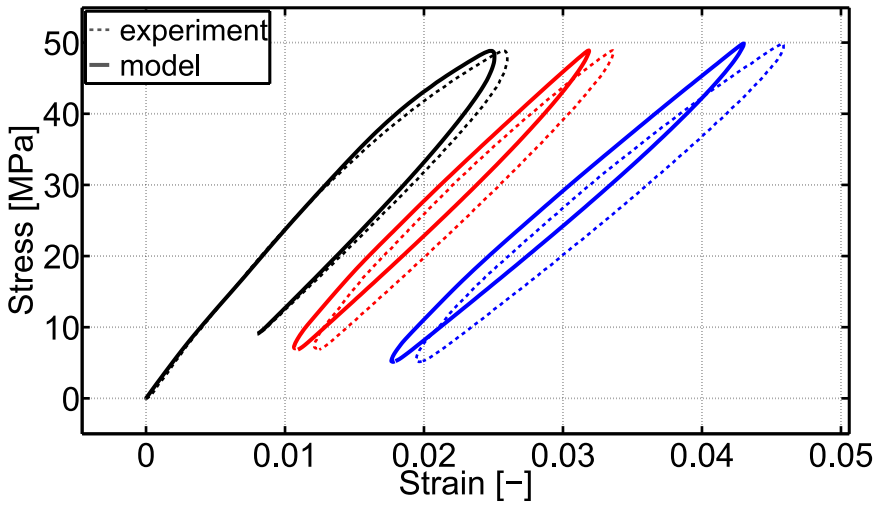

(f) Stress (σ_{11}) vs. strain (ε_{11}) for the 1^{st}, 10^{th} and the 99^{th} cycles, represented in black, red and blue, respectively

Figure II.9: Stress-controlled cyclic test: 100 cycles performed at 1 Hz with a top stress level of 50 MPa. These data are used for the validation.

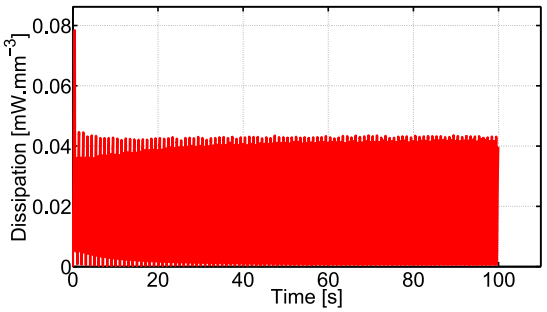

(a) Dissipation ($\dot{\Phi}$) vs. time

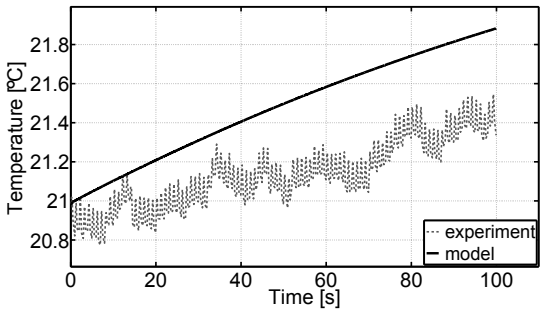

(b) Temperature (T) vs. time

Figure II.10: Assessment of the temperature elevation induced by the dissipation through the uncoupled "0D" thermal analysis (see Appendix C) for the stress-controlled cyclic tests: 100 cycles performed at 1 Hz with a top stress level of 30 MPa (see Figure II.7).

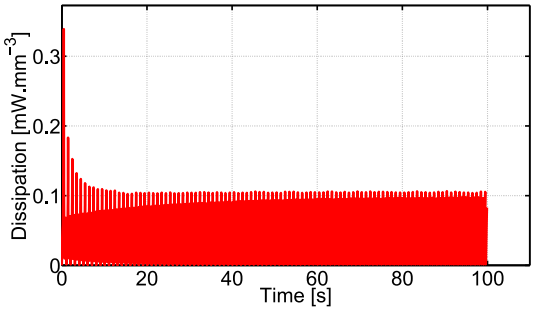

(a) Dissipation ($\dot{\Phi}$) vs. time

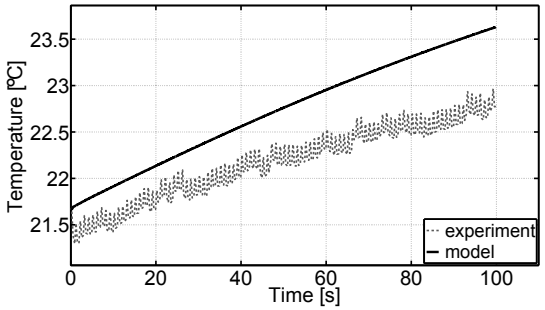

(b) Temperature (T) vs. time

Figure II.11: Assessment of the temperature elevation induced by the dissipation through the uncoupled "0D" thermal analysis (see Appendix C) for the stress-controlled cyclic tests: 100 cycles performed at 1 Hz with a top stress level of 40 MPa (see Figure II.8).

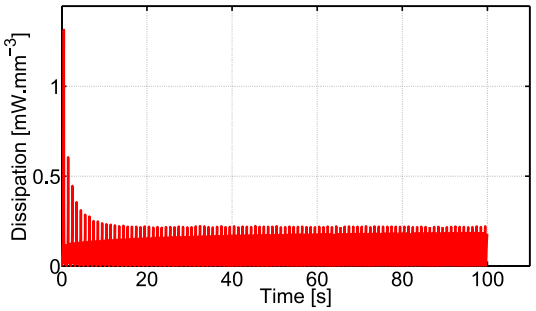

(a) Dissipation ($\dot{\Phi}$) vs. time

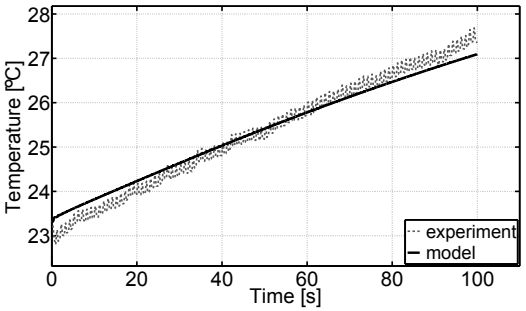

(b) Temperature (T) vs. time

Figure II.12: Assessment of the temperature elevation induced by the dissipation through the uncoupled "0D" thermal analysis (see Appendix C) for the stress-controlled cyclic tests: 100 cycles performed at 1 Hz with a top stress level of 50 MPa (see Figure II.9).

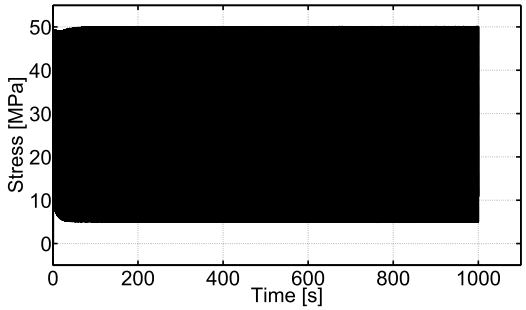

(a) Applied stress (σ_{11}) vs. time

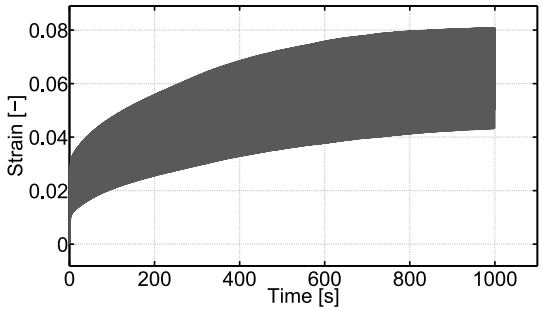

(b) Experimental strain response (ε_{11}) vs. time

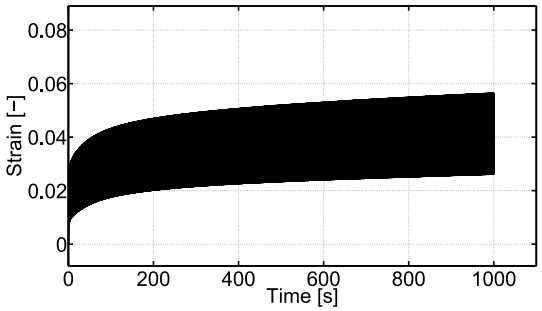

(c) Simulated strain response (ε_{11}) vs. time

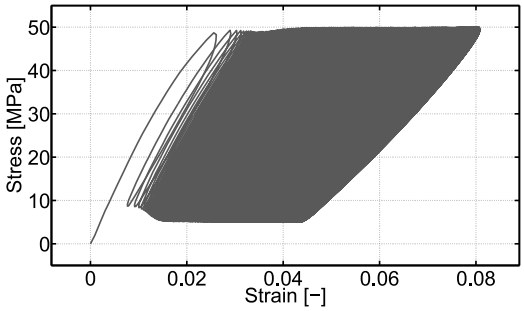

(d) Stress (σ_{11}) vs. strain (ε_{11}), experiment

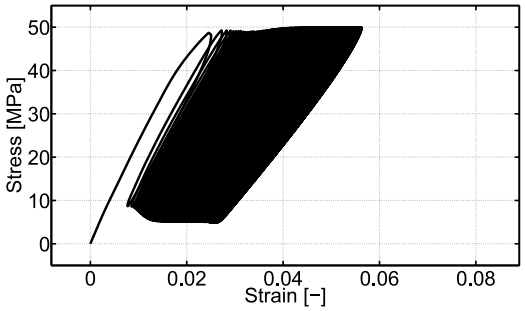

(e) Stress (σ_{11}) vs. strain (ε_{11}), simulation

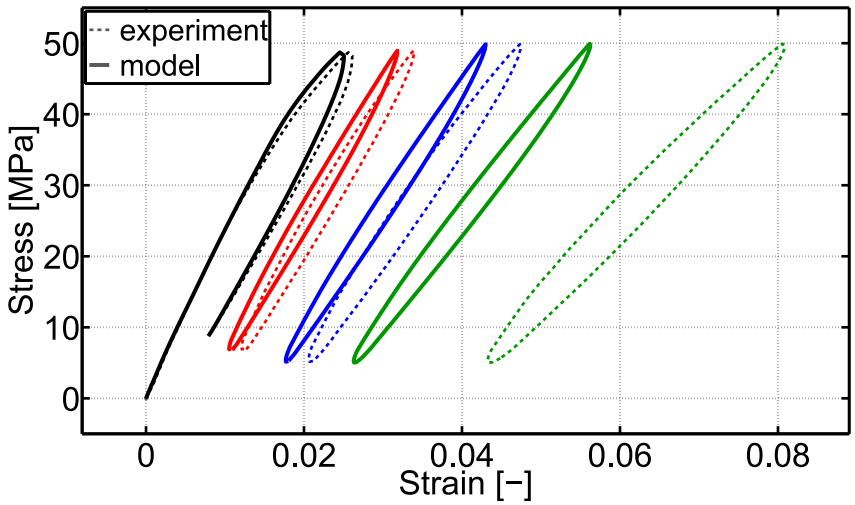

(f) Stress (σ_{11}) vs. strain (ε_{11}) for the 1^{st}, 10^{th}, 100^{th} and the 999^{th} cycles, represented in black, red, blue and green, respectively

Figure II.13: Stress-controlled cyclic test: 1000 cycles performed at 1 Hz with a top stress level of 50 MPa.

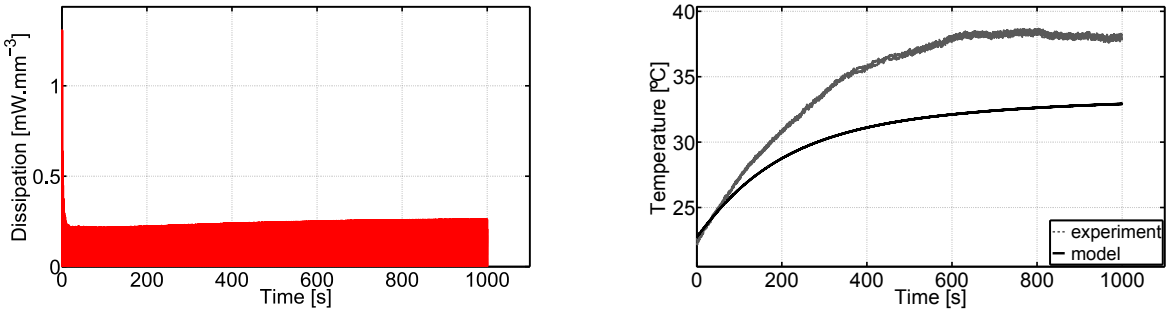

(a) Dissipation ($\dot{\Phi}$) vs. time

(b) Temperature (T) vs. time

Figure II.14: Assessment of the temperature elevation induced by the dissipation through the uncoupled "0D" thermal analysis (see Appendix C) for the stress-controlled cyclic tests: 1000 cycles performed at 1 Hz with a top stress level of 50 MPa (see Figure II.13).

5 Numerical simulations

All the simulations presented in this section were carried out with the parameters previously identified for the polyamide 6-6 in Table II.4.

5.1 Mechanical responses and dissipative behaviour of a material point

In order to provide a better understanding of the proposed constitutive model, its dissipative behaviour is illustrated through the four following uni-axial simulations carried out on a single material point:

- Simulation 1: stress relaxation
  A strain of 0.04 is first applied on the material in 5 s. This strain is then held for 300 s before returning back to zero in 5 s. In a final stage, the material is kept at zero strain for another 300 s. The results of this simulation are presented in Figure II.15. Note that the computation is carried out with a constant time increment of 0.05 s

- Simulation 2: creep and strain recovery
  A stress of 50 MPa is first applied on the material in 5 s. This stress is then held for 300 s before returning back to zero in 5 s. In a final stage, the material is kept at zero stress for another 300 s. The results of this simulation are presented in Figure II.16. Note that the computation is carried out with a constant time increment of 0.05 s

- Simulation 3: cyclic strain
  The material is subjected to a cyclic triangular strain signal. The latter oscillates between 0.04 and 0 with a frequency of 1 Hz. 20 cycles are performed. The results of this simulation are presented in Figure II.17. Note that the computation is carried out with a constant time increment of 0.005 s, i.e. 200 time increments per cycle.

- Simulation 4: cyclic stress
  The material is subjected to a cyclic triangular stress signal. The latter oscillates between 50 and 0 MPa with a frequency of 1 Hz. 20 cycles are performed. The results of this simulation are presented in Figure II.18. Note that the computation is carried out with a constant time increment of 0.005 s, i.e. 200 time increments per cycle.

First of all, in terms of energy balance (see Figures II.15g, II.16g, II.17g and II.18g), it can be noticed that the strain energy W_ε is well equal to the sum of the stored and dissipated energies, $\rho\psi$ and Φ, respectively. Moreover the dissipated energy always increases or remains constant ($\dot{\Phi} \geq 0$), which is well in accordance with the Clausius Duhem inequality (II.22).

In the simulation 1 (see Figure II.15), during a relaxation stage, the stress gradually decreases under the action of a constant strain (see Figures II.15a, II.15b and II.15c). The material exhibits an energy transfer as the strain energy W_ε does not evolve, while the stored energy $\rho\psi$ is converted into dissipated energy Φ (see Figure II.15g). This energy transfer is mainly caused by the viscoelastic mechanism. The latter acts during the time necessary for all the Kelvin-Voigt branches to reach an equilibrium (see Figure II.15d). The development of the viscoplastic strain and damage mainly occurs during the first loading stage. However,

it can be noticed that, a small amount of viscoplasticity and damage is also generated at the beginning of the first relaxation, until the stress decreases below the current yield threshold: namely when $f < 0$ (see Figures II.15d and II.15e).

In the simulation 2 (see Figure II.16), during the creep stage, the strain gradually increases under the action of a constant stress (see Figures II.16a, II.16b and II.16c). All the dissipative mechanisms (viscoelasticity, viscoplasticity and damage) are active and evolve according to the constant applied stress (see Figures II.16d and II.16e). Over this stage, the material both stores and dissipates energy ($\rho\dot{\psi} > 0$ and $\dot{\Phi} > 0$). In the next stage, the material is unloaded and left free of stress. The elastic strain as well as the 1^{st} viscoelastic strain are quasi-instantaneously recovered, whereas a certain amount of time is necessary to recover the other viscoelastic strains (see Figure II.16d). Note that the viscoelastic strain of the 1^{st} Kelvin-Voigt branch is quasi-instantaneously recovered because its characteristic time is far lower than the time length of the unloading. During the strain recovery stage, the material exhibits an energy transfer as the strain energy W_e does not evolve, while the stored energy $\rho\psi$ is converted into dissipated energy Φ (see Figure II.16g). At the end of the simulation, the quasi totality of the viscoelastic strains have returned back to zero and only the viscoplastic strain remains along with its associated stored energy $\rho\psi_p$ (see Figures II.16d and II.16g). The latter is irrecoverable, as explained in Section 2.2.2.

In the simulation 3 (see Figure II.17), when a cyclic strain is applied on the material, an overall relaxation is observed as the stress decreases from one cycle to another under the action of the mean strain. Similarly, in the simulation 4 (see Figure II.18), when a cyclic stress is applied on the material, an overall creep is observed as the strain increases from one cycle to another under the action of the mean stress. This behaviour is partially caused by the growth in viscoplastic strain and damage acting when the stress exceeds the current yield threshold, namely when $f < 0$. This actually occurs at each cycle, when the stress approaches its top level, creating an accumulation of viscoplastic strain and damage throughout the whole cyclic loading. Besides the coupled viscoplasticity and damage, this overall relaxation or creep is also caused by viscoelasticity and more especially by the Kelvin-Voigt branches having a characteristic time far greater than the time length of a single cycle, the 2^{nd}, 3^{rd} and 4^{th} Kelvin-Voigt branches in the present case. These branches are over-damped as they do not have the time to significantly move within a cycle but only do on a larger range of time. Oppositely, the 1^{st} Kelvin-Voigt branch is under-damped as it characteristic time is far lower than the time length of a single cycle. Consequently, this branch has the time to significantly move within a cycle. Nevertheless, the small retard effect of the 1^{st} Kelvin-Voigt branch generates a phase shift in the oscillating material response. This can be clearly observed in the stress-strain space by the hysteresis loops. It must be noticed that, after a certain number of cycles, most of the dissipation comes from this under-damped viscoelastic mechanism and that the amount of dissipated energy is almost the same at each cycle.

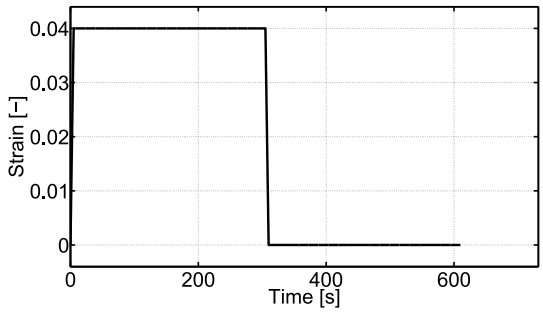

(a) Applied strain (ε_{11}) vs. time

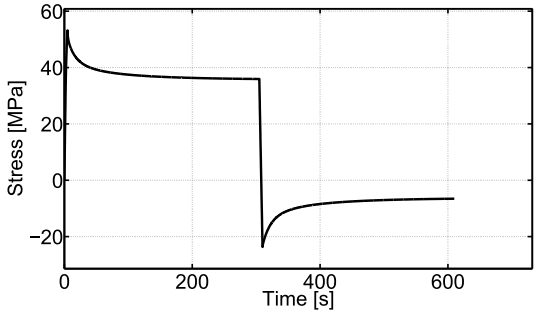

(b) Stress response (σ_{11}) vs. time

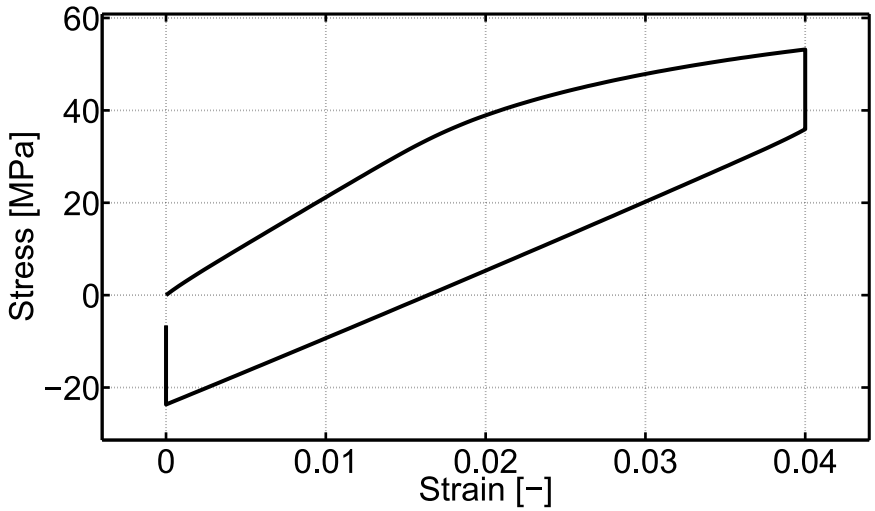

(c) Stress (σ_{11}) vs. strain (ε_{11})

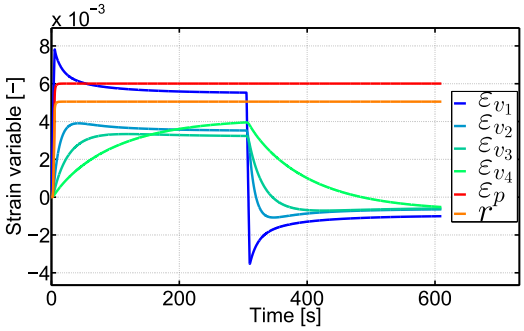

(d) Strain internal state variables (component 11 of the $\boldsymbol{\varepsilon_{v_i}}$ and $\boldsymbol{\varepsilon_p}$, and r) vs. time

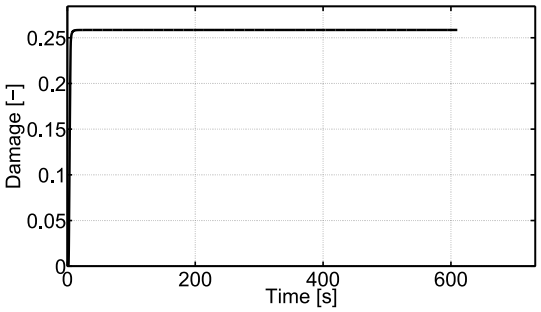

(e) Damage (D) vs. time

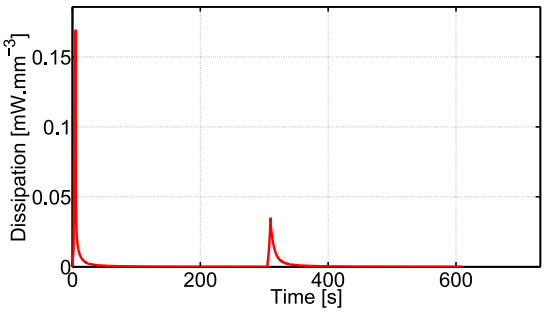

(f) Dissipation ($\dot{\Phi}$) vs. time

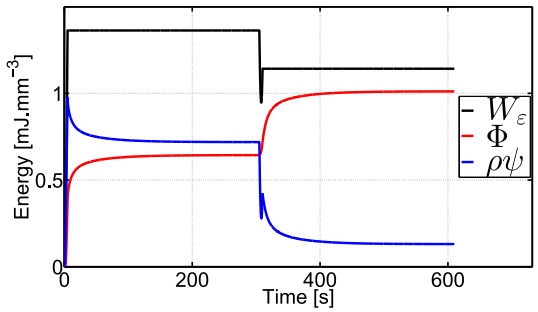

(g) Strain, dissipated and stored energies (W_ε, Φ and $\rho\psi$, respectively) vs. time

Figure II.15: Simulation 1: stress relaxation.

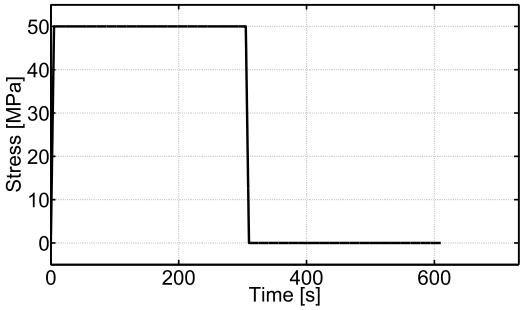

(a) Applied stress (σ_{11}) vs. time

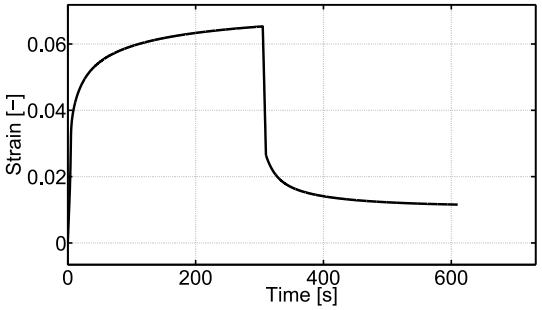

(b) Strain response (ε_{11}) vs. time

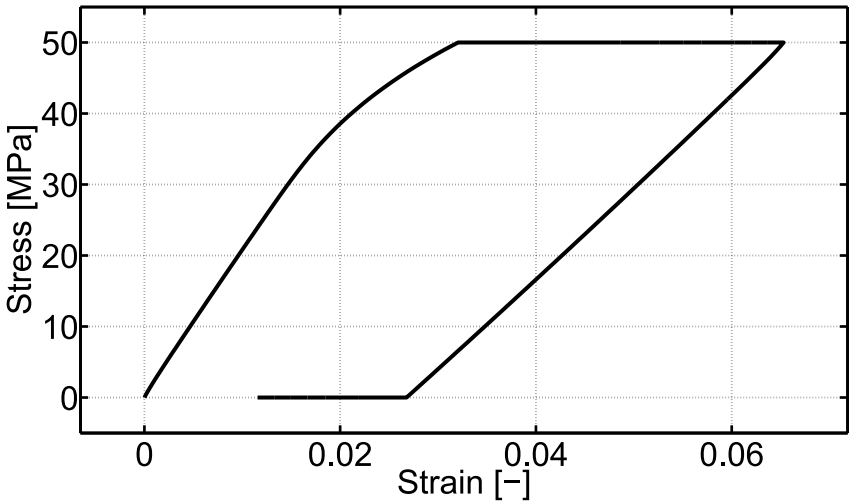

(c) Stress (σ_{11}) vs. strain (ε_{11})

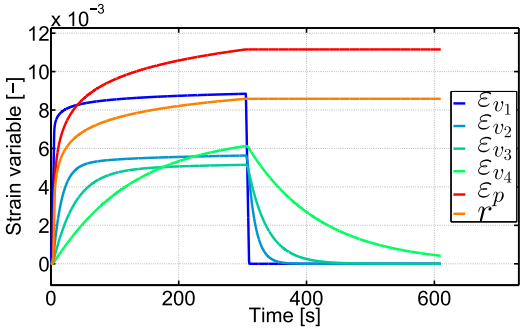

(d) Strain internal state variables (component 11 of the $\boldsymbol{\varepsilon}_{\boldsymbol{v}_i}$ and $\boldsymbol{\varepsilon}_{\boldsymbol{p}}$, and r) vs. time

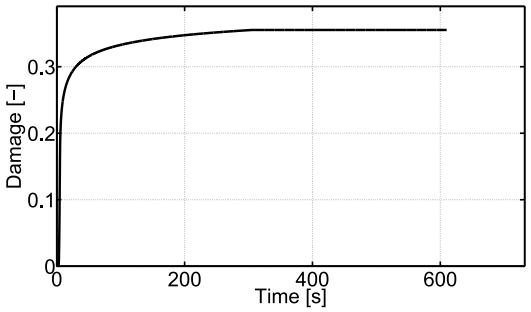

(e) Damage (D) vs. time

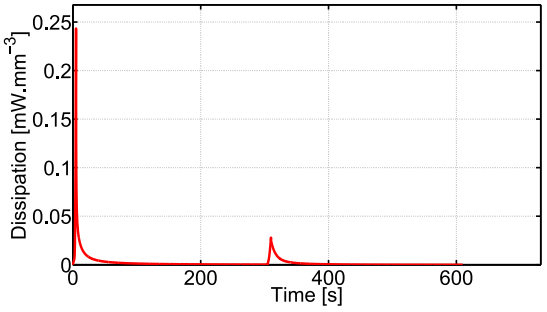

(f) Dissipation ($\dot{\Phi}$) vs. time

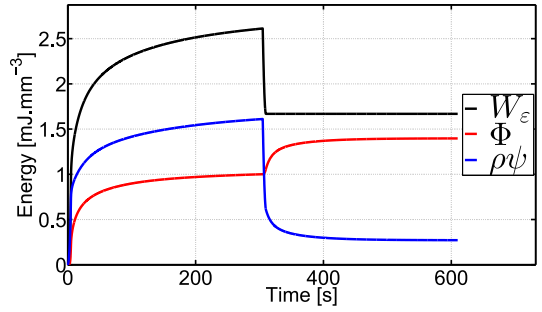

(g) Strain, dissipated and stored energies (W_ε, Φ and $\rho\psi$, respectively) vs. time

Figure II.16: Simulation 2: creep and strain recovery.

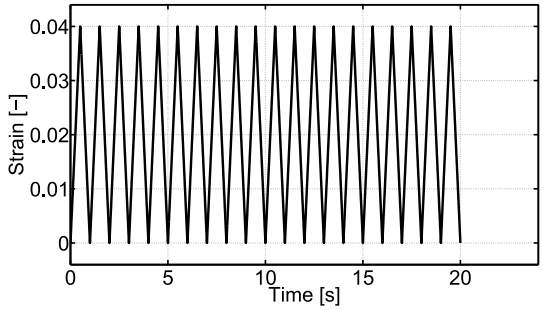

(a) Applied strain (ε_{11}) vs. time

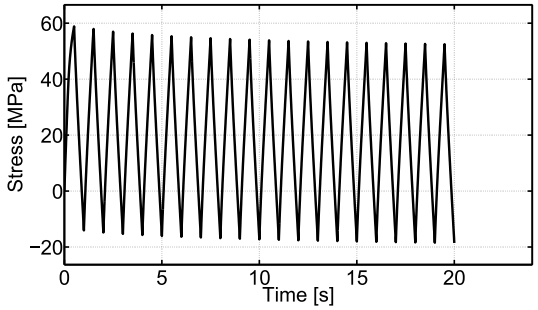

(b) Stress response (σ_{11}) vs. time

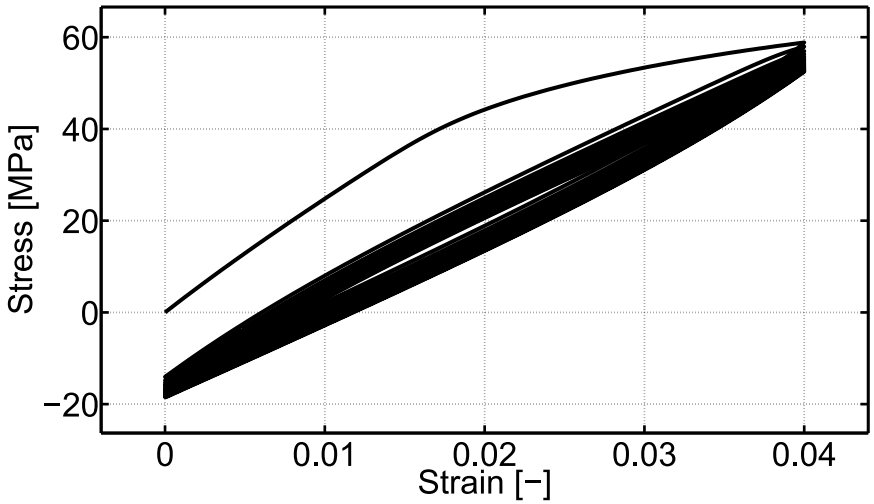

(c) Stress (σ_{11}) vs. strain (ε_{11})

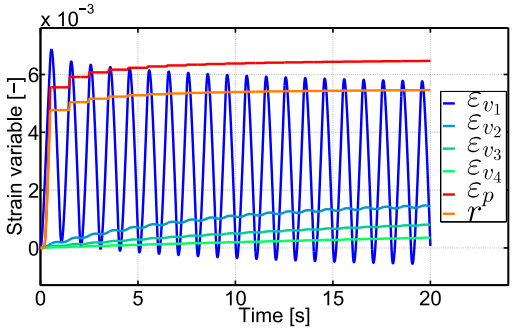

(d) Strain internal state variables (component 11 of the $\boldsymbol{\varepsilon_{v_i}}$ and $\boldsymbol{\varepsilon_p}$, and r) vs. time

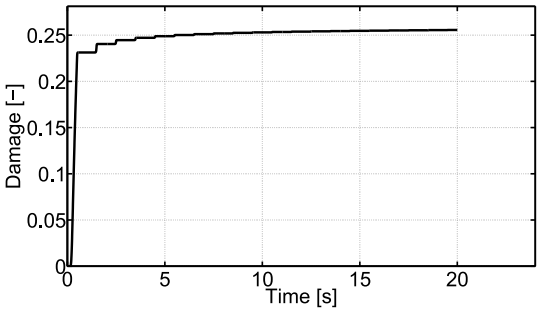

(e) Damage (D) vs. time

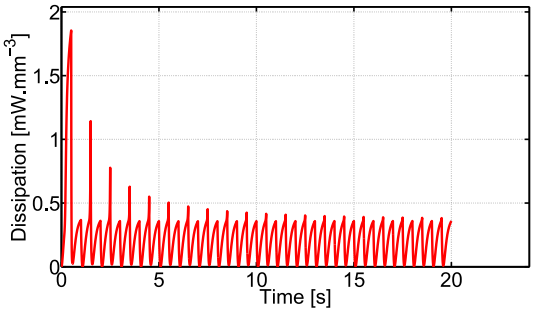

(f) Dissipation ($\dot{\Phi}$) vs. time

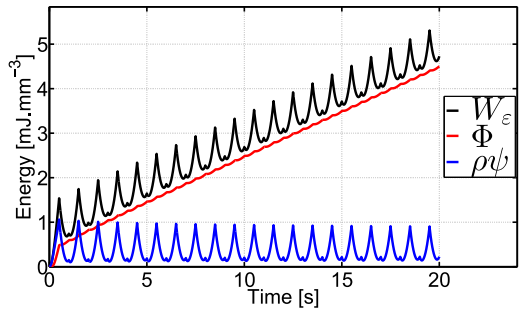

(g) Strain, dissipated and stored energies (W_ε, Φ and $\rho\psi$, respectively) vs. time

Figure II.17: Simulation 3: cyclic strain.

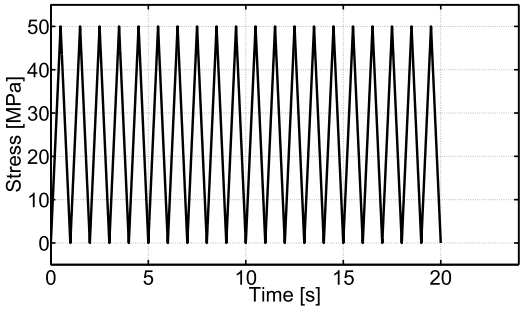

(a) Applied stress (σ_{11}) vs. time

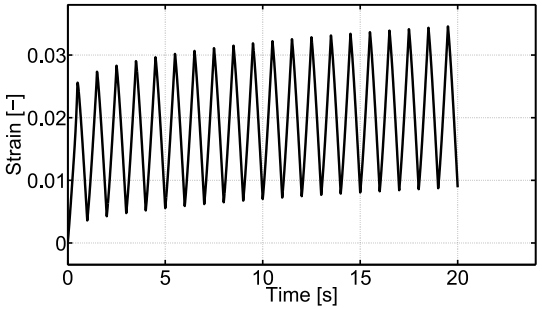

(b) Strain response (ε_{11}) vs. time

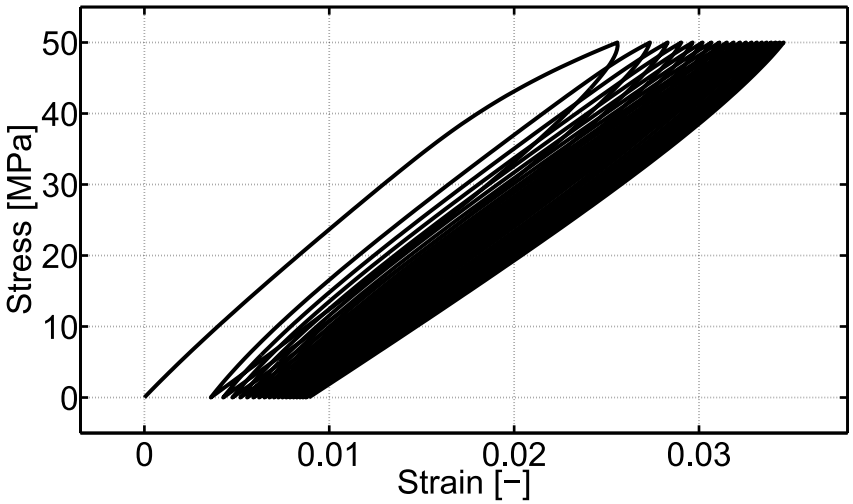

(c) Stress (σ_{11}) vs. strain (ε_{11})

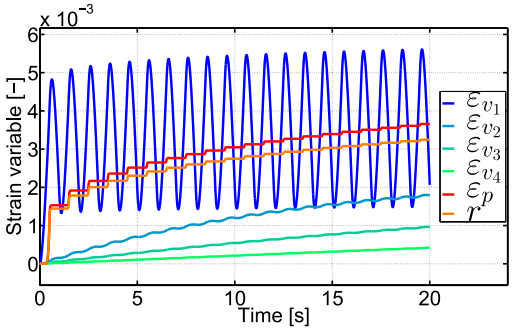

(d) Strain internal state variables (component 11 of the $\boldsymbol{\varepsilon}_{\boldsymbol{v}_i}$ and $\boldsymbol{\varepsilon}_{\boldsymbol{p}}$, and r) vs. time

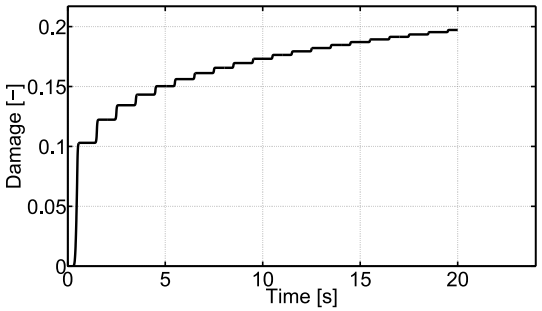

(e) Damage (D) vs. time

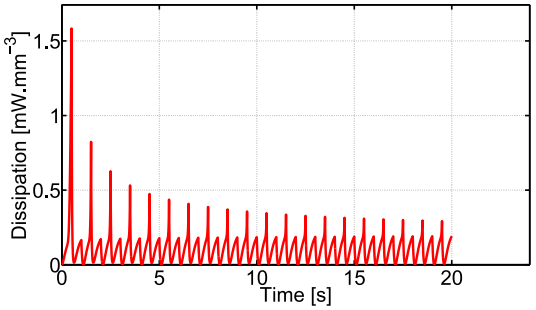

(f) Dissipation ($\dot{\Phi}$) vs. time

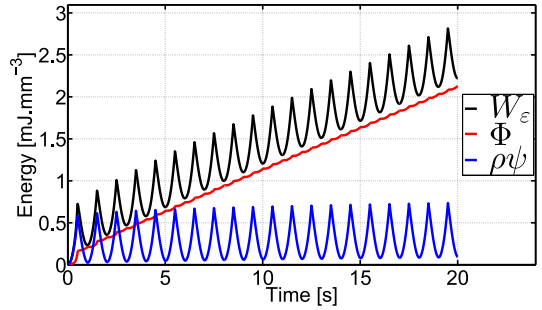

(g) Strain, dissipated and stored energies (W_ε, Φ and $\rho\psi$, respectively) vs. time

Figure II.18: Simulation 4: cyclic stress.

5.2 Structural FE application and model capabilities

To illustrate the capabilities of model in simulating the mechanical response of a 3D body through the FE method, the present section deals with an example of FE analysis carried out on a bracket (see Figure II.19a). The latter is made of polyamide 6-6 with the previously identified parameters (see Table II.4). The bottom face of the bracket is clamped, while a cyclic loading along the x direction is applied on the holes located at the top (see Figure II.19c). This load is set up on a master node that lies at the centre of the hole and is linked to it using a tie constraint. Due to symmetry, half of the geometry is represented and appropriate boundary conditions are set on the plane of symmetry, i.e. the displacements perpendicular to the plane of symmetry are set to zero. Note that the mesh, shown in Figure II.19b, contains 43997 nodes and 28213 second order tetrahedral elements (C3D10 in *ABAQUS*). A cycle of loading is defined as follows: first, a load of -5 kN is applied in 0.5 s on the bracket (the half represented). This load is subsequently held for 2 s before being released in 0.5 s. In a last step, the bracket is left free of loading during another 2 s. This cycle is repeated 10 times (see Figure II.20a). The computation is carried out with a constant time increment of 0.01 s, i.e. 500 time increments per cycle.

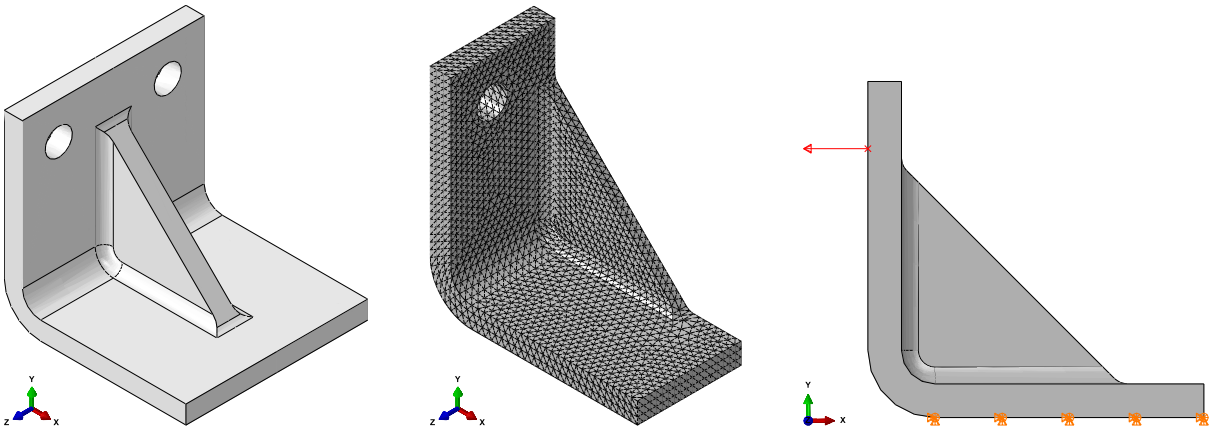

(a) Bracket (dimensions in mm: $200 \times 200 \times 200$)

(b) Meshed bracket, half of the structure is represented due to symmetry

(c) Loading and boundary conditions applied on the bracket

Figure II.19: Example of FE analysis: Bracket.

First of all, it is worth noticing that the proposed implicit implementation and especially the formulation of the tangent operator (see Section 3) show a good efficiency as for each time increment, only one or two iterations are necessary to reach the global convergence.

Figure II.20b shows the displacement of the master node, on which the load is applied. Thus, the creep effects previously described (see Section 5.1) can be observed at the scale of the structure. At first, the bracket exhibits a rapid creep response, as the displacement of the master node gradually increases each time the load is held constant within each cycle. This rapid creep is predominately triggered by the Kelvin-Voigt branches having short characteristic times compared to the time length of a single cycle. Afterwards, the bracket is also subjected to a secondary creep occurring throughout the repeated cycles the bracket, as the displacement also increases from one cycle to another. This secondary creep is mainly caused by the Kelvin-Voigt Branches having a long characteristic times. As shown in Figure II.21, the viscoplasticity and damage initiate at the most stressed location of the structure. They gradually grow and spread around this location as the stress exceeds

the yield threshold. This growth acts at each time the structure is loaded, creating an accumulation of viscoplastic strain and damage throughout the repeated cycles.

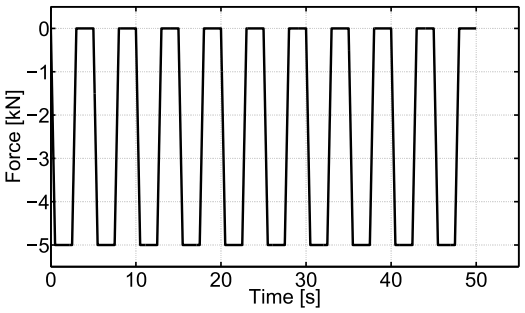

(a) Applied force along the x axis vs. time

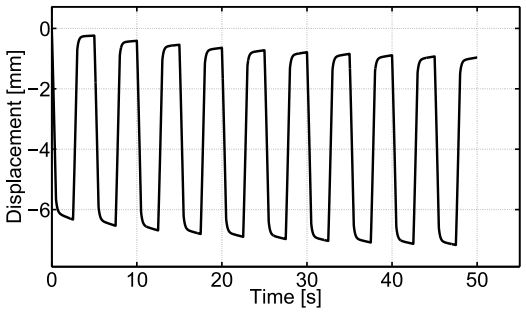

(b) Resulting displacement along the x axis vs. time

Figure II.20: Applied force and resulting displacement of the master node (located at the centre of the hole).

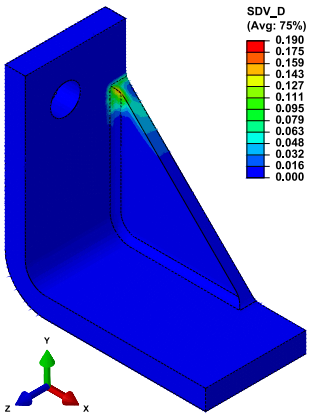

(a) Damage (D) field at the end of the 1^{st} cycle ($t = 5$ s)

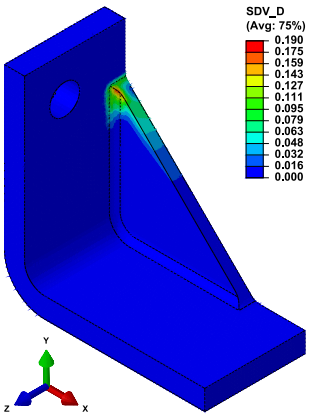

(b) Damage (D) field at the end of the 3^{rd} cycle ($t = 15$ s)

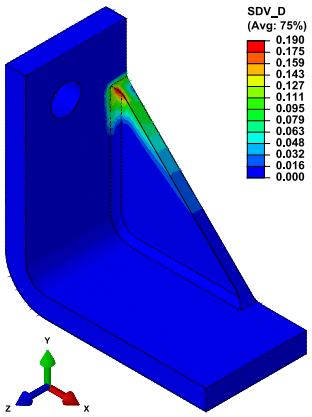

(c) Damage (D) field at the end of the 10^{th} cycle ($t = 50$ s)

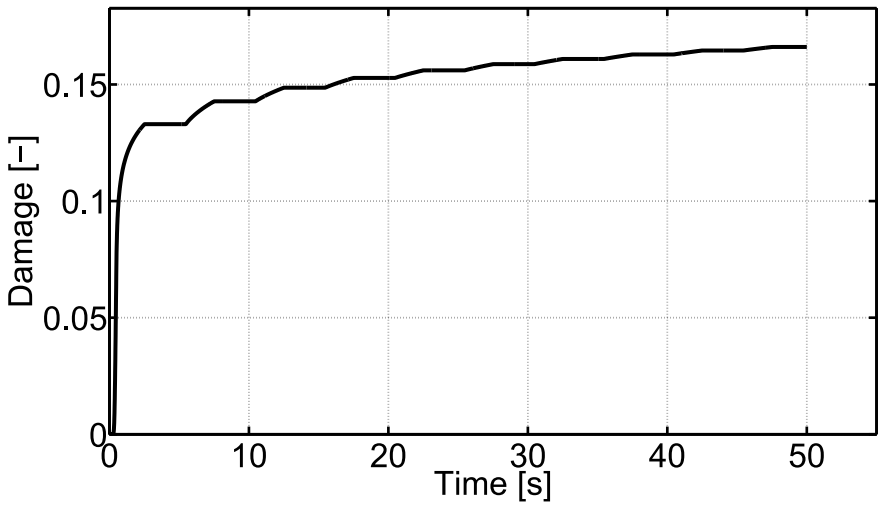

(d) Damage (D) vs. time at the most stressed integration point

Figure II.21: Evolution of damage (D) within the bracket.

6 Conclusions

In this chapter, a phenomenological multi-mechanisms constitutive model for thermoplastic polymers has been proposed. The latter is intended to be used as matrix phase in the multi-scale approach for the whole woven composite in Chapter IV. The constitutive equations are formulated in a proper thermodynamical formalism and account for viscoelasticity, viscoplasticity and ductile damage. The viscoelastic contribution is based on a series of Kelvin-Voigt branches, enabling to represent time-dependent effects (creep and relaxation), acting on several time length. The damage mechanism is based on the well-known concept of effective stress, which permits, in a straightforward manner, to include anelastic deformation mechanisms through a coupled formulation. Moreover, the damage is called as ductile as its evolution is directly governed by the viscoplasticy.

The constitutive equations of the model are provided along with an implicit resolution scheme based on the "convex cutting plane" form of the "return mapping algorithm" as well as the formulation of the tangent operator. The latter is implemented into the FE solver *ABAQUS/Standard*.

The proposed model is successfully identified for the polyamide 6-6 through a suitable experimental program including several types of tests, namely: monotonic, creep and cyclic tests. The good agreement between experimental and numerical results demonstrates the capabilities of the model to capture, with a single set of parameters, the mechanical response of thermoplastic polymers under various conditions and especially cyclic loading.

Examples of simulations where the material is subjected to complex uni-axial loading conditions have been performed in order to provide a better understanding of the model and to identify the influence of each non-linear mechanism (viscoelasticity, viscoplasticity and damage). These analyses highlighted the importance of the multi-mechanism formulation to capture the time-dependent response of thermoplastic polymers, especially under cyclic loading. Indeed, the coupled viscoplasticity and damage as well as the Kelvin-Voigt branches having a long characteristic time, all together, mainly enable to capture the accumulation of strain and damage throughout repeated cycles. Oppositely, the Kelvin-Voigt branches having a short characteristic time are more appropriate to represent the hysteresis loops occurring among each single cycle, and produce most of the dissipation over a long period of time. Finally, the capabilities of the proposed model along with its numerical implementation are demonstrated through an example of FE analysis.

Chapter III

Hybrid micromechanical-phenomenological modelling of anisotropic damage and anelasticity induced by micro-cracks in the yarns

Contents

The content of the present chapter was the scope of a peer-reviewed paper entitled **"Hybrid micromechanical-phenomenological modelling of anisotropic damage and anelasticity induced by micro-cracks in unidirectional composites"** published in *Composite Structures* [165].

1 Introduction

As previously mentioned, at the microscopic scale a yarn is an assembly of fibres as a bundle. The yarns are then composed of numerous unidirectionally oriented fibres embedded in the matrix. Consequently, their behaviour can be considered as equivalent to the one of a unidirectional composite. In such materials, the damage mechanisms are governed by the specific arrangement of the reinforcement, leading to an anisotropic evolution of their mechanical response. In the case of unidirectional composites reinforced with stiff fibres (e.g., glass or carbon), the longitudinal behaviour exhibits a linear elastic response up to the material brittle failure due to fibres breakage. The presence of continuous fibrous reinforcements actually prevents the appearance of others damage mechanisms in the fibre direction. The transverse tension and the in-plane shear responses generally exhibit a progressive stiffness degradation prior to failure. Indeed, the transverse damage is induced by the appearance of a diffuse micro-crack network that initiates by debonding at the fibre/matrix interfaces (Figure III.1a) and propagates by coalescence (Figure III.1b).

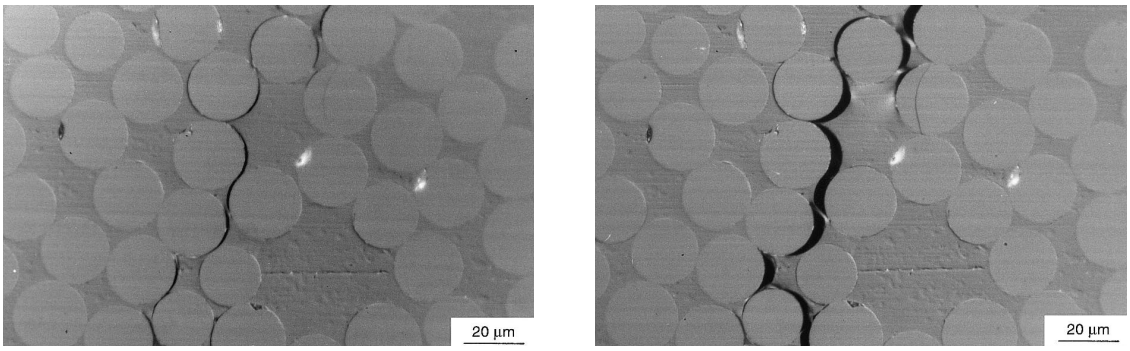

(a) Initiation of the micro-cracks by debonding of the fibre/matrix interfaces

(b) Coalescences turning into micro-cracks

Figure III.1: Transverse damage mechanism in unidirectional composites [64].

Most of the modelling efforts have therefore focused on the definition of damage variables related to the previously described behaviour. Continuum Damage Mechanics (CDM) along with the concept of effective stress formulated within the framework of thermodynamics [109, 110] is particularly adapted for such a description. Initially developed in the context of isotropic material response, the CDM was adapted to the anisotropic case of unidirectional composites [106, 95, 93, 5, 25, 26, 119]. The effects of micro-cracks are usually accounted through the introduction of several damage state variables that directly define the reduction of the material stiffness. In addition, the anelastic mechanisms are generally described by a plastic-like strain tensor whose evolution is governed by a yield function written in the effective stress space in order to account for the coupling with the damage. Nevertheless, if the use of CDM is convenient and straightforward in the isotropic case, its extension to anisotropy may lead to the following issues:

- Several damage state variables are assumed to capture properly the anisotropic evolution of the material response. Each variable is associated with an evolution equation that potentially depends on several field variables (temperature, stress) where multiaxial couplings may be included. Such a modelling strategy leads to an important number of material parameters with additional difficulties regarding their identification.

- The definition of the effective stress tensor is required to account for coupling effects with the anelastic mechanisms. In the case of anisotropic materials the physical meaning of the effective stress is not obvious [110].

To overcome those issues, the evolution of the mechanical response of such composites can be rather based on the evolution of the micro-crack network itself through micromechanics [105, 104, 155].

The main objective of this chapter is to propose a computationally efficient, hybrid micromechanical-phenomenological model that has a reduced number of internal variables. The evolution of these variables is controlled by criteria that depend on local stress estimations, providing hence a physically based description of the damage mechanisms.

The model proposed in this chapter accounts for anisotropic damage and anelasticity induced by micro-cracks in unidirectional composites. The damage is introduced through a micromechanical description of a Representative Volume Element (RVE) containing micro-cracks. Those defects are quantified by a unique internal state variable whose evolution is governed by a local stress criterion. The anisotropic evolution of the stiffness as well as the connection between overall and local stress-strain fields are therefore determined using micromechanical relationships that are directly incorporated within the constitutive equations. In that sense, the proposed model is based on a hybrid micromechanical-phenomenological formulation [40, 201, 169]. A novelty of the proposed model consists in accounting for anelastic deformation mechanisms by introducing the concept of damage induced anelasticity, where permanent strains are assumed to be caused by non-closure effect of the micro-cracks. The constitutive equations are then expressed within the framework of thermodynamics of irreversible processes applied to the overall medium, describing its mechanical response under the small strain assumption and isothermal conditions.

Compared to classical CDM models for unidirectional composites [106, 95, 93, 5, 25, 26, 119], the present modelling strategy leads to a reduced number of parameters with a certain ease regarding their identification. Moreover, the hybrid micromechanical-phenomenological formulation brings a physical basis to the model, while its practical use remains as computationally efficient as any purely phenomenological approach.

This chapter is structured as follows: In Section 2, the constitutive equations, the thermodynamical framework and the micro-mechanical aspects of the proposed model are presented. Section 4 focuses on the identification strategy of the model parameters. The latter is illustrated from experimental data of a flax-epoxy unidirectional composite taken from the literature. Section 5 presents illustrative examples of simulations (including a 3D FE analysis) where the material is subjected to complex loading conditions. To finish, Section 6 summarizes the main conclusions related to this chapter.

2 Constitutive equations and thermodynamical framework

The main idea of the proposed model is to link, through micromechanical concepts, the overall stiffness reduction of a unidirectional composite with the evolution of a single scalar state variable γ_c that quantifies the state of the involved damage mechanism, the oriented micro-cracking in the present case. This stiffness reduction is represented under the form of a fourth order tensor $\mathbb{D}(\gamma_c)$ that gradually lowers the initial stiffness tensor $\mathbb{C}_\mathbf{0}$ of the material, the latter having transversely isotropic properties as it represents the elastic behaviour of the undamaged unidirectional composite (initial material). The tensor $\mathbb{D}(\gamma_c)$ is evaluated by homogenization of the initial material in which a micro-crack density γ_c is introduced (Figure III.2). The latter is defined as a void volume fraction created when the material is being damaged. Due to the microstructure arrangement, the micro-cracks are forced to propagate in a plane parallel to the fibre direction $\vec{x}_1$. Moreover, if the material is mainly loaded in plane stress (plane $\vec{x}_1, \vec{x}_2$) as it is often the case, then the propagation plane of the micro-cracks can be considered as being perpendicular to the second direction $\vec{x}_2$ and consequently always oriented in the same plane (Figure III.2).

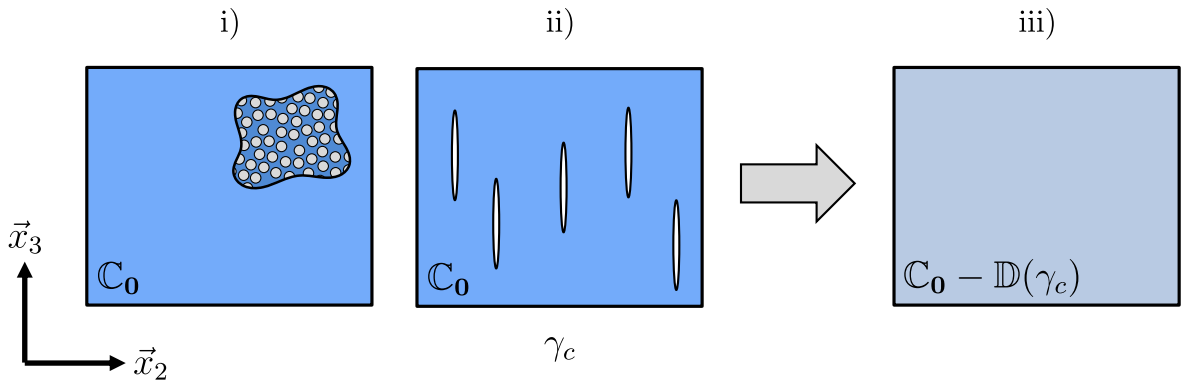

Figure III.2: i) Initial state: transversely isotropic. ii) Damaged state: introduction of a micro-crack density γ_c (void volume fraction) in the RVE. iii) Evaluation of the stiffness reduction induced by γ_c by homogenization.

Damage in such type of materials generally brings about permanent strains due to the micro-cracks non-closure and the resultant sliding with friction [106, 95, 25, 26, 119]. In the present model, these damage induced permanent strains are phenomenologically described by an anelastic strain tensor denoted by $\boldsymbol{\varepsilon_s}$. The total strain is then expressed by summation of the elastic strain $\boldsymbol{\varepsilon_e}$ with the anelastic strain $\boldsymbol{\varepsilon_s}$:

$$\boldsymbol{\varepsilon} = \boldsymbol{\varepsilon_e} + \boldsymbol{\varepsilon_s}. \tag{III.1}$$

The observable state variable of the model is the total strain $\boldsymbol{\varepsilon}$ while the internal state variables are γ_c and $\boldsymbol{\varepsilon_s}$. The elastic strain $\boldsymbol{\varepsilon_e}$ is not considered as a state variable but, for convenience, is expressed as the difference between the total strain and the anelastic strain.

2.1 State laws

According to the framework of thermodynamics [67, 68, 69, 109, 33] , which is briefly described in Appendix B, the state laws are based on a state potential. For the proposed

model, the Helmholtz free energy is chosen to describe the energetic state of the material. The latter is formulated as a stored energy function of the state variables:

$$\rho\psi(\boldsymbol{\varepsilon}, \boldsymbol{\varepsilon_s}, \gamma_c) = \frac{1}{2}(\boldsymbol{\varepsilon} - \boldsymbol{\varepsilon_s}) : \left[\mathbb{C}_\mathbf{0} - \mathbb{D}(\gamma_c)\right] : (\boldsymbol{\varepsilon} - \boldsymbol{\varepsilon_s}). \tag{III.2}$$

The associated thermodynamic variables, namely the stress $\boldsymbol{\sigma}$, $-\boldsymbol{\sigma}$ and the energy density release $-Y_c$, are obtained from the derivation of the potential with respect to the state variables $\boldsymbol{\varepsilon}$, $\boldsymbol{\varepsilon_s}$ and γ_c, respectively:

$$\boldsymbol{\sigma} = \rho\frac{\partial\psi}{\partial\boldsymbol{\varepsilon}} = \left[\mathbb{C}_\mathbf{0} - \mathbb{D}(\gamma_c)\right] : (\boldsymbol{\varepsilon} - \boldsymbol{\varepsilon_s}), \tag{III.3}$$

$$-\boldsymbol{\sigma} = \rho\frac{\partial\psi}{\partial\boldsymbol{\varepsilon_s}}, \tag{III.4}$$

$$-Y_c = \rho\frac{\partial\psi}{\partial\gamma_c} = -\frac{1}{2}(\boldsymbol{\varepsilon} - \boldsymbol{\varepsilon_s}) : \frac{\partial\mathbb{D}(\gamma_c)}{\partial\gamma_c} : (\boldsymbol{\varepsilon} - \boldsymbol{\varepsilon_s}). \tag{III.5}$$

The state and associated variables of the proposed model are summarized in Table III.1.

State variables		Associated variables
Observable	internal	-
$\boldsymbol{\varepsilon}$		$\boldsymbol{\sigma}$
	$\boldsymbol{\varepsilon_s}$	$-\boldsymbol{\sigma}$
	γ_c	$-Y_c$

Table III.1: State and associated variables of the proposed model.

2.2 Micromechanical aspects

Obviously, the state laws formulated on the previous section depend on the exact physical signification given to the micro-crack density γ_c along with the definition of the stiffness reduction tensor $\mathbb{D}(\gamma_c)$. As previously mentioned, in the proposed model it has been chosen to identify these quantities using micromechanical concepts [105, 104, 155, 40].

2.2.1 Definition of the stiffness reduction

By assuming micro-cracks as oriented quasi-flat ellipsoidal inclusions of void, an explicit expression of the stiffness tensor $\mathbb{D}(\gamma_c)$ can be obtained according to the void volume fraction γ_c, also referred as the micro-crack density [127, 128, 130, 202]. The voids represent the micro-discontinuities as a part of the material that is unable to sustain stress. This is taken into account by considering zero stiffness tensor for the void inclusions. Using mean-field approaches [172], the overall stiffness of the damaged composite, namely $\mathbb{C}_\mathbf{0} - \mathbb{D}(\gamma_c)$, is determined from a two-phases RVE consisting of a volume fraction γ_c of void inclusions

(with zero stiffness) embedded in a reference medium (the virgin part of the material in the present case). This gives:

$$\mathbb{C}_{\mathbf{0}} - \mathbb{D}(\gamma_c) = (1-\gamma_c)\mathbb{C}_{\mathbf{0}} : \mathbb{A}_{\mathbf{0}}(\gamma_c). \tag{III.6}$$

In the above equation, $\mathbb{A}_{\mathbf{0}}(\gamma_c)$ is the strain localisation tensor in the virgin part of the material that is to be defined. The strain localisation in the void inclusions is represented by the tensor $\mathbb{A}_{\boldsymbol{c}}(\gamma_c)$. It is well established [172] that, for a two-phases RVE, one can write the following relationship between the strain localisation tensors:

$$(1-\gamma_c)\mathbb{A}_{\mathbf{0}}(\gamma_c) + \gamma_c\mathbb{A}_{\boldsymbol{c}}(\gamma_c) = \mathbb{I}. \tag{III.7}$$

According to the micromechanical scheme of Mori-Tanaka [137], the strain localisation in the inclusions $\mathbb{A}_{\boldsymbol{c}}(\gamma_c)$ is calculated from the strain localisation in the reference medium $\mathbb{A}_{\mathbf{0}}(\gamma_c)$, the latter is then directly deduced from (III.7):

$$\mathbb{A}_{\boldsymbol{c}}(\gamma_c) = \mathbb{T}_{\boldsymbol{c}} : \mathbb{A}_{\mathbf{0}}(\gamma_c) \qquad \text{and} \qquad \mathbb{A}_{\mathbf{0}}(\gamma_c) = \big(\mathbb{I} + \gamma_c(\mathbb{T}_{\boldsymbol{c}} - \mathbb{I})\big)^{-1}, \tag{III.8}$$

where $\mathbb{T}_{\boldsymbol{c}}$ is the interaction tensor obtained from the solution of [59]. For void inclusions with zero stiffness, this interaction tensor can be easily expressed as:

$$\mathbb{T}_{\boldsymbol{c}} = \big(\mathbb{I} - \mathbb{S}_{\boldsymbol{E}}\big)^{-1}. \tag{III.9}$$

$\mathbb{S}_{\boldsymbol{E}}$ is the well-known Eshelby tensor [59] that depends on the stiffness tensor of the reference medium $\mathbb{C}_{\mathbf{0}}$ and the relative dimensions a_1, a_2 and a_3 (Figure III.3) of the void ellipsoidal inclusions. Because of the anisotropic properties of the reference medium ($\mathbb{C}_{\mathbf{0}}$), the Eshelby tensor $\mathbb{S}_{\boldsymbol{E}}$ must be numerically evaluated using the methodology proposed by [66] that is briefly presented in Appendix F. Finally, the introduction of (III.7) and (III.8) into (III.6) leads to the following formulation of the overall stiffness tensor of the damaged material, highlighting the expression of the stiffness reduction tensor $\mathbb{D}(\gamma_c)$:

$$\mathbb{C}_{\mathbf{0}} - \mathbb{D}(\gamma_c) = \mathbb{C}_{\mathbf{0}} - \gamma_c\mathbb{C}_{\mathbf{0}} : \mathbb{T}_{\boldsymbol{c}} : \mathbb{A}_{\mathbf{0}}(\gamma_c), \tag{III.10}$$

thus,

$$\mathbb{D}(\gamma_c) = \gamma_c\mathbb{C}_{\mathbf{0}} : \mathbb{T}_{\boldsymbol{c}} : \mathbb{A}_{\mathbf{0}}(\gamma_c). \tag{III.11}$$

Besides computing the stiffness reduction, the strain localisation tensors (III.8) allow to define the local strain fields, and more especially the one in the virgin part of the material:

$$\boldsymbol{\varepsilon}_{\mathbf{0}}(\boldsymbol{\varepsilon}, \boldsymbol{\varepsilon}_{\boldsymbol{s}}, \gamma_c) = \mathbb{A}_{\mathbf{0}}(\gamma_c) : (\boldsymbol{\varepsilon} - \boldsymbol{\varepsilon}_{\boldsymbol{s}}). \tag{III.12}$$

Similarly, the local stress in the virgin part of the material $\boldsymbol{\sigma}_{\mathbf{0}} = \mathbb{C}_{\mathbf{0}} : \boldsymbol{\varepsilon}_{\mathbf{0}}$ can be written either in terms of strain $\boldsymbol{\varepsilon}$, or in terms of stress $\boldsymbol{\sigma}$, if (III.3) is substituted:

$$\boldsymbol{\sigma}_{\mathbf{0}}(\boldsymbol{\varepsilon}, \boldsymbol{\varepsilon}_{\boldsymbol{s}}, \gamma_c) = \mathbb{C}_{\mathbf{0}} : \mathbb{A}_{\mathbf{0}}(\gamma_c) : (\boldsymbol{\varepsilon} - \boldsymbol{\varepsilon}_{\boldsymbol{s}}) \qquad \text{or} \qquad \boldsymbol{\sigma}_{\mathbf{0}}(\boldsymbol{\sigma}, \gamma_c) = \mathbb{B}_{\mathbf{0}}(\gamma_c) : \boldsymbol{\sigma}, \tag{III.13}$$

where the stress localisation tensor $\mathbb{B}_{\mathbf{0}}(\gamma_c)$ is obtained by introducing (III.3) into (III.13) while considering (III.6). This gives:

$$\mathbb{B}_{\mathbf{0}}(\gamma_c) = \mathbb{C}_{\mathbf{0}} : \mathbb{A}_{\mathbf{0}}(\gamma_c) : \big[\mathbb{C}_{\mathbf{0}} - \mathbb{D}(\gamma_c)\big]^{-1} = \frac{\mathbb{I}}{1-\gamma_c}. \tag{III.14}$$

From equations (III.8) and (III.14), it is easy to verify that, when the material is undamaged: $\mathbb{A}_{\mathbf{0}}(\gamma_c = 0) = \mathbb{B}_{\mathbf{0}}(\gamma_c = 0) = \mathbb{I}$, $\boldsymbol{\varepsilon}_{\mathbf{0}} = (\boldsymbol{\varepsilon} - \boldsymbol{\varepsilon}_{\boldsymbol{s}})$ and $\boldsymbol{\sigma}_{\mathbf{0}} = \boldsymbol{\sigma}$.

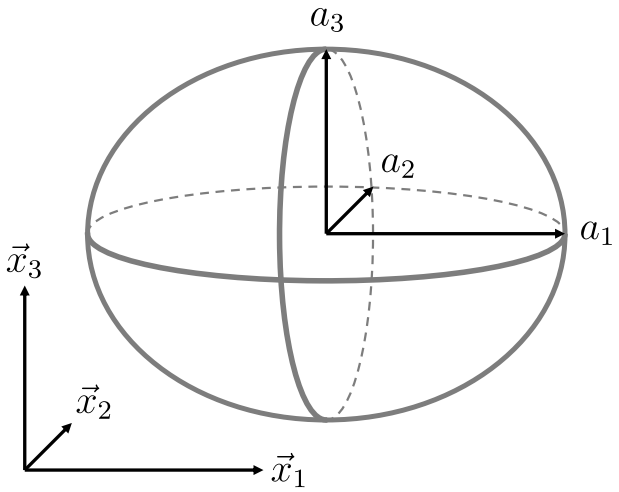

Figure III.3: Ellipsoid with its relative dimensions.

Note that the interaction tensor $\mathbb{T}_{\boldsymbol{c}}$ is directly calculated from the Eshelby tensor $\mathbb{S}_{\boldsymbol{E}}$ in (III.9) and consequently does not depend on any field variable. Therefore, $\mathbb{T}_{\boldsymbol{c}}$ can be considered as an input of the model and is hence computed only one time prior to any analysis. Such consideration is particularly important since the numerical evaluation of the Eshelby tensor is a computationally expensive task that should be avoided in a numerical process.

It is also important to point out that, although the tensors $\mathbb{S}_{\boldsymbol{E}}$, $\mathbb{T}_{\boldsymbol{c}}$ and $\mathbb{A}_{\boldsymbol{0}}$ do not have the major symmetry, the tensor $\mathbb{D}(\gamma_c)$ always does. Indeed, for a two-phase RVE (composite and voids in the present case) the major symmetry of the homogenized stiffness tensor is ensured with the micromechanical scheme of Mori-Tanaka [18]. This point is essential because it allows the definition of a thermodynamic state potential, as formulated in (III.2) for the proposed model.

As mentioned in the introduction (Section 1), CDM-based model needs several damage state variables to consider anisotropic damage. With the proposed approach the definition of damage is provided through a micromechanical description. The anisotropic stiffness reduction induced by the micro-cracks is computed as a tensorial function which directly depends on the micro-crack density γ_c. The latter is denoted as an internal state variable, which has a physical signification from a micromechanical point of view.

2.2.2 Geometrical aspects of the voids

The orientation as well as the quasi-flat aspect of the void ellipsoidal inclusions imply specific conditions on their relative dimensions (Figure III.3). Indeed, the flattening ratios δ_1 and δ_3 must tend to infinite values:

$$\delta_1 = \frac{a_1}{a_2} \to \infty, \qquad \delta_3 = \frac{a_3}{a_2} \to \infty. \tag{III.15}$$

In practice, large enough values of flattening ratios are utilized for the numerical evaluation of the stiffness reduction. The latter is also influenced by the micro-cracks shape ratio δ_c, where

$$\delta_c = \frac{\delta_1}{\delta_3} = \frac{a_1}{a_3}. \tag{III.16}$$

If $\delta_c = 1$, then the shape of the micro-cracks is perfectly circular (penny shape). If $\delta_c \to \infty$, then the micro-cracks get across the volume element along $\vec{x}_1$ (see Figure III.4a), whereas in the opposite case, when $\delta_c \to 0$, the micro-cracks get across the volume element along $\vec{x}_3$ (see Figure III.4b).

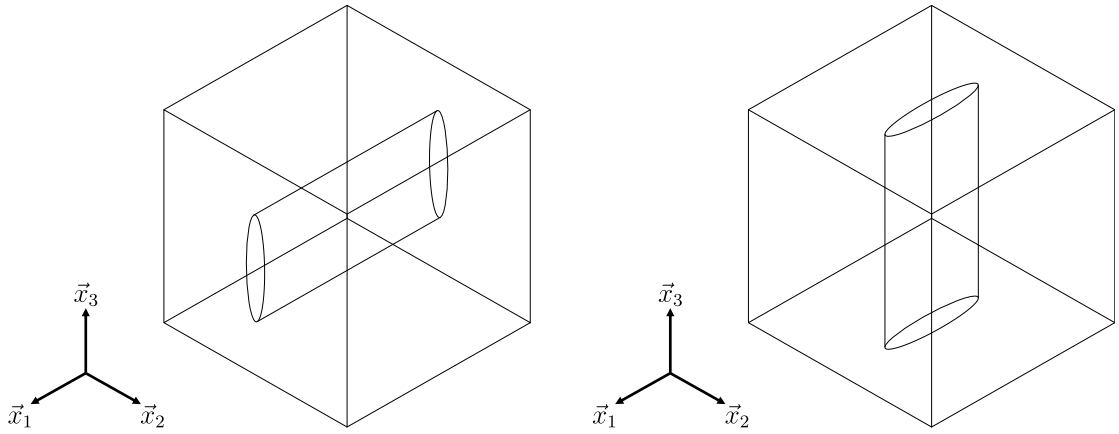

(a) crossing micro-crack along $\vec{x}_1$ ($\delta_c \to \infty$) (b) crossing micro-crack along $\vec{x}_3$ ($\delta_c \to 0$)

Figure III.4: Illustration of the crossing micro-cracks configurations.

As an example, the stiffness reduction tensor $\mathbb{D}(\gamma_c)$ has been determined (Figures III.5 and III.6) for several configurations of void inclusions, as detailed in Table III.2. For these computations, stiffness properties taken from a flax-epoxy unidirectional composite have been considered. These properties have been extracted from the experimental data of [119] as shown later in Section 4. The initial stiffness tensor of this material, namely $\mathbb{C}_\mathbf{0}$, is presented below with the help of the Voigt notation.

$$\mathbb{C}_\mathbf{0} = \begin{pmatrix} 21975 & 2678 & 2678 & 0 & 0 & 0 \\ & 5711 & 1942 & 0 & 0 & 0 \\ & & 5711 & 0 & 0 & 0 \\ & & & 2100 & 0 & 0 \\ & & & & 2100 & 0 \\ \text{sym.} & & & & & 1885 \end{pmatrix} \text{ MPa.} \tag{III.17}$$

Note that $\mathbb{C}_\mathbf{0}$ is well transversely isotropic, since $C_{0_{2222}} = C_{0_{3333}}$, $C_{0_{1122}} = C_{0_{1133}}$, $C_{0_{1212}} = C_{0_{1313}}$ and $C_{0_{2323}} = \frac{1}{2}(C_{0_{2222}} - C_{0_{2233}}) = \frac{1}{2}(C_{0_{3333}} - C_{0_{2233}})$.

configuration of the void inclusions	flattening ratios		shape ratio
	$\delta_1 = \frac{a_1}{a_2}$	$\delta_3 = \frac{a_3}{a_2}$	$\delta_c = \frac{\delta_1}{\delta_3} = \frac{a_1}{a_3}$
circular micro-cracks (penny shape)	100	100	1
circular micro-cracks (penny shape)	200	200	1
circular micro-cracks (penny shape)	300	300	1
circular micro-cracks (penny shape)	400	400	1
crossing micro-cracks along $\vec{x}_1$	400000	400	1000
crossing micro-cracks along $\vec{x}_3$	400	400000	0.001

Table III.2: Flattening and shape ratios of the void inclusions.

As expected, it can be noticed that the presence of micro-cracks does not affect all the terms of the stiffness reduction tensor in the same way, leading to an anisotropic stiffness reduction. On Figures III.5 and III.6, it can be observed that the terms 1122, 2222, 2233, 1212 and 2323 of the stiffness are the most reduced, while the terms 1111, 3333 and 1313 are almost not affected for the considered range of micro-crack density. The flattening of the voids inclusions appears to have a shift effect on the stiffness reduction. The influence of the flattening ratios δ_1 and δ_3 seems to become negligible from a certain value. Similar observations have been reported by [127] and validate the choice of large finite values to represent infinite ratios. Regarding the shape of the cracks, it can be noticed that the micro-cracks shape ratio δ_c mainly influences the stiffness reduction of the in-plane shear (term 1212), that appears to be more important when the micro-cracks get across the volume element along $\vec{x}_1$, namely when $\delta_c \to \infty$.

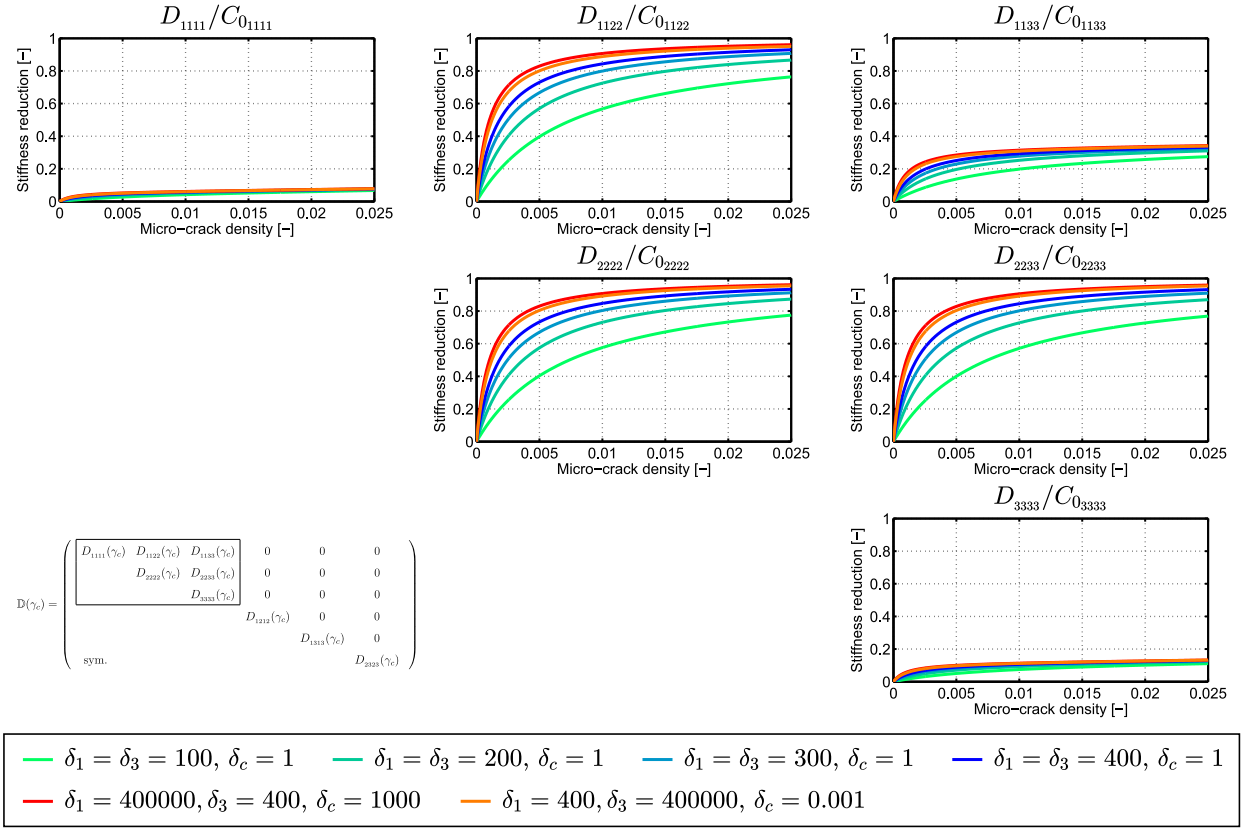

Figure III.5: Relative components of the stiffness reduction tensor (upper left quadrant) for several values of void flattening and shape ratios.

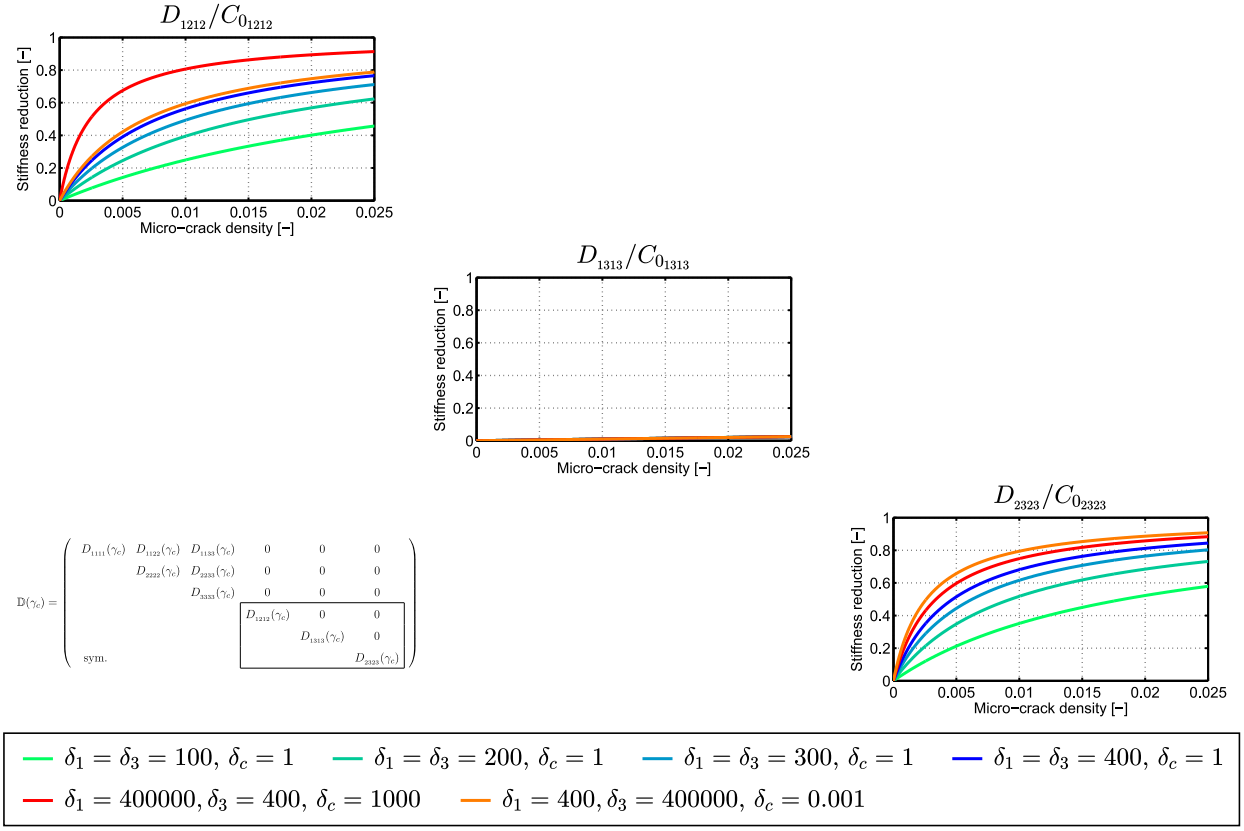

Figure III.6: Relative components of the stiffness reduction tensor (lower right quadrant) for several values of void flattening and shape ratios.

2.3 Evolution laws

The second law of thermodynamics implies that the mechanical dissipation has to be always positive or null through the Clausius-Duhem inequality (see Section 1.3 in Appendix B). Considering isothermal conditions (see Section 2 in Appendix B), the rate of the dissipated energy Φ is expressed by the difference between the rate of the strain energy W_ε and the rate of the stored energy $\rho\psi$, in which equations (III.3), (III.4) and (III.5) are substituted:

$$\begin{aligned}\dot{\Phi} &= \dot{W}_\varepsilon - \rho\dot{\psi} \geq 0 \\ &= \boldsymbol{\sigma} : \dot{\boldsymbol{\varepsilon}} - \rho\left(\frac{\partial\psi}{\partial\boldsymbol{\varepsilon}} : \dot{\boldsymbol{\varepsilon}} + \frac{\partial\psi}{\partial\boldsymbol{\varepsilon_s}} : \dot{\boldsymbol{\varepsilon}}_{\boldsymbol{s}} + \frac{\partial\psi}{\partial\gamma_c}\dot{\gamma}_c\right) \geq 0 \\ &= \boldsymbol{\sigma} : \dot{\boldsymbol{\varepsilon}}_{\boldsymbol{s}} + Y_c\dot{\gamma}_c \geq 0.\end{aligned} \tag{III.18}$$

From an energetic point of view, it is worth noticing that, according to the proposed model formulation, the internal energy function $\rho\psi$ presented in (III.2) is only associated with the elastic part of the total strain. Indeed, in this formalism, there is no energetic term linked to the anelastic strain $\boldsymbol{\varepsilon_s}$ that could permanently store energy in the material, like a hardening function in the case of plasticity. Consequently, $\rho\psi$ is fully and instantaneously recoverable when the stress is released. Thus, the non-linear mechanisms of the proposed model only dissipate and do not store energy in an unrecoverable manner (see Figure III.7). Note that this latter point is an assumption of the model.

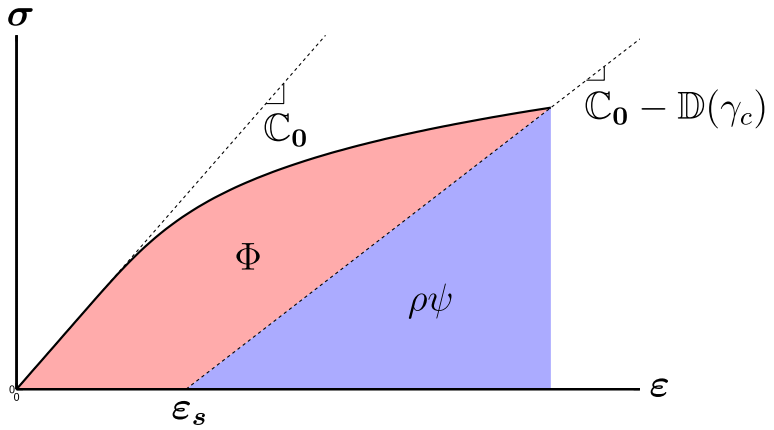

Figure III.7: Balance between the dissipated (Φ) and stored ($\rho\psi$) energies for the proposed model.

2.3.1 Damage activation and development

Classically, in most of the CDM models for unidirectional composites [106, 95, 93, 5, 25, 26, 119], the damage variables are driven by a criterion based on their associated variables, namely the energy density releases. With the present formulation, such a control would be inappropriate, since the growth of oriented micro-cracks is only generated under a certain type of stress state, namely when σ_{22} and σ_{12} are involved. For this reason, it is proposed to drive the development of the micro-crack density γ_c by an anisotropic quadratic interaction criterion [76, 148] expressed from the local stress in the virgin part of the material (III.13). This criterion, in its general form, is given by:

$$H_c(\boldsymbol{\sigma_0}) = \sqrt{\boldsymbol{\sigma_0} : \mathbb{H} : \boldsymbol{\sigma_0}}. \tag{III.19}$$

In the above equation, $\mathbb{H}$ is a fourth order tensor configured in such a way that H_c stays sensitive only to the components 22 and 12 of $\boldsymbol{\sigma_0}$. With the help of the Voigt notation, this gives:

$$H_c^2 = \begin{Bmatrix} \sigma_{0_{11}} \\ \sigma_{0_{22}} \\ \sigma_{0_{33}} \\ \sigma_{0_{12}} \\ \sigma_{0_{13}} \\ \sigma_{0_{23}} \end{Bmatrix}^T \times \begin{pmatrix} 0 & 0 & 0 & 0 & 0 & 0 \\ & \frac{1}{R_{22}^2} & 0 & 0 & 0 & 0 \\ & & 0 & 0 & 0 & 0 \\ & & & \frac{1}{R_{12}^2} & 0 & 0 \\ & & & & 0 & 0 \\ \text{sym.} & & & & & 0 \end{pmatrix} \times \begin{Bmatrix} \sigma_{0_{11}} \\ \sigma_{0_{22}} \\ \sigma_{0_{33}} \\ \sigma_{0_{12}} \\ \sigma_{0_{13}} \\ \sigma_{0_{23}} \end{Bmatrix} = \left(\frac{\sigma_{0_{22}}}{R_{22}}\right)^2 + \left(\frac{\sigma_{0_{12}}}{R_{12}}\right)^2. \quad \text{(III.20)}$$

As illustrated in Figure III.8a, R_{22} and R_{12} denote the initial thresholds in pure transverse tension and in pure in-plane shear, respectively. According to the relationships (III.13) and (III.14), the local stress $\boldsymbol{\sigma_0}$ and the overall stress $\boldsymbol{\sigma}$ have the same direction and a nearly equal amplitude since the micro-crack density γ_c takes relatively small values. Nevertheless, a criterion based on this local stress $\boldsymbol{\sigma_0}$ is more appropriate as it accounts for the neat part of the material sustaining the loading.

The development of the micro-crack density is formulated in such a way that the damage initiates only when H_c exceeds 1. After this stage, the micro-crack density γ_c is expressed as a function g of the maximal value reached by the criterion H_c in the whole loading history, noted hereafter as $\sup(H_c)$. The function g is chosen as a Weibull-like law [192] that is commonly utilized in micromechanics-based models to express the evolution of various types of damage mechanisms like micro-cracking [42, 130] or interface debonding [107, 199, 46]. Thus, in the proposed model, the development of the micro-crack density is expressed as follows:

$$\gamma_c = g\big(\sup(H_c)\big) = \gamma_c^\infty \left[1 - \exp\left(-\left[\frac{\big\langle \sup(H_c) - 1\big\rangle_+}{S}\right]^\beta\right)\right], \quad \text{(III.21)}$$

where S and β are the length and exponent parameters, respectively. γ_c^∞ denotes the level of micro-crack saturation such that $\gamma_c \leq \gamma_c^\infty$, as shown in Figure III.8b. If no saturation appears experimentally, then the parameter γ_c^∞ can be simply fixed to a large enough value so that only the first part of the Weibull function ($0 < \sup(H_c) < 1+S$) acts (Figure III.8b).

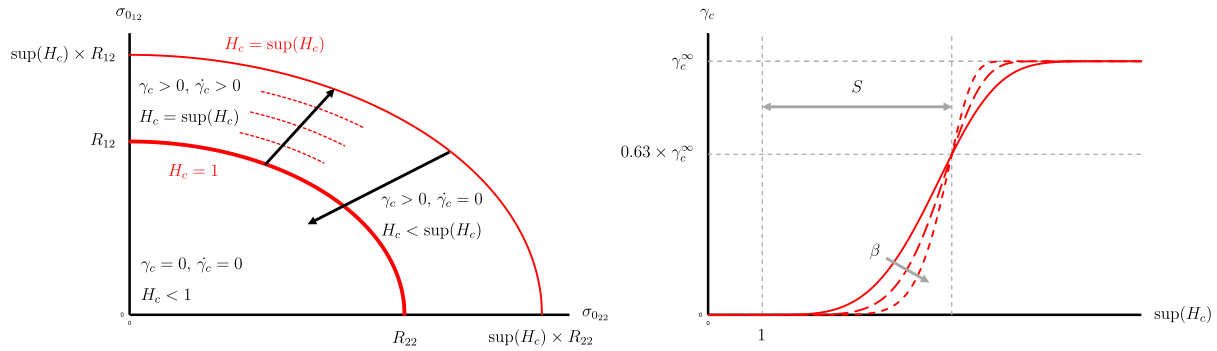

(a) Stress criterion H_c (b) Weibull-like law

Figure III.8: Development of the micro-crack density.

It is worth noticing that the development relationship (III.21) accounts well for the irreversible aspect of damage, implying that $\dot{\gamma}_c \geq 0$. Indeed, as illustrated in Figure III.8a,

damage is activated and evolves ($\dot{\gamma}_c > 0$) when $H_c = \sup(H_c)$, while it remains constant ($\dot{\gamma}_c = 0$) when $H_c < \sup(H_c)$. From a thermodynamic point of view, the inequality $Y_c \geq 0$ ensures that the dissipation related to the stiffness reduction is always positive or null, i.e. $Y_c \dot{\gamma}_c \geq 0$.

2.3.2 Evolution law for anelasticity

Classically, in most of the CDM models for unidirectional composites [106, 95, 93, 5, 25, 26, 119], the anelastic mechanisms are formulated in a similar manner as plasticity, where the anelastic strains are governed by a yield criterion written in the effective stress space [109, 110]. Alternatively, the proposed approach considers that the anelasticity occurs as permanent strains caused by the micro-cracks non-closure upon unloading. Therefore, this anelasticity is a direct consequence of the micro-cracking that is represented by the internal state variable γ_c. Accordingly, the evolution of the anelastic strain $\boldsymbol{\varepsilon_s}$ is directly linked to the variable of the micro-crack density γ_c, making the two mechanisms directly coupled and simultaneously activated. This evolution is expressed through the normality of a convex indicative function given by:

$$F(\boldsymbol{\sigma}, Y_c) = H_s(\boldsymbol{\sigma}) + Y_c \qquad \text{where} \qquad H_s(\boldsymbol{\sigma}) = \sqrt{\boldsymbol{\sigma} : \mathbb{F} : \boldsymbol{\sigma}}. \tag{III.22}$$

In the above equation, H_s is another anisotropic quadratic interaction criterion [76, 148] in which the fourth order tensor $\mathbb{F}$ is configured in such a way that H_s stays sensitive only to the components 22 and 12 of $\boldsymbol{\sigma}$. With the help of the Voigt notation, this gives:

$$H_s^2 = \begin{Bmatrix} \sigma_{11} \\ \sigma_{22} \\ \sigma_{33} \\ \sigma_{12} \\ \sigma_{13} \\ \sigma_{23} \end{Bmatrix}^T \times \begin{pmatrix} 0 & 0 & 0 & 0 & 0 & 0 \\ & a_{22}^2 & 0 & 0 & 0 & 0 \\ & & 0 & 0 & 0 & 0 \\ & & & a_{12}^2 & 0 & 0 \\ & & & & 0 & 0 \\ \text{sym.} & & & & & 0 \end{pmatrix} \times \begin{Bmatrix} \sigma_{11} \\ \sigma_{22} \\ \sigma_{33} \\ \sigma_{12} \\ \sigma_{13} \\ \sigma_{23} \end{Bmatrix}, \tag{III.23}$$

where a_{22} and a_{12} are material parameters. The normality of the indicative function $F(\boldsymbol{\sigma}, Y_c)$ allows to express the rate of γ_c and $\boldsymbol{\varepsilon_s}$ through a common multiplier λ ($\dot{\lambda} \geq 0$):

$$\dot{\gamma}_c = \frac{\partial F}{\partial Y_c}\dot{\lambda} = \dot{\lambda}, \tag{III.24}$$

$$\dot{\boldsymbol{\varepsilon}}_{\boldsymbol{s}} = \frac{\partial F}{\partial \boldsymbol{\sigma}}\dot{\lambda} = \frac{\partial H_s}{\partial \boldsymbol{\sigma}}\dot{\lambda} = \frac{\mathbb{F} : \boldsymbol{\sigma}}{H_s(\boldsymbol{\sigma})}\dot{\lambda}. \tag{III.25}$$

The evolution of the multiplier, that appears to be the rate of the micro-crack density itself ($\dot{\lambda} = \dot{\gamma}_c \geq 0$), that is obtained through the damage development relationship (III.21). Then, by introducing (III.24) into (III.25) the evolution of the anelastic strain $\boldsymbol{\varepsilon_s}$ eventually takes the form of a flow equation:

$$\dot{\boldsymbol{\varepsilon}}_{\boldsymbol{s}} = \boldsymbol{\Lambda_s}(\boldsymbol{\sigma})\dot{\gamma}_c \qquad \text{where} \qquad \boldsymbol{\Lambda_s}(\boldsymbol{\sigma}) = \frac{\mathbb{F} : \boldsymbol{\sigma}}{H_s(\boldsymbol{\sigma})}. \tag{III.26}$$

It is worth noticing that $H_s(\boldsymbol{\sigma})$ is related to the direction of the anelastic strain, whereas $H_c(\boldsymbol{\sigma_0})$ is related to the damage activation and development, as expressed in (III.21). In that sense, the anelastic strain is governed by a non-associative flow rule. The form of $\mathbb{F}$ in (III.23) implies that only the components 22 and 12 of the anelastic strain tensor $\boldsymbol{\varepsilon_s}$ are active and evolve with the micro-crack density, namely when $\dot{\gamma}_c > 0$. In addition, it is worth noting that the anelastic mechanism can be deactivated by setting $a_{22} = 0$ and $a_{12} = 0$.

2.4 Remarks and discussion

With the present model, the damage development and the direction of the anelastic strain are governed by the stress criteria H_c (III.20) and H_s (III.23), respectively. Although simple, the choices of these criteria are motivated by the fact that each one involves only two parameters that can be easily identified, as detailed in Section 4. It is worth recalling that the criteria H_c and H_s are both formulated as anisotropic quadratic interaction criteria based on the work of [76] and [148]. These criteria imply symmetric envelopes in the stress space. Consequently, they cannot account for asymmetric effects such as the difference in response between tension and compression. Nevertheless, H_c and H_s can be easily replaced by other criteria [82, 185, 74, 73, 84] accounting for more complicated multi-axial coupling and asymmetric effects. Such advanced criteria though would require additional parameters that need to be identified from experiments including tension-compression, and combined loading conditions. In the absence of such data, the proposed quadratic interaction criteria remain the best compromise.

As mentioned at the beginning of Section 2, the present model considers that the micro-cracks are always oriented in the same direction. This orientation is conditioned by the reinforcement and by an assumed plane stress state. In certain cases, this hypothesis could be violated. Indeed, according to the well-established Puck criterion [167, 168], it is known that the cracking plane may exhibit different types of orientation, especially when a transverse compressive stress is involved ($\sigma_{22} < 0$). The present modelling approach can be combined with such criterion to account for a load dependent micro-cracks orientation. However, integrating this feature may lead to several modelling difficulties. First, when the material is subjected to highly non-proportional loading, different cracking planes exist and may interact each other. Second, even though advanced algorithms have been already developed for the determination of a potential cracking plane [193, 175], the computational cost related to this task is often prohibitive and the application of the algorithms in non-linear FE schemes is not straightforward.

The introduction of local damage in FE structural analyses may cause additional difficulties, related to the localization effects. Indeed, this well-known unstable phenomenon caused by the loss of ellipticity of the system of equations cannot be described correctly with phenomenological models using local variables. Usually, in FE computations the localization is activated under any small perturbation, which may be caused by defects in the material, irregularities in the geometry of the structure or non-homogeneous boundary conditions. The numerical solution is then mesh dependent and the actual results are not reliable. Often, size effects and localization mechanisms can be captured with non-local models [48, 191, 75, 87, 98], which use gradients of the variables and introduce a characteristic length. In the current work the proposed damage model is formulated and implemented in the framework of CDM with the assumption of diffuse damage prior to localization. All the numerical calculations are performed well before any unstable phenomenon occurs, thus the analyses do not suffer from the loss of uniqueness. For structural applications the model can be considered accurate as long as the material at every point of the structure does not reach the limit where localization appears. Note that the same remarks are also applicable for the constitutive model previously presented in Chapter II.

2.5 Summary of the constitutive equations

In summary, the proposed model can be described by the set of constitutive equations given above in Table III.3.

Observable state variable	Associated variable (state law)	
$\boldsymbol{\varepsilon}$	$\boldsymbol{\sigma} = \rho\dfrac{\partial\psi}{\partial\boldsymbol{\varepsilon}} = \left[\mathbb{C}_{\mathbf{0}} - \mathbb{D}(\gamma_c)\right] : (\boldsymbol{\varepsilon} - \boldsymbol{\varepsilon_s})$	
Internal state variables	Associated variables (state laws)	Evolution laws
$\boldsymbol{\varepsilon_s}$	$-\boldsymbol{\sigma} = \rho\dfrac{\partial\psi}{\partial\boldsymbol{\varepsilon_s}}$	$\dot{\boldsymbol{\varepsilon}}_{\boldsymbol{s}} = \dfrac{\partial F}{\partial\boldsymbol{\sigma}}\dot{\lambda} = \boldsymbol{\Lambda_s}(\boldsymbol{\sigma})\dot{\gamma}_c$
γ_c	$-Y_c = \rho\dfrac{\partial\psi}{\partial\gamma_c}$	$\dot{\gamma}_c = \dfrac{\partial F}{\partial Y_c}\dot{\lambda} = \dot{\lambda}$
Micromechanical variables	Local mean strain and stress in the virgin part of the material	
$\boldsymbol{\varepsilon_0}$	$\boldsymbol{\varepsilon_0} = \mathbb{A}_{\mathbf{0}}(\gamma_c) : (\boldsymbol{\varepsilon} - \boldsymbol{\varepsilon_s})$	
$\boldsymbol{\sigma_0}$	$\boldsymbol{\sigma_0} = \mathbb{C}_{\mathbf{0}} : \mathbb{A}_{\mathbf{0}}(\gamma_c) : (\boldsymbol{\varepsilon} - \boldsymbol{\varepsilon_s})$ or $\boldsymbol{\sigma_0} = \mathbb{B}_{\mathbf{0}}(\gamma_c) : \boldsymbol{\sigma}$	
Multiplier	Criterion	Active ($\dot{\lambda} > 0$) if $H_c = \sup(H_c)$
$\lambda = \gamma_c$	$H_c = \sqrt{\boldsymbol{\sigma_0} : \mathbb{H} : \boldsymbol{\sigma_0}}$	$\gamma_c = g\big(\sup(H_c)\big)$

Table III.3: Summary of the constitutive equations.

3 Numerical implementation: Backward Euler time implicit algorithm

The proposed constitutive model is implemented into the FE solver *ABAQUS/Standard* through a User MATerial subroutine (UMAT). The latter is based on the "convex cutting plane" form of the "return mapping algorithm" [179, 145, 178], which is described in this section for this model.

3.1 Residual

When considering the backward Euler time-implicit method, it is convenient to write the equations governing the evolutions of the state variables under the form of residual functions that must satisfy a nullity condition. With the proposed model, the damage development relationship (III.21) is written under the form of scalar function ϕ_{γ_c} that takes negative values when damage is not active ($\dot{\gamma}_c = 0$), or that must remain null when damage is active ($\dot{\gamma}_c > 0$):

$$\phi_{\gamma_c}(H_c, \gamma_c) = g(H_c) - \gamma_c \leq 0, \qquad \begin{cases} \text{if} & \phi_{\gamma_c} < 0, \quad \dot{\gamma}_c = 0 \\ \text{if} & \phi_{\gamma_c} = 0, \quad \dot{\gamma}_c > 0 \end{cases} . \tag{III.27}$$

Moreover, the proposed implementation is based on the "convex cutting plane" form of the "return mapping algorithm" [179, 145, 178], which does not require to integrate the flow equation (III.26) as a residual function.

The implicit implementation of the proposed model requires to linearise the above residual, the criterion H_c, as well as the stress. The details of these calculations are provided in Appendix E.

3.2 Computation of the stress

3.2.1 Stress prediction

In order to initiate the computation of the stress, the internal state variables are assumed not to evolve at first ($\Delta\gamma_c^{(n+1)(k=0)} = 0$ and $\boldsymbol{\varepsilon_s}^{(n+1)(k=0)} = \mathbf{0}$), while the total strain at the end of the increment is given by $\boldsymbol{\varepsilon}^{(n+1)} = \boldsymbol{\varepsilon}^{(n)} + \Delta\boldsymbol{\varepsilon}^{(n+1)}$. Thus, the stress is predicted along with the residual ϕ_{γ_c}. The latter is then checked to identify whether the damage mechanism is active or not:

- If $\phi_{\gamma_c}^{(n+1)(k=0)} \leq 0$, then the damage is not active and consequently, the stress does not need to be corrected.

- If $\phi_{\gamma_c}^{(n+1)(k=0)} > 0$, then the damage is active. Thus, the "stress correction" is required.

3.2.2 Stress correction

The "stress correction" consists in returning the residual ϕ_{γ_c} back to zero by developing the internal state variables, while the total strain does not evolve: $\delta\boldsymbol{\varepsilon}^{(n+1)(k)} = \mathbf{0}$. Accordingly, the internal state variables are updated at each iteration k by:

$$\gamma_c^{(n+1)(k+1)} = \gamma_c^{(n+1)(k)} + \delta\gamma_c^{(n+1)(k)}, \tag{III.28}$$

$$\boldsymbol{\varepsilon}_{\boldsymbol{s}}^{(n+1)(k+1)} = \boldsymbol{\varepsilon}_{\boldsymbol{s}}^{(n+1)(k)} + \delta\boldsymbol{\varepsilon}_{\boldsymbol{s}}^{(n+1)(k)}, \tag{III.29}$$

where $\delta\gamma_c^{(n+1)(k)}$ is obtained from the nullity condition of the residual ϕ_{γ_c}:

$$\phi_{\gamma_c}^{(n+1)(k)} + \delta\phi_{\gamma_c}^{(n+1)(k)} = 0. \tag{III.30}$$

In the above equation, $\delta\phi_{\gamma_c}^{(n+1)(k)}$ is expressed by linearisation. After proper calculation (E.2), this gives (all the quantities are taken at the increment $^{(n+1)(k)}$):

$$\delta\phi_{\gamma_c} = A_{\gamma_c H_c}\delta H_c + A_{\gamma_c\gamma_c}\delta\gamma_c. \tag{III.31}$$

In the same manner (E.3), δH_c is written as:

$$\delta H_c = B_{H_c\gamma_c}\delta\gamma_c. \tag{III.32}$$

By introducing (III.32) into (III.31) while considering (III.30), the unknown value of $\delta\gamma_c$ is computed from the known value of the residual ϕ_{γ_c}:

$$\delta\gamma_c = \frac{-\phi_{\gamma_c}}{K_{\gamma_c\gamma_c}} \qquad \text{where} \qquad K_{\gamma_c\gamma_c} = A_{\gamma_c H_c}B_{H_c\gamma_c} + A_{\gamma_c\gamma_c}. \tag{III.33}$$

Furthermore, according to the "convex cutting plane" method [1], $\delta\boldsymbol{\varepsilon}_{\boldsymbol{s}}^{(n+1)(k)}$ is directly linked to $\delta\gamma_c^{(n+1)(k)}$ by:

$$\delta\boldsymbol{\varepsilon}_{\boldsymbol{s}}^{(n+1)(k)} = \boldsymbol{\Lambda}_{\boldsymbol{s}}(\boldsymbol{\sigma}^{(n+1)(k)})\delta\gamma_c^{(n+1)(k)}. \tag{III.34}$$

Once the internal state variables are updated, the stress and the residual ϕ_{γ_c} are reassessed through the relationships (III.3) and (III.27), respectively. This correction procedure is iteratively repeated (k loop) until the convergence is reached, namely when $|\phi_{\gamma_c}^{(n+1)(k+1)}| \leq 0 + \delta$.

3.3 Tangent operator

Besides the computation of the stress, the global finite element solver also requires the tangent operator $\mathbb{C}_{\boldsymbol{t}}$, which defines the current rate in the variation of stress with the variation of total strain. As previously mentioned, the proposed implementation is based on the "convex cutting plane" form of the "return mapping algorithm", which utilizes the continuum tangent operator [178]. The formulation of the latter is obtained by identifying a linear relationship between $d\boldsymbol{\sigma}$ and $d\boldsymbol{\varepsilon}$ through a continuum description. To do so, the stress-strain relationship is written in differential form and the evolution equations are substituted.

If the "return mapping algorithm" stops at the "stress prediction", then the damage mechanism is not active ($\dot{\gamma}_c = 0$). In this case, the tangent operator is simply given by the current elastic stiffness: $\mathbb{C}_{\boldsymbol{t}} = \mathbb{C}_{\mathbf{0}} - \mathbb{D}(\gamma_c)$. However, if the "return mapping algorithm"

1. Note that, according to the "convex cutting plane" method [179, 145, 178], the flow equation (III.26) is explicitly integrated within the correction procedure. This is why in (III.34) the flows $\boldsymbol{\Lambda}_{\boldsymbol{s}}$ is calculated from the previously updated state (taken at the increment $^{(n+1)(k)}$). Nevertheless, it is worth pointing out that the time integration remains implicit. Despite this simplification, the "convex cutting plane" method provides a good accuracy compared to other schemes, while involving less computational cost [171, 170, 83].

passes to the "stress corection", then the damage mechanism is active ($\dot{\gamma_c} > 0$). In this case, the stress-strain relationship (III.3) is written in differential form. After proper calculation (E.4), this gives:

$$d\boldsymbol{\sigma} = \mathbb{B}_{\boldsymbol{\sigma\varepsilon}} : d\boldsymbol{\varepsilon} + \boldsymbol{B}_{\boldsymbol{\sigma\gamma_c}} d\gamma_c. \tag{III.35}$$

The fact that the damage mechanism is active implies that $d\phi_{\gamma_c} = 0$. Written in differential form (E.2), this condition becomes:

$$d\phi_{\gamma_c} = A_{\gamma_c H_c} dH_c + A_{\gamma_c \gamma_c} d\gamma_c = 0. \tag{III.36}$$

In the same manner (E.3), dH_c is written as:

$$dH_c = \boldsymbol{B}_{\boldsymbol{H_c\varepsilon}} : d\boldsymbol{\varepsilon} + B_{H_c\gamma_c} d\gamma_c. \tag{III.37}$$

By introducing (III.37) into (III.36), a linear relationship can be identified between $d\gamma_c$ and $d\boldsymbol{\varepsilon}$:

$$d\gamma_c = \boldsymbol{X}_{\boldsymbol{\gamma_c\varepsilon}} : d\boldsymbol{\varepsilon} \qquad \text{where} \qquad \boldsymbol{X}_{\boldsymbol{\gamma_c\varepsilon}} = \frac{-A_{\gamma_c H_c} \boldsymbol{B}_{\boldsymbol{H_c\varepsilon}}}{K_{\gamma_c \gamma_c}}. \tag{III.38}$$

Finally, the substitution of (III.38) into (III.35) leads to the formulation of the tangent operator $\mathbb{C}_{\boldsymbol{t}}$:

$$d\boldsymbol{\sigma} = \mathbb{C}_{\boldsymbol{t}} : d\boldsymbol{\varepsilon} \qquad \text{where} \qquad \mathbb{C}_{\boldsymbol{t}} = \mathbb{B}_{\boldsymbol{\sigma\varepsilon}} + \boldsymbol{B}_{\boldsymbol{\sigma\gamma_c}} \otimes \boldsymbol{X}_{\boldsymbol{\gamma_c\varepsilon}}. \tag{III.39}$$

4 Model identification and experimental validation

In this section, a suitable procedure is proposed for the identification of the model. This procedure is illustrated with experimental data coming from the work of [119] on a flax-epoxy composite. Note that, compared to classical unidirectional composites with stiff fibres (e.g., glass or carbon), the case of the flax-epoxy is unusual. Indeed, due to the nature of the flax fibres, a slightly non-linear response can be observed in the longitudinal direction. It is important to mention that this peculiar aspect of the flax-epoxy composite cannot be properly captured with the proposed model. The latter has been preferentially developed for classical unidirectional composites and therefore assumes a linear response in the longitudinal direction. However, the transverse and in-plane shear behaviour in the flax-epoxy composite involves the same mechanisms than those described by the model. Consequently, in this study, the attention is more focused on the description of the transverse and in-plane shear, while in the longitudinal direction, the response is considered as being linear elastic with an average slope (see Figure III.12a).

All the experimental data come from uni-axial tests performed on symmetric and balanced laminated specimens (Figure III.9a). In these conditions, neither tension-shear nor tension-bending couplings appear. Thus, the overall laminate exhibits a purely uni-axial stress state in the specimen's coordinate system $(\vec{x}, \vec{y}, \vec{z})$. However, each single layer (Figure III.9b), due to its orientation, is subjected to complex plane stress states in its local coordinate system $(\vec{x}_1, \vec{x}_2, \vec{x}_3)$. During the test a longitudinal strain ε_{xx} was applied on the specimens, while the responses in terms of transversal strain ε_{yy} and longitudinal stress σ_{xx} were monitored. Based on the individual behaviour of each single layer, the non-linear response of such multi-layered composite is simulated through a homogenization scheme. Although the non-linear extension of the classical laminate theory is commonly used for this purpose [21, 154], it is convenient to consider instead a scheme based on periodic homogenization [34] in order to keep the constitutive model in its 3D formalism. Both methods actually provide the same results as long as laminates with a symmetric stacking are considered.

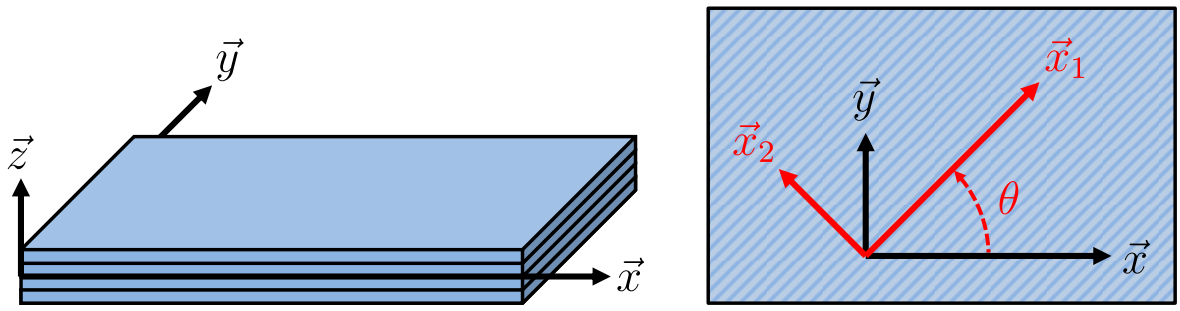

(a) Laminate: multi-layered composite (b) Single layer

Figure III.9: Definition of a laminate, $(\vec{x}, \vec{y}, \vec{z})$ is the coordinate system of the laminate, while $(\vec{x}_1, \vec{x}_2, \vec{x}_3)$ is the material one within a single layer.

It is proposed to identify, at first, the parameters related to the micro-crack density evolution (III.21) and the anelasticity (III.26) in the transverse tension, namely, R_{22}, S, β, γ_c^∞ and a_{22}. These parameters can be assessed with a $[90^o]_{16}$ laminated specimen repeatedly loaded and unloaded at progressively increasing maximum stress levels (Figure III.10a). Indeed, with this stacking sequence, the layers are only subjected to a uni-axial stress state in the transverse direction ($\sigma_{22} = \sigma_{xx}$) so that the transverse elastic strain ($\varepsilon_{22} - \varepsilon_{s_{22}}$) is

given by:

$$(\varepsilon_{_{22}} - \varepsilon_{s_{22}}) = S_{_{2222}}(\gamma_c)\ \sigma_{_{22}}. \tag{III.40}$$

In the above equation $S_{_{2222}}(\gamma_c)$ is the term 2222 of the current compliance tensor $\mathbb{S}(\gamma_c)$. Furthermore, $\mathbb{S}_{\mathbf{0}}$ represents the initial compliance tensor. They are expressed as follows:

$$\mathbb{S}(\gamma_c) = \big[\mathbb{C}_{\mathbf{0}} - \mathbb{D}(\gamma_c)\big]^{-1}, \qquad \mathbb{S}_{\mathbf{0}} = \mathbb{C}_{\mathbf{0}}^{-1}. \tag{III.41}$$

For convenience, equation (III.40) is written under the following form:

$$\sigma_{_{22}} = \big[E_{0_{_2}} - D_{_2}(\gamma_c)\big](\varepsilon_{_{22}} - \varepsilon_{s_{22}}), \tag{III.42}$$

where $E_{0_{_2}}$ is the initial transverse Young modulus, while $D_{_2}(\gamma_c)$ represents the transverse uni-axial stiffness reduction. They are given by:

$$E_{0_{_2}} = \frac{1}{S_{0_{2222}}}, \qquad D_{_2}(\gamma_c) = \frac{1}{S_{0_{2222}}} - \frac{1}{S_{_{2222}}(\gamma_c)}. \tag{III.43}$$

It is important to mention that $D_{_2}(\gamma_c)$ is not a term of the stiffness reduction tensor $\mathbb{D}(\gamma_c)$ but it is related to latter the by the above relationship. When performing the test, at each stress level, the load release allows a direct measurement of the stiffness reduction $D_{_2}$ as well as the anelastic strain $\varepsilon_{s_{22}}$, as illustrated in Figure III.10a. Subsequently, considering the relationship (III.43), the micro-crack density corresponding to each stiffness reduction measurement is recovered (see Figure III.10b). Once the damage threshold R_{22} is identified (Figure III.10a), it becomes easy to compute the stress criterion H_c from (III.20) and (III.13). For a uni-axial positive stress state in the transverse direction, H_c is reduced to:

$$H_c = \frac{\sigma_{_{22}}}{(1-\gamma_c)R_{22}}. \tag{III.44}$$

Then, the parameters S, β, γ_c^{∞} of the function g (III.21), that expresses the relationship between the micro-crack density γ_c and the criterion H_c, can be easily identified from the obtained experimental points (Figure III.11a). Note that, for the considered material, it is observed that the saturation of damage is not reached at the end of the experiments (Figure III.11a). Thus, the parameter γ_c^{∞}, corresponding to the saturation regime, is set to a large enough value (see Table III.4) so that only the first part of the function g (III.21) is acting, as explained in Section 2.3.1. Still considering a uni-axial stress state in the transverse direction, the evolution law governing the anelastic strain (III.26) can be reduced to:

$$\varepsilon_{s_{22}} = a_{22}\gamma_c. \tag{III.45}$$

Then, in the same way, the parameter a_{22} is identified from the experimental points (Figure III.11b).

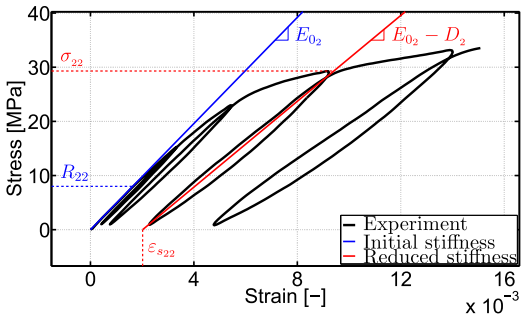

(a) Stress (σ_{xx}) vs. strain (ε_{xx}) curve for a $[90^o]_{16}$ laminate

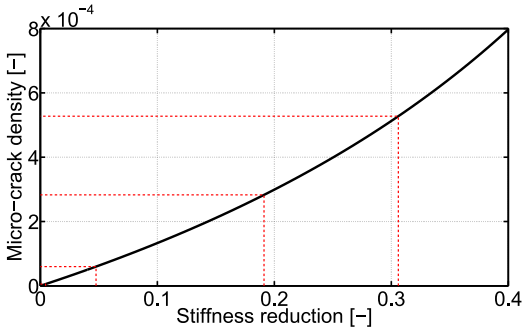

(b) Micro-crack density (γ_c) vs. relative stiffness reduction (D_2/E_{0_2})

Figure III.10: For each stress level ($\sigma_{22} = \sigma_{xx}$), the stiffness reduction (D_2) as well as the anelastic strain ($\varepsilon_{s_{22}}$) are measured. Thereafter, from (III.43), the micro-crack density (γ_c) corresponding to each measurement of stiffness reduction is recovered.

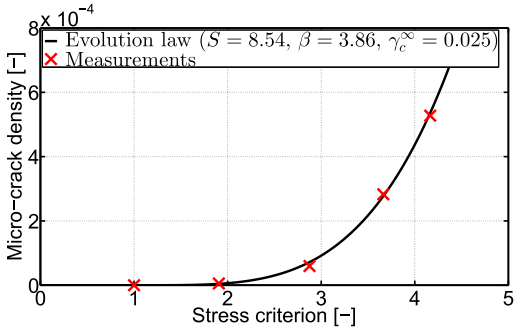

(a) Micro-crack density (γ_c) vs. stress criterion (H_c)

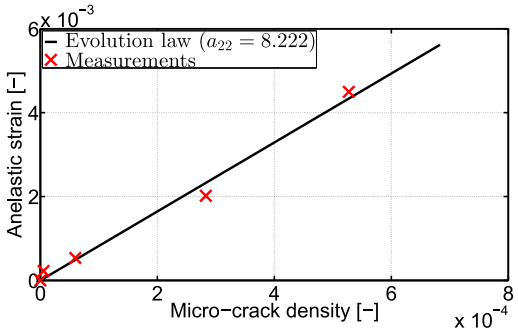

(b) Anelastic strain ($\varepsilon_{s_{22}}$) vs. micro-crack density (γ_c)

Figure III.11: Identification of the parameters related to the micro-crack density evolution and the anelasticity in the transverse direction, namely S, β, γ_c^∞ and a_{22}.

Similarly to the previously described procedure, the remaining parameters, R_{12} and a_{12}, could be determined from an in-plane shear test. Since pure shear tests are not easy to perform, it has been chosen to identify these parameters by means of reverse engineering, from a test performed on a $[\pm 45^o]_{4s}$ laminated specimen, where the damage is mainly governed by shear stress fields. Then the two remaining parameters are obtained by minimizing a cost function formulated from the least squares between the numerical and experimental mechanical response of the specimen [131, 129]. The obtained parameters are listed in Table III.4.

Feature	Parameter	value	unit
Pure transverse tension threshold	R_{22}	8	MPa
Pure in-plane shear threshold	R_{12}	6	MPa
Weibull length parameter	S	8.54	-
Weibull exponent parameter	β	3.86	-
Micro-cracks saturation (fixed)	γ_c^∞	0.025	-
Transverse tension anelasticity parameter	a_{22}	8.222	-
In-plane shear anelasticity parameter	a_{12}	3.054	-

Table III.4: Identified parameters for flax-epoxy unidirectional composite.

The initial stiffness properties are provided in (III.17). They have been evaluated by measuring the initial slopes of the tensile tests performed on $[0^o]_{16}$, $[90^o]_{16}$ and $[\pm 45^o]_{4s}$ laminated specimens. It is worth recalling that, as explained in Section 2.2.1, the initial stiffness tensor $\mathbb{C}_\mathbf{0}$ is required to compute the stiffness reduction along with a chosen configuration of void inclusions, in the present case: "crossing micro-cracks along $\vec{x}_1$" (see Table III.2).

Figures III.12a, III.12b and III.12c show the comparison between the simulated and experimental data used for the identification, respectively, the tensile tests performed on $[0^o]_{16}$, $[90^o]_{16}$ and $[\pm 45^o]_{4s}$ laminates. Despite a slight deviation on the transverse response on the $[\pm 45^o]_{4s}$ laminate (see Figure III.12c), the overall good agreement between the simulations and the experiments demonstrates the capability of the model to capture the behaviour of unidirectional composites with a rather low number of material parameters.

Furthermore, in order to validate the identified model, Figure III.12d shows a comparison between the simulated and experimental data performed on a $[\pm 67.5^o]_{4s}$ laminate that were not used for the identification. As it can be seen, the model provides a good overall prediction for both longitudinal and transversal responses. For the transverse behaviour, both loading and unloading stages are excellently captured. With respect to the longitudinal direction, the model provides the same order of stress, but overestimates the initial slope compared to the experiment, which induces a deviation of the stress-strain predicted curve.

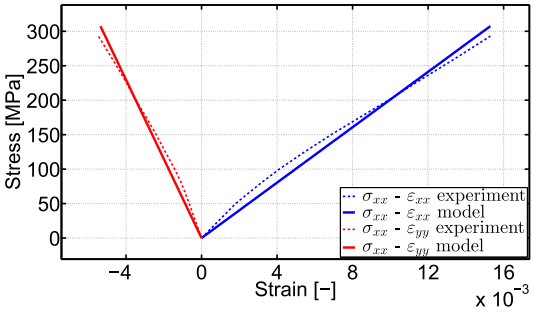

(a) Stress vs. strain for a $[0^o]_{16}$ laminate

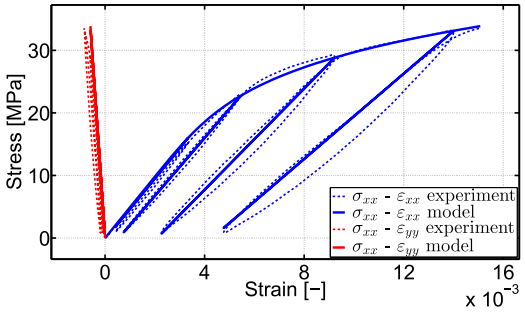

(b) Stress vs. strain for a $[90^o]_{16}$ laminate

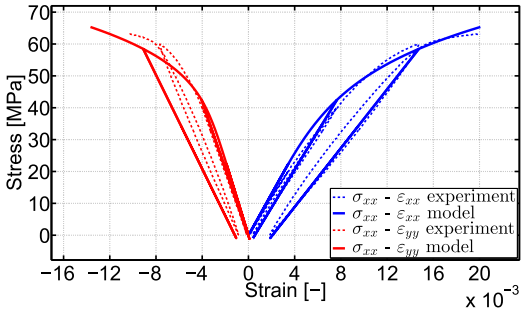

(c) Stress vs. strain for a $[\pm 45^o]_{4s}$ laminate

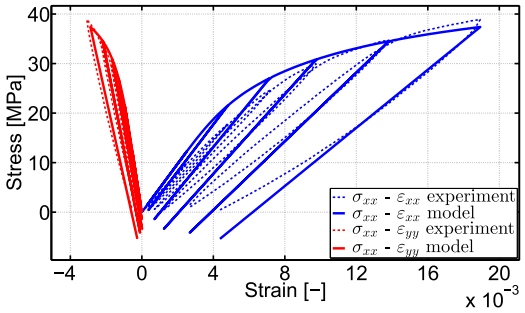

(d) Stress vs. strain for a $[\pm 67.5^o]_{4s}$ laminate

Figure III.12: Stress (σ_{xx}) vs. strain (ε_{xx} an ε_{yy}) for different configurations of laminate, comparison between model and experiments. The $[0^o]_{16}$, $[90^o]_{16}$ and $[\pm 45^o]_{4s}$ laminates are used for the identification, while the $[\pm 67.5^o]_{4s}$ laminate is kept for the validation.

5 Numerical simulations

All the simulations presented in this section were carried out with the parameters previously identified for the flax-epoxy in Table III.4.

5.1 Mechanical responses and dissipative behaviour of a material point

In order to provide a better understanding of the proposed model, its dissipative behaviour is illustrated through the two following simulations carried out on a single material point:

- Simulation 1: in-plane shear
  An in-plane shear stress σ_{12} of 20 MPa is applied on the material before returning back to zero. This cycle is repeated 2 times with an increase of 5 MPa at each cycle. The results of this simulation are presented in Figure III.13. Note that the computation is carried out with a constant time increment of 0.2 s.

- Simulation 2: non-proportional combined transverse tension and in-plane shear
  The material is first loaded with a transverse normal stress σ_{22} of 25 MPa that is held constant for a certain period of time. While σ_{22} is held, an in-plane shear stress σ_{12} of 15 MPa is applied and then released. Subsequently, the transversal stress σ_{22} is fully unloaded. The results of this simulation are presented in Figure III.14. Note that the computation is carried out with a constant time increment of 0.2 s.

First of all, in terms of energy balance (see Figures III.13g and III.14f), it can be noticed that the strain energy W_ε is well equal to the sum of the stored and dissipated energies, $\rho\psi$ and Φ, respectively. Moreover the dissipated energy always increases or remains constant ($\dot{\Phi} \geq 0$), which is well in accordance with the Clausius Duhem inequality (III.18).

In the simulation 1 (see Figure III.13), during the first loading stage, the development of the micro-cracking initiates when the stress exceeds the damage threshold, namely when $H_c > 1$. The micro-crack density is next growing along with the anelastic strain as the material keeps being loaded (Figures III.13d and III.13e). This growth stops when the material is unloaded and restarts in the following cycles, when the maximal value of H_c is reached again, namely when $H_c = \sup(H_c)$. Let's remark that the the material dissipates energy when the damage mechanism is active (Figures III.13f and III.13g) and recovers all its stored energy when fully unloaded. Indeed, as explained in Section 2.3, the model assumes that $\rho\psi$ is fully recoverable.

In the simulation 2 (see Figure III.14), during the first stage (0 s $< t <$ 40 s), when the transverse stress σ_{22} is applied on the material, a growth of micro-crack density is first generated and is accompanied by anelastic strain in the transverse direction (Figures III.14c and III.14d), both along with their related dissipations (Figures III.14e and III.14f). Next, the transverse stress is held and no change in the overall material response is observed, as expected, since no time dependency effects is accounted for with the proposed model (no creep or relaxation). In the second stage (40 s $< t <$ 80 s), the transverse stress σ_{22} is still being held and an in-plane shear stress σ_{12} is applied in addition, before being subsequently released. The micro-crack density is growing again, but at this time, anelastic strains are

generated in both transverse and shear directions (Figures III.14c and III.14d). The material dissipates energy during the application of the shear stress and recovers a part of its stored energy when the shear stress is released (Figures III.14e and III.14f). Finally, in the last stage (80 s $< t <$ 120 s) the transverse stress is unloaded and the remaining part of the stored energy returns back to zero (Figure III.14f), as $\rho\psi$ is fully recoverable.

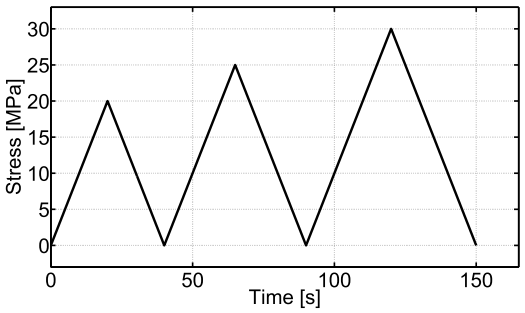

(a) Applied stress (σ_{12}) vs. time

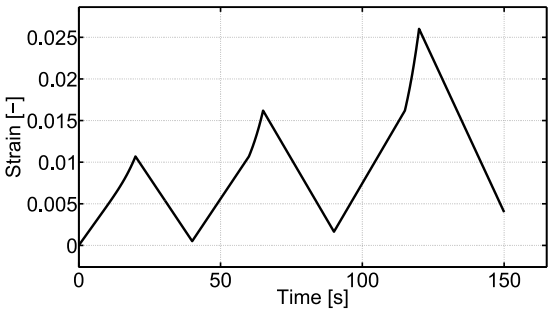

(b) Strain response ($2\varepsilon_{12}$) vs. time

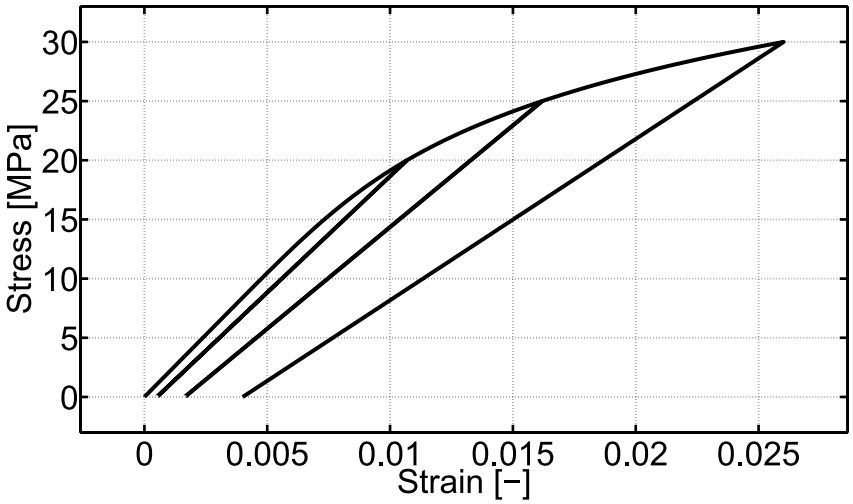

(c) Stress (σ_{12}) vs. strain ($2\varepsilon_{12}$)

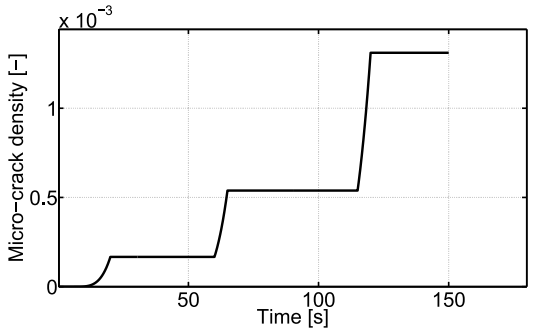

(d) Micro-crack density (γ_c) vs. time

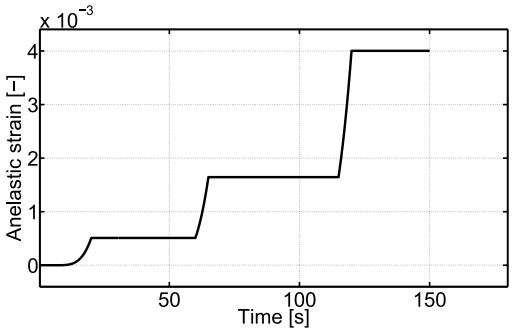

(e) Anelastic strain ($2\varepsilon_{s_{12}}$) vs. time

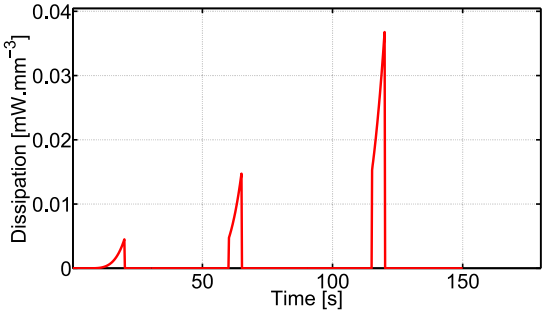

(f) Dissipation ($\dot{\Phi}$) vs. time

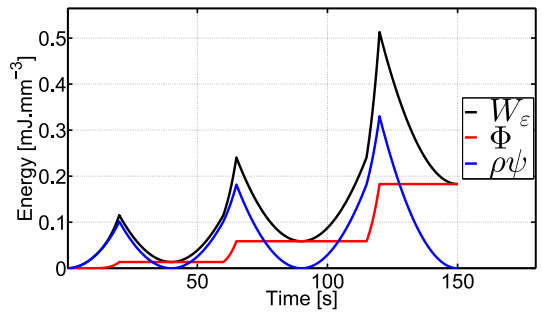

(g) Strain (W_ε), dissipated (Φ) and stored ($\rho\psi$) energies vs. time

Figure III.13: Simulation 1: in-plane shear.

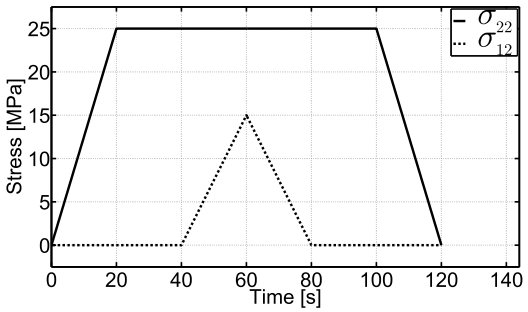

(a) Applied stress (σ_{22} and σ_{12}) vs. time

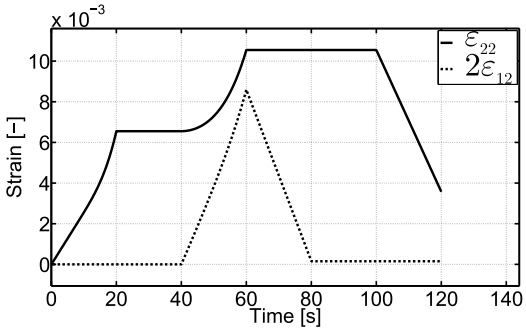

(b) Strain response (ε_{22} and $2\varepsilon_{12}$) vs. time

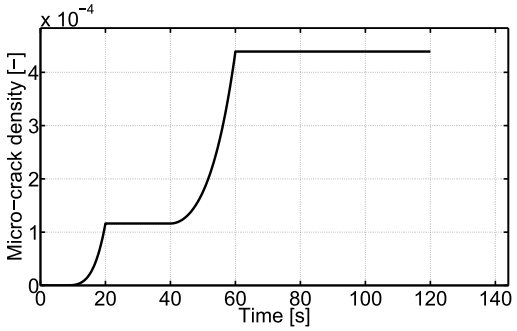

(c) Micro-crack density (γ_c) vs. time

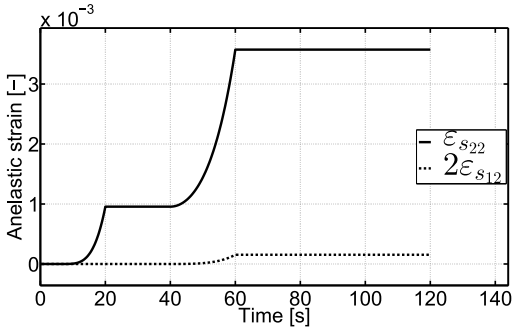

(d) Anelastic strain ($\varepsilon_{s_{22}}$ and $2\varepsilon_{s_{12}}$) vs. time

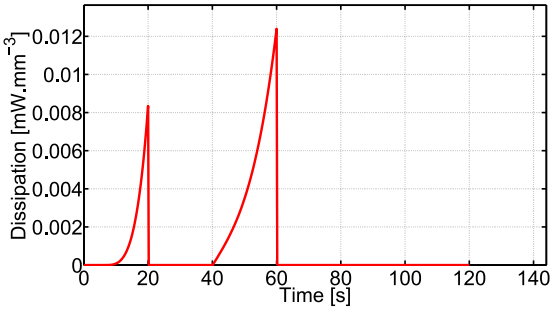

(e) Dissipation ($\dot{\Phi}$) vs. time

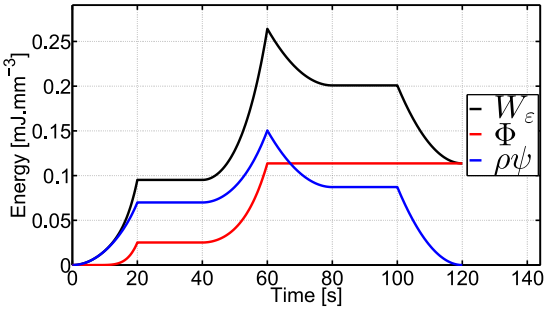

(f) Strain (W_ε), dissipated (Φ) and stored ($\rho\psi$) energies vs. time

Figure III.14: Simulation 2: non-proportional combined transverse tension and in-plane shear.

5.2 Structural FE application and model capabilities

To illustrate the capabilities of the model in simulating the mechanical response of a 3D body through the FE method, the present section deals with an example of FE analysis carried out on a laminated Meuwissen-like specimen [132, 131]. The latter is made of 8 layers of flax-epoxy unidirectional composite (see properties in Table III.4) with the following stacking sequence: $[0^o/+45^o/-45^o/90^o]_s$ (see Figure III.9 for the definition of a laminate). Each layer has a thickness of 0.5 mm, making a total thickness of 4 mm, among which half of it is represented due to symmetry (see Figure III.15a). The mesh contains 12825 nodes and 10752 first order hexahedral elements (C3D8 in *ABAQUS*). As shown on Figure III.15b, the left face (located in $-x$) of the specimen is clamped in the plane (the displacements along the z axis are left free), while the displacements along the y axis are set to zero on the right face (located in $+x$), on which a load along the x axis is also applied.

The specimen (the half represented) is thus loaded in 50 s with a force of 6.5 kN before being unloaded in another 50 s (see Figure III.16a). Note that, a multi-point constraint equation is utilized to force the displacements along the x axis to be equal on all the right face, so that the left and right faces always remain parallel during the deformation of the specimen. In addition, appropriate boundary conditions are set on the plane of symmetry, i.e. the displacements perpendicular to the plane of symmetry are set to zero (face located in $-z$). The computation is carried out with constant time increment of 0.5 s.

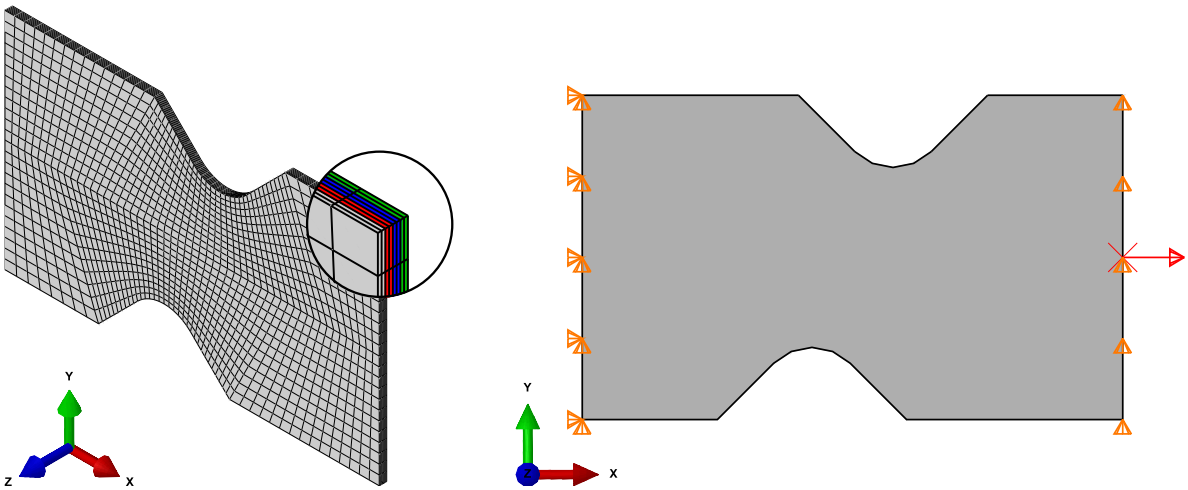

(a) Meshed Meuwissen specimen (in-plane dimensions in mm: 100×60), a half of the thickness is represented due to symmetry

(b) Loading and boundary conditions applied on the Meuwissen specimen

Figure III.15: Example of FE analysis: Meuwissen specimen.

First of all, it is worth noticing that the proposed implicit implementation and especially the formulation of the tangent operator (see Section 3) show a good efficiency as for each time increment, only one or two iterations are necessary to reach the global convergence.

Figure III.16b shows the displacement of the right face on which the load is applied. This displacement is increasing as the specimen is being loaded. During this first stage, the overall response of the structure is slightly non-linear due to the development of the micro-cracking and its related anelasticty at the most stressed locations (see Figure III.17). When the load is being released, the displacement is decreasing with a lower slope as the structure has lost a part of its stiffness. Once fully unloaded, it can be observed that the specimen keeps an overall deformation as a consequence of the remaining anelastic strains.

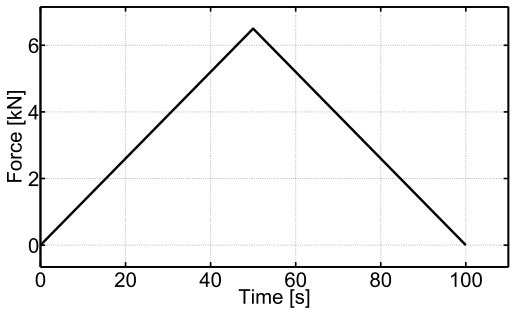

(a) Applied force along the x axis vs. time

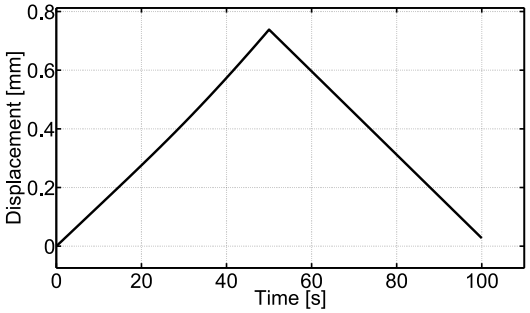

(b) Resulting displacement along the x axis vs. time

Figure III.16: Applied force and resulting displacement of the right face (located in $+x$).

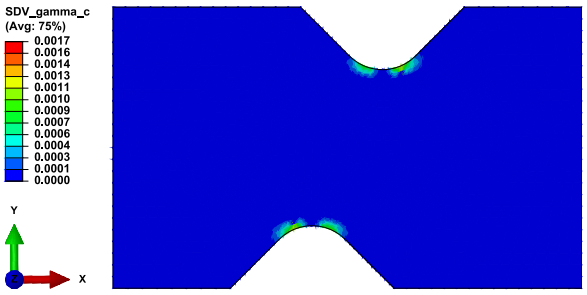

(a) Micro-crack density (γ_c) field at the middle of the 0^o layer

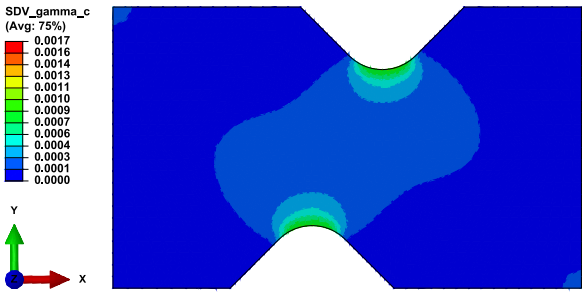

(b) Micro-crack density (γ_c) field at the middle of the 90^o layer

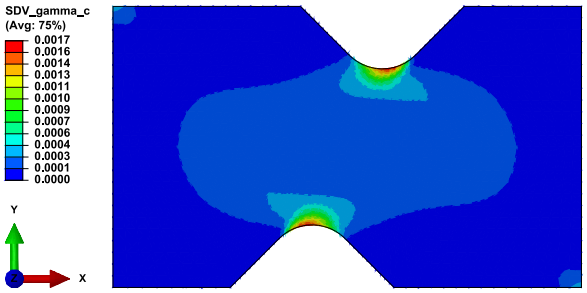

(c) Micro-crack density (γ_c) field at the middle of the $+45^o$ layer

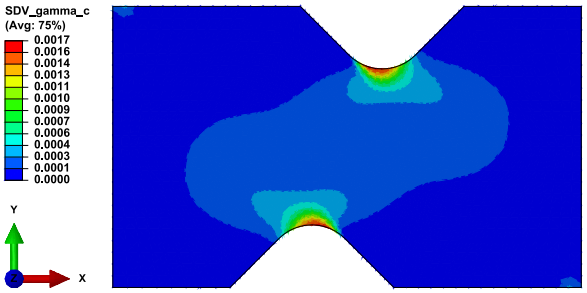

(d) Micro-crack density (γ_c) field at the middle of the -45^o layer

Figure III.17: Micro-crack density (γ_c) field within each layer of the Meuwissen specimen, at the end of the simulation.

6 Conclusions

In this chapter, a hybrid micromechanical-phenomenological constitutive model has been proposed to predict the mechanical behaviour of unidirectional composites and is intended to be used as yarn phase in the multi-scale modelling approach of the whole woven composites in Chapter IV. The constitutive equations are formulated in the framework of thermodynamics and account for anisotropic damage and anelasticty induced by the presence of a diffuse oriented micro-crack network in an initially transversely isotropic medium. The representation of damage is achieved through a micromechanical description of a micro-cracked RVE. This gives a better description of the physical damage mechanism and its influence of the overall material response. Furthermore, anelastic deformation mechanisms are phenomenologically introduced through the new concept of damage induced anelasticity, where permanent strains are assumed to be caused by the non-closure effect of the micro-cracks. This modelling strategy leads to a reduced number of parameters with a certain ease regarding their identification, compared to classical models for unidirectional composites.

The constitutive equations of the model are provided along with an implicit resolution scheme based on the "convex cutting plane" form of the "return mapping algorithm" as well as the formulation of the tangent operator. The latter is implemented into the FE solver *ABAQUS/Standard*.

The identification and the prediction capabilities have been validated from experimental data for flax-epoxy unidirectional composite. The model appears to be well adapted to describe the transverse tension and the in-plane shear responses of unidirectional composites.

Illustrative examples of simulations are performed in order to provide a better understanding of the model and to identify the influence of the involved mechanisms. Finally, the capabilities of the proposed model along with its numerical implementation are demonstrated through an example of FE analysis.

Chapter IV

Multi-scale analysis of the cyclic and time-dependent behaviour of thermoplastic-based woven composites

Contents

1 Introduction

Thermoplastic-based woven composites are known to have a complex behaviour inherent to the coupling between the microstructure effects and the rheological properties of the thermoplastic matrix. The polymeric matrix plays a key role in the development of the damage mechanisms over long periods of time. In recent years, the modelling of such composites has been at the focal point of many research interests, highlighting two main approaches in this purpose:

- On one hand, the overall behaviour of thermoplastic-based composites can be described in a purely phenomenological manner. However, the complexity of these composites requires models integrating numerous features like anisotropic, damage, anelasticity and/or viscous effects [95, 79, 153, 152, 80, 81, 124, 101, 4, 187, 91, 92, 119, 60]. Such a modelling strategy generally leads to a large number of parameters that may be difficult to identify. Besides this fact, once the model's parameters are identified, they are only valid for a unique microstructure configuration, which is a real limitation towards the integration of the local behaviours and processes. Moreover, the experimental data required for the identification may be costly and complicated to obtain. Despite this drawback, phenomenological models are generally numerically efficient and suitable for large-scale structural applications.

- On the other hand, the composites response can be also described through multi-scale approaches. The main advantage of this modelling strategy is that the local behaviours of the constituents are directly integrated along with the geometric definition of the microstructure. Thereby, the evolutions of the local deformation processes and the damage mechanisms are considered at the microscopic scale through the local responses of the different phases, as well as the microstructure interactions. This brings about a more physical description of the damage mechanisms. Moreover, as long as the local behaviours are known, the variability of the microstructure can be accounted for. Nevertheless, such a multi-scale modelling strategy may be difficult to apply for the simulation of large-scale structures, especially if the scale transition implies the resolution of a FE system. Indeed, even though the connection of a FE unit cell to each integration point of a macroscopic FE model is feasible through the FE^2 method [61, 63, 62, 9, 182, 184, 183], the computational cost involved in such a process is highly expensive and the dedicated numerical techniques are still under development. This prevents its direct use for industrial applications.

Considering these two different methodologies, it is possible to combine their advantages, while getting around their issues. The main idea is to employ the multi-scale modelling approach to generate a "virtual test" database that could be subsequently utilized to identify a purely phenomenological model [65, 2]. Hence, the multi-scale model is only used to perform simulations on a single macroscopic material point, so-called "virtual tests". These "virtual tests" can be obtained within a reasonable and acceptable computational time, and for a reduced cost. Moreover, any type of test can be simulated, for example: monotonic, cyclic, multi-axial or non-proportional loading conditions. Once the "virtual test" database is established, the next step is to identified from it a phenomenological model, able to reproduce the overall response of the composite, which in turn can be utilized for the simulation of a large-scale structures. The present multi-scale modelling approach is intended to be developed in this context. In a complementary purpose, the proposed multi-scale model

can also be utilized to analyse the influence of each individual component and the local processes, as well as the architecture of the microstructure on the macroscopic response of the composite.

It is important to mention that such approach is entirely modular, as it results from the assembly of several sub-models and from the geometric definition of the microstructure. Thus, if a composite with another composition and/or another periodic microstructure is to be studied, then the present multi-scale approach is still valid and only the ingredients should change.

This final chapter studies the cyclic and more generally the time-dependent response of thermoplastic-based woven composites through the proposed multi-scale model. The latter is built from the local constitutive models of the matrix and the yarns, presented in Chapters II and III, respectively. They are assembled together with the help of the multi-scale modelling approach presented in Chapter I.

This chapter is structured as follows: Section 2 briefly presents the experimental evaluation of the microstructure geometrical characteristics. Section 3 focuses on the experimental identification of the parameters of the yarn phase that remain unknown. The validation of the multi-scale model is achieved by comparing the predictions of the model against experimental data obtained from quasi-static and cyclic loading conditions. Section 4 presents illustrative examples of simulations where the composite is subjected to complex loading configurations. Among them: monotonic, creep, cyclic and non-proportional multiaxial loading conditions. Finally, Section 5 summarizes the main conclusions related to this chapter.

2 Unit cell and microstructure characteristics

For the studied composite, whose microstructure follows the geometric definition introduced in Section 3.1 of Chapter I (recalled in Figure IV.1a), the characteristic dimensions a, b and l are evaluated through of X-Ray computed tomography (see Figure IV.2a). h is obtained by dividing the total thickness of the provided plates by the number of layers they contain. Note that the parameter δ has been deliberately over-sized in order to ensure a proper enough meshing within the matrix domain. The average values considered for the multi-scale model are listed in Table IV.1. Additionally, it is recalled that the architecture of the woven reinforcement of the studied composite is 2-2 twill weave pattern as shown in Figure IV.1b.

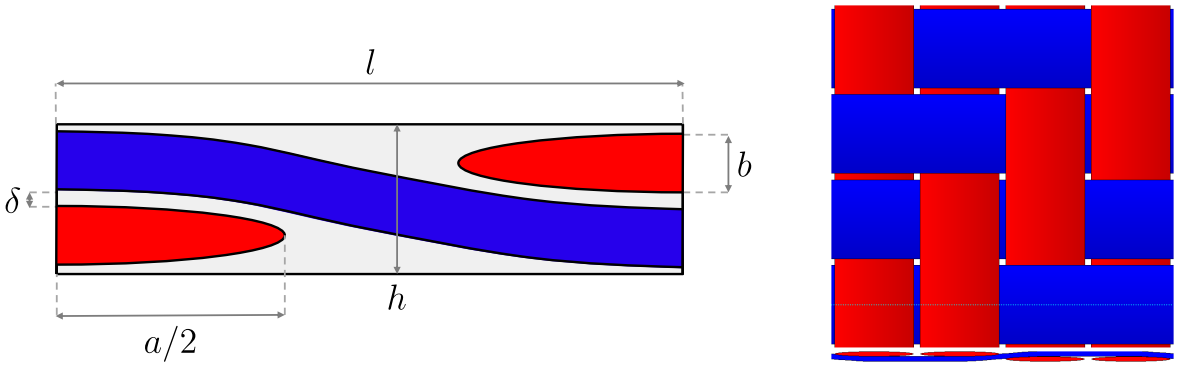

(a) Characteristic dimensions of a woven microstructure

(b) 2-2 Twill weave pattern

Figure IV.1: Geometric definition of the microstructure. The grey domain represents the matrix phase, while the blue and red domains are the warp and weft yarns, respectively.

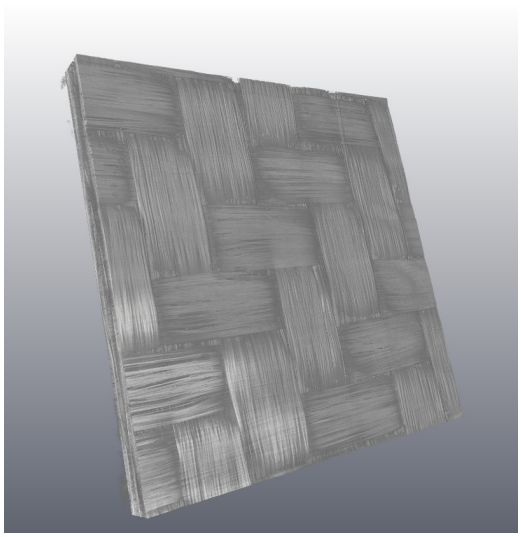

(a) 3D reconstruction of the microstructure of the studied composite using X-Ray computed tomography with a voxel size of 6 μm

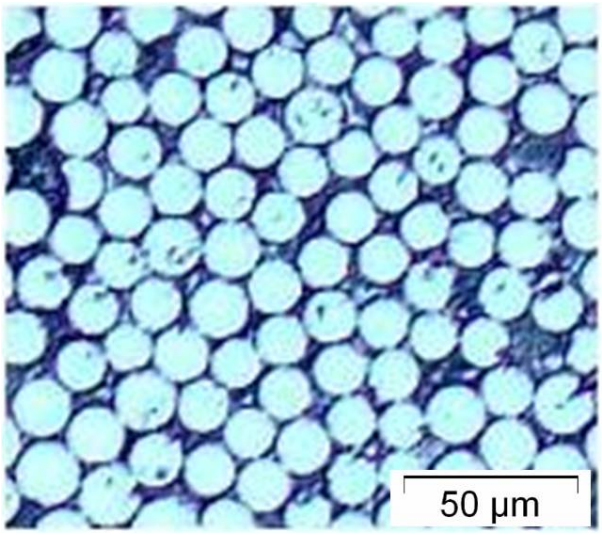

(b) Intra-yarn micrography, the diameter of the fibres is about 17 μm

Figure IV.2: Experimental observations of the microstructure of the studied composite.

Characteristic dimensions	a	b	l	h	δ
Values (mm)	3.46	0.21	3.75	0.5	0.025

Table IV.1: Characteristic dimensions of the microstructure, adopted values for the studied composite.

Using the data of Table IV.1, the unit cell of the studied composite is generated and subsequently meshed through the *TexGen* utilities (see Section 3.2 in Chapter I). Note that, under this configuration, the unit cell yields to a yarn volume fraction of 59%. Furthermore, analyses from micrography have shown that the intra-yarn fibre volume fraction is about 85%. This volume fraction corresponds to a high compaction as the fibres are almost all in contact with each-other (see Figure IV.2b). Overall, the fibre volume fraction in the whole composite is about 50%, which is well in accordance with the supplier data.

As previously mentioned, the constitutive models presented in Chapters II and III are assigned to the matrix and yarn phases, respectively.

3 Experimental identification, strategy and validation

3.1 Experimental procedure and testing

Similar environmental conditions to the unfilled polyamide 6-6 matrix (see Section 4.1 in Chapter II) were considered for the composite: $RH = 50\%$ and $T = 23^oC$ (room temperature) with the same experimental procedure regarding the RH conditioning of the material.

The experimental program was carried out on tensile laminated specimens (see Figures IV.3a and IV.3b) axially loaded along the $\vec{x}$ direction. Symmetric and balanced $[\pm\theta]_s$ stacking sequences are considered for the specimens with the following angles: $\theta = 0^o$, 15^o, 30^o and 45^o. It is recalled that, under this configuration, neither tension-shear nor tension-bending couplings appear, so the whole laminate can be axially loaded without generating any unsuitable shear deformations or curvatures. The thickness of a single layer is about 0.5 mm, making a total thickness of 2 mm for the whole laminated specimens. In order to obtain experimental data that are reasonably representative of the macroscopic response of the composite, rectangular specimens with large enough dimensions were considered: a length of 250 mm and a width of 45 mm. Depending on the orientation, 2 to 3 unit cells are included across the width (see Figure IV.3c). The tensile tests were performed with a servo-hydraulic tensile machine at room temperature. During the tests, the axial strain $\overline{\varepsilon}_{xx}$ is locally measured by means of an extensometer, while the axial stress $\overline{\sigma}_{xx}$ is monitored by a load cell.

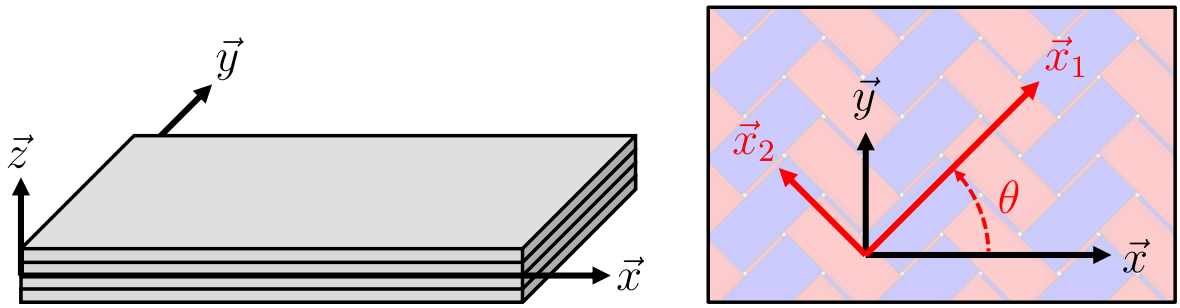

(a) Laminate: multi-layered composite

(b) Single layer

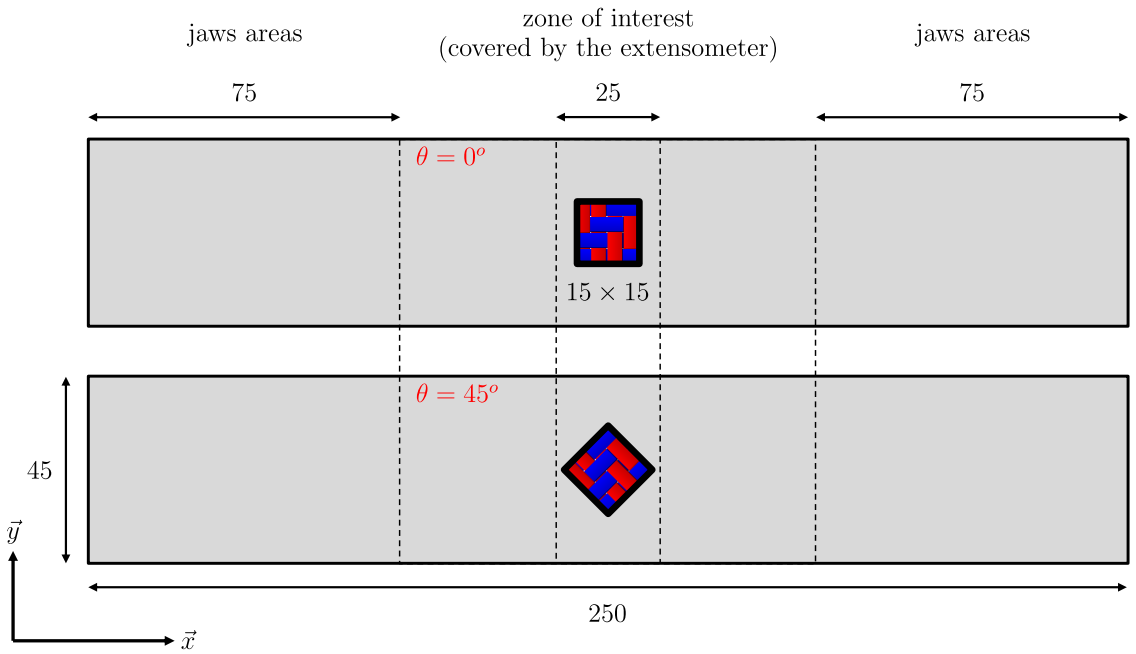

(c) Geometry and adopted dimensions of the tensile laminated specimens (dimensions in mm)

Figure IV.3: Tensile laminated specimens $[\pm\theta]_s$, $(\vec{x}, \vec{y}, \vec{z})$ is the coordinate system of the laminate, while $(\vec{x}_1, \vec{x}_2, \vec{x}_3)$ is the material one within a single layer.

For the purpose of the identification, it is necessary to numerically simulate the uni-axial responses of the laminated specimens, in order to be compared to the experimental results. As already discussed in Section 4 in Chapter III, the response of a multi-layered composite is usually simulated through the classical laminate theory [21, 154]. Alternatively, a scheme based on periodic homogenization can also be utilized for symmetric laminates [34]. In an even simpler approach, the uni-axial response of a $[\pm\theta]_s$ laminate can be simulated by considering only one single layer with appropriate stress-strain conditions arising from the configuration of such laminates. Indeed, the balanced stacking sequence prevents the whole laminate from deforming in in-plane shear. This is why, in every single layer, $2\overline{\varepsilon}_{xy} = 0$. As a consequence, a non-null in-plane shear stress ($\overline{\sigma}_{xy}$) is induced in each layer. Nevertheless, this stress takes opposite values from a $+\theta$ layer to a $-\theta$ layer and consequently vanishes at the scale of the whole laminate. Thus, in order to simulate the uni-axial response of a $[\pm\theta]_s$ laminated specimen, the following stress-strain states, defined in the specimen's coordinate system $(\vec{x}, \vec{y}, \vec{z})$, are applied to the unit cell with the help of the off-axis control proposed in

Section 2.2.2 in Chapter I. For the simulation of a strain-controlled test, this gives [1]:

$$\left\{\begin{array}{lcl} \overline{\varepsilon}_{xx} &=& \overline{\varepsilon}_{xx}(t) \\ \overline{\varepsilon}_{yy} &=& \text{unknown} \\ \overline{\varepsilon}_{zz} &=& \text{unknown} \\ 2\overline{\varepsilon}_{xy} &=& 0 \\ 2\overline{\varepsilon}_{xz} &=& \text{unknown} \approx 0 \\ 2\overline{\varepsilon}_{yz} &=& \text{unknown} \approx 0 \end{array}\right\}, \quad \left\{\begin{array}{lcl} \overline{\sigma}_{xx} &=& \text{unknown} \\ \overline{\sigma}_{yy} &=& 0 \\ \overline{\sigma}_{zz} &=& 0 \\ \overline{\sigma}_{xy} &=& \text{unknown} \neq 0 \\ \overline{\sigma}_{xz} &=& 0 \\ \overline{\sigma}_{yz} &=& 0 \end{array}\right\}. \tag{IV.1}$$

In the same principle, the simulation of a stress-controlled test is performed with:

$$\left\{\begin{array}{lcl} \overline{\varepsilon}_{xx} &=& \text{unknown} \\ \overline{\varepsilon}_{yy} &=& \text{unknown} \\ \overline{\varepsilon}_{zz} &=& \text{unknown} \\ 2\overline{\varepsilon}_{xy} &=& 0 \\ 2\overline{\varepsilon}_{xz} &=& \text{unknown} \approx 0 \\ 2\overline{\varepsilon}_{yz} &=& \text{unknown} \approx 0 \end{array}\right\}, \quad \left\{\begin{array}{lcl} \overline{\sigma}_{xx} &=& \overline{\sigma}_{xx}(t) \\ \overline{\sigma}_{yy} &=& 0 \\ \overline{\sigma}_{zz} &=& 0 \\ \overline{\sigma}_{xy} &=& \text{unknown} \neq 0 \\ \overline{\sigma}_{xz} &=& 0 \\ \overline{\sigma}_{yz} &=& 0 \end{array}\right\}, \tag{IV.2}$$

where the axial strain and stress, namely $\overline{\varepsilon}_{xx}$ and $\overline{\sigma}_{xx}$, can be compared to the experimental results.

For the experimental program, two types of tests that are suitable for the identification and the validation of the multi-scale model are proposed:

- Quasi-static tests:
  The laminated specimens are repeatedly loaded and unloaded at progressively increasing stress levels until failure. These tests are performed at a relatively slow strain rate (about 3.5×10^{-3} s^{-1}).

- Stress-controlled cyclic tests:
  The laminated specimens are subjected to a sinusoidal stress signal oscillating between a top and a bottom stress level at a frequency of 1 Hz during 100 s, i.e. 100 cycles. For the $[0^o]_4$, $[\pm 15^o]_s$ and $[\pm 30^o]_s$ specimens, about 80% of the quasi-static ultimate stress is considered for the top stress level. However, for the $[\pm 45^o]_s$ specimens, as they exhibit a much more ductile response, top stress level of 95 MPa is taken instead, in order to keep a moderate strain amplitude. Note that the bottom stress level is about 10 MPa, same for all the specimens.

Similarly to the unfilled polyamide 6-6 in Section 4 in Chapter II, during the stress-controlled cyclic tests, thermal measurements were carried out by means of an IR thermal camera. Although the proposed multi-scale model is formulated for isothermal conditions, an estimation of the self-heating will be assessed by integrating the macroscopic dissipation $\overline{\dot{\Phi}}$ as heat source in an uncoupled thermal analysis (see Appendix C). Thus, the estimated temperature elevation will be compared to the one experimentally observed. Assuming uniform thermomechanical fields in the area of interest, the "0D" heat equation integrated over the volume of the unit cell takes the following form:

$$\overline{\rho c}\left(\dot{T}(t) + \frac{T(t) - T_\infty}{\tau}\right) = \overline{\dot{\Phi}}(t), \tag{IV.3}$$

1. In the specimen's coordinate system $(\vec{x}, \vec{y}, \vec{z})$, the rotated unit cell presents a fully anisotropic response (in the plane xy), leading to tension-shear coupling. This is why the shear stress $\overline{\sigma}_{xy}$ can take non-null values when the shear strain $2\overline{\varepsilon}_{xy}$ is set to zero.

where $\overline{\rho}$ and $\overline{c}$ stand for the macroscopic density and specific heat capacity, respectively. It should be pointed out that characteristic time τ quantifies the heat losses which are assumed to be proportional to the difference between the current temperature of the composite $T(t)$ and the its equilibrium temperature T_∞ (room temperature). The thermal data utilized in this chapter are listed in Table IV.2.

Feature	Parameter	value	unit
Macroscopic density	$\overline{\rho}$	1.870×10^{-9}	$\mathrm{T.mm^{-3}}$
Macroscopic specific heat capacity	$\overline{c}$	$0.990 \times 10^{+9}$	$\mathrm{mJ.T^{-1}.{}^{o}C^{-1}}$
Characteristic time (heat losses)	τ	149	s

Table IV.2: Parameters of the uncoupled "0D" thermal problem for the composite. The values for the macroscopic density and the specific heat capacity are provided by the industrial partners. The characteristic time τ was evaluated for the laminated specimens (see Figures II.3 and II.4) using the methodology proposed by [20] that is briefly presented in Section 3 in Appendix C.

3.2 Identification strategy

It is recalled that the matrix has been already identified from experiments directly performed on the unfilled polyamide 6-6 (see Section 4 in Chapter II) whose parameters are listed in Table II.4. Regarding the yarns, the identification procedure proposed in Section 4 in Chapter III is not applicable in the present case, since it is impossible to isolate this component in order to perform mechanical tests on it. Instead, it is proposed to identify the yarns parameters from the macroscopic response of the whole woven composite. In this purpose, a reverse engineering algorithm is utilized, similarly to the approach used for the unfilled matrix described in Section 4.2 in Chapter II.

It is also important to recall that the behaviour of the yarns is assumed to be time-independent. Thus, for the whole multi-scale model, the overall time-dependency is only caused by the matrix phase. With this in mind, the parameters related to the yarns are identified only from the quasi-static tests, while the stress-controlled cyclic tests are kept for the validation.

3.3 Identification and experimental validation

Beforehand, the initial stiffness of the yarns is estimated by means of periodic homogenization (see Section 1 in Appendix G) so that only the parameters related to the damage and the anelasticity in the yarns are identified through the reverse engineering procedure. The obtained values of these parameters are listed in the lower part of Table IV.3, while the initial elastic properties are recalled in the upper part of the same table. Note that, the stiffness reduction induced by micro-cracks in the yarns (see Section 2 in Appendix G) is computed considering the following configuration for the void inclusions: "crossing micro-

cracks along $\vec{x}_1$" (see Figure III.4a and Table III.2). The behaviour of the isolated yarns is illustrated through basics examples in Section 3 of Appendix G.

Feature	Parameter	value	unit
Transversely isotropic stiffness tensor	$C_{0_{1111}}$	65822	MPa
(non-null components)	$C_{0_{1122}} = C_{0_{1133}}$	7041	MPa
	$C_{0_{2222}} = C_{0_{3333}}$	23947	MPa
	$C_{0_{2233}}$	6971	MPa
	$C_{0_{1212}} = C_{0_{1313}}$	8661	MPa
	$C_{0_{2323}} = \frac{1}{2}(C_{0_{2222}} - C_{0_{2233}})$	8488	MPa
Pure transverse tension threshold	R_{22}	20.0	MPa
Pure in-plane shear threshold	R_{12}	7.5	MPa
Weibull length parameter	S	12.3	-
Weibull exponent parameter	β	2.75	-
Micro-cracks saturation (fixed)	γ_c^∞	0.025	-
Transverse tension anelasticity parameter	a_{22}	3.60	-
In-plane shear anelasticity parameter	a_{12}	2.15	-

Table IV.3: Identified parameters for the yarns. The initial stiffness properties (in the upper part of the table) are computed by means of periodic homogenization (see Section 1 in Appendix G), while the damage and anelastic parameters (in the lower part of the table) are obtained from the response of the whole woven composite by reverse engineering.

Figures IV.4, IV.5, IV.6 and IV.7 show the numerical simulations provided by the multi-scale model and the experimental data for the quasi-static tests performed with the $[0^o]_4$, $[\pm 15^o]_s$, $[\pm 30^o]_s$ and $[\pm 45^o]_s$ specimens, respectively. First of all, it is observed that the response of the $[0^o]_4$ specimen is quasi-elastic, as only a small amount of overall damage and anelasticity are generated before the composite brutally fails at a relatively high level of stress (about 430 MPa). On the contrary, for the $[\pm 45^o]_s$ specimen, the response is much more ductile and no failure occurs at the end of the test[2]. For the $[\pm 15^o]_s$ and $[\pm 30^o]_s$ specimens, the composite exhibits an intermediate response between the ones observed with the $[0^o]_4$ and $[\pm 45^o]_s$.

This important difference of behaviour for the different layers angles brings out the strong anisotropy induced by the microstructure which is, overall, well captured by the multi-scale model. Indeed, for the $[0^o]_4$, $[\pm 15^o]_s$ and $[\pm 30^o]_s$ specimens, the simulated quasi-static responses are in good agreement with the experiments (see Figures IV.4, IV.5 and IV.6). For the $[\pm 45^o]_s$ specimen, the multi-scale model overestimates the quasi-static response. Nevertheless, same order of stress levels and a similar tendency are obtained. This deviation may be caused by eventual missing damage mechanisms occurring under significant in-plane

2. If no failure occurs, the test stops at 0.1 of strain, which is the limit of the extensometer.

shear stress levels (not taken into account in the present multi-scale model), like the debonding at the yarns/matrix interface for example.

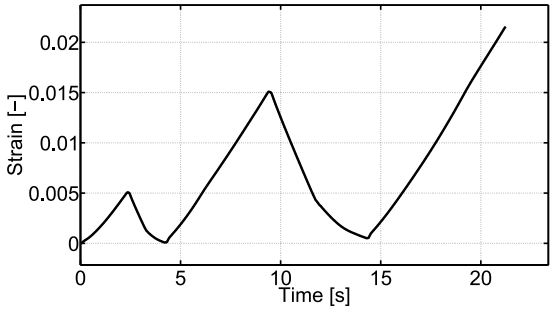

(a) Applied strain ($\overline{\varepsilon}_{xx}$) vs. time

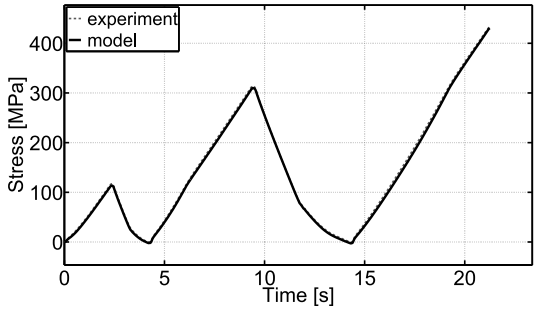

(b) Stress response ($\overline{\sigma}_{xx}$) vs. time

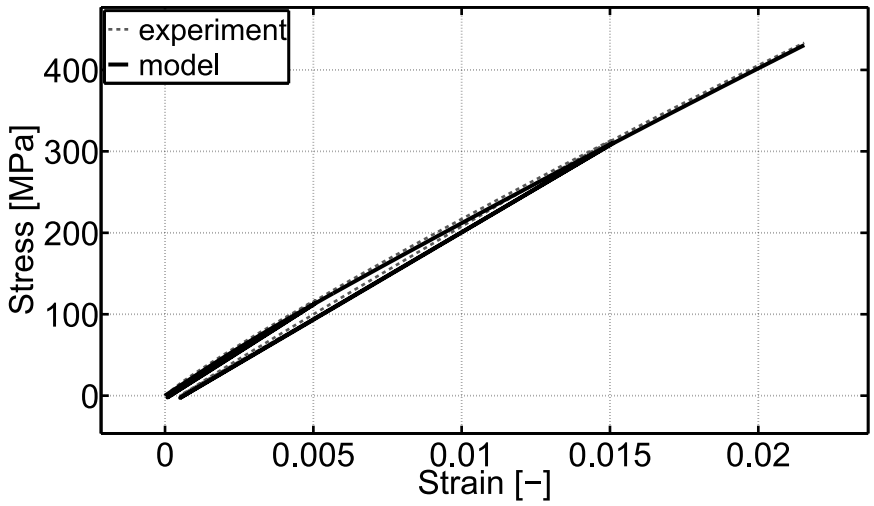

(c) Stress ($\overline{\sigma}_{xx}$) vs. strain ($\overline{\varepsilon}_{xx}$)

Figure IV.4: Quasi-static test for a $[0^o]_4$ laminated specimen. These data are used for the identification.

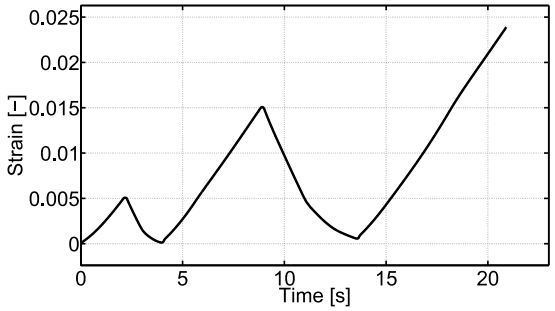

(a) Applied strain ($\overline{\varepsilon}_{xx}$) vs. time

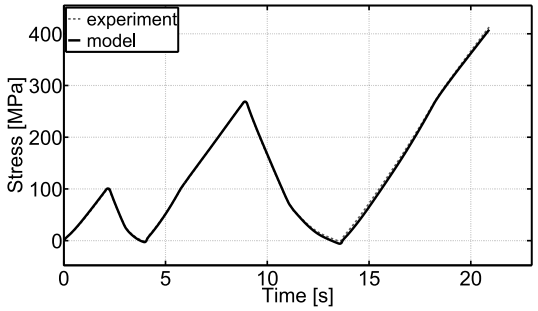

(b) Stress response ($\overline{\sigma}_{xx}$) vs. time

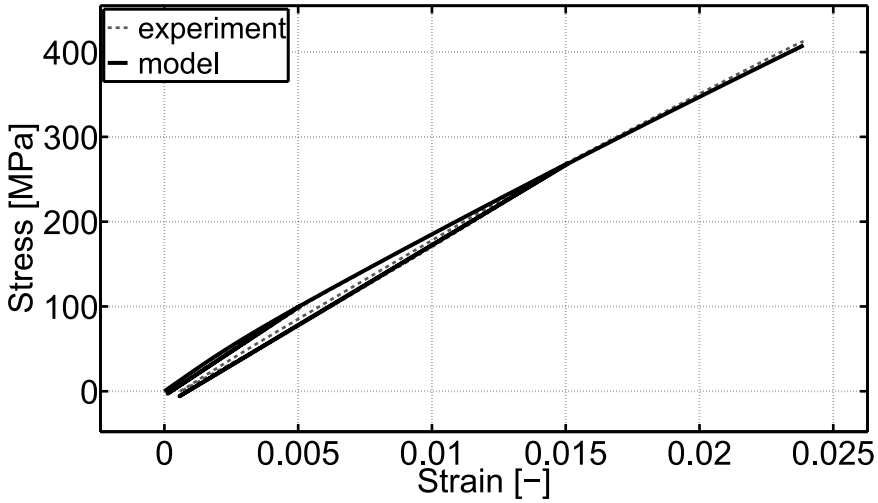

(c) Stress ($\overline{\sigma}_{xx}$) vs. strain ($\overline{\varepsilon}_{xx}$)

Figure IV.5: Quasi-static test for a $[\pm 15^o]_s$ laminated specimen. These data are used for the identification.

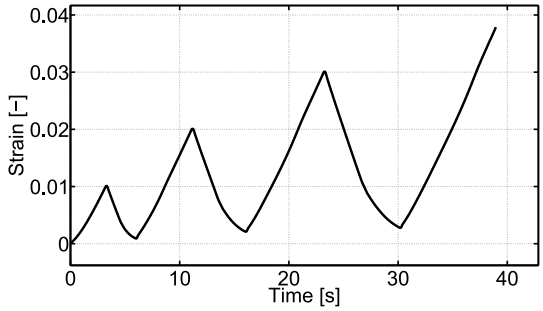

(a) Applied strain ($\overline{\varepsilon}_{xx}$) vs. time

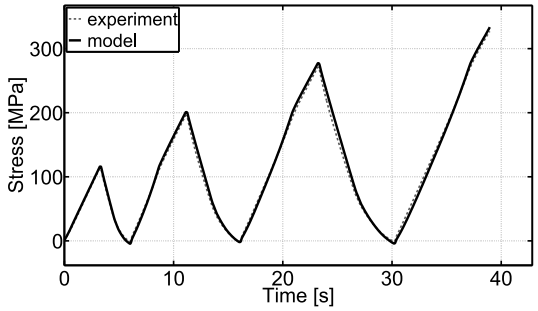

(b) Stress response ($\overline{\sigma}_{xx}$) vs. time

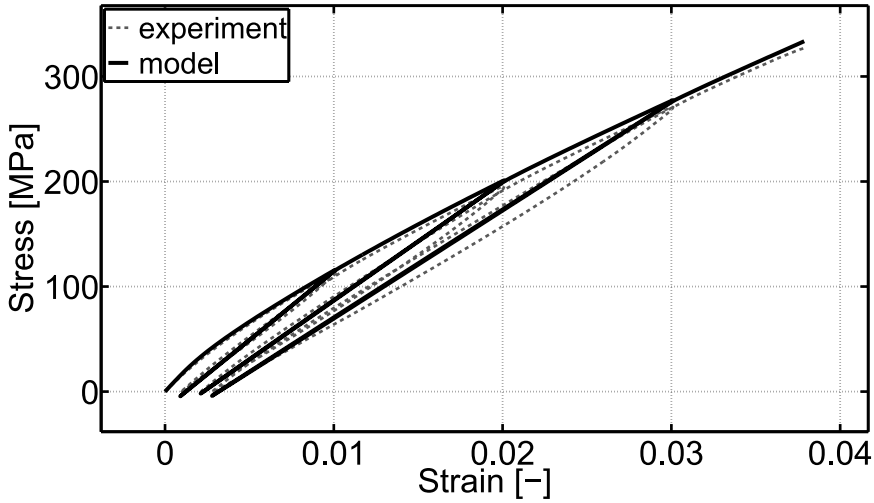

(c) Stress ($\overline{\sigma}_{xx}$) vs. strain ($\overline{\varepsilon}_{xx}$)

Figure IV.6: Quasi-static test for a $[\pm 30^o]_s$ laminated specimen. These data are used for the identification.

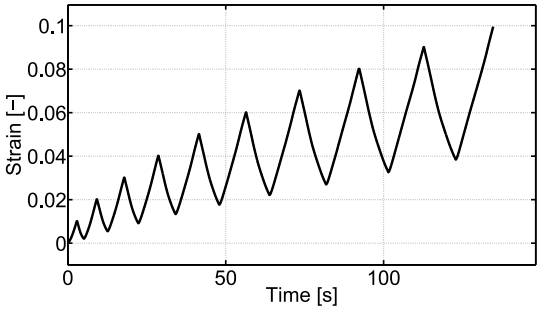

(a) Applied strain ($\overline{\varepsilon}_{xx}$) vs. time

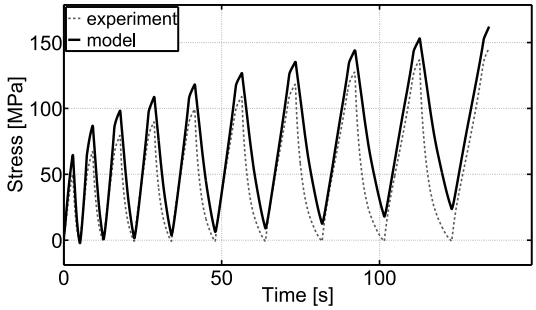

(b) Stress response ($\overline{\sigma}_{xx}$) vs. time

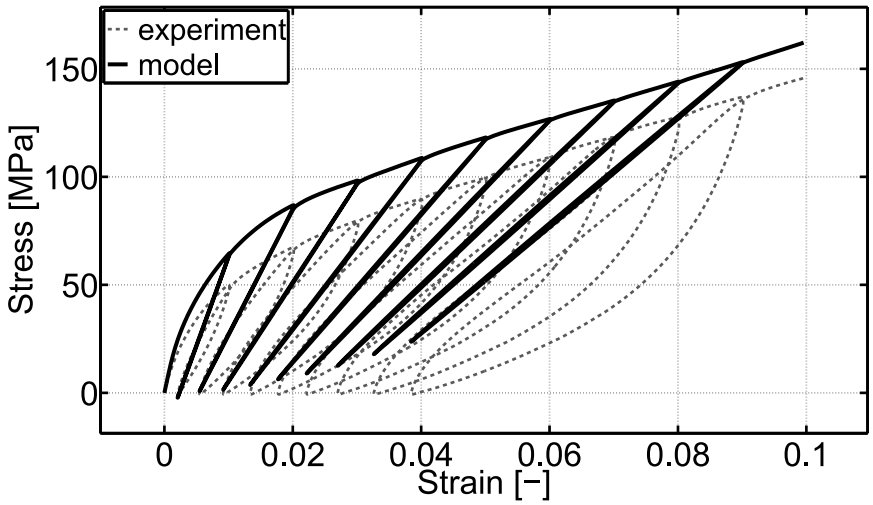

(c) Stress ($\overline{\sigma}_{xx}$) vs. strain ($\overline{\varepsilon}_{xx}$)

Figure IV.7: Quasi-static test for a $[\pm 45^o]_s$ laminated specimen. These data are used for the identification.

Figures IV.8, IV.9, IV.10 and IV.11 show the predictions provided by the multi-scale model and the experimental data obtained for the stress-controlled cyclic tests performed with the $[0^o]_4$, $[\pm 15^o]_s$, $[\pm 30^o]_s$ and $[\pm 45^o]_s$ specimens, respectively. It is recalled that these tests were not used for the identification. Note that the failure occurred after 80 and 71 cycles for the $[0^o]_4$ and $[\pm 30^o]_s$ specimens, respectively. For the other specimens, no failure occurred before the completion of the 100 cycles. When the composite is subjected to a cyclic loading, phenomena directly inherited from the matrix phase can be clearly observed, namely: the accumulation of strain accompanied by a progressive stiffness reduction (see Sections 4.3 and 5.1 In Chapter II). Nevertheless, according to the layers angles, the amplitudes of these phenomena are quite different and, once more, bring out the anisotropy induced by the microstructure. Note that, overall, similar tendencies are predicted by the multi-scale model, compared to the experimental results. The macroscopic strain responses are in relatively good agreement for the $[0^o]_4$ and the $[\pm 15^o]_s$ specimens, while the overall accumulation of strain and damage is underestimated for the $[\pm 30^o]_s$ and $[\pm 45^o]_s$ specimens. As previously mentioned, this emphasizes that other mechanisms and/or other time-dependent features in the yarn phase may be involved when the composite is mainly loaded in in-plane shear.

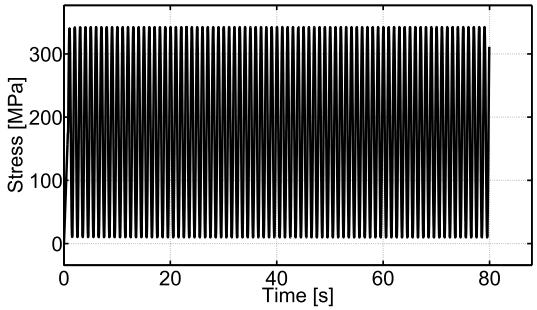

(a) Applied stress ($\overline{\sigma}_{xx}$) vs. time

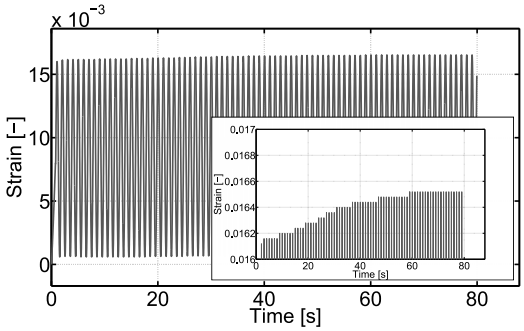

(b) Experimental strain response ($\overline{\varepsilon}_{xx}$) vs. time

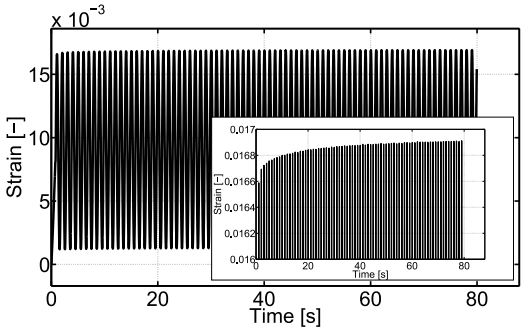

(c) Simulated strain response ($\overline{\varepsilon}_{xx}$) vs. time

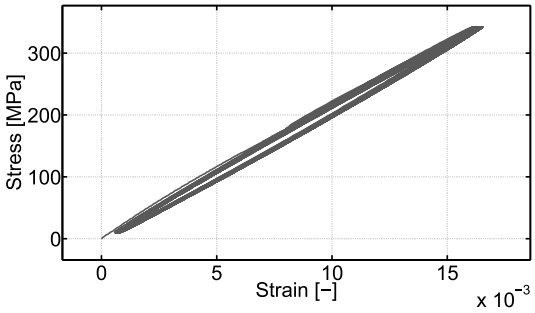

(d) Stress ($\overline{\sigma}_{xx}$) vs. strain ($\overline{\varepsilon}_{xx}$), experiement

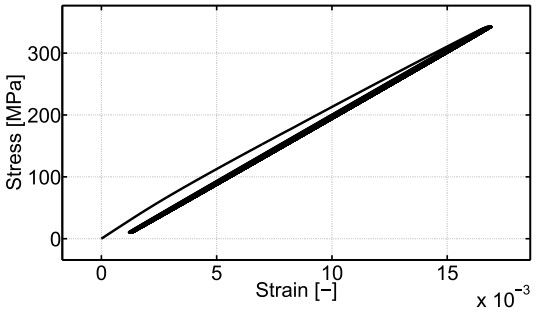

(e) Stress ($\overline{\sigma}_{xx}$) vs. strain ($\overline{\varepsilon}_{xx}$), simulation

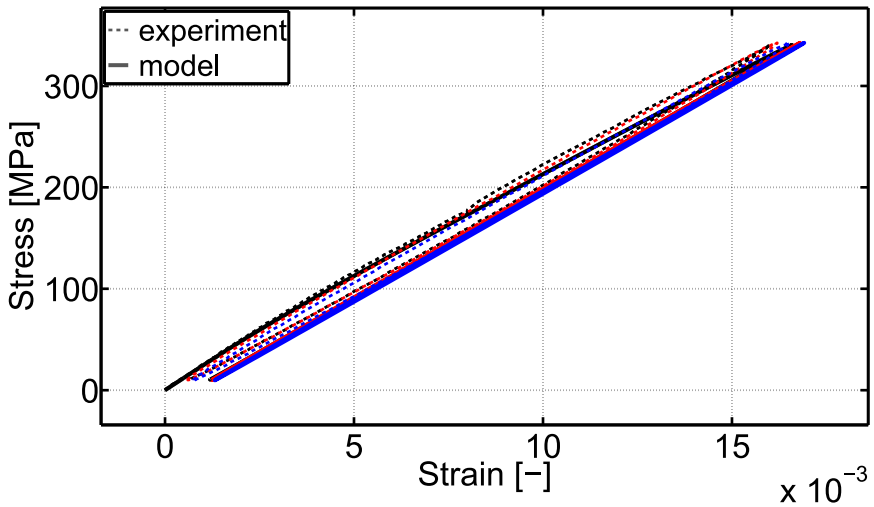

(f) Stress ($\overline{\sigma}_{xx}$) vs. strain ($\overline{\varepsilon}_{xx}$) for the 1^{st}, 10^{th} and 79^{th} cycles, represented in black, red and blue, respectively

Figure IV.8: Stress-controlled cyclic test: 100 cycles performed at 1 Hz for a $[0^o]_4$ laminated specimen. These data are used for the validation.

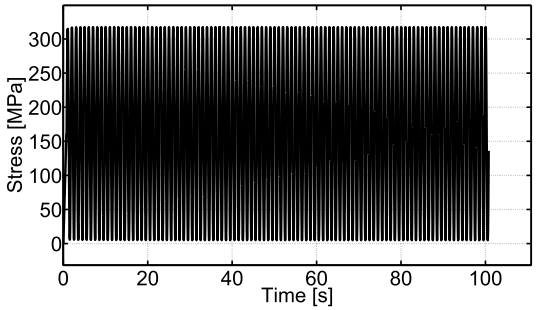

(a) Applied stress ($\overline{\sigma}_{xx}$) vs. time

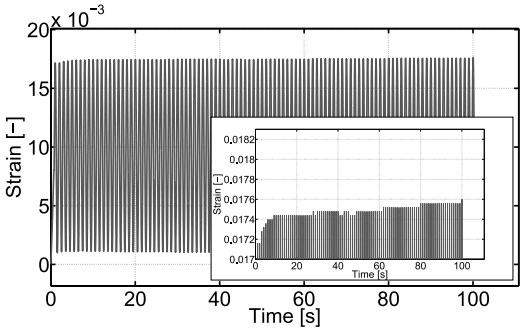

(b) Experimental strain response ($\overline{\varepsilon}_{xx}$) vs. time

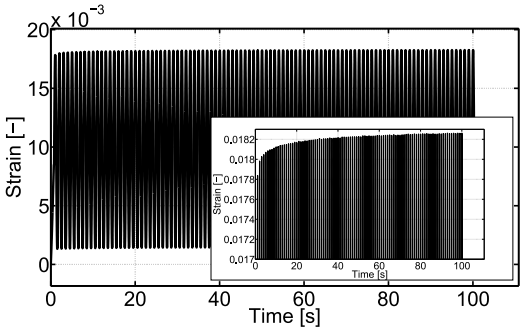

(c) Simulated strain response ($\overline{\varepsilon}_{xx}$) vs. time

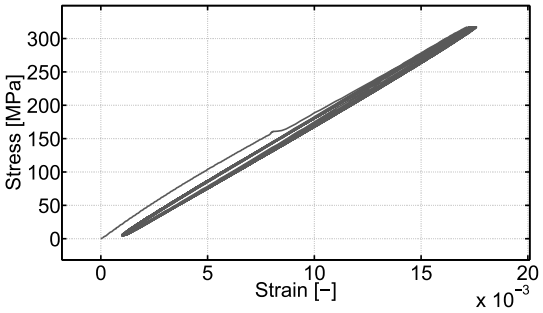

(d) Stress ($\overline{\sigma}_{xx}$) vs. strain ($\overline{\varepsilon}_{xx}$), experiement

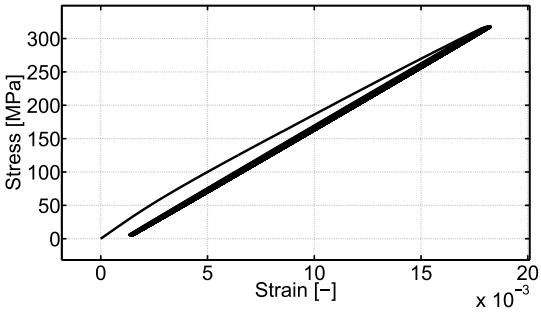

(e) Stress ($\overline{\sigma}_{xx}$) vs. strain ($\overline{\varepsilon}_{xx}$), simulation

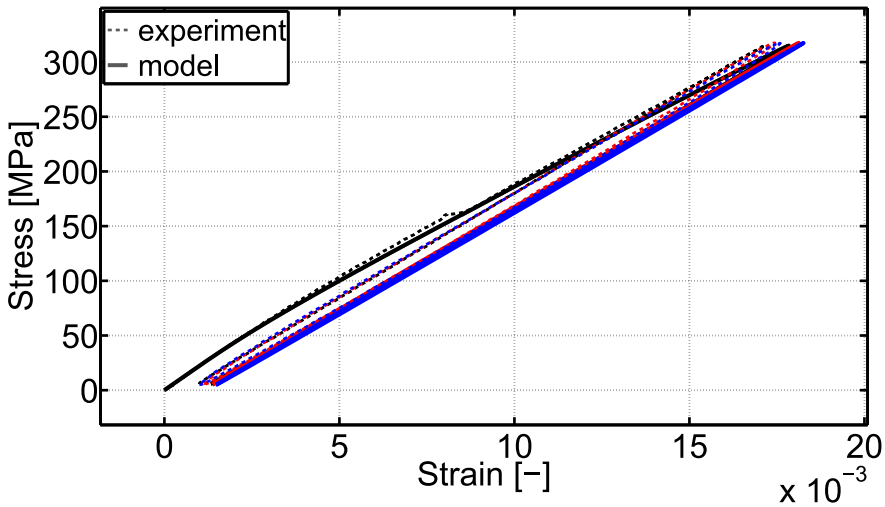

(f) Stress ($\overline{\sigma}_{xx}$) vs. strain ($\overline{\varepsilon}_{xx}$) for the 1^{st}, 10^{th} and 100^{th} cycles, represented in black, red and blue, respectively

Figure IV.9: Stress-controlled cyclic test: 100 cycles performed at 1 Hz for a $[\pm 15^o]_s$ laminated specimen. These data are used for the validation.

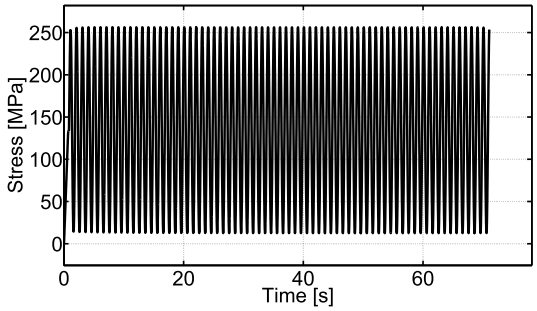

(a) Applied stress ($\overline{\sigma}_{xx}$) vs. time

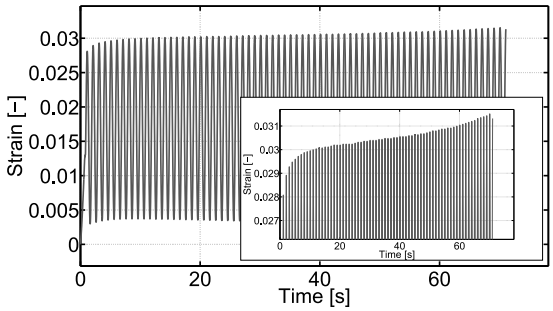

(b) Experimental strain response ($\overline{\varepsilon}_{xx}$) vs. time

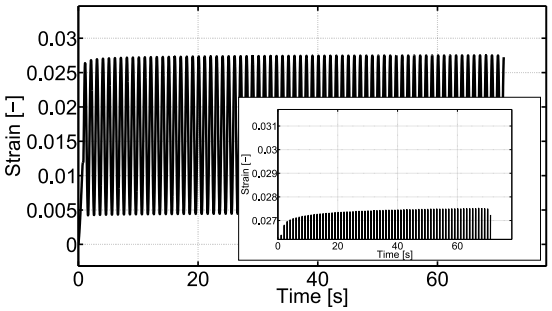

(c) Simulated strain response ($\overline{\varepsilon}_{xx}$) vs. time

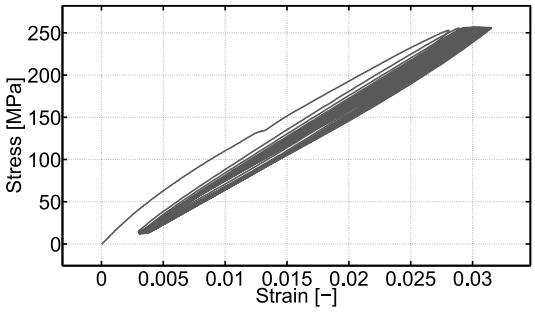

(d) Stress ($\overline{\sigma}_{xx}$) vs. strain ($\overline{\varepsilon}_{xx}$), experiement

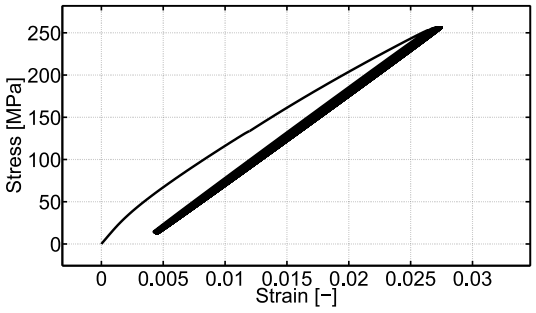

(e) Stress ($\overline{\sigma}_{xx}$) vs. strain ($\overline{\varepsilon}_{xx}$), simulation

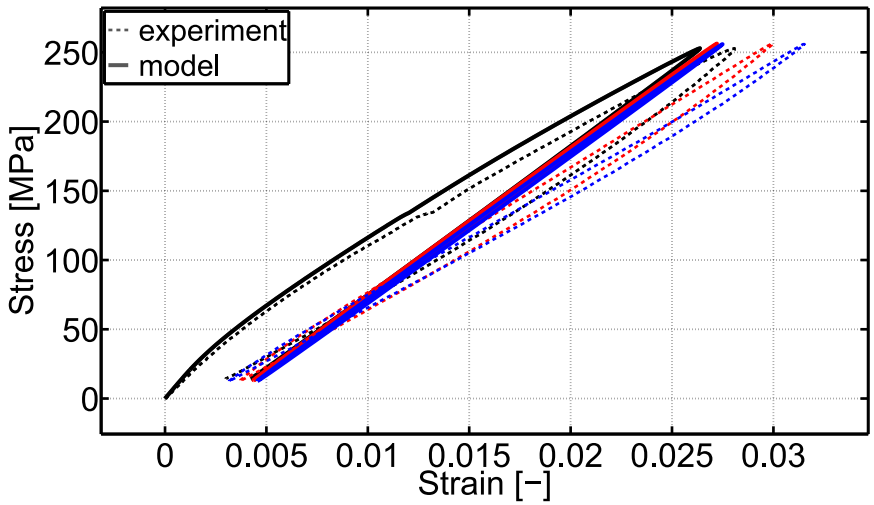

(f) Stress ($\overline{\sigma}_{xx}$) vs. strain ($\overline{\varepsilon}_{xx}$) for the 1^{st}, 10^{th} and 70^{th} cycles, represented in black, red and blue, respectively

Figure IV.10: Stress-controlled cyclic test: 100 cycles performed at 1 Hz for a $[\pm 30^o]_s$ laminated specimen. These data are used for the validation.

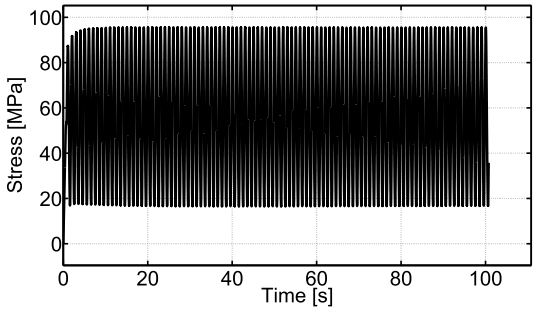

(a) Applied stress ($\overline{\sigma}_{xx}$) vs. time

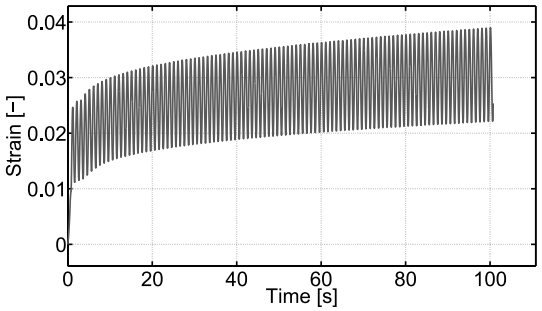

(b) Experimental strain response ($\overline{\varepsilon}_{xx}$) vs. time

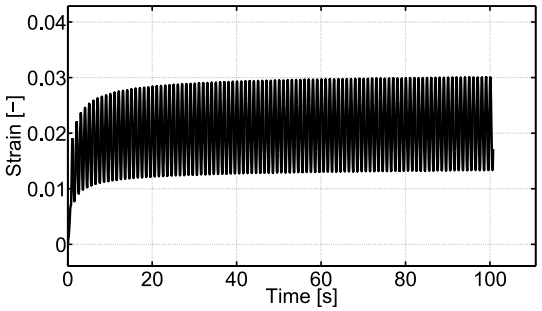

(c) Simulated strain response ($\overline{\varepsilon}_{xx}$) vs. time

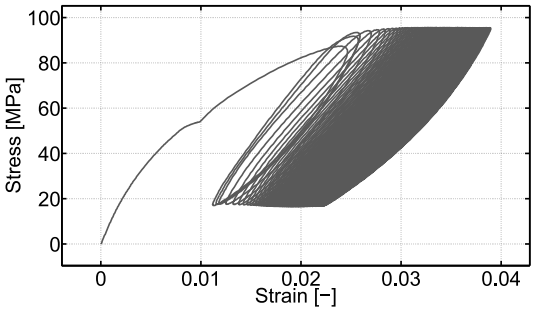

(d) Stress ($\overline{\sigma}_{xx}$) vs. strain ($\overline{\varepsilon}_{xx}$), experiement

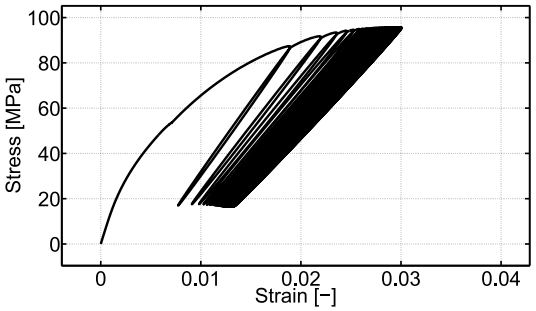

(e) Stress ($\overline{\sigma}_{xx}$) vs. strain ($\overline{\varepsilon}_{xx}$), simulation

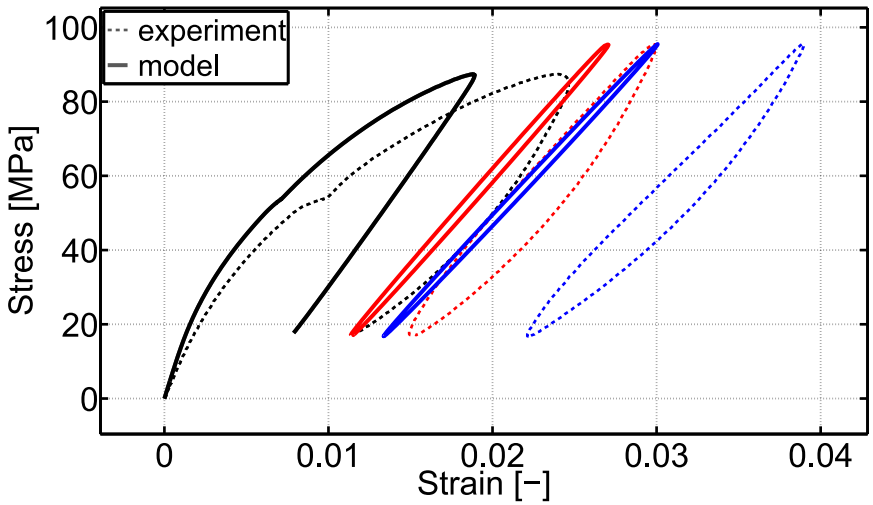

(f) Stress ($\overline{\sigma}_{xx}$) vs. strain ($\overline{\varepsilon}_{xx}$) for the 1^{st}, 10^{th} and 100^{th} cycles, represented in black, red and blue, respectively

Figure IV.11: Stress-controlled cyclic test: 100 cycles performed at 1 Hz for a $[\pm 45^o]_s$ laminated specimen. These data are used for the validation.

Regarding the temperature measurements, it can be noticed that, within the 100 cycles performed during the tests, temperature elevations remain relatively low (about 3.5 to 4 ^{o}C) for the $[0^o]_4$ and $[\pm 15^o]_s$ specimens (see Figures IV.12 and IV.13). Thus, the isothermal conditions can be reasonably considered as correct for these cases. However, for the $[\pm 30^o]_s$ and $[\pm 45^o]_s$ specimens, the temperature elevations start becoming significant (see Figures IV.14 and IV.15), making the isothermal assumption no longer valid. This point may also explain why a deviation is observed for these specimens between the experimental response and the one simulated with the multi-scale model, which is formulated under isothermal conditions. Moreover, as it has been also observed for the unfilled polyamide 6-6 matrix (see Section 4.3 in Chapter II), the temperature elevations are far from the stabilized regime within 100 cycles and consequently a significant temperature increase is likely to occur after a more important number of cycles.

It is worth pointing out that the hysteresis loops upon the loading/unloading stages of each single cycle are not well reproduced by the multi-scale model. This is likely due to the sub-model of the yarn phase, which, unlike the one of the matrix, does not integrate any viscoelastic mechanism and time-dependent features in general. This point can also be concluded from an energetic point of view. Indeed, the elevations of temperature computed from the uncoupled "0D" thermal analyses (see Figures IV.12, IV.13, IV.14 and IV.15) are far lower than the ones experimentally observed (especially for the the $[\pm 30^o]_s$ and $[\pm 45^o]_s$ specimens), evidencing that the multi-scale model does not capture accurately the energy dissipated by the composite. Integrating viscoelastic mechanisms within the yarn phase might likely resolve this issue.

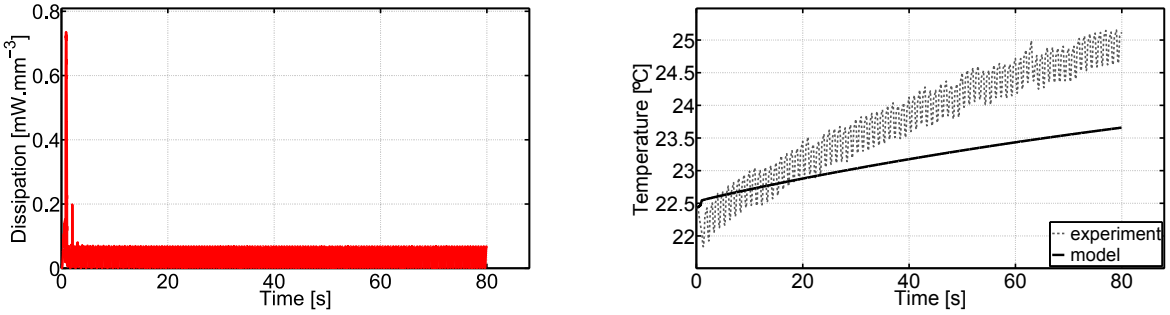

(a) Dissipation ($\dot{\Phi}$) vs. time

(b) Temperature (T) vs. time

Figure IV.12: Assessment of the temperature elevation induced by the dissipation through the uncoupled "0D" thermal analysis (see Appendix C) for the stress-controlled cyclic test: 100 cycles performed at 1 Hz for a $[0^o]_4$ laminated specimen (see Figure IV.8).

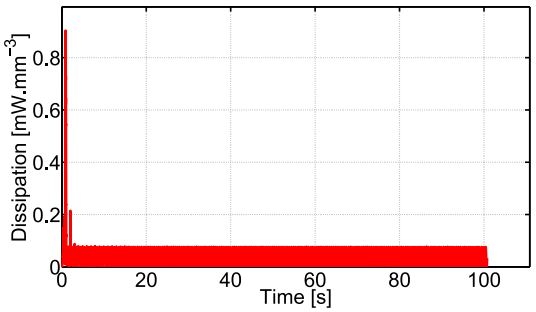

(a) Dissipation ($\bar{\dot{\Phi}}$) vs. time

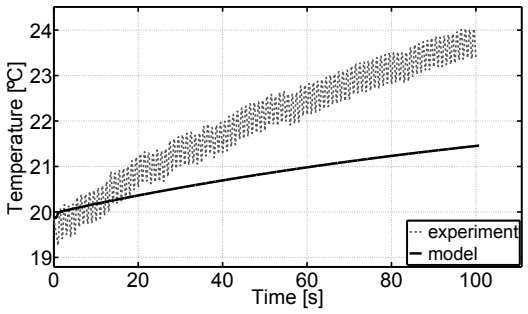

(b) Temperature (T) vs. time

Figure IV.13: Assessment of the temperature elevation induced by the dissipation through the uncoupled "0D" thermal analysis (see Appendix C) for the stress-controlled cyclic test: 100 cycles performed at 1 Hz for a $[\pm 15^o]_s$ laminated specimen (see Figure IV.9).

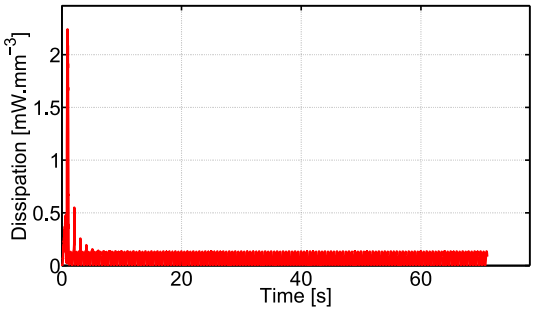

(a) Dissipation ($\bar{\dot{\Phi}}$) vs. time

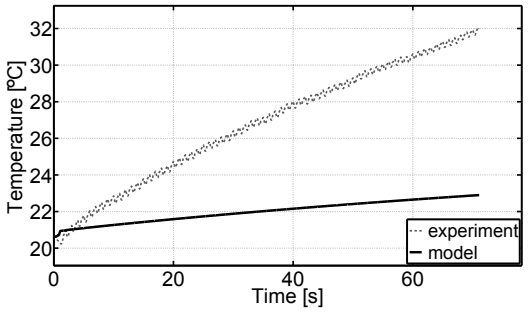

(b) Temperature (T) vs. time

Figure IV.14: Assessment of the temperature elevation induced by the dissipation through the uncoupled "0D" thermal analysis (see Appendix C) for the stress-controlled cyclic test: 100 cycles performed at 1 Hz for a $[\pm 30^o]_s$ laminated specimen (see Figure IV.10).

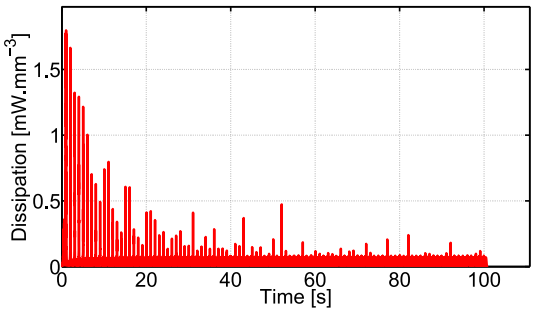

(a) Dissipation ($\bar{\dot{\Phi}}$) vs. time

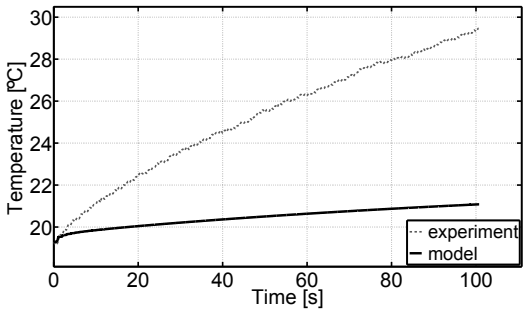

(b) Temperature (T) vs. time

Figure IV.15: Assessment of the temperature elevation induced by the dissipation through the uncoupled "0D" thermal analysis (see Appendix C) for the stress-controlled cyclic test: 100 cycles performed at 1 Hz for a $[\pm 45^o]_s$ laminated specimen (see Figure IV.11).

4 Numerical simulations, mechanical responses and dissipative behaviour of a macroscopic material point

All the simulations presented in this section were carried out with the parameters previously identified for the matrix and the yarns in Tables II.4 and IV.3, respectively.

In order to provide a better understanding of the multi-scale model, its dissipative behaviour is illustrated through examples of simulations carried out on a single macroscopic material point, so-called "virtual tests" (see Section 1). In these examples, the composite is subjected to warp tension, in-plane shear and combined warp tension and in-plane shear stress states (see Figure IV.16). The following simulations (or set of simulations) are proposed:

- Simulation set 1: Monotonic warp tension
  A normal strain in the warp direction $\overline{\varepsilon}_{11}$ of 0.02 is applied on the material in 1 s for the first simulation, 10 s for the second one and 100 s for the third one, providing a strain rate of 2×10^{-2}, 2×10^{-3} and 2×10^{-4} s^{-1}, respectively. The results of these simulations are presented in Figures IV.17 and IV.18. Note that the computations are carried out with a constant time increment equal to $1/200^{th}$ of the total duration of the corresponding simulation.

- Simulation set 2: Monotonic in-plane shear
  An in-plane shear strain $2\overline{\varepsilon}_{12}$ of 0.05 is applied on the composite in 1 s for the first simulation, 10 s for the second one and 100 s for the third one, providing a strain rate of 5×10^{-2}, 5×10^{-3} and 5×10^{-4} s^{-1}, respectively. The results of these simulations are presented in Figures IV.19 and IV.20. Note that the computations are carried out with a constant time increment equal to $1/200^{th}$ of the total duration of the corresponding simulation.

- Simulation 3: warp tension creep and strain recovery
  A normal stress in the warp direction $\overline{\sigma}_{11}$ of 350 MPa is first applied on the composite in 5 s. This stress is then held for 300 s before returning back to zero in 5 s. In a final stage, the composite is kept at zero stress for another 300 s. The results of this simulation are presented in Figures IV.21 and IV.22. Note that the computation is carried out with a constant time increment of 0.05 s.

- Simulation 4: in-plane shear creep and strain recovery
  An in-plane shear stress $\overline{\sigma}_{12}$ of 40 MPa is first applied on the composite in 5 s. This stress is then held for 300 s before returning back to zero in 5 s. In a final stage, the composite is kept at zero stress for another 300 s. The results of this simulation are presented in Figures IV.23 and IV.24. Note that the computation is carried out with a constant time increment of 0.05 s.

- Simulation 5: cyclic warp tension stress
  The composite is subjected to a cyclic triangular stress signal in the warp direction $\overline{\sigma}_{11}$. The latter oscillates between 350 and 0 MPa with a frequency of 1 Hz. 20 cycles are performed. The results of this simulation are presented in Figures IV.25 and IV.26. Note that the computation is carried out with a constant time increment of 0.005 s, i.e. 200 time increments per cycle.

- Simulation 6: cyclic in-plane shear stress
  The composite is subjected to a cyclic triangular in-plane shear stress signal $\overline{\sigma}_{12}$. The latter oscillates between 40 and 0 MPa with a frequency of 1 Hz. 20 cycles are performed. The results of this simulation are presented in Figures IV.27 and IV.28. Note that the computation is carried out with a constant time increment of 0.005 s, i.e. 200 time increments per cycle.

- Simulation set 7: Non-proportional combined warp tension and in-plane shear
  The composite is subjected to a combined warp tension and in-plane shear stress state, which is applied through two different loading paths having the same amplitudes:
  - Path 1: A normal stress in the warp direction $\overline{\sigma}_{11}$ of 200 MPa is first applied in 5 s. In the next stage, $\overline{\sigma}_{11}$ is held constant, while an in-plane shear stress $\overline{\sigma}_{12}$ of 30 MPa is applied in 5 s. Afterwards, both $\overline{\sigma}_{11}$ and $\overline{\sigma}_{12}$ are held constant for 5 s before being released in another 5 s.
  - Path 2: An in-plane shear stress $\overline{\sigma}_{12}$ of 30 MPa is first applied in 5 s. In the next stage, $\overline{\sigma}_{12}$ is held constant, while a normal stress in the warp direction $\overline{\sigma}_{11}$ of 200 MPa is applied in 5 s. Afterwards, both $\overline{\sigma}_{11}$ and $\overline{\sigma}_{12}$ are held constant for 5 s before being released in another 5 s.

  The results of these simulations are presented in Figures IV.29, IV.30 and IV.31. Note that the computations are carried out with a constant time increment of 0.05.

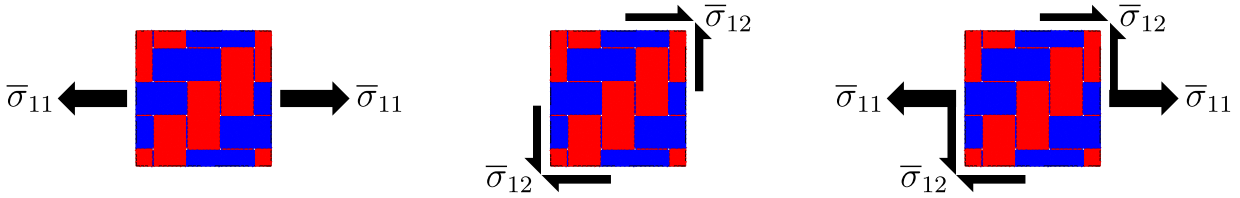

(a) Warp tension (b) In-plane shear (c) Combined warp tension and in-plane shear

Figure IV.16: Illustrations of the simulated loading configurations.

In all the simulations, the energy balance is well respected (see Figures IV.21e, IV.23e, IV.25e, IV.27e, IV.29f and IV.29g): the macroscopic strain energy $\overline{W}_\varepsilon$ is always equal to the sum of the macroscopic stored and dissipated energies, $\overline{\rho\psi}$ and $\overline{\Phi}$, respectively. Moreover the macroscopic dissipated energy always increases ($\dot{\overline{\Phi}} \geq 0$), which is in accordance with the Clausius Duhem inequality written in its macroscopic formalism in equation (I.7).

The results of these simulations are presented in four different subsections. The first one is dedicated to the simulation sets 1 and 2 (Section 4.1: Monotonic loading), the second one to the simulations 3 and 4 (Section 4.2: Creep and strain recovery), the third one to the simulations 5 and 6 (Section 4.3: Cyclic loading), and the fourth one to the simulation set 7 (Section 4.4: Non-proportional combined warp tension and in-plane shear).

4.1 Monotonic loading

In the simulation set 1 (see Figures IV.17 and IV.18), when the composite is loaded in the warp direction, most of the load is carried by the warp yarns in their longitudinal direction (see Figure IV.18c). Meanwhile, a lesser part of this load is also carried by the weft yarns in their transverse direction (see Figure IV.18d), causing micro-cracking to develop only in these yarns (see Figure IV.18f). In the matrix, most of the stresses are concentrated in the yarns-crossing areas, leading to the development of some damage in these locations (see Figures IV.18a and IV.18b). Nevertheless, the degradations occurring in the weft yarns and in the matrix seem to have limited consequences at the macroscopic scale, as most of the load is carried by the warp yarns in their longitudinal direction, which behave elastically with an important stiffness. For this reason, the response of the composite remains quasi-linear and the overall rate effect appears to be almost not observable (see Figure IV.17).

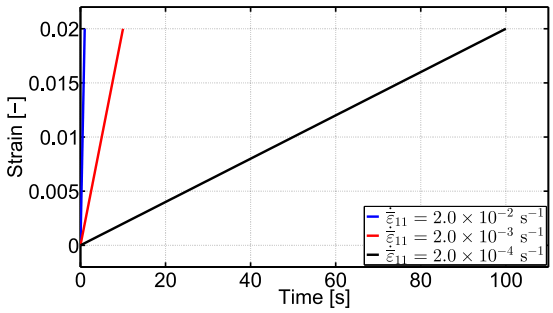

(a) Applied strain ($\bar{\varepsilon}_{11}$) vs. time

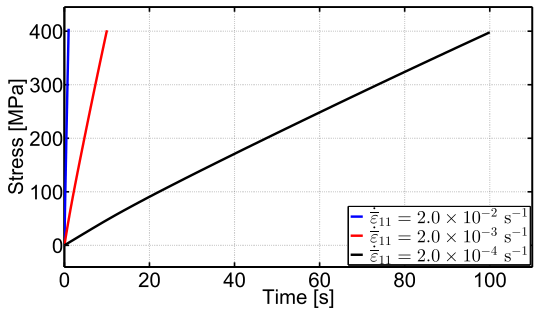

(b) Stress response ($\bar{\sigma}_{11}$) vs. time

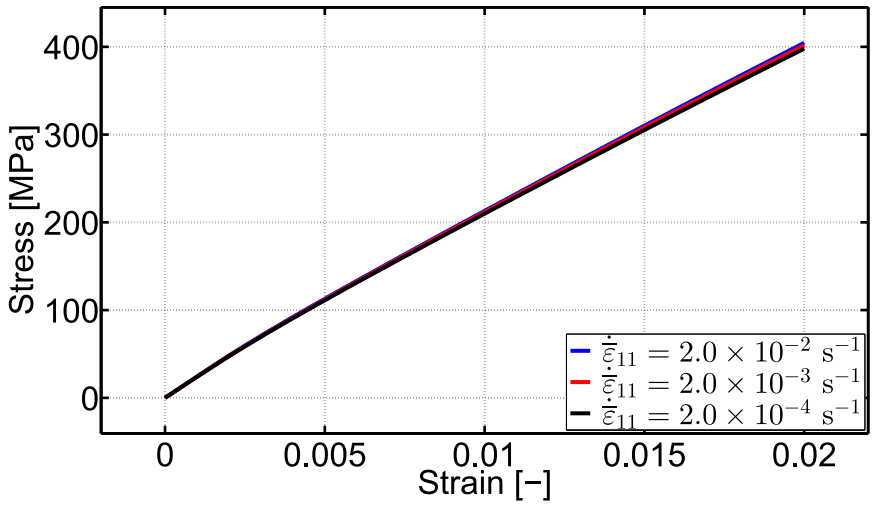

(c) Stress ($\bar{\sigma}_{11}$) vs. strain ($\bar{\varepsilon}_{11}$)

Figure IV.17: Simulation set 1: monotonic warp tension.

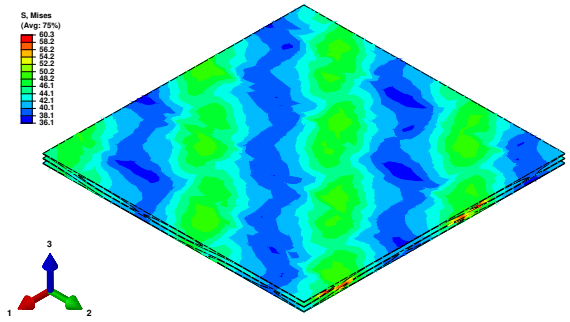

(a) Local equivalent Von Mises stress (eq($\boldsymbol{\sigma}$)) in the matrix

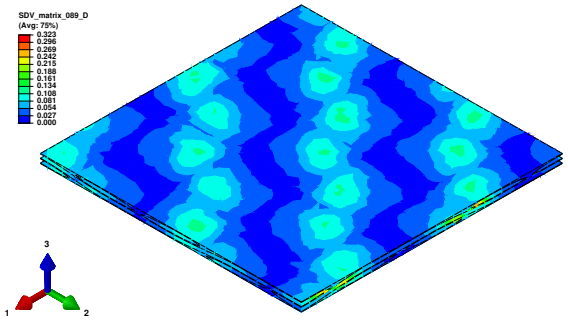

(b) Local damage (D) in the matrix

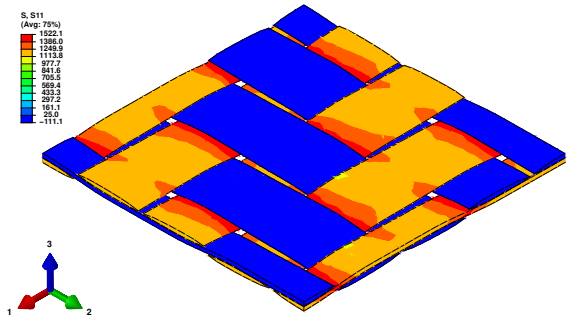

(c) Local longitudinal stress (σ_{11}) in the yarns

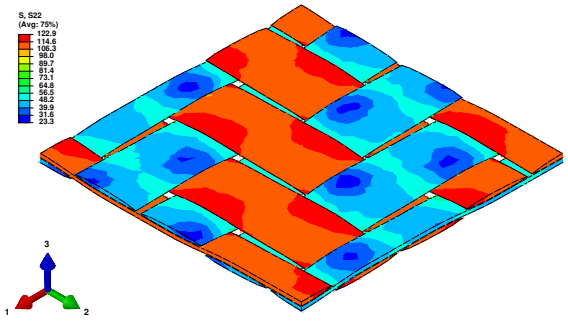

(d) Local transverse stress (σ_{22}) in the yarns

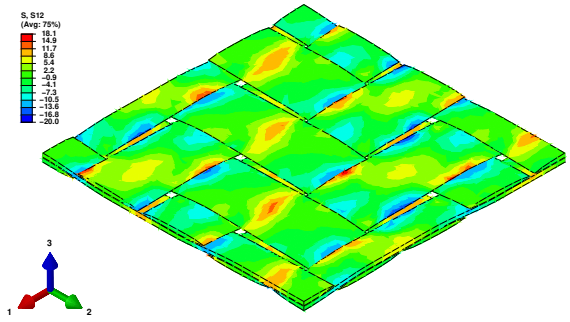

(e) Local in-plane shear stress (σ_{12}) in the yarns

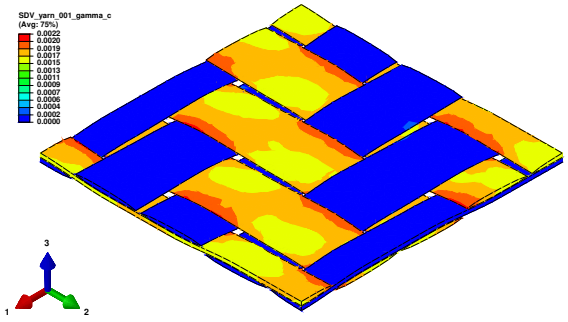

(f) Local micro-crack density (γ_c) in the yarns

Figure IV.18: Simulation set 1: monotonic warp tension, local fields at the end of the simulation performed with $\dot{\bar{\varepsilon}}_{11} = 2.0 \times 10^{-2}$ s^{-1}. Note that the local stresses in the yarns are expressed in the local coordinate system of each yarn material point (see Figure I.10d).

In the simulation set 2 (see Figures IV.19 and IV.20), when the composite is loaded in in-plane shear, there are almost neither longitudinal nor transverse stresses generated in the yarns (see Figures IV.20c and IV.20d), which are only subjected to in-shear stress fields (see Figure IV.20e). This brings about a fast growth of the micro-cracking and the stiffness reduction in both warp and weft yarns (see Figure IV.20f). Then, the overall load is progressively transferred to the matrix where the stresses are mainly concentrated in the inter-yarns areas and damage develops (see Figures IV.20a and IV.20b). Note that those

degradation mechanisms have a significant influence on the macroscopic in-plane shear response of the composite, which appears to be more matrix-dominated, as the rate effect can be clearly observed (see Figure IV.19c).

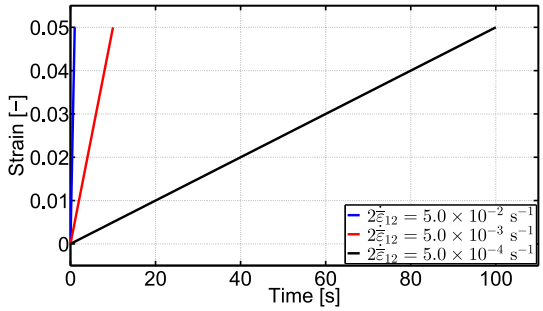

(a) Applied strain ($2\overline{\varepsilon}_{12}$) vs. time

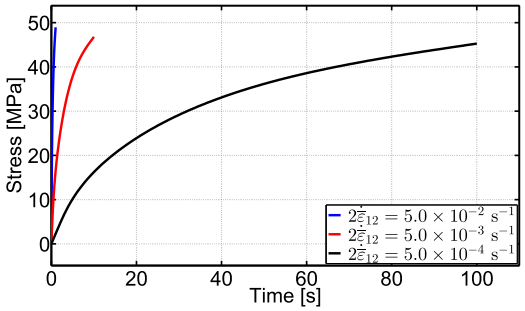

(b) Stress response ($\overline{\sigma}_{12}$) vs. time

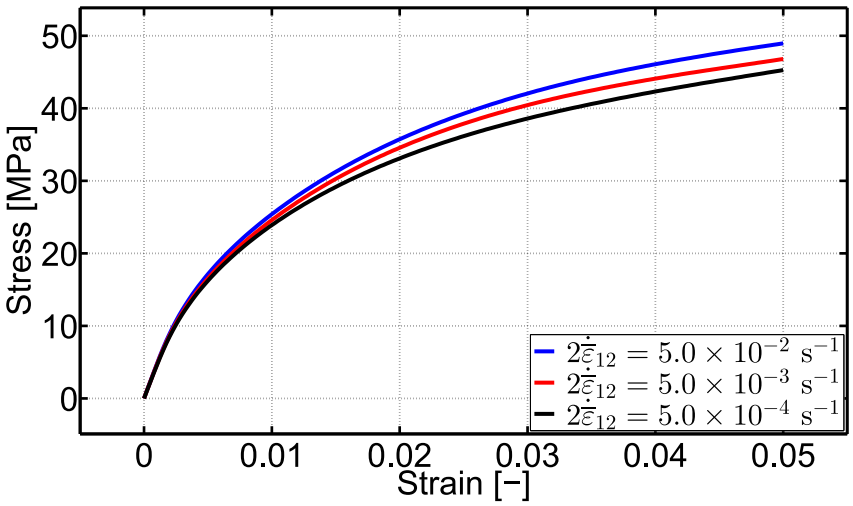

(c) Stress ($\overline{\sigma}_{12}$) vs. strain ($2\overline{\varepsilon}_{12}$)

Figure IV.19: Simulation set 2: monotonic in-plane shear.

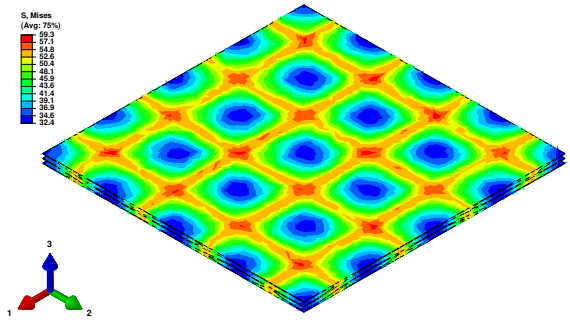

(a) Local equivalent Von Mises stress (eq($\boldsymbol{\sigma}$)) in the matrix

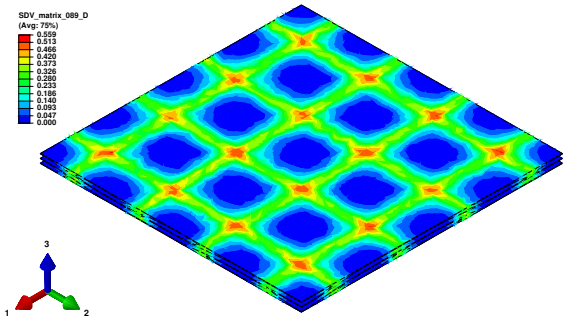

(b) Local damage (D) in the matrix

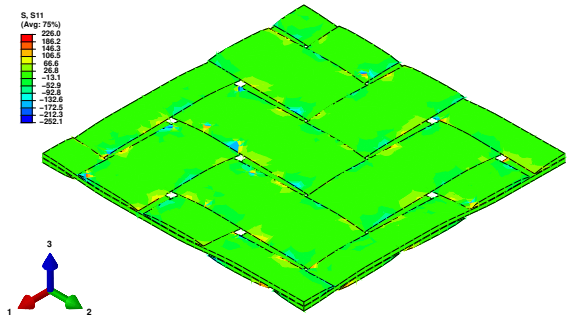

(c) Local longitudinal stress (σ_{11}) in the yarns

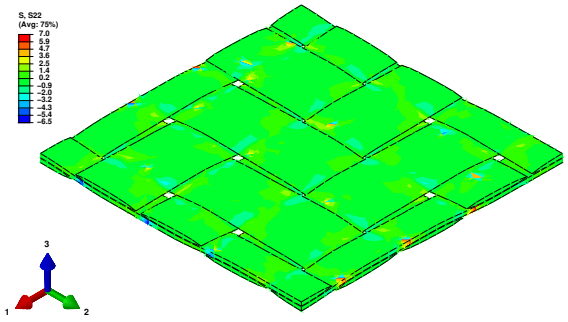

(d) Local transverse stress (σ_{22}) in the yarns

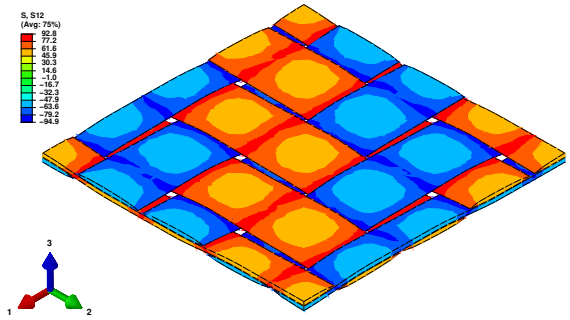

(e) Local in-plane shear stress (σ_{12}) in the yarns

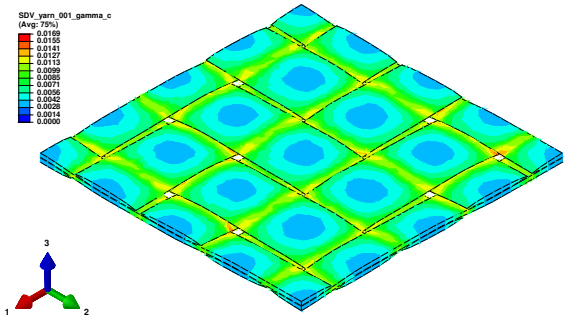

(f) Local micro-crack density (γ_c) in the yarns

Figure IV.20: Simulation set 2: monotonic in-plane shear, local fields at the end of the simulation performed with $2\dot{\bar{\varepsilon}}_{12} = 5.0 \times 10^{-2}$ s^{-1}. Note that the local stresses in the yarns are expressed in the local coordinate system of each yarn material point (see Figure I.10d).

4.2 Creep and strain recovery

In the simulations 3 and 4 (see Figures IV.21, IV.22, IV.23 and IV.24), during the creep stage, similarly to the unfilled matrix (see Section 5.1 in Chapter II), the macroscopic strain increases under the action of a constant macroscopic stress. Over this period, the composite both stores and dissipates energy ($\overline{\rho}\dot{\overline{\psi}} > 0$ and $\dot{\overline{\Phi}} > 0$). In the next stage, the composite is unloaded and left free of stress. A part of the macroscopic strain is quasi-instantaneously

recovered, whereas another part is recovered through a certain amount of time, at the end of which an irrecoverable part remains (see Figures IV.21b and IV.23b). During this strain recovery stage, the stored energy is converted into dissipated energy (see Figures IV.21e and IV.23e). The macroscopic creep response of the composite is caused by the time-dependent behaviour of the matrix phase, as well as the microstructure interactions between the matrix and the yarn phases. Although the sub-model of the yarns does not account for any time-dependent feature, a micro-crack density growth is observed within the yarn phase (see Figures IV.22 and IV.24). Indeed, when the matrix locally creeps and gets damaged, a part of its sustained load is gradually transferred to the yarns, leading to an increase of micro-crack density in this phase. Moreover, in warp tension the macroscopic creep is quite low, in contrast to the in-plane shear. This is due to the fact that, in the latter case, the behaviour of the composite is mainly matrix-dominated.

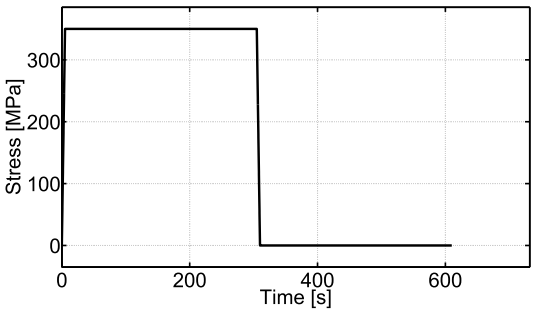

(a) Applied stress ($\overline{\sigma}_{11}$) vs. time

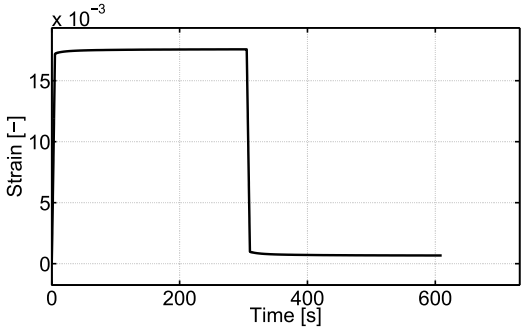

(b) Strain response ($\overline{\varepsilon}_{11}$) vs. time

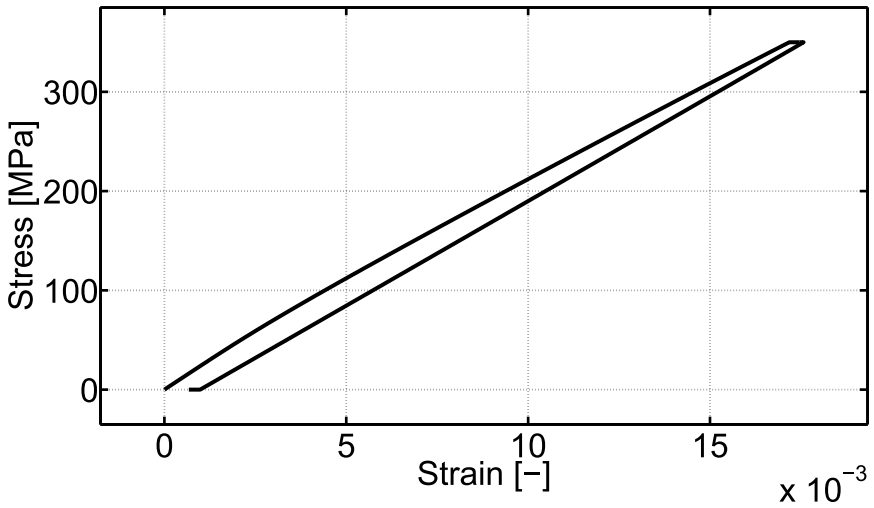

(c) Stress ($\overline{\sigma}_{11}$) vs. strain ($\overline{\varepsilon}_{11}$)

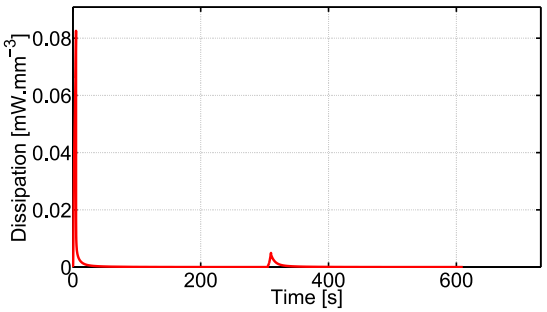

(d) Dissipation ($\dot{\overline{\Phi}}$) vs. time

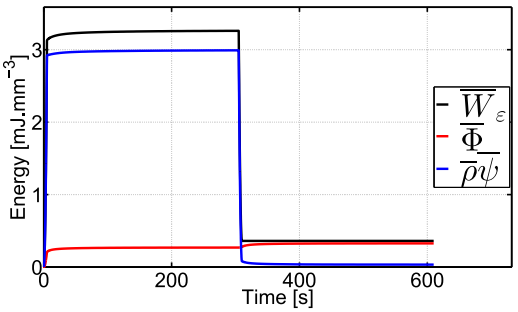

(e) Strain, dissipated and stored energies ($\overline{W}_\varepsilon$, $\overline{\Phi}$ and $\overline{\rho\psi}$, respectively) vs. time

Figure IV.21: Simulation 3: warp tension creep and strain recovery.

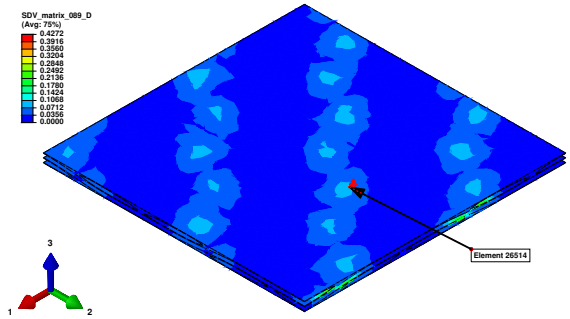

(a) Local damage (D) in the matrix at the end of the loading stage ($t = 5$ s)

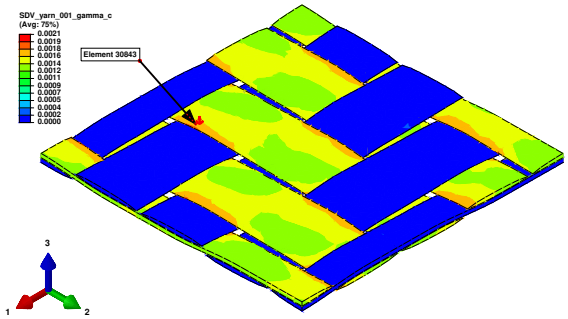

(b) Local micro-crack density (γ_c) in the yarns at the end of the loading stage ($t = 5$ s)

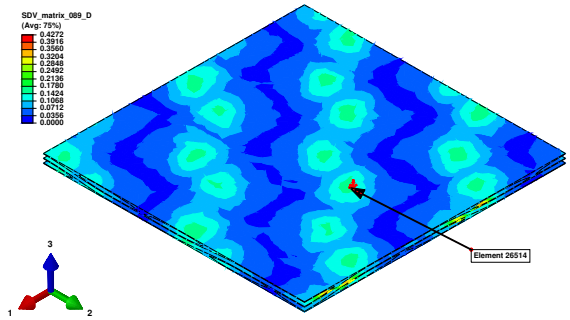

(c) Local damage (D) in the matrix at the end of the creep stage ($t = 305$ s)

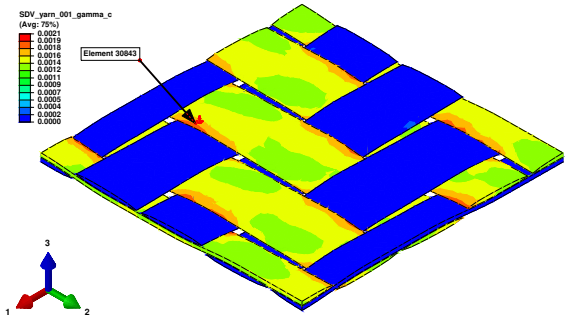

(d) Local micro-crack density (γ_c) in the yarns at the end of the creep stage ($t = 305$ s)

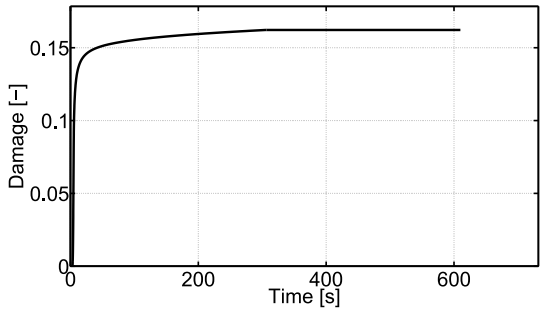

(e) Local damage (D) in the matrix, for the element 26514 marked above in Figures IV.22a and IV.22c

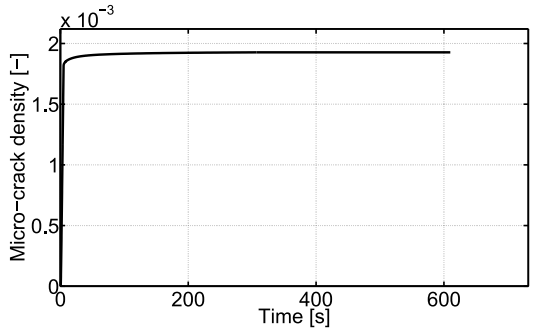

(f) Local micro-crack density (γ_c) in the yarns, for the element 30843 marked above in Figures IV.22b and IV.22d

Figure IV.22: Simulation 3: warp tension creep and strain recovery, local fields.

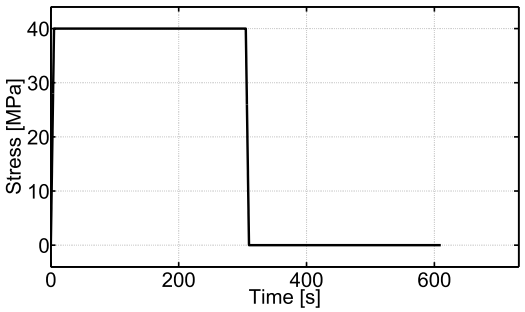

(a) Applied stress ($\overline{\sigma}_{12}$) vs. time

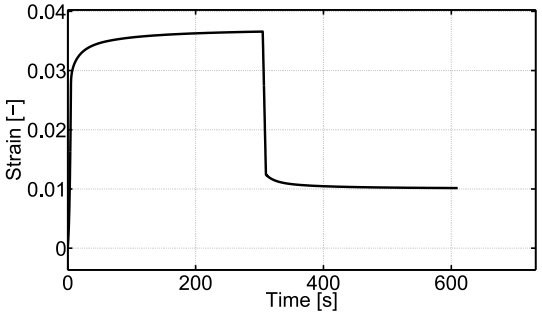

(b) Strain response ($2\overline{\varepsilon}_{12}$) vs. time

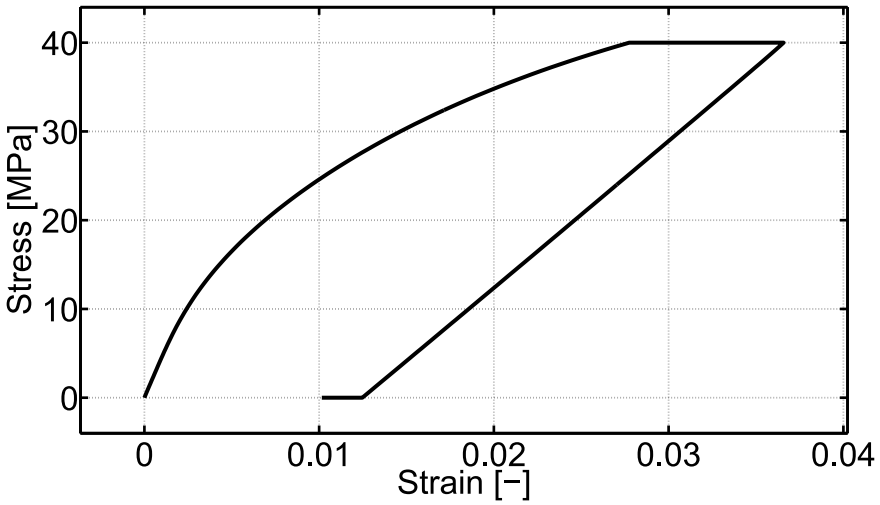

(c) Stress ($\overline{\sigma}_{12}$) vs. strain ($2\overline{\varepsilon}_{12}$)

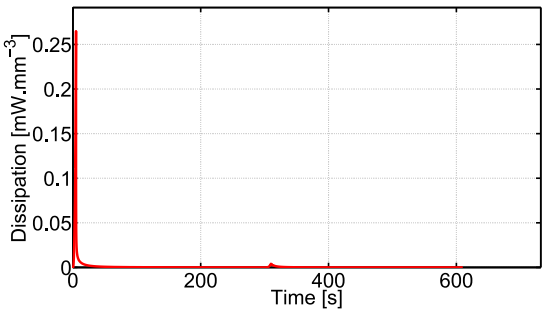

(d) Dissipation ($\dot{\overline{\Phi}}$) vs. time

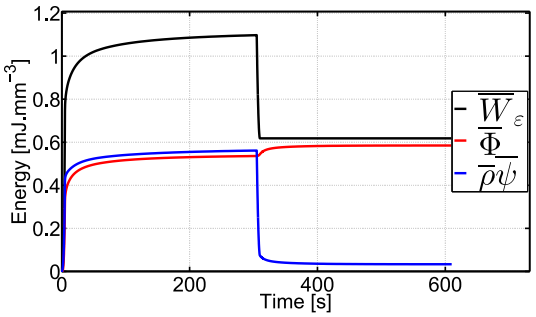

(e) Strain, dissipated and stored energies ($\overline{W}_\varepsilon$, $\overline{\Phi}$ and $\overline{\rho\psi}$, respectively) vs. time

Figure IV.23: Simulation 4: in-plane shear creep and strain recovery.

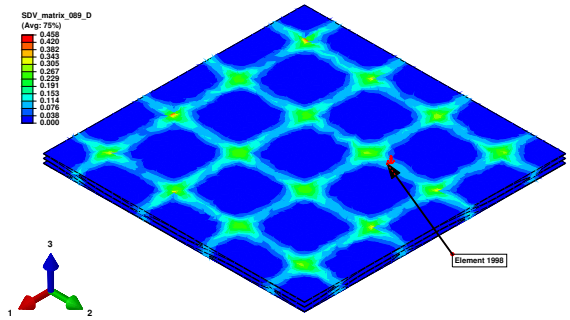

(a) Local damage (D) in the matrix at the end of the loading stage ($t = 5$ s)

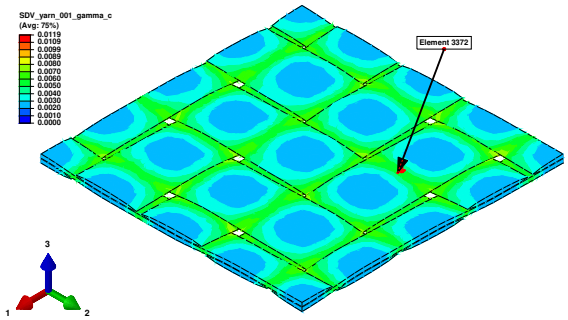

(b) Local micro-crack density (γ_c) in the yarns at the end of the loading stage ($t = 5$ s)

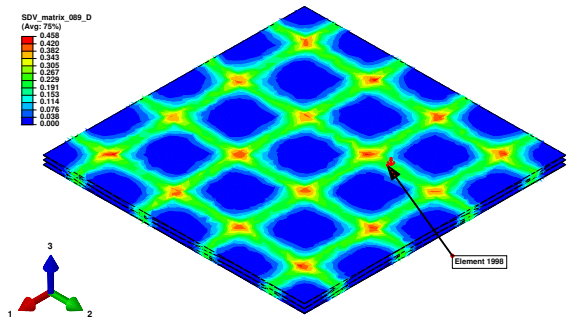

(c) Local damage (D) in the matrix at the end of the creep stage ($t = 305$ s)

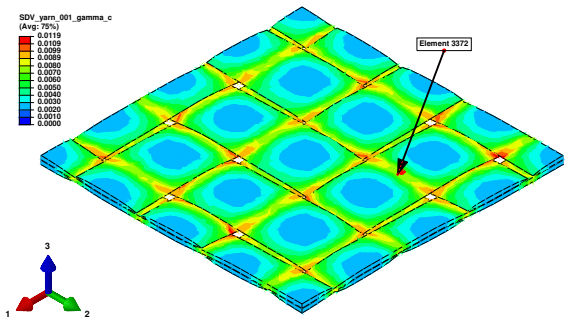

(d) Local micro-crack density (γ_c) in the yarns at the end of the creep stage ($t = 305$ s)

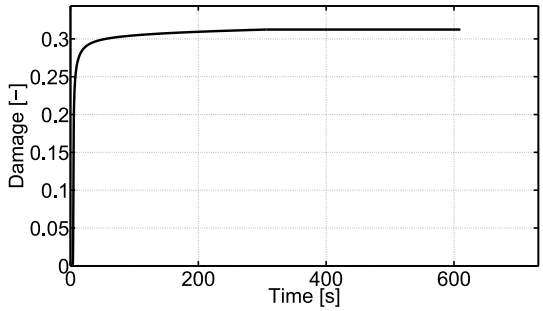

(e) Local damage (D) in the matrix, for the element 1998 marked above in Figures IV.24a and IV.24c

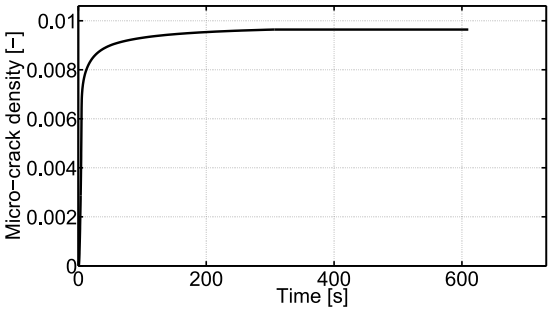

(f) Local micro-crack density (γ_c) in the yarns, for the element 3372 marked above in Figures IV.24b and IV.24d

Figure IV.24: Simulation 4: in-plane shear creep and strain recovery, local fields.

4.3 Cyclic loading

In the simulations 5 and 6 (see Figures IV.25, IV.26, IV.27 and IV.28), under cyclic stress conditions, the composite exhibits an overall creep as the macroscopic strain increases from one cycle to another under the action of the mean macroscopic stress. Through the repeated cycles, damage accumulates in the matrix and is accompanied by a micro-crack growth in yarns due to the microstructure interactions. This leads to a gradual reduction of the composite stiffness throughout the repeated cycles and an increase of the remaining strain upon unloading. As previously remarked for the simulations 3 and 4, and for the same reasons,

this phenomenon is much more important when the composite is loaded in in-plane shear. Moreover, despite being hardly observable (especially in warp tension), hysteresis loops inherited from the viscoelasticity of the matrix phase (see Section 5.1 in Chapter II) can be observed at the macroscopic scale, bringing a certain amount of dissipated energy at each cycle. This matrix-related dissipation represents, after a certain number of cycles, most of the total macroscopic dissipated energy.

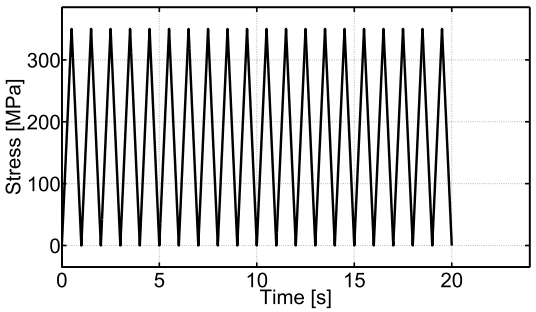

(a) Applied stress ($\overline{\sigma}_{11}$) vs. time

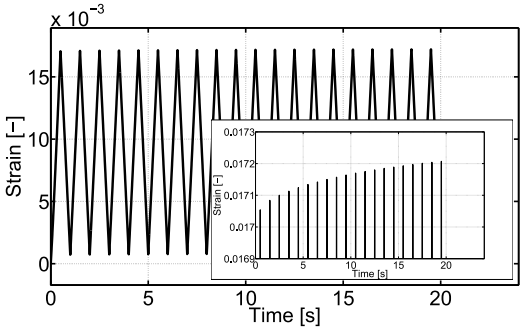

(b) Strain response ($\overline{\varepsilon}_{11}$) vs. time

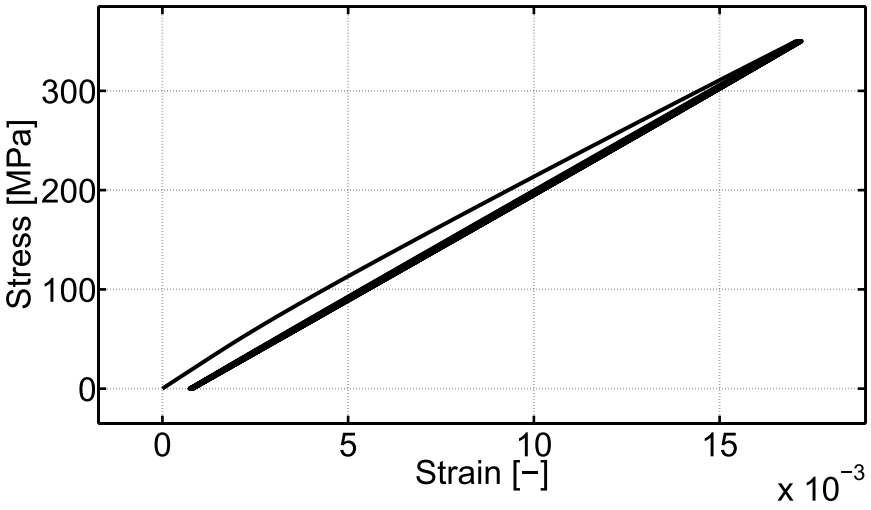

(c) Stress ($\overline{\sigma}_{11}$) vs. strain ($\overline{\varepsilon}_{11}$)

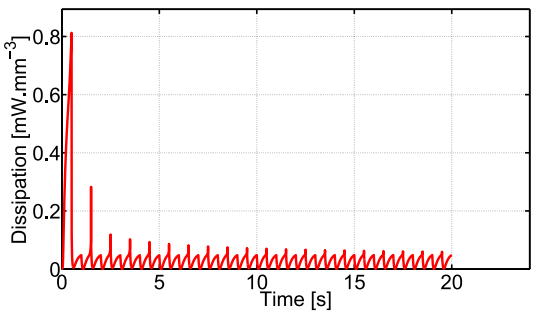

(d) Dissipation ($\dot{\overline{\Phi}}$) vs. time

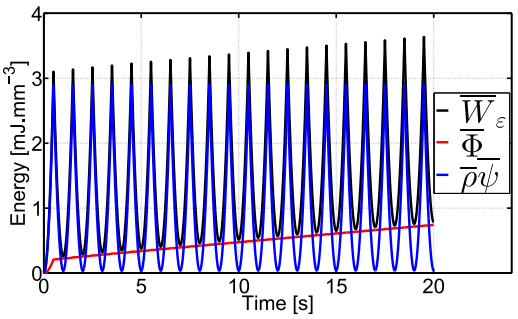

(e) Strain, dissipated and stored energies ($\overline{W}_\varepsilon$, $\overline{\Phi}$ and $\overline{\rho\psi}$, respectively) vs. time

Figure IV.25: Simulation 5: cyclic warp tension stress.

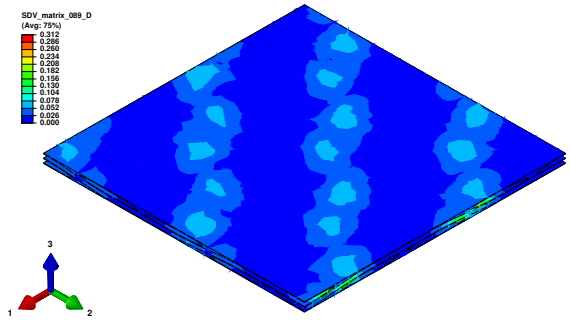

(a) Local damage (D) in the matrix at the end of the 1^{st} cycle ($t = 1$ s)

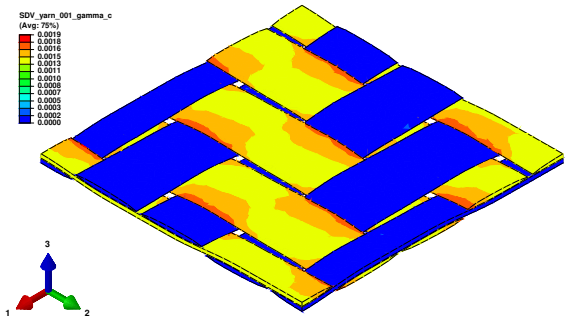

(b) Local micro-crack density (γ_c) in the yarns at the end of the 1^{st} cycle ($t = 1$ s)

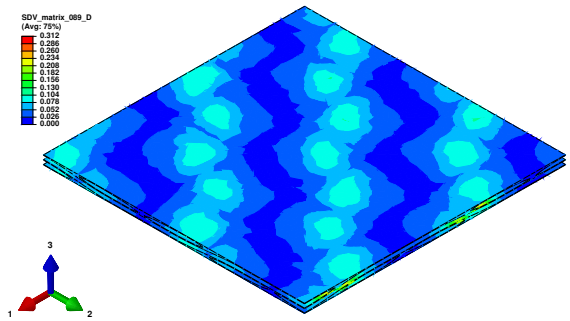

(c) Local damage (D) in the matrix at the end of the 10^{th} cycle ($t = 10$ s)

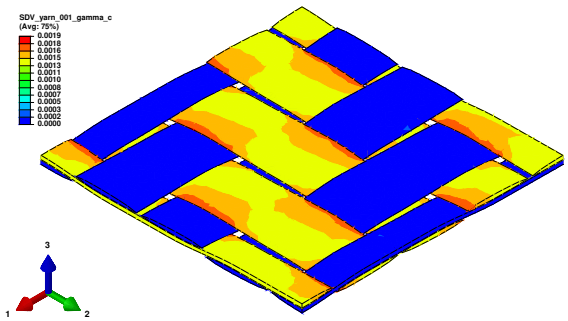

(d) Local micro-crack density (γ_c) in the yarns at the end of the 10^{th} cycle ($t = 10$ s)

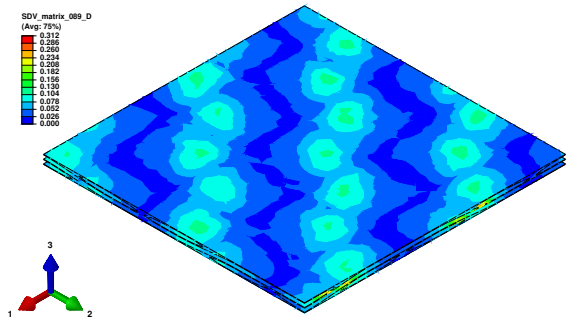

(e) Local damage (D) in the matrix at the end of the 20^{th} cycle ($t = 20$ s)

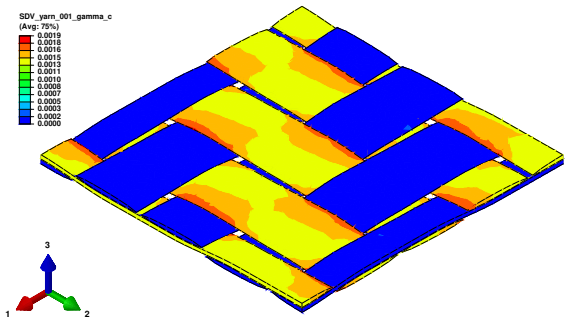

(f) Local micro-crack density (γ_c) in the yarns at the end of the 20^{th} cycle ($t = 20$ s)

Figure IV.26: Simulation 5: cyclic warp tension stress, local fields.

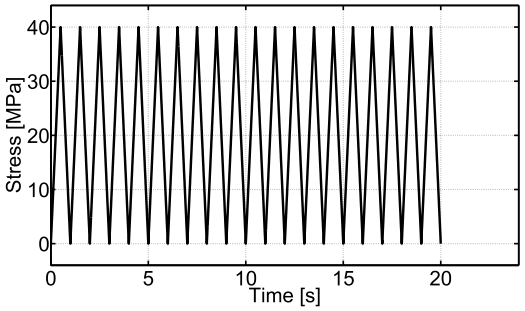

(a) Applied stress ($\overline{\sigma}_{12}$) vs. time

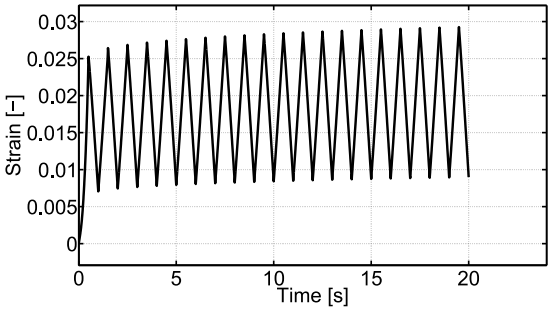

(b) Strain response ($2\overline{\varepsilon}_{12}$) vs. time

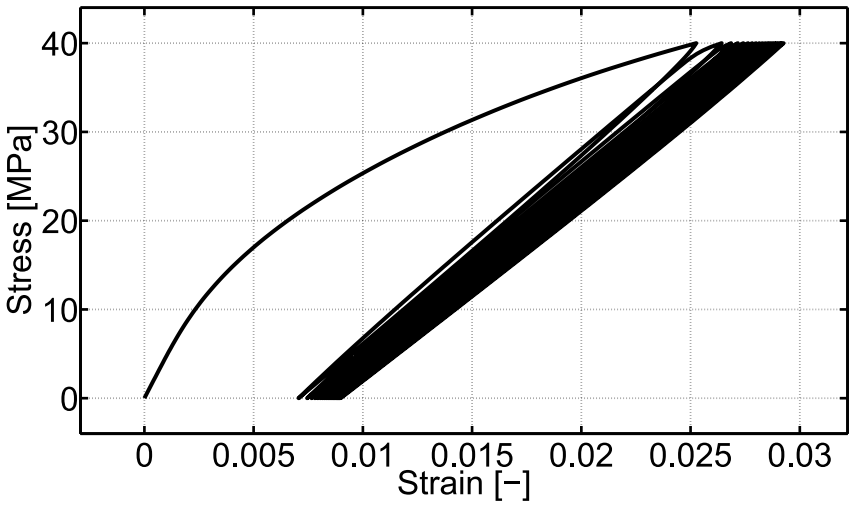

(c) Stress ($\overline{\sigma}_{12}$) vs. strain ($2\overline{\varepsilon}_{12}$)

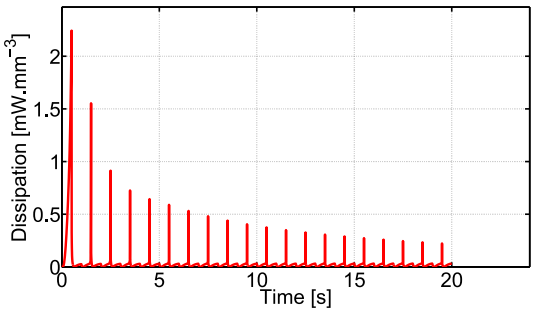

(d) Dissipation ($\dot{\overline{\Phi}}$) vs. time

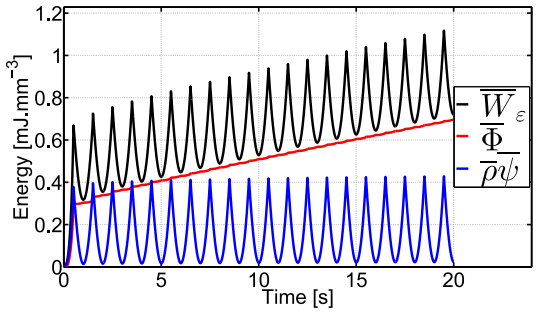

(e) Strain, dissipated and stored energies ($\overline{W}_\varepsilon$, $\overline{\Phi}$ and $\overline{\rho\psi}$, respectively) vs. time

Figure IV.27: Simulation 6: cyclic in-plane shear stress.

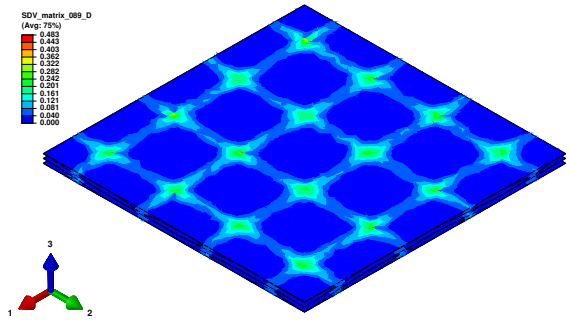

(a) Local damage (D) in the matrix at the end of the 1^{st} cycle ($t = 1$ s)

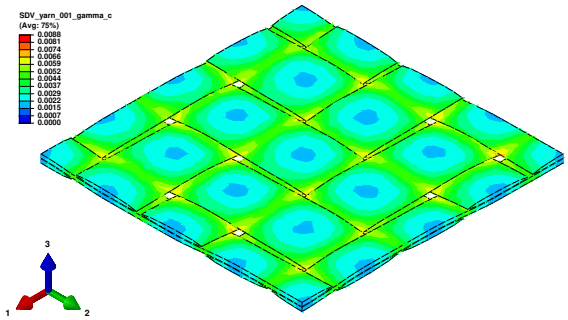

(b) Local micro-crack density (γ_c) in the yarns at the end of the 1^{st} cycle ($t = 1$ s)

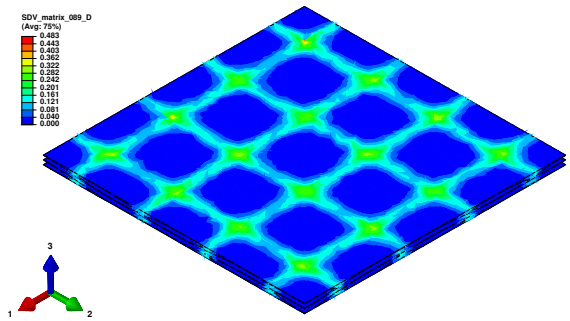

(c) Local damage (D) in the matrix at the end of the 10^{th} cycle ($t = 10$ s)

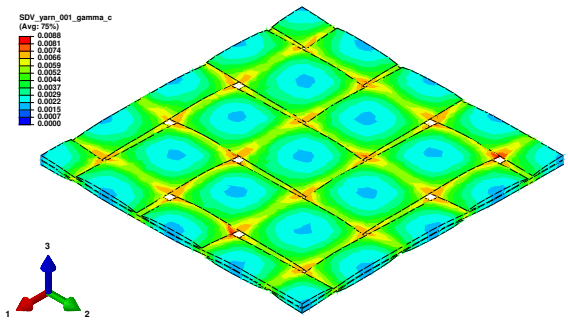

(d) Local micro-crack density (γ_c) in the yarns at the end of the 10^{th} cycle ($t = 10$ s)

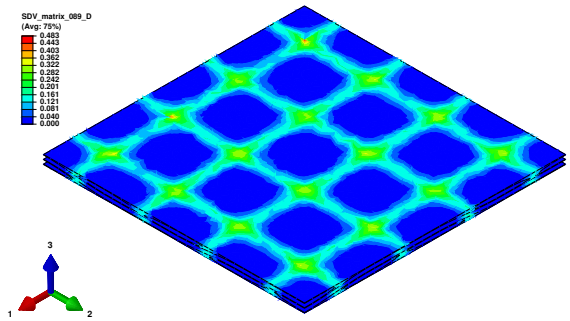

(e) Local damage (D) in the matrix at the end of the 20^{th} cycle ($t = 20$ s)

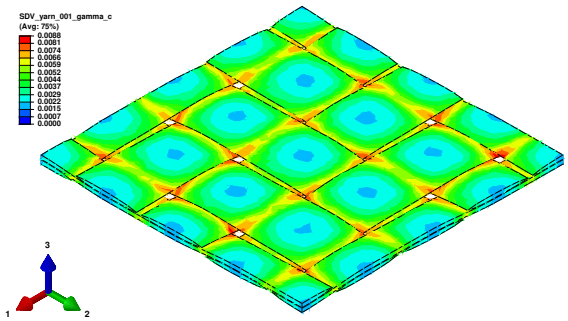

(f) Local micro-crack density (γ_c) in the yarns at the end of the 20^{th} cycle ($t = 20$ s)

Figure IV.28: Simulation 6: cyclic in-plane shear stress, local fields.

4.4 Non-proportional combined warp tension and in-plane shear

The simulation set 7 (see Figures IV.29, IV.30 and IV.31) highlights the importance of the loading path when the composite is subjected to combined stress state. Although the same stress amplitudes are applied for both paths 1 and 2, it can be noticed that the amplitudes of the strain responses are quite different. The maximal value of the normal strain $\overline{\varepsilon}_{11}$ resulting from the path 1 is slightly greater than the one obtained from the path

2. Indeed, for the path 1, the normal stress $\overline{\sigma}_{11}$ is held longer than for the path 2. Consequently, the composite is exposed more time to creep in the warp direction. Similarly, the maximal value of the in-plane shear strain $2\overline{\varepsilon}_{12}$ resulting from the path 2 is far greater than the one obtained from the path 1. Indeed, for the path 2, the in-plane shear stress $\overline{\sigma}_{12}$ is held longer than for the path 1. Consequently, the composite is exposed more time to creep in in-plane shear. Nevertheless, the difference in the strain amplitudes is much more important in in-plane shear, as in this case the behaviour of the composite is more matrix-dominated and therefore exhibits more creep. From an energetic point of view (see Figures IV.29f and IV.29g), the composite has dissipated more energy with the loading path 1 than with the path 2, whereas the maximal amount of stored energy is approximately the same for both paths. However, a larger part of this stored energy has been recovered with the path 2. Overall, the loading path 1 involves more strain energy than the path 2.

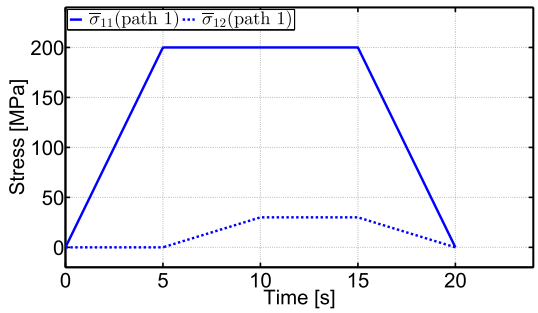

(a) Path 1: applied stresses ($\overline{\sigma}_{11}$ and $\overline{\sigma}_{12}$) vs. time

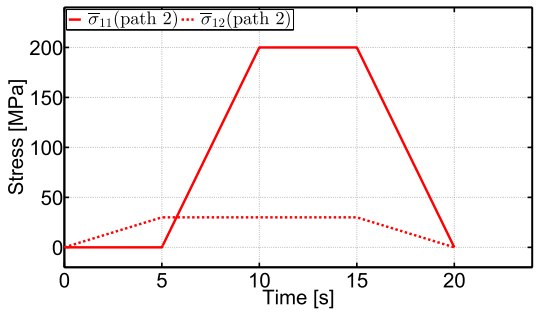

(b) Path 2: applied stresses ($\overline{\sigma}_{11}$ and $\overline{\sigma}_{12}$) vs. time

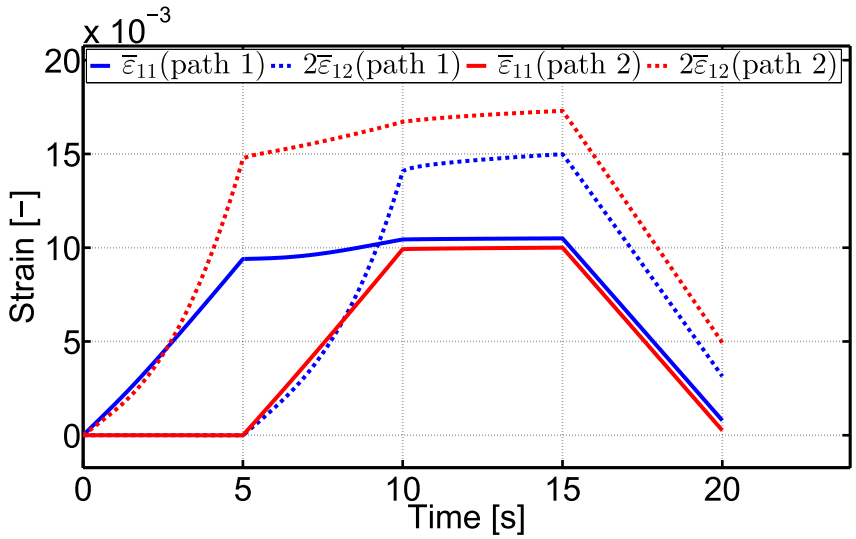

(c) Paths 1 and 2: strain responses ($\overline{\varepsilon}_{11}$ and $2\overline{\varepsilon}_{12}$) vs. time

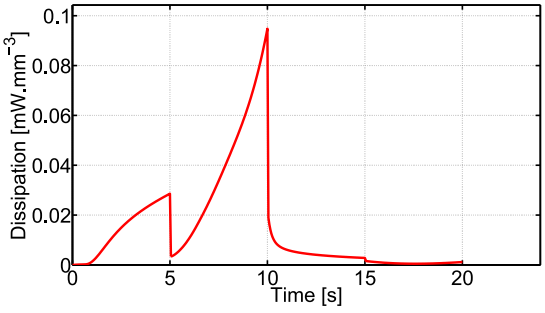

(d) Path 1: dissipation ($\dot{\overline{\Phi}}$) vs. time

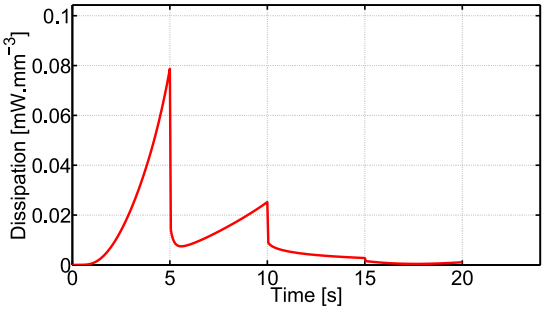

(e) Path 2: dissipation ($\dot{\overline{\Phi}}$) vs. time

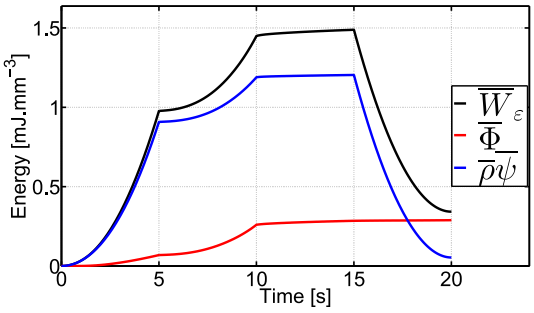

(f) Path 1: strain, dissipated and stored energies ($\overline{W}_\varepsilon$, $\overline{\Phi}$ and $\overline{\rho\psi}$, respectively) vs. time

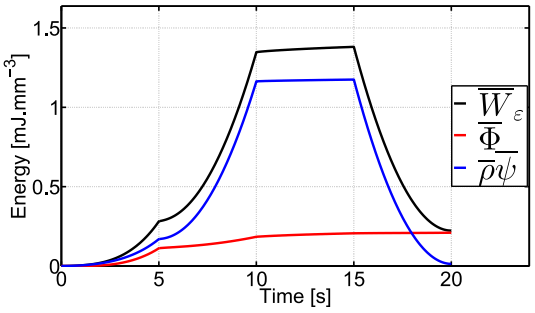

(g) Path 2: strain, dissipated and stored energies ($\overline{W}_\varepsilon$, $\overline{\Phi}$ and $\overline{\rho\psi}$, respectively) vs. time

Figure IV.29: Simulation set 7: non-proportional combined warp tension and in-plane shear.

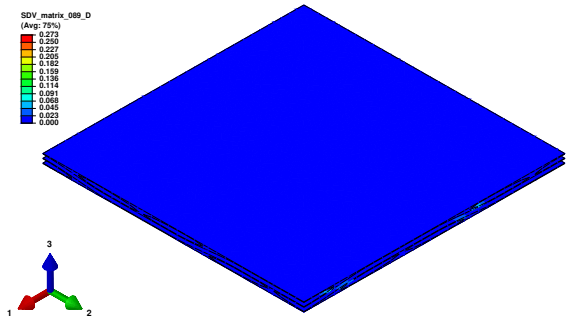

(a) Path 1: local damage (D) in the matrix at $t = 5$ s ($\overline{\sigma}_{11} = 200$ MPa and $\overline{\sigma}_{12} = 0$ MPa)

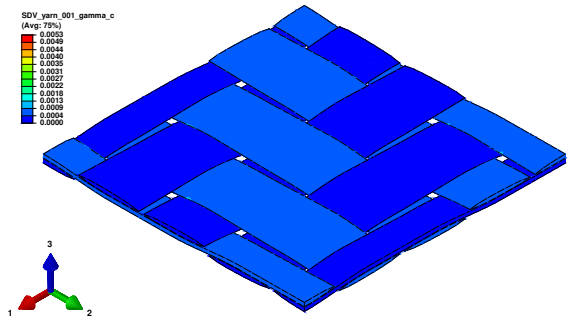

(b) Path 1: local micro-crack density (γ_c) in the yarns at $t = 5$ s ($\overline{\sigma}_{11} = 200$ MPa and $\overline{\sigma}_{12} = 0$ MPa)

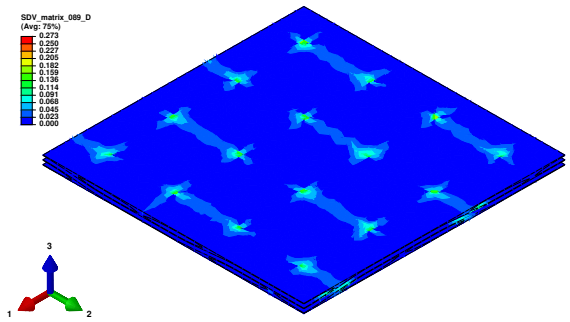

(c) Path 1: local damage (D) in the matrix at $t = 10$ s ($\overline{\sigma}_{11} = 200$ MPa and $\overline{\sigma}_{12} = 30$ MPa)

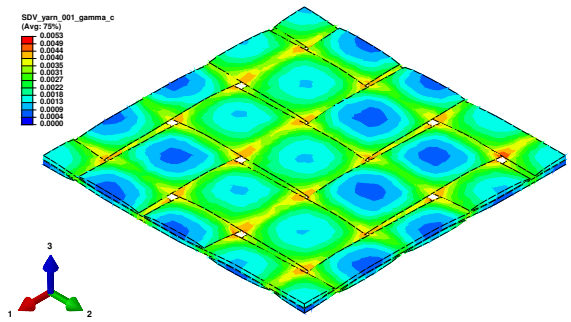

(d) Path 1: local micro-crack density (γ_c) in the yarns at $t = 10$ s ($\overline{\sigma}_{11} = 200$ MPa and $\overline{\sigma}_{12} = 30$ MPa)

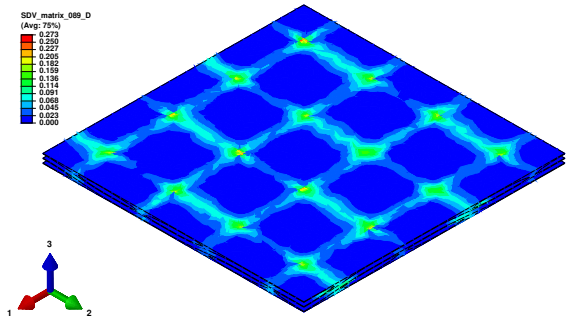

(e) Path 1: local damage (D) in the matrix at $t = 15$ s ($\overline{\sigma}_{11} = 200$ MPa and $\overline{\sigma}_{12} = 30$ MPa)

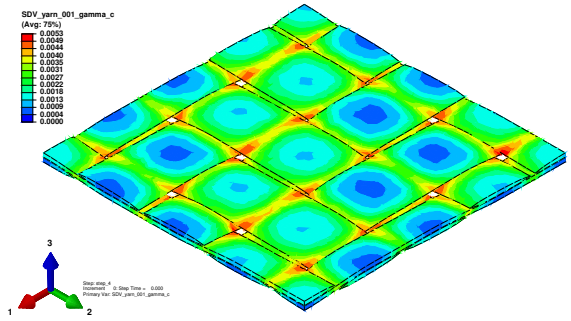

(f) Path 1: local micro-crack density (γ_c) in the yarns at $t = 15$ s ($\overline{\sigma}_{11} = 200$ MPa and $\overline{\sigma}_{12} = 30$ MPa)

Figure IV.30: Simulation set 7: non-proportional combined warp tension and in-plane shear, local fields for the loading path 1.

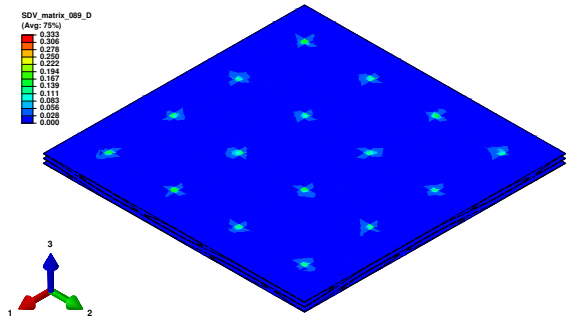

(a) Path 2: local damage (D) in the matrix at $t = 5$ s ($\overline{\sigma}_{11} = 0$ MPa and $\overline{\sigma}_{12} = 30$ MPa)

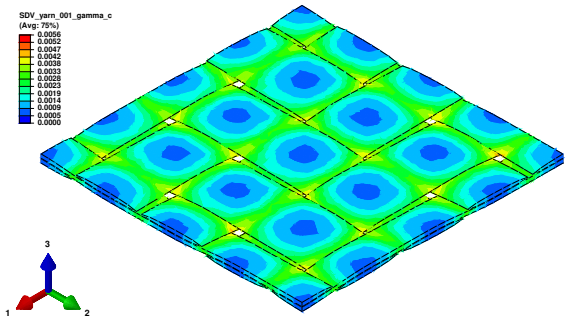

(b) Path 2: local micro-crack density (γ_c) in the yarns at $t = 5$ s ($\overline{\sigma}_{11} = 0$ MPa and $\overline{\sigma}_{12} = 30$ MPa)

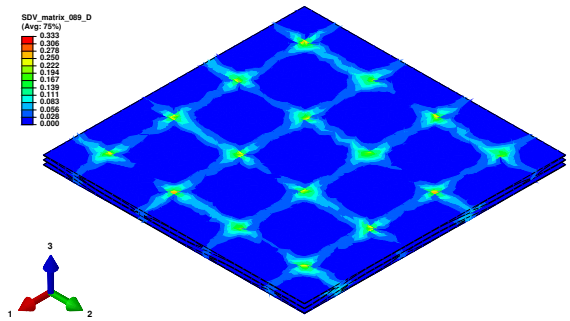

(c) Path 2: local damage (D) in the matrix at $t = 10$ s ($\overline{\sigma}_{11} = 200$ MPa and $\overline{\sigma}_{12} = 30$ MPa)

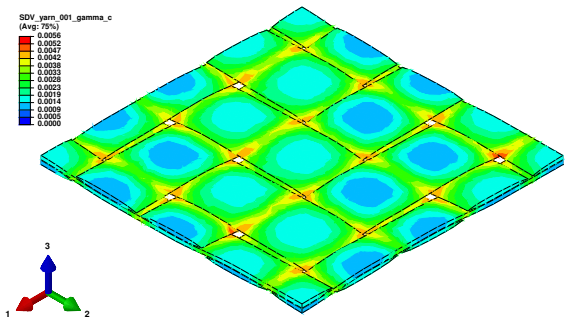

(d) Path 2: local micro-crack density (γ_c) in the yarns at $t = 10$ s ($\overline{\sigma}_{11} = 200$ MPa and $\overline{\sigma}_{12} = 30$ MPa)

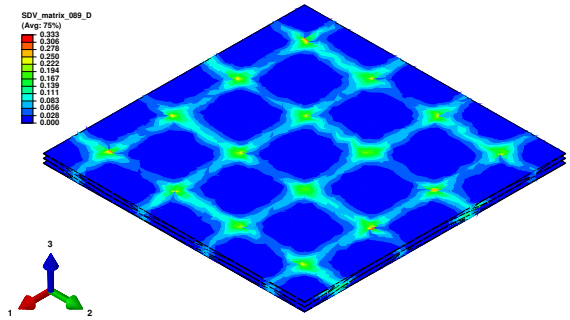

(e) Path 2: local damage (D) in the matrix at $t = 15$ s ($\overline{\sigma}_{11} = 200$ MPa and $\overline{\sigma}_{12} = 30$ MPa)

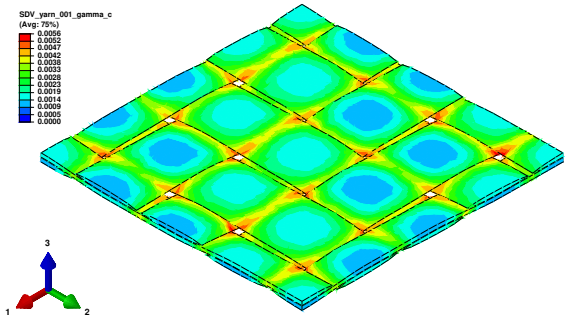

(f) Path 2: local micro-crack density (γ_c) in the yarns at $t = 15$ s ($\overline{\sigma}_{11} = 200$ MPa and $\overline{\sigma}_{12} = 30$ MPa)

Figure IV.31: Simulation set 7: non-proportional combined warp tension and in-plane shear, local fields for the loading path 2.

5 Conclusions

In this final chapter, a multi-scale model for thermoplastic-based woven composites is built from the local constitutive models of the matrix and the yarns, presented in Chapters II and III, respectively. They are assembled together with the help of the multi-scale modelling approach presented in Chapter I.

The unit cell of the studied composite is generated from microstructural data extracted from X-Ray computed tomography. The unknown parameters of the yarn phase are identified from experimental tests performed on $[0^o]_s$, $[\pm 15^o]_s$, $[\pm 30^o]_s$ and $[\pm 45^o]_s$ laminated specimens under quasi-static conditions. Afterwards the predictions of the multi-scale model are compared to similar tests where the composite is subjected to cyclic loading conditions. The good agreements between the predicted tendencies and the experiments demonstrate the capabilities of the multi-scale model to capture the anisotropic response of the composite induced by the microstructure, as well as the time-dependent effects inherent to the matrix phase, namely: the accumulation of strain and damage under cyclic loading. The predictions are quite accurate for the $[0^o]_s$ and $[\pm 15^o]_s$ laminated specimens, while a deviation can be observed for the $[\pm 30^o]_s$ and $[\pm 45^o]$ ones, especially under cyclic loading. This emphasizes that there may be other damage mechanisms (such as debonding at yarn/matrix interface) and/or time-dependent features in the yarns (such as viscoelasticity) involved when the composite is preferentially loaded in in-plane shear. Those ones are not taken into account in the present multi-scale model.

Additional examples are proposed to illustrate the capabilities of the multi-scale model towards performing "virtual tests", as well as analysing the influence of the local deformation processes on the macroscopic behaviour of the composite. These simulations have shown that, under warp tension, the local damage mechanisms mainly occurs in the weft yarns and the matrix. Nevertheless, these degradations do not have a significant impact on the macroscopic response as the much of the load is carried by the warp yarns, which exhibit an elastic and stiff response in their longitudinal direction. Oppositely, under in-plane shear, the macroscopic response is much more matrix-dominated, as the local damage mechanisms occur in both warp en weft yarns, leading to a rapid load transfer to the matrix phase. In this case, the degradation mechanisms play a significant role on the macroscopic response, where the time-dependent effects related to the matrix phase are clearly observable. Moreover, it is worth pointing out that these matrix-related time-dependent effects interact though the microstructure with the yarn phase, whose damage mechanism is time-independent. Besides damage in the matrix, these microstructural interactions create a growth in the intra-yarn damage, when the composite is subjected to a constant or cyclic stress levels. Finally, the multi-scale model enables to analyse the effect of the loading path when the composite is subjected to combined stress states, highlighting the importance of this latter point.

Version française du Chapitre IV

Analyse multi-échelle du comportement cyclique et dépendant du temps des composites tissés à matrice thermoplastique

Sommaire

1 Introduction

Les composites tissés à matrice de thermoplastique sont connus pour avoir un comportement complexe dû au couplage entre les effets de microstructure et les propriétés rhéologiques de la matrice thermoplastique. En effet, la matrice polymérique joue un rôle clé dans le développement des mécanismes d'endommagement sur le long terme. Au cours des dernières années, la modélisation de tels composites a donné lieu à deux principales approches:

- D'une part, le comportement global des composites à matrice thermoplastique peut être décrit de manière purement phénoménologique. Cependant, la complexité de leur comportement nécessite l'utilisation de modèles intégrant de nombreuses caractéristiques comme l'anisotropie, l'endommagement, l'anélasticité et/ou les effets visqueux [95, 79, 153, 152, 80, 81, 124, 101, 4, 187, 91, 92, 119, 60]. Une telle stratégie de modélisation conduit généralement à un grand nombre de paramètres qui peuvent être difficiles à identifier. En plus de cela, une fois les paramètres du modèle identifiés, ils ne sont valables que pour une configuration unique de microstructure, ce qui constitue une réelle limitation dans l'intégration des comportements et des processus locaux. De plus, les données expérimentales requises pour l'identification peuvent être coûteuses et compliquées à obtenir. Malgré cet inconvénient, les modèles phénoménologiques sont généralement numériquement efficaces et par conséquent adaptés pour le calcul de structures.

- D'autre part, la réponse mécanique des composites peut également être décrite à travers des approches multi-échelles. Le principal avantage de cette stratégie de modélisation est que les comportements locaux des constituants sont directement intégrés avec la définition géométrique de la microstructure. Ainsi, les évolutions des mécanismes de déformation et d'endommagement sont considérées à l'échelle microscopique à travers les comportements locaux des différentes phases, et les interactions de microstructure. Cela entraîne une description plus physique des mécanismes d'endommagement. De plus, tant que les comportements locaux sont connus, la variabilité de la microstructure peut être prise en compte. Néanmoins, la modélisation multi-échelle peut être difficile à appliquer pour le calcul de structures, notamment si la transition d'échelle implique la résolution d'un système EF. En effet, même si la connexion d'une cellule unitaire EF à chaque point d'intégration d'un macro-modèle EF est réalisable par la méthode FE^2 [61, 63, 62, 9, 182, 184, 183], le temps de calcul impliqué par un tel processus est très long et les techniques numériques associées sont encore en développement. Cela empêche son utilisation directe dans le cadre d'applications industrielles.

En considérant ces deux approches de modélisation, il est possible de combiner leurs avantages, tout en contournant leurs inconvéniants. L'idée est d'utiliser la modélisation multi-échelles pour générer une base de données "d'essais virtuels" qui pourrait être utilisée par la suite pour identifier un modèle purement phénoménologique [65, 2]. Ainsi, le modèle multi-échelle n'est utilisé que pour effectuer des simulations sur un seul point matériel macroscopique, que l'on appelle "essais virtuels". Ces "essais virtuels" peuvent être obtenus avec des temps de calcul raisonnables et pour un coût réduit. De plus, tout type d'essai peut être simulé, par exemple: chargements monotones, cycliques ou encore multiaxiaux non proportionnels. Une fois la base de données "d'essais virtuels" établie, l'étape suivante consiste à en identifier un modèle phénoménologique, capable de reproduire le comporte-

ment global du composite, qui à son tour peut être utilisé pour le calcul de structures. L'approche de modélisation multi-échelle présentée dans cette thèse est principalement destinée à cet usage. Par ailleurs, le modèle multi-échelle proposé peut également être utilisé pour analyser l'influence de chaque constituant et de la microstructure sur le comportement macroscopique du composite.

Il est important de préciser qu'une telle approche est entièrement modulaire, car elle résulte de l'assemblage de plusieurs sous-modèles et de la représentation géométrique de la microstructure. Ainsi, si un composite avec une autre composition et/ou une autre microstructure périodique doit être étudié, alors l'approche multi-échelle actuelle est toujours valide et seuls les ingrédients sont à changer.

Danc ce dernier chapitre, le comportement cyclique et plus généralement, le comportement dependant du temps des composites tissés à matrice thermoplastique est étudié à travers le modèle multi-échelle proposé. Ce dernier est construit à partir des modèles constitutifs locaux de la matrice et des torons, présentés dans les Chapitres II et III, respectivement. Ils sont assemblés à l'aide de l'approche de modélisation multi-échelle présentée au chapitre I.

Ce chapitre est structuré de la manière suivante: la Section 2 présente brièvement la caracterisation expérimentale de la microstructure. La Section 3 porte sur l'identification expérimentale des paramètres relatifs à la loi de comportement des torons qui restent inconnus. Le modèle multi-échelle est validé en comparant les simulations numériques aux données expérimentales. Ces dernières proviennent d'essais quasi-statiques et cycliques. La Section 4 présente des exemples de simulations où le composite est soumis à des conditions de chargement complexes: chargements monotones, fluage, chargements cycliques et chargements multiaxiaux non-proportionnels. Enfin, la Section 5 résume les principales conclusions relatives à ce chapitre.

2 Caractéristiques de la microstructure et de la cellule unitaire

Pour le composite étudié, dont la microstructure suit la définition géométrique présentée en Section 3.1 du Chapitre I (rappelée en Figure IV.1a), les dimensions caractéristiques a, b et l ont été évaluées par microtomographie à rayons X (voir Figure IV.2a). h a été obtenu en divisant l'épaisseur totale des plaques fournies par le nombre de couches qu'elles contiennent. En ce qui concerne le paramètre δ, ce dernier a été délibérément surdimensionné afin d'assurer un maillage suffisamment propre de la matrice. Les valeurs moyennes considérées pour le modèle multi-échelle sont listées dans le Tableau IV.1. En outre, il est rappelé que le renfort tissé du composite étudié est un sergé 2-2, comme illustré sur la Figure IV.1b.

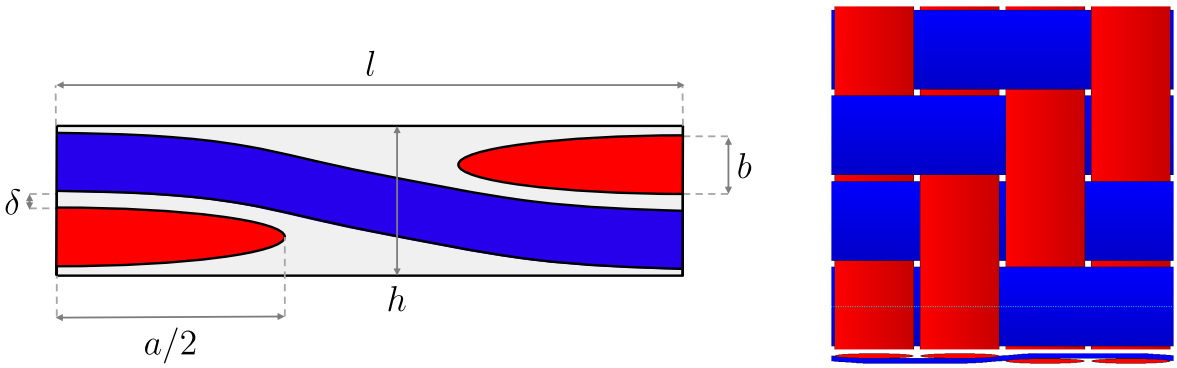

(a) Dimensions caractéristiques d'une microstructure tissée

(b) Motif de tissage de type sergé 2-2

Figure IV.1: Définition géométrique de la microstructure. Le domaine gris représente la phase matricielle, tandis que les domaines bleu et rouge représentent les torons de chaîne et de trame, respectivement.

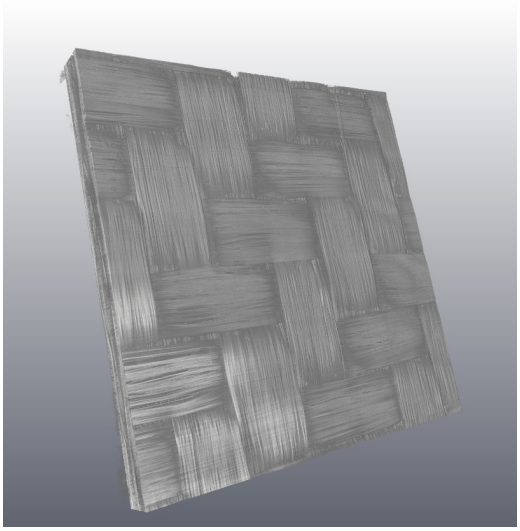

(a) Reconstruction 3D de la microstructure du composite étudié par microtomographie à rayons X (résolution: 6 μm)

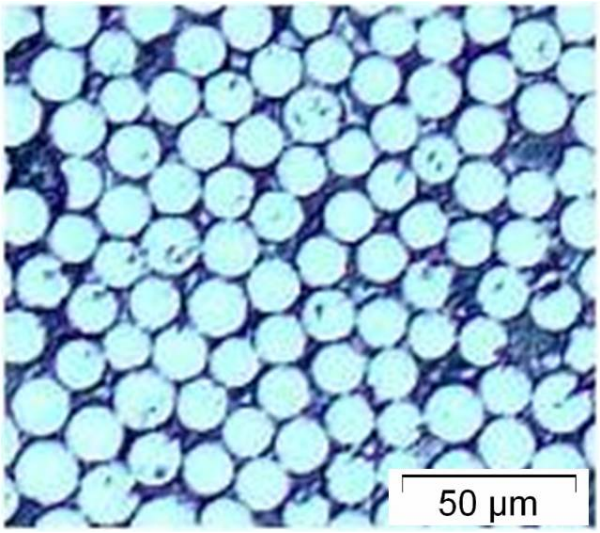

(b) Micrographie de l'intra-toron, le diamètre des fibres est d'environ 17 μm

Figure IV.2: Observations expérimentales de la microstructure du composite étudié.

Dimensions caractéristiques	a	b	l	h	δ
Valeurs (mm)	3.46	0.21	3.75	0.5	0.025

Tableau IV.1: Dimensions caractéristiques de la microstructure, valeurs considérées pour le composite étudié.

En utilisant les données du Tableau IV.1, la cellule unitaire du composite étudié a été générée, puis maillée via le logiciel *TexGen* (voir Section 3.2 in Chapter I). Dans cette configuration, la cellule unitaire a une fraction volumique de toron de 59%. De plus, les analyses effectuées par micrographie ont permis de déterminer la fraction volumique de fibres dans les torons: environ 85%. Cette fraction volumique correspond à une forte compaction puisque les fibres sont presque toutes en contact les unes avec les autres (voir Figure IV.2b). Au final, la fraction volumique de fibres dans l'ensemble du composite est d'environ 50%, ce qui est bien en accord avec les données du fournisseur.

Comme mentionné précédemment, les modèles constitutifs présentés dans les Chapitres II et III sont affectés aux phases de matrice et des torons, respectivement.

3 Identification expérimentale, stratégie et validation

3.1 Procédure expérimentale

Les essais présentés dans cette section ont étés réalisés dans les mêmes conditions environnementales que celles considérées pour la matrice polyamide 6-6 seule (voir Section 4.1 du Chapitre II): $RH = 50\%$ et $T = 23^oC$ (température ambiante), avec la même procédure expérimentale concernant le conditionnement RH du matériau.

Les essais expérimentaux ont été réalisés sur des éprouvettes stratifiées (voir Figures IV.3a and IV.3b) chargées axialement suivant la direction $\vec{x}$. Les éprouettes présentent des séquences d'empilement symétriques et équilibrées de type $[\pm\theta]_s$, avec les angles suivants: $\theta = 0^o$, 15^o, 30^o et 45^o. Rappelons qu'avec ce type de configuration, aucun couplage traction-cisaillement ou traction-flexion n'apparaît. De cette manière, les éprouvettes peuvent être chargées en traction pure, sans générer de déformation en cisaillement et sans effets de courbure. L'épaisseur du pli est d'environ 0.5 mm, ce qui donne une épaisseur totale de 2 mm pour l'ensemble des éprouvettes. Afin d'obtenir des données expérimentales raisonnablement représentatives de la réponse macroscopique du composite, des éprouvettes rectangulaires avec des dimensions suffisamment importantes ont été considérées: une longueur de 250 mm et une largeur de 45 mm. Selon l'orientation, 2 à 3 cellules unitaires sont comprises dans toute la largeur de l'éprouvette (voir Figure IV.3c). Les essais de traction ont été réalisés à température ambiante avec une machine de traction à commande hydraulique. Pendant les essais, la déformation axiale $\overline{\varepsilon}_{xx}$ est mesurée localement au moyen d'un extensomètre, tandis que la contrainte axiale $\overline{\sigma}_{xx}$ est enregistrée par une cellule de force.

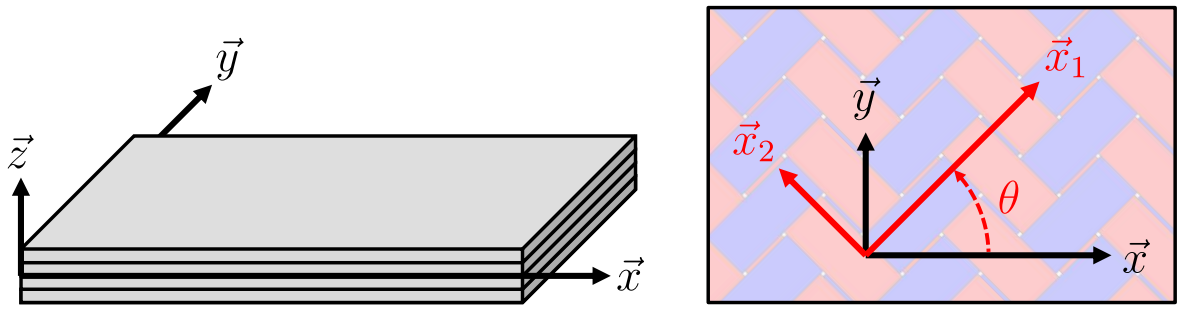

(a) Stratifié: composite multicouche

(b) Pli ou couche élémentaire

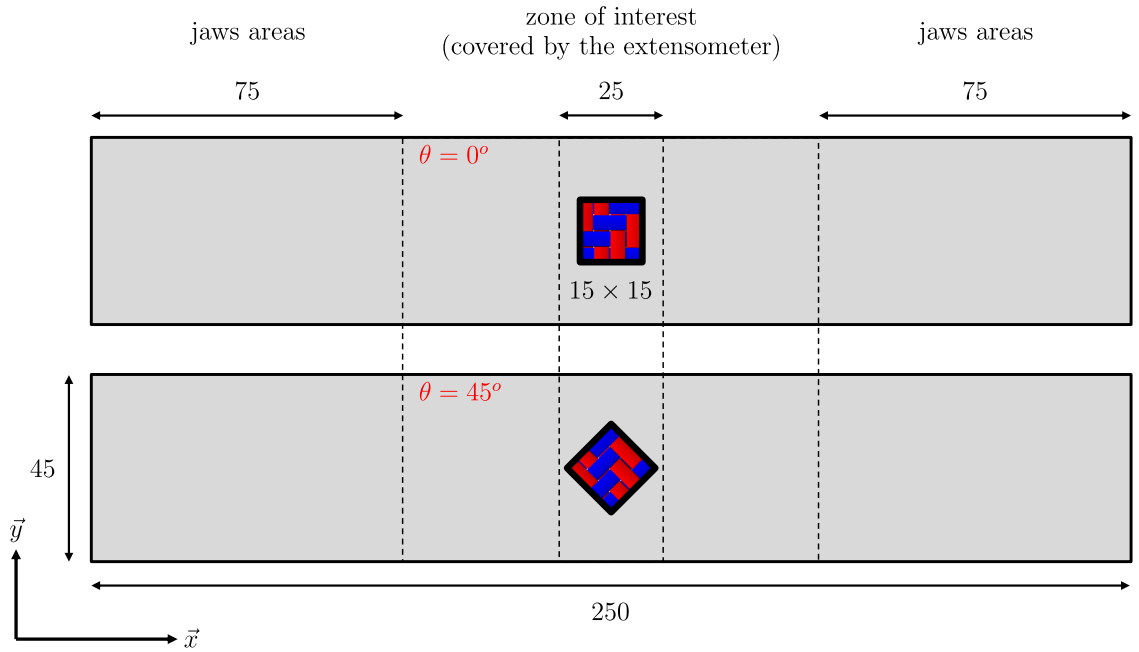

(c) Géométrie et dimensions adoptées pour les éprouvettes de traction (dimensions en mm)

Figure IV.3: Eprouvettes de traction stratifiées $[\pm\theta]_s$, $(\vec{x}, \vec{y}, \vec{z})$ désigne le repère de référence du stratifié, tandis que $(\vec{x}_1, \vec{x}_2, \vec{x}_3)$ désigne le repère matériau du pli élémentaire.

Pour les besoins de l'identification, il est nécessaire de simuler numériquement les réponses uni-axiales des éprouvettes stratifiées, afin de les comparer aux résultats expérimentaux. Comme nous l'avons déjà vu dans la Section 4 du Chapitre III, la réponse d'un composite multicouche est généralement simulée à l'aide de la théorie classique des stratifiés [21, 154]. Alternativement, un schéma basé sur l'homogénéisation périodique peut également être utilisé pour les stratifiés symétriques [34]. Dans une approche encore plus simple, la réponse uniaxiale d'un stratifié $[\pm\theta]_s$ peut être simulée en ne considérant qu'une seule couche avec des conditions de contrainte-déformation appropriées. Ces dernières résultent de la configuration particulière de ce type de stratifiés. En effet, la séquence d'empilement équilibrée empêche toute déformation du stratifié en cisaillement plan. Ainsi dans chaque couche élémentaire $2\overline{\varepsilon}_{xy} = 0$. Ce qui génère une contrainte de cisaillement plan non nulle $(\overline{\sigma}_{xy})$ dans cette même couche. Néanmoins, cette contrainte prend des valeurs opposées d'une couche $+\theta$ à une couche $-\theta$ et par conséquent disparaît à l'échelle de l'ensemble du stratifié. Ainsi, afin de simuler la réponse uni-axiale d'une éprouvette stratifiée $[\pm\theta]_s$, les états de contrainte-déformation suivants, définis dans le repère de référence du stratifié $(\vec{x}, \vec{y}, \vec{z})$, sont appliqués à la cellule unitaire à l'aide d'un pilotage hors-axes, comme expliqué dans la Section 2.2.2 du Chapite I. Pour la simulation d'un essai piloté en déformation, cela

donne [1]:

$$\left\{\begin{array}{rcl} \overline{\varepsilon}_{xx} &=& \overline{\varepsilon}_{xx}(t) \\ \overline{\varepsilon}_{yy} &=& \text{inconnu} \\ \overline{\varepsilon}_{zz} &=& \text{inconnu} \\ 2\overline{\varepsilon}_{xy} &=& 0 \\ 2\overline{\varepsilon}_{xz} &=& \text{inconnu} \approx 0 \\ 2\overline{\varepsilon}_{yz} &=& \text{inconnu} \approx 0 \end{array}\right\}, \quad \left\{\begin{array}{rcl} \overline{\sigma}_{xx} &=& \text{inconnu} \\ \overline{\sigma}_{yy} &=& 0 \\ \overline{\sigma}_{zz} &=& 0 \\ \overline{\sigma}_{xy} &=& \text{inconnu} \neq 0 \\ \overline{\sigma}_{xz} &=& 0 \\ \overline{\sigma}_{yz} &=& 0 \end{array}\right\}. \tag{IV.1}$$

Dans le même principe, la simulation d'un essai piloté en contrainte est réalisée avec:

$$\left\{\begin{array}{rcl} \overline{\varepsilon}_{xx} &=& \text{inconnu} \\ \overline{\varepsilon}_{yy} &=& \text{inconnu} \\ \overline{\varepsilon}_{zz} &=& \text{inconnu} \\ 2\overline{\varepsilon}_{xy} &=& 0 \\ 2\overline{\varepsilon}_{xz} &=& \text{inconnu} \approx 0 \\ 2\overline{\varepsilon}_{yz} &=& \text{inconnu} \approx 0 \end{array}\right\}, \quad \left\{\begin{array}{rcl} \overline{\sigma}_{xx} &=& \overline{\sigma}_{xx}(t) \\ \overline{\sigma}_{yy} &=& 0 \\ \overline{\sigma}_{zz} &=& 0 \\ \overline{\sigma}_{xy} &=& \text{inconnu} \neq 0 \\ \overline{\sigma}_{xz} &=& 0 \\ \overline{\sigma}_{yz} &=& 0 \end{array}\right\}, \tag{IV.2}$$

où la déformation et la contrainte axiale, à savoir $\overline{\varepsilon}_{xx}$ et $\overline{\sigma}_{xx}$, peuvent être comparées aux résultats expérimentaux.

Pour la campagne expérimentale, deux types d'essais adaptés à l'identification et à la validation du modèle multi-échelle sont proposés:

- Essais quasi-statiques:
  Les éprouvettes stratifiées sont chargées et déchargées de manière répétée en augmentant à chaque chargement le niveau de contrainte, et ce jusqu'à rupture. Ces tests sont effectués à une vitesse de déformation relativement lente (de l'ordre de 3.5×10^{-3} s^{-1}).

- Essais cycliques contrôlés en contrainte:
  Les éprouvettes stratifiées sont soumises à une charge cyclique de forme sinusoïdale. Cette charge oscille entre un niveau de contrainte max et min à une frenquence de 1 Hz pendant 100 s, soit 100 cycles. Pour les éprouvettes $[0^o]_4$, $[\pm 15^o]_s$ et $[\pm 30^o]_s$, environ 80% de la contrainte à rupture en quasi-statiques est considérée pour le niveau de contrainte max. Cependant, en ce qui concerne les éprouvettes $[pm45^o]_s$, ces dernières présentent une réponse beaucoup plus ductile. Par conséquent, un niveau de contrainte max de 95 MPa a été choisi, afin de garder une amplitude de déformation modérée. Le niveau de contrainte min est d'environ 10 MPa, et est le même pour toutes les éprouvettes.

De la même manière que pour le polyamide 6-6 seul (voir la Section 4 du Chapitre II), des mesures de température ont été effectuées lors des essais cycliques, au moyen d'une caméra thermique IR. Bien que le modèle multi-échelle proposé soit formulé dans l'hypothèse de conditions isothermes, une estimation de l'auto-échauffement sera évaluée en intégrant la dissipation macroscopique $\overline{\dot{\Phi}}$ en tant que terme source dans une analyse thermique découplée (voir Annexe C). Ainsi, l'élévation de température estimée sera comparée à celle observée expérimentalement. En supposant des champs thermomécaniques uniformes dans la zone

1. Dans le repère de référence du stratifié $(\vec{x}, \vec{y}, \vec{z})$, de par l'orientation de couche élémentaire, la cellule unitaire présente une réponse entièrement anisotrope (dans le plan xy), conduisant à un couplage traction-cisaillement. C'est pourquoi la contrainte de cisaillement $\overline{\sigma}_{xy}$ peut prendre des valeurs non nulles lorsque la déformation de cisaillement $2\overline{\varepsilon}_{xy}$ est mise à zéro.

d'intérêt, l'équation de la chaleur "0D" intégrée sur le volume de la cellule unitaire prend la forme suivante:

$$\overline{\rho c}\left(\dot{T}(t) + \frac{T(t) - T_\infty}{\tau}\right) = \dot{\overline{\Phi}}(t), \tag{IV.3}$$

où $\overline{\rho}$ et $\overline{c}$ représentent respectivement la masse volumique et la capacité calorifique à léchelle macroscopique. Le temps caractéristique τ quantifie les pertes de chaleur supposées proportionnelles à la différence entre la température actuelle du composite $T(t)$ et sa température à l'équilibre T_∞ (température ambiante). Les données thermiques utilisées dans ce chapitre sont répertoriées dans le Tableau IV.2.

Caractéristique	Paramètre	valeur	unité
Masse volumique macroscopique	$\overline{\rho}$	1.870×10^{-9}	$\mathrm{T.mm^{-3}}$
Capacité calorifique macroscopique	$\overline{c}$	$0.990 \times 10^{+9}$	$\mathrm{mJ.T^{-1}.{}^{o}C^{-1}}$
Temps caractéristique (pertes de chaleur)	τ	149	s

Tableau IV.2: Paramètres du problème thermique "0D" découplé pour le composite. Les valeurs pour la masse volumique et la capacité calorifique ont été fournies par les partenaires industriels. Le temps caractéristique τ a été évalué pour les éprouvettes stratifiées (voir Figures II.3 et II.4) en utilisant la méthodologie proposée par [20], qui est brièvement présentée dans la Section 3 de l'Annexe C.

3.2 Stratégie d'identification

Il est rappelé que la matrice a déjà été identifiée à partir d'essais directement réalisés sur le polyamide 6-6 seul (voir Section 4 du Chapitre II), dont les paramètres sont listés dans le Tableau II.4. En ce qui concerne les torons, la procédure d'identification proposée en Section 4 du Chapite III n'est pas applicable dans le cas présent, du fait qu'il est impossible d'isoler ce composant pour effectuer sur celui-ci des essais mécaniques. A la place, il est proposé d'identifier les paramètres des torons à partir de la réponse macroscopique de tout le composite tissé. Pour ce faire, un algorithme de résolution par méthode inverse a été utilisé, identiquement à ce qui a été fait pour le polyamide 6-6 seul en Section 4.2 du Chapitre II.

Il est également important de rappeler que le comportement des torons est supposé indépendant du temps. Ainsi, pour l'ensemble du modèle multi-échelle, la dépendance au temps de tout le composite est uniquement due à la matrice. Les paramètres liés aux torons sont donc identifiés uniquement à partir des essais quasi-statiques, tandis que les essais cycliques sont conservés pour la validation.

3.3 Identification et validation expérimentale

Au préalable, la raideur initiale des torons est estimée par homogénéisation périodique (voir Section 1 de l'Annexe G), de sorte que seuls les paramètres liés à l'endommagement et à l'anélasticité des torons soient identifiés par méthode inverse. Les valeurs obtenues pour ces paramètres sont listées dans la partie inférieure du Tableau IV.3, tandis que les

propriétés élastiques initiales sont rappelées dans la partie supérieure de ce même tableau. Il est important de préciser que la perte de la rigidité induite par les microfissures dans les torons (voir Section 2 de l'Annexe G) est calculée en considérant la configuration suivante pour les inclusions de vides: "crossing micro-cracks along $\vec{x}_1$" (voir la Figure III.4a et le Tableau III.2). Le comportement des torons isolés est illustré à travers quelques exemples dans la Section 3 de l'Annexe G.

Caractéristique	Paramètre	valeur	unité
Tenseur de rigidités, isotrope transverse	$C_{0_{1111}}$	65822	MPa
(composantes non nulles)	$C_{0_{1122}} = C_{0_{1133}}$	7041	MPa
	$C_{0_{2222}} = C_{0_{3333}}$	23947	MPa
	$C_{0_{2233}}$	6971	MPa
	$C_{0_{1212}} = C_{0_{1313}}$	8661	MPa
	$C_{0_{2323}} = \frac{1}{2}(C_{0_{2222}} - C_{0_{2233}})$	8488	MPa
Seuil d'endo. en traction transverse	R_{22}	20.0	MPa
Seuil d'endo. en cisaillement plan	R_{12}	7.5	MPa
1^{er} Paramètre de la loi de Weibull	S	12.3	-
2^{eme} Paramètre de la loi de Weibull	β	2.75	-
Saturation de la microfissuration (fixée)	γ_c^∞	0.025	-
Anélasticité en traction transverse	a_{22}	3.60	-
Anélasticité en cisaillement plan	a_{12}	2.15	-

Tableau IV.3: Paramètres identifiés pour les torons. Les raideurs initiales (dans la partie supérieure du tableau) sont calculées par homogénéisation périodique (voir Section 1 de l'Annexe G), tandis que les paramètres d'endommagement et d'anélasticité (dans la partie inférieure du tableau) sont obtenus par méthode inverse à partir de la réponse de tout le composite tissé.

Les Figures IV.4, IV.5, IV.6 et IV.7 montrent les simulations numériques obtenues avec le modèle multi-échelle et les données expérimentales des essais quasi-statiques effectués avec les éprouvettes $[0^o]_4$, $[\pm 15^o]_s$, $[\pm 30^o]_s$ et $[\pm 45^o]_s$, respectivement. Tout d'abord, on observe que la réponse de l'éprouvette $[0^o]_4$ est quasi-élastique. A l'échelle macroscopique, le composite ne présente quasiment pas d'endommagement, ni d'anelasticité, avant que la rupture ne se produise à un niveau de contrainte relativement élevé (environ 430 MPa). A l'inverse, pour l'éprouvette $[\pm 45^o]_s$, la réponse est beaucoup plus ductile et la rupture ne survient pas à la fin de l'éssai [2]. Pour les éprouvettes $[\pm 15^o]_s$ et $[\pm 30^o]_s$, le composite présente une réponse intermédiaire entre celles observées avec les $[0^o]_4$ et $[\pm 45^o]_s$.

Cette importante différence de comportement entre les différents angles de stratification fait ressortir la forte anisotropie induite par la microstructure, qui est globalement

2. Si la rupture ne survient pas, l'essai s'arrête lorque la déformation atteint 0.1, ce qui est la limite de l'extensomètre.

bien capturée par le modèle multi-échelle. De bons accords sont obtenus entre les réponses quasi-statiques simulées et les résultats expérimentaux pour les éprouvettes $[0^o]_4$, $[\pm 15^o]_s$ et $[\pm 30^o]_s$. Pour l'éprouvette $[\pm 45^o]_s$, le modèle multi-échelle surestime la réponse quasi-statique. Néanmoins, la tendance obtenue reste proche de ce qui est observé expérimentalement, avec des ordres de grandeur similaires. Cet écart est surement dû au fait que d'autres mécanismes d'endommagement, non pris en compte par le modèle multi-échelle, interviennent, comme la décohésion des interfaces torons/matrice par exemple.

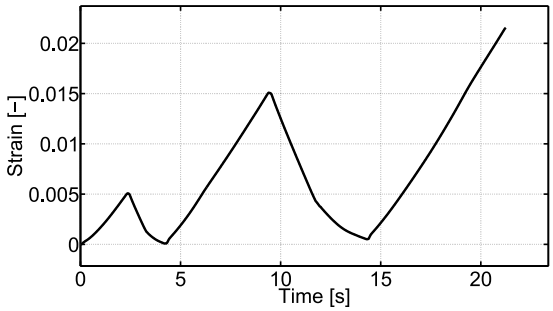

(a) Déformation appliquée ($\overline{\varepsilon}_{xx}$) - temps

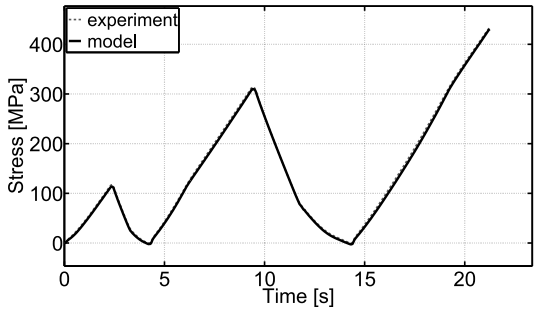

(b) Réponse en contrainte ($\overline{\sigma}_{xx}$) - temps

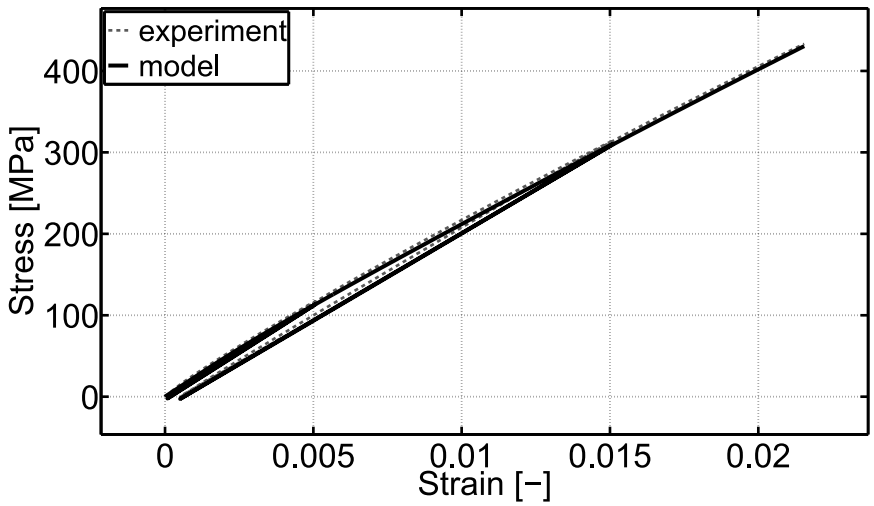

(c) Contrainte ($\overline{\sigma}_{xx}$) - déformation ($\overline{\varepsilon}_{xx}$)

Figure IV.4: Essai quasi-statique pour une éprouvette stratifiée $[0^o]_4$. Ces données sont utilisées pour l'identification.

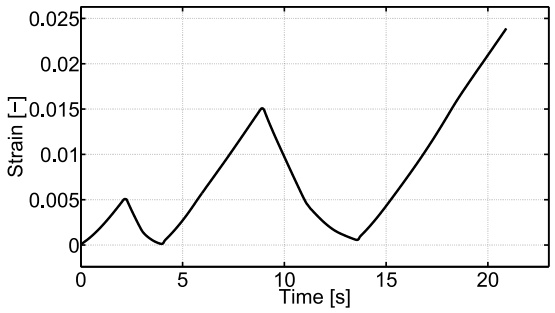

(a) Déformation appliquée ($\overline{\varepsilon}_{xx}$) - temps

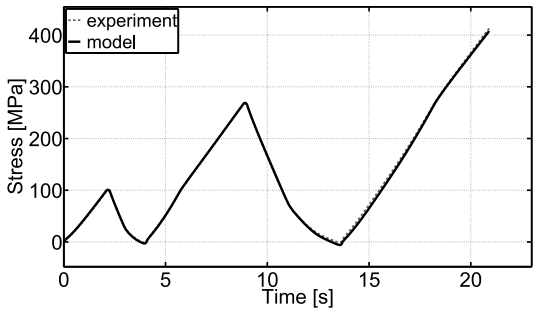

(b) Réponse en contrainte ($\overline{\sigma}_{xx}$) - temps

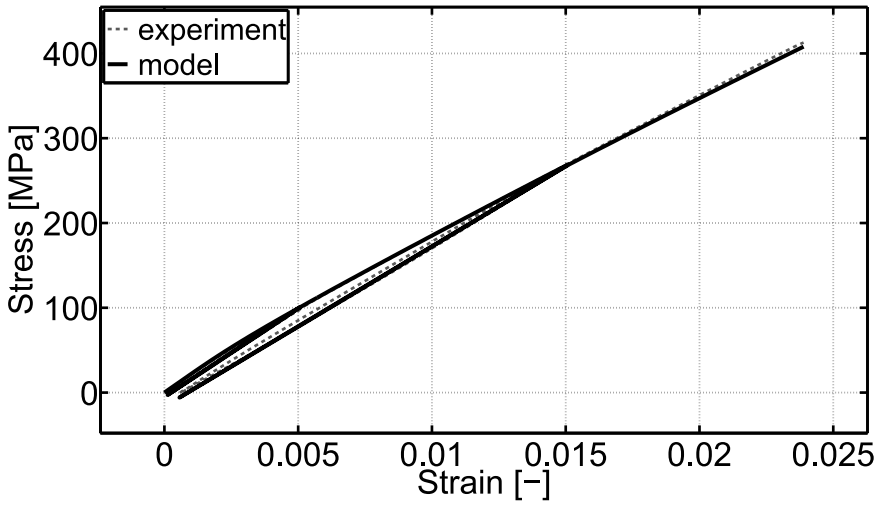

(c) Contrainte ($\overline{\sigma}_{xx}$) - déformation ($\overline{\varepsilon}_{xx}$)

Figure IV.5: Essai quasi-statique pour une éprouvette stratifiée $[\pm 15^o]_s$. Ces données sont utilisées pour l'identification.

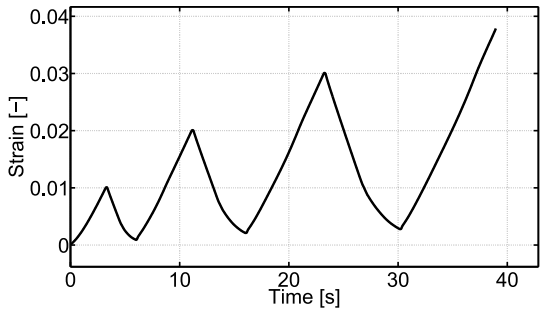

(a) Déformation appliquée ($\overline{\varepsilon}_{xx}$) - temps

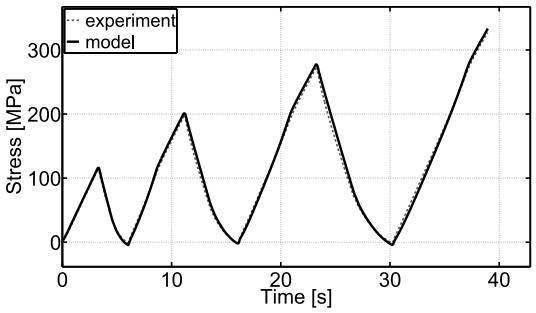

(b) Réponse en contrainte ($\overline{\sigma}_{xx}$) - temps

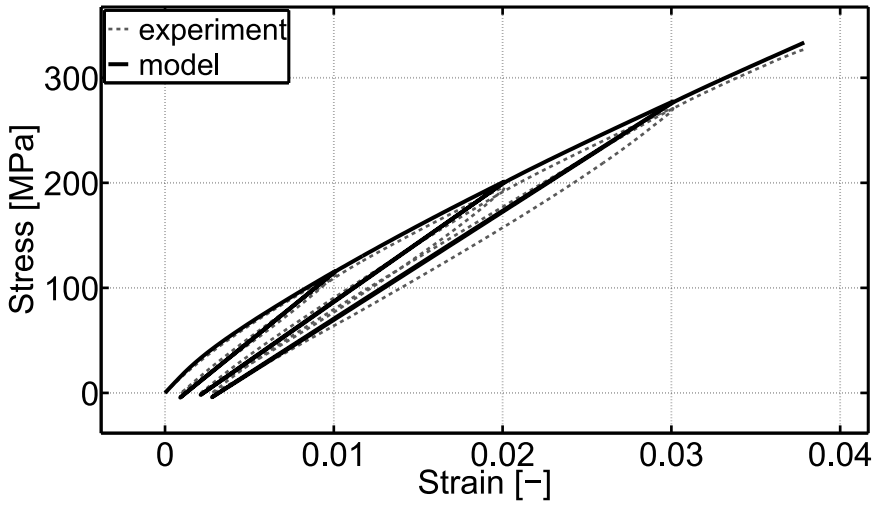

(c) Contrainte ($\overline{\sigma}_{xx}$) - déformation ($\overline{\varepsilon}_{xx}$)

Figure IV.6: Essai quasi-statique pour une éprouvette stratifiée $[\pm 30^o]_s$. Ces données sont utilisées pour l'identification.

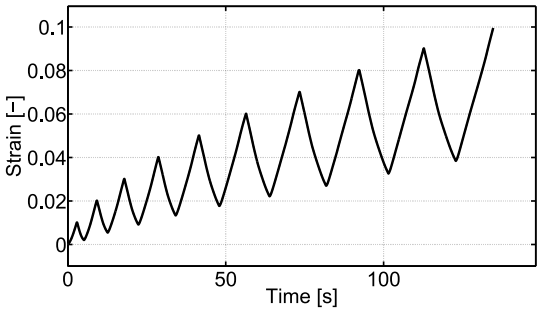

(a) Déformation appliquée ($\overline{\varepsilon}_{xx}$) - temps

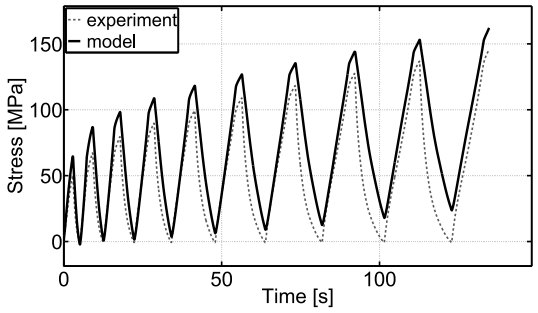

(b) Réponse en contrainte ($\overline{\sigma}_{xx}$) - temps

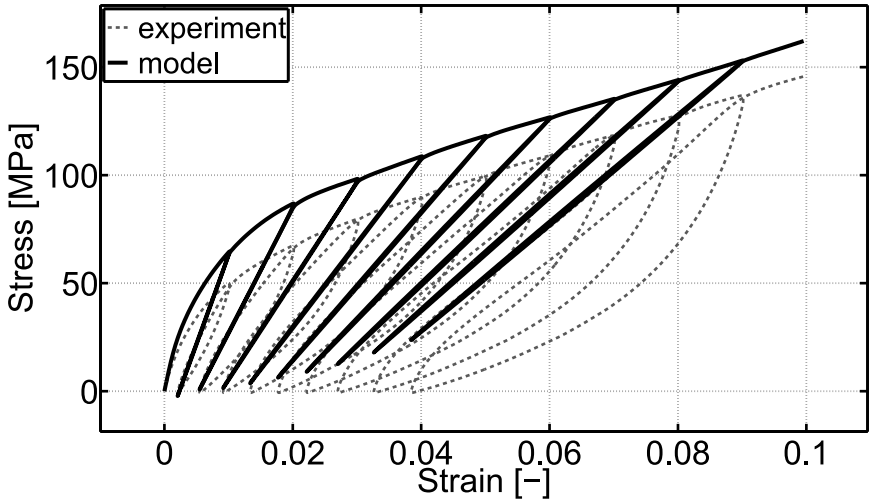

(c) Contrainte ($\overline{\sigma}_{xx}$) - déformation ($\overline{\varepsilon}_{xx}$)

Figure IV.7: Essai quasi-statique pour une éprouvette stratifiée $[\pm 45^o]_s$. Ces données sont utilisées pour l'identification.

Les Figures IV.8, IV.9, IV.10 et IV.11 montrent les prédictions données par le modèle multi-échelle et les résultats expérimentaux pour les essais cycliques contrôlés en contrainte effectués pour les éprouvettes $[0^o]_4$, $[\pm 15^o]_s$, $[\pm 30^o]_s$ et $[\pm 45^o]_s$, respectivement. Il est rappelé que ces essais n'ont pas été utilisés pour l'identification. Précisons que la rupture est survenue au bout de 80 et 71 cycles, pour les éprouvettes $[0^o]_4$ et $[\pm 30^o]_s$, respectivement. Pour les autres éprouvettes, aucune rupture ne s'est produite avant la fin des 100 cycles programmés. Lorsque le composite est soumis à un chargement cyclique, des phénomènes provenant directement de la matrice peuvent être clairement observés, à savoir: l'accumulation de déformation accompagnée d'une perte progressive de rigidité (voir Sections 4.3 et 5.1 du Chapitre II). Néanmoins, en fonction de l'angles de stratification des plis, les amplitudes de ces phénomènes sont assez différentes et mettent une fois de plus en évidence l'anisotropie induite par la microstructure. Globalement, le modèle multi-échelle fournit des tendances similaires aux résultats expérimentaux. Les réponses macroscopiques prédites sont relativement précises pour les éprouvettes $[0^o]_4$ et $[\pm 15^o]_s$, alors que l'accumulation de l'endommagement et de la déformation est sous-estimée pour les éprouvettes $[\pm 30^o]_s$ et $[\pm 45^o]_s$. Comme mentionné précédemment, cela met en évidence que d'autres mécanismes peuvent être impliqués et/ou qu'un comportement dépendant du temps intervient dans les torons, lorsque le composite est principalement chargé en cisaillement plan.

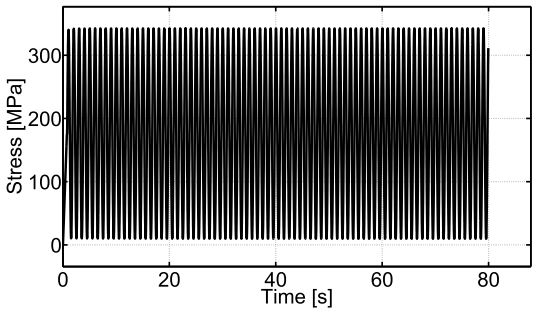

(a) Contrainte appliquée ($\overline{\sigma}_{xx}$) - temps

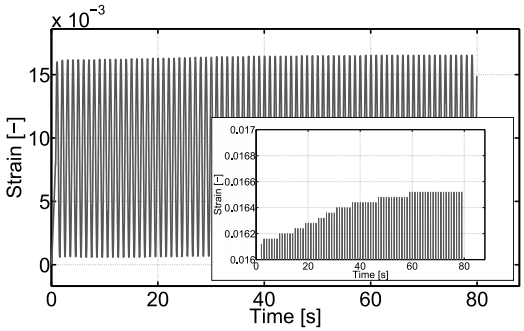

(b) Réponse expérimentale en déformation ($\overline{\varepsilon}_{xx}$) - temps

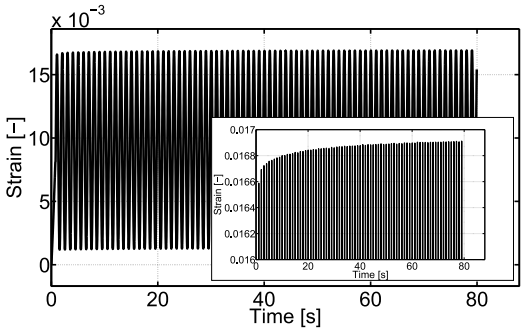

(c) Réponse simulée en déformation ($\overline{\varepsilon}_{xx}$) - temps

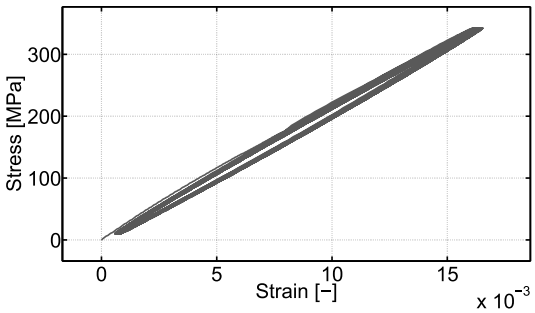

(d) Contrainte ($\overline{\sigma}_{xx}$) - déformation ($\overline{\varepsilon}_{xx}$), expérience

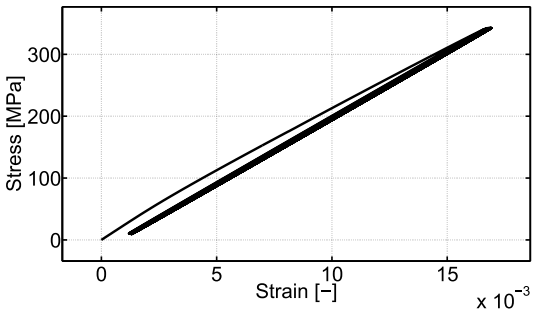

(e) Contrainte ($\overline{\sigma}_{xx}$) - déformation ($\overline{\varepsilon}_{xx}$), simulation

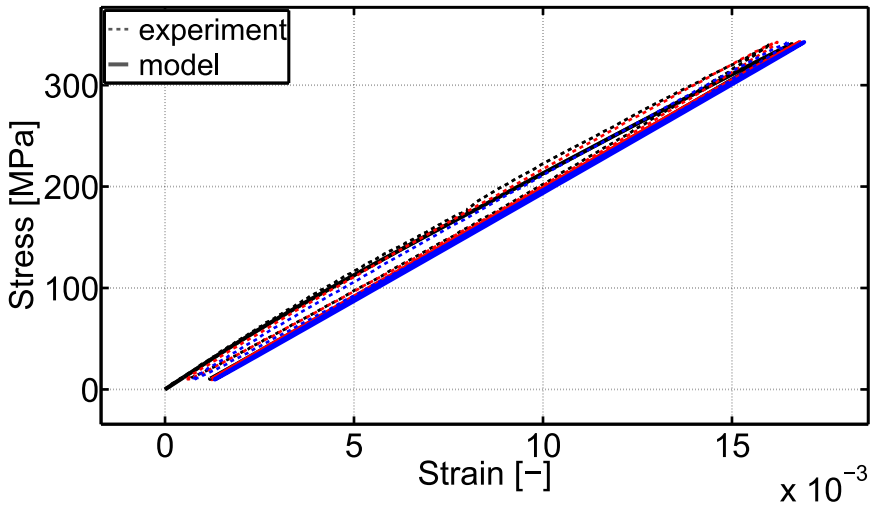

(f) Contrainte ($\overline{\sigma}_{xx}$) - déformation ($\overline{\varepsilon}_{xx}$) pour les 1^{er}, 10^{eme} et 79^{eme} cycles, représentés en noir, rouge et bleu, respectivement

Figure IV.8: Essai cyclique contrôlé en contrainte: 100 cycles effectués à 1 Hz pour une éprouvette stratifiée $[0^o]_4$. Ces données sont utilisées pour la validation.

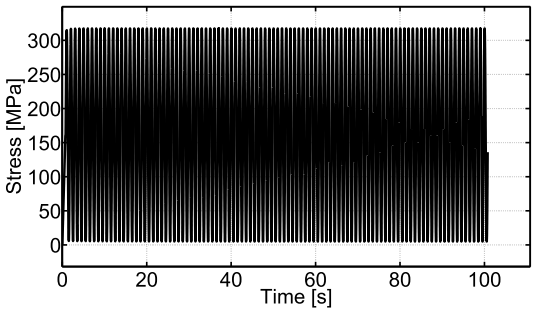

(a) Contrainte appliquée ($\overline{\sigma}_{xx}$) - temps

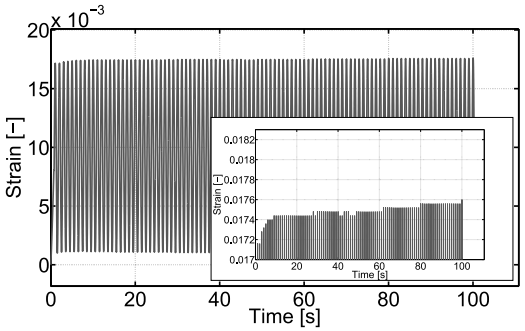

(b) Réponse expérimentale en déformation ($\overline{\varepsilon}_{xx}$) - temps

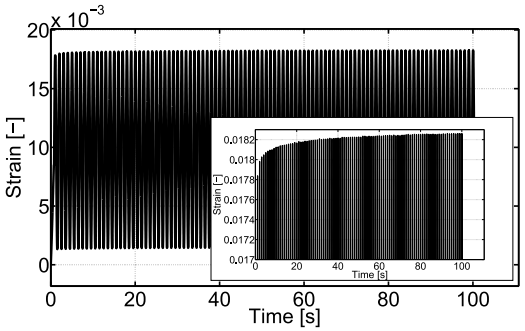

(c) Réponse simulée en déformation ($\overline{\varepsilon}_{xx}$) - temps

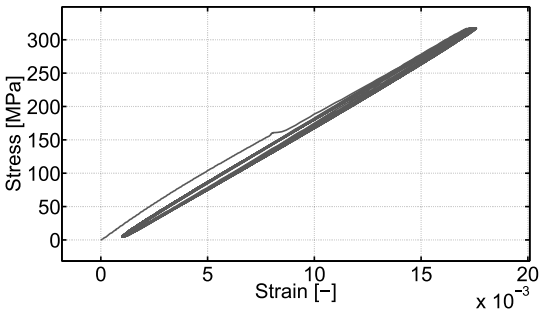

(d) Contrainte ($\overline{\sigma}_{xx}$) - déformation ($\overline{\varepsilon}_{xx}$), expérience

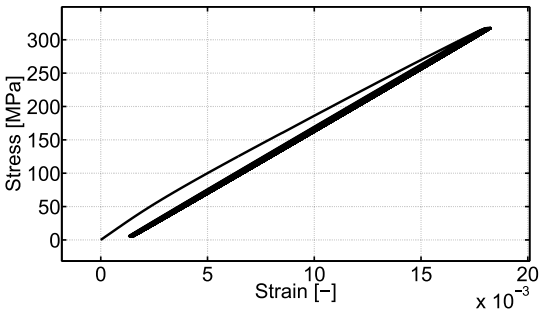

(e) Contrainte ($\overline{\sigma}_{xx}$) - déformation ($\overline{\varepsilon}_{xx}$), simulation

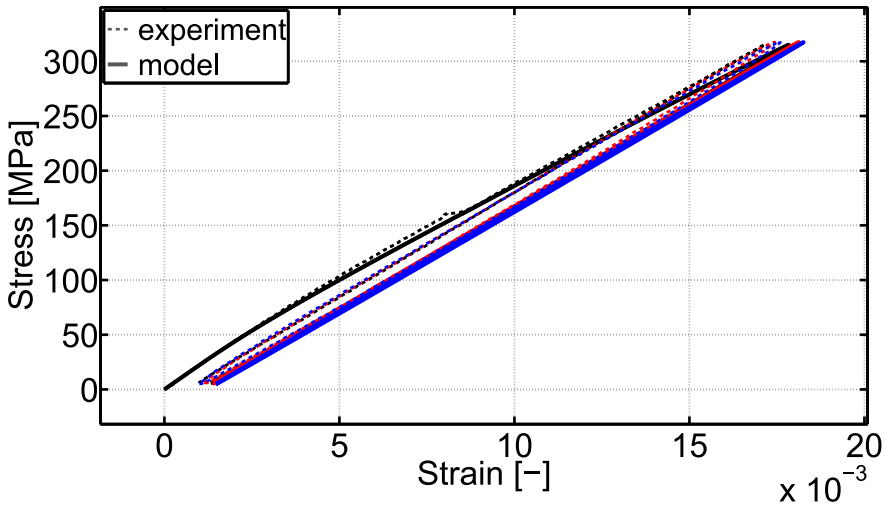

(f) Contrainte ($\overline{\sigma}_{xx}$) - déformation ($\overline{\varepsilon}_{xx}$) pour les 1^{er}, 10^{eme} et 100^{eme} cycles, représentés en noir, rouge et bleu, respectivement

Figure IV.9: Essai cyclique contrôlé en contrainte: 100 cycles effectués à 1 Hz pour une éprouvette stratifiée $[\pm 15^o]_s$. Ces données sont utilisées pour la validation.

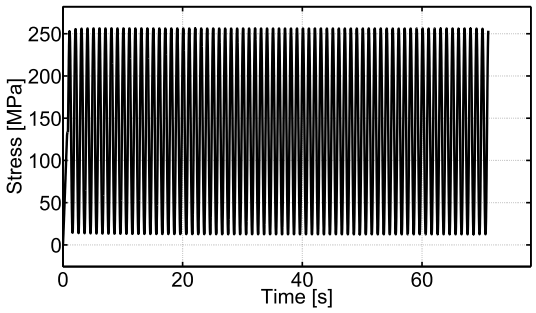

(a) Contrainte appliquée ($\overline{\sigma}_{xx}$) - temps

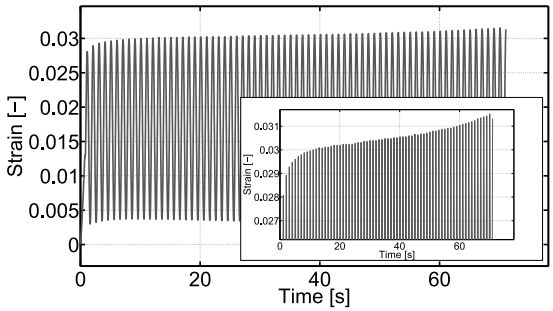

(b) Réponse expérimentale en déformation ($\overline{\varepsilon}_{xx}$) - temps

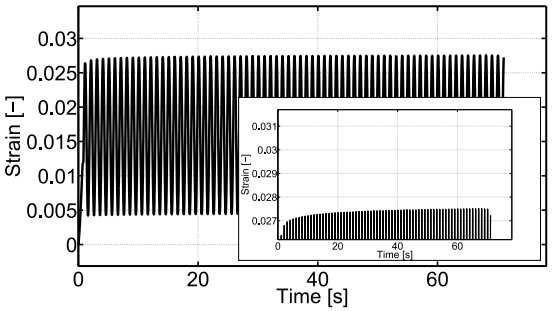

(c) Réponse simulée en déformation ($\overline{\varepsilon}_{xx}$) - temps

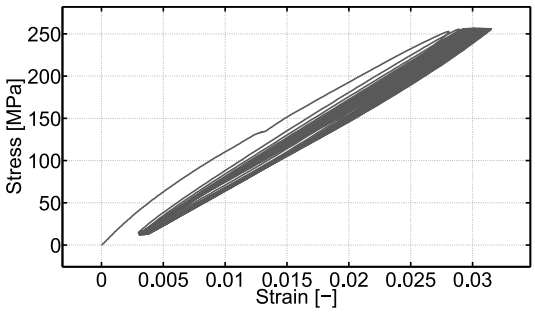

(d) Contrainte ($\overline{\sigma}_{xx}$) - déformation ($\overline{\varepsilon}_{xx}$), expérience

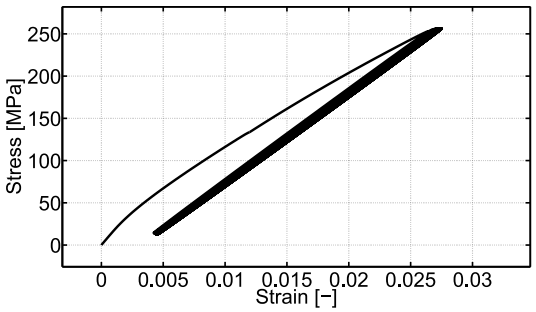

(e) Contrainte ($\overline{\sigma}_{xx}$) - déformation ($\overline{\varepsilon}_{xx}$), simulation

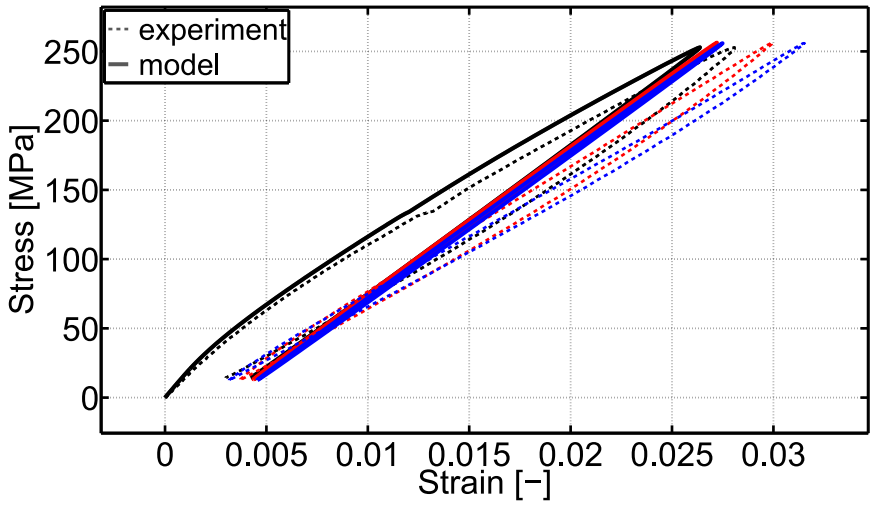

(f) Contrainte ($\overline{\sigma}_{xx}$) - déformation ($\overline{\varepsilon}_{xx}$) pour les 1^{er}, 10^{eme} et 70^{eme} cycles, représentés en noir, rouge et bleu, respectivement

Figure IV.10: Essai cyclique contrôlé en contrainte: 100 cycles effectués à 1 Hz pour une éprouvette stratifiée $[\pm 30^o]_s$. Ces données sont utilisées pour la validation.

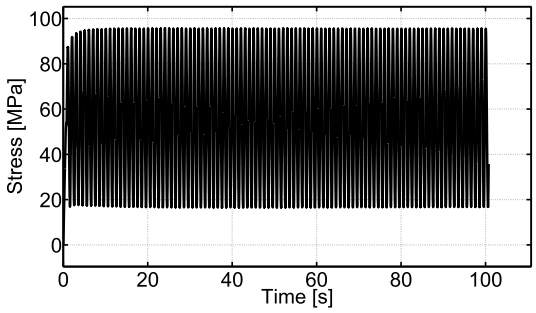

(a) Contrainte appliquée ($\overline{\sigma}_{xx}$) - temps

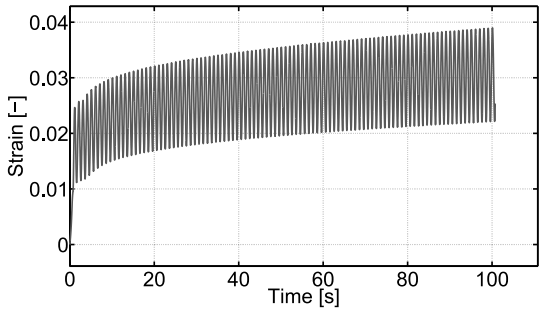

(b) Réponse expérimentale en déformation ($\overline{\varepsilon}_{xx}$) - temps

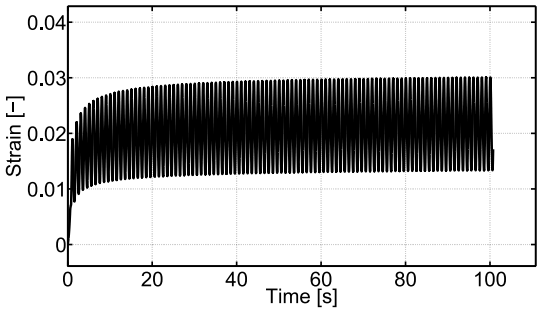

(c) Réponse simulée en déformation ($\overline{\varepsilon}_{xx}$) - temps

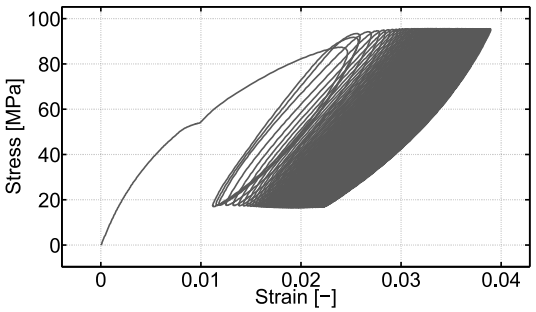

(d) Contrainte ($\overline{\sigma}_{xx}$) - déformation ($\overline{\varepsilon}_{xx}$), expérience

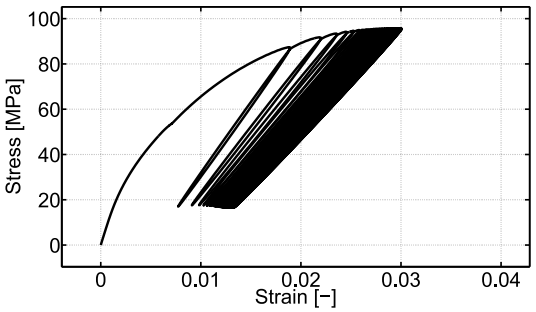

(e) Contrainte ($\overline{\sigma}_{xx}$) - déformation ($\overline{\varepsilon}_{xx}$), simulation

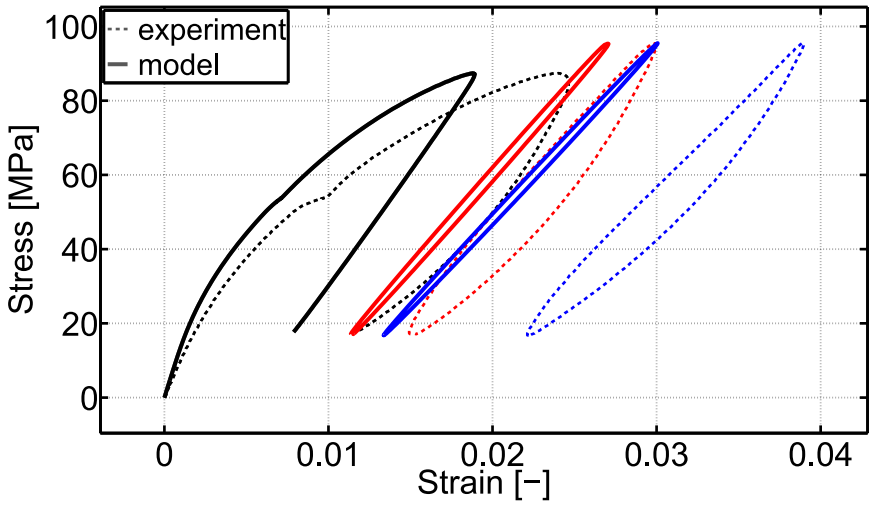

(f) Contrainte ($\overline{\sigma}_{xx}$) - déformation ($\overline{\varepsilon}_{xx}$) pour les 1^{er}, 10^{eme} et 100^{eme} cycles, représentés en noir, rouge et bleu, respectivement

Figure IV.11: Essai cyclique contrôlé en contrainte: 100 cycles effectués à 1 Hz pour une éprouvette stratifiée $[\pm 45^o]_s$. Ces données sont utilisées pour la validation.

En ce qui concerne les mesures de température, on peut remarquer que, dans les 100 cycles effectués pendant les essais, les élévations de température restent relativement faibles (3.5 à 4 ^{o}C) pour les éprouvettes $[0^o]_4$ et $[\pm 15^o]_s$ (voir Figures IV.12 et IV.13). Ainsi, les conditions isothermes peuvent raisonnablement être considérées comme correctes dans ces cas. Cependant, pour les échantillons $[\pm 30^o]_s$ et $[\pm 45^o]_s$, les élévations de température commencent à devenir significatives (voir Figures IV.14 et IV.15), rendant l'hypothèse des conditions isothermes non valide. Cela peut également expliquer les écarts observés pour ces éprouvettes, entre les réponses expérimentales et celles simulées avec le modèle multi-échelle, qui est formulé dans l'hypothèse de conditions isothermes. De plus, comme cela a également été observé pour la matrice polyamide 6-6 seule (voir Section 4.3 du Chapitre II), les élévations de température sont loin d'avoir atteint le régime stabilisé dans les 100 cycles effectués. Ce signifie qu'une augmentation significative de la température est susceptible de se produire si un nombre de cycles plus important est appliqué au composite.

Il convient de remarquer que les boucles d'hystérésis qui apparaissent à chaque cycle ne sont pas bien reproduites par le modèle multi-échelle. Ceci est probablement dû au sous-modèle des torons, qui, contrairement à celui de la matrice, n'intègre aucun mécanisme viscoélastique et aucun mécanisme dependant du temps en général. La même conclusion peut être faite d'un point de vue énergétique. En effet, les élévations de température calculées à partir des analyses thermiques "0D" découplées (voir Figures IV.12, IV.13, IV.14 et IV.15) sont beaucoup plus faibles que celles observées expérimentalement (en particulier pour les éprouvettes $[\pm 30^o]_s$ et $[\pm 45^o]_s$). Cela montre que le modèle multi-échelle ne capture pas précisément l'énergie dissipée par le composite. L'intégration de mécanismes viscoélastiques dans les torons pourrait très certainement résoudre ce problème.

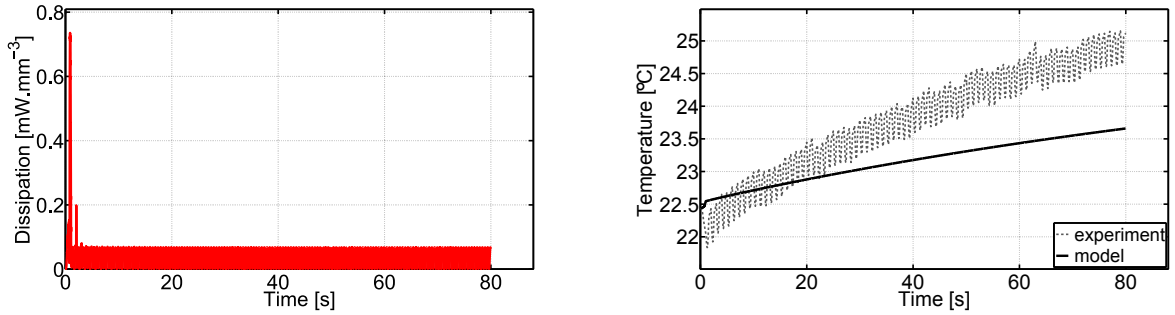

(a) Dissipation ($\dot{\overline{\Phi}}$) - temps

(b) Température (T) - temps

Figure IV.12: Elévation de température induite par la dissipation évaluée à partir de l'analyse thermique "0D" découplée (voir l'Annexe C) pour un essai cyclique contrôlé en contrainte: 100 cycles effectués à 1 Hz pour une éprouvette stratifiée $[0^o]_4$ (Figure IV.8).

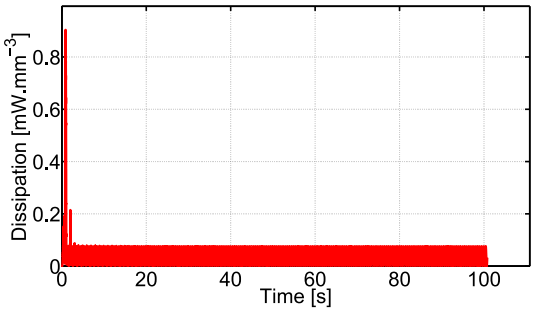

(a) Dissipation ($\dot{\bar{\Phi}}$) - temps

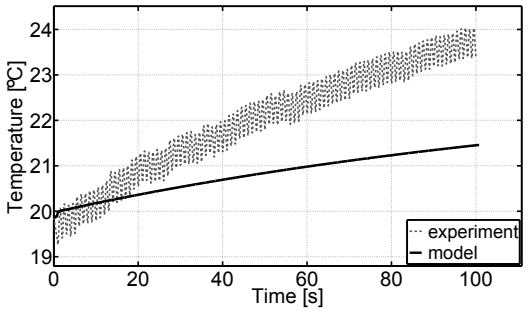

(b) Température (T) - temps

Figure IV.13: Elévation de température induite par la dissipation évaluée à partir de l'analyse thermique "0D" découplée (voir l'Annexe C) pour un essai cyclique contrôlé en contrainte: 100 cycles effectués à 1 Hz pour une éprouvette stratifiée $[\pm 15^o]_s$ (Figure IV.9).

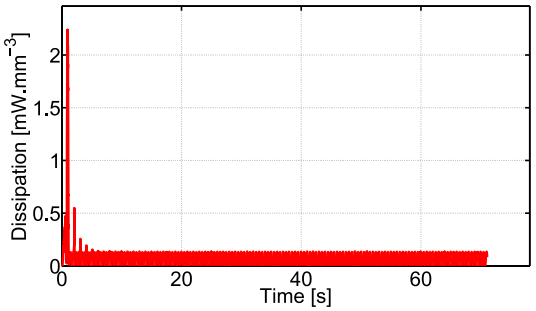

(a) Dissipation ($\dot{\bar{\Phi}}$) - temps

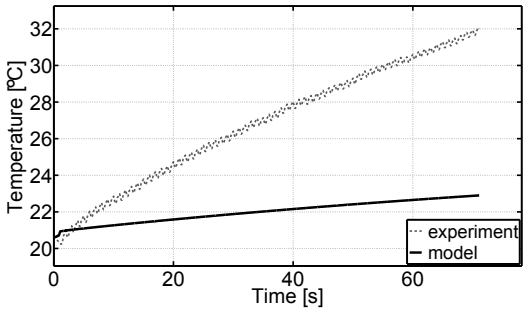

(b) Température (T) - temps

Figure IV.14: Elévation de température induite par la dissipation évaluée à partir de l'analyse thermique "0D" découplée (voir l'Annexe C) pour un essai cyclique contrôlé en contrainte: 100 cycles effectués à 1 Hz pour une éprouvette stratifiée $[\pm 30^o]_s$ (Figure IV.10).

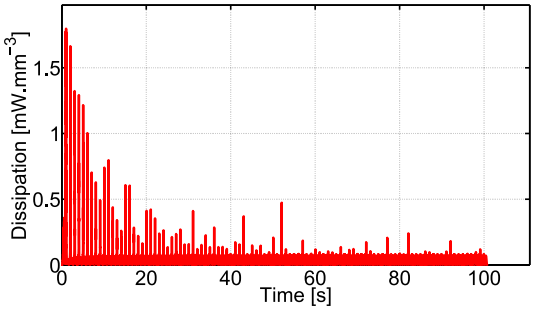

(a) Dissipation ($\dot{\bar{\Phi}}$) - temps

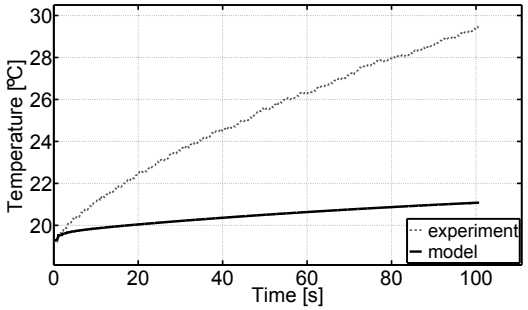

(b) Température (T) - temps

Figure IV.15: Elévation de température induite par la dissipation évaluée à partir de l'analyse thermique "0D" découplée (voir l'Annexe C) pour un essai cyclique contrôlé en contrainte: 100 cycles effectués à 1 Hz pour une éprouvette stratifiée $[\pm 45^o]_s$ (Figure IV.11).

4 Simulations numériques, réponses mécaniques et comportement dissipatif d'un point matériel macroscopique

Toutes les simulations présentées dans cette section ont été réalisées avec les paramètres précédemment identifiés pour la matrice et les torons dans les Tableaux II.4 et IV.3, respectivement.

Afin de mieux comprendre le modèle multi-échelle, son comportement dissipatif est illustré par des exemples de simulations réalisées sur un seul point matériel macroscopique, dits "essais virtuels" (voir Section 1). Dans ces exemples, le composite est soumis à de la traction sens chaîne, à du cisaillement plan et à des états de contrainte combinants traction sens chaîne et cisaillement plan (voir Figure IV.16). Les simulations (ou jeux de simulations) suivantes sont proposées:

- Jeu de simulations 1: traction monotone sens chaîne
  Une déformation dans le sens chaîne $\overline{\varepsilon}_{11}$ de 0.02 est appliquée au matériau en 1 s pour la première simulation, 10 s pour la seconde et 100 s pour la troisième. Ce qui correspond à une vitesse de déformation de 2×10^{-2}, 2×10^{-3} et 2×10^{-4}, respectivement. Les résultats de ces simulations sont présentés en Figures IV.17 et IV.18. Ces calculs sont effectués avec un incrément de temps constant égal à $1/200^{eme}$ de la durée totale de la simulation correspondante.

- Jeu de simulations 2: cisaillement plan monotone
  Une déformation en cisaillement de 0.05 est appliquée au matériau en 1 s pour la première simulation, 10 s pour la seconde et 100 s pour la troisième. Ce qui correspond à une vitesse de déformation de 5×10^{-2}, 5×10^{-3} and 5×10^{-4} s^{-1}, respectivement. Les résultats de ces simulations sont présentés en Figures IV.19 et IV.20. Ces calculs sont effectués avec un incrément de temps constant égal à $1/200^{eme}$ de la durée totale de la simulation correspondante.

- Simulation 3: fluage et recouvrance en traction sens chaîne
  Une contrainte normale sens chaîne $\overline{\sigma}_{11}$ de 350 MPa est appliquée en 5 s sur le composite, dans un premier temps. Cette contrainte est ensuite maintenue pendant 300 s, avant de retourner à zéro en 5 s. Dans une dernière étape, le composite est laissé libre de contrainte pour encore 300 s. Les résultats de cette simulation sont présentés en Figures IV.21 et IV.22. Ce calcul est effectué avec un incrément de temps constant de $0,05$ s.

- Simulation 4: fluage et recouvrance en cisaillement plan
  Une contrainte de cisaillement plan $\overline{\sigma}_{12}$ de 40 MPa est appliquée en 5 s sur le composite, dans un premier temps. Cette contrainte est ensuite maintenue pendant 300 s, avant de retourner à zéro en 5 s. Dans une dernière étape, le composite est laissé libre de contrainte pour encore 300 s. Les résultats de cette simulation sont présentés en Figures IV.23 et IV.24. Ce calcul est effectué avec un incrément de temps constant de $0,05$ s.

- Simulation 5: traction cyclique sens chaîne
  Le composite est soumis à une contrainte cyclique dans le sens chaîne $\overline{\sigma}_{11}$ (signal triangulaire). Cette dernière oscille entre 350 et 0 MPa avec une fréquence de 1 Hz. 20

cycles sont effectués. Les résultats de cette simulation sont présentés en Figures IV.25 et IV.26. Ce calcul est effectué avec un incrément de temps constant de $0,005$ s, soit 200 incréments de temps par cycles.

- Simulation 6: cisaillement plan cyclique
  Le composite est soumis à une contrainte cyclique en cisaillement plan $\overline{\sigma}_{12}$ (signal triangulaire). Cette dernière oscille entre 40 et 0 MPa avec une fréquence de 1 Hz. 20 cycles sont effectués. Les résultats de cette simulation sont présentés en Figures IV.25 et IV.26. Ce calcul est effectué avec un incrément de temps constant de $0,005$ s, soit 200 incréments de temps par cycles.

- Jeu de simulations 7: traction sens chaîne et cisaillement plan combinés non proportionnellement
  Le composite est soumis à un état de contrainte combinant traction sens chaîne et cisaillement plan qui est appliqué à travers deux chemins de chargement différents ayant les mêmes amplitudes:
  - Chemin 1: Une contrainte normale sens chaîne $\overline{\sigma}_{11}$ de 200 MPa est appliquée en 5 s dans un premier temps. $\overline{\sigma}_{11}$ est ensuite maintenue constante, tandis qu'une contrainte de cisaillement plan $\overline{\sigma}_{12}$ de 30 MPa est appliquée en 5 s. Ces deux contraintes $\overline{\sigma}_{11}$ et $\overline{\sigma}_{12}$ sont maintenues pendant 5 s, avant de retourner à zéro en encore 5 s.
  - Chemin 2: Une contrainte de cisaillement plan $\overline{\sigma}_{12}$ de 30 MPa est appliquée en 5 s dans un premier temps. $\overline{\sigma}_{12}$ est ensuite maintenue constante, tandis qu'une contrainte normale sens chaîne $\overline{\sigma}_{11}$ de 200 MPa est appliquée en 5 s. Ces deux contraintes $\overline{\sigma}_{11}$ et $\overline{\sigma}_{12}$ sont maintenues pendant 5 s, avant de retourner à zéro en encore 5 s.

  Les résultats de ces simulations sont présentés en Figures IV.29, IV.30 et IV.31. Ces calculs sont effectués avec un incrément de temps constant de $0,05$ s.

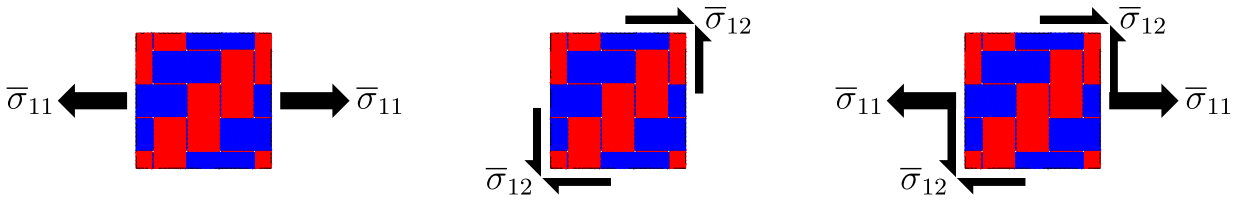

(a) Traction sens chaîne (b) Cisaillement plan (c) Traction sens chaîne et cisaillement plan combinés

Figure IV.16: Illustrations des configurations de chargement simulées.

Dans toutes les simulations, le bilan énergétique est bien respecté (Voir Figures IV.21e, IV.23e, IV.25e, IV.27e, IV.29f et IV.29g): l'énergie de déformation macroscopique $\overline{W}_{\varepsilon}$ est toujours bien égale à la somme des énergies macroscopiques stockées et dissipées, $\overline{\rho\psi}$ et $\overline{\Phi}$. De plus, l'énergie dissipée macroscopique ne fait qu'augmenter ($\dot{\overline{\Phi}} \geq 0$), ce qui est bien en accord avec l'inégalité de Clausius Duhem écrite dans son formalisme macroscopique dans l'équation (I.7).

Les résultats de ces simulations sont présentés dans quatre sous-sections différentes. La première est dédiée aux jeux de simulations 1 et 2 (Section 4.1: Chargements monotones),

la seconde aux simulations 3 et 4 (Section 4.2: Fluage et recouvrance), la troisième aux simulations 5 et 6 (Section 4.3: Chargements cycliques) et le quatrième au jeu de simulation 7 (Section 4.4: Chargements non proportionnels, traction sens chaîne et cisaillement plan combinés).

4.1 Chargements monotones

Dans le jeu de simulation 1 (voir Figures IV.17 et IV.18), lorsque le composite est chargé dans le sens chaîne, la plus grande partie de l'effort est supportée par les torons de chaîne dans leur direction longitudinale (voir Figure IV.18c). Au même moment, une part moindre de cet effort est également transmise aux torons de trame dans leur direction transversale (voir Figure IV.18d), ce qui provoque de la microfissuration dans ces derniers (voir Figure IV.18f). Dans la matrice, la plupart des contraintes sont concentrées dans les zones de croisement entre torons, conduisant à l'apparition d'endommagement dans ces zones (voir Figures IV.18a and IV.18b).

Néanmoins, les dégradations survenant dans les torons de trame et dans la matrice semblent avoir des conséquences limitées à l'échelle macroscopique, car la plus grande partie de la charge est portée par les torons de chaîne dans leur direction longitudinale, qui se comportent élastiquement avec une rigidité importante. Pour cette raison, la réponse du composite reste quasi-linéaire et l'effet de vitesse à l'échelle macroscopique n'est presque pas visible (voir Figure IV.17).

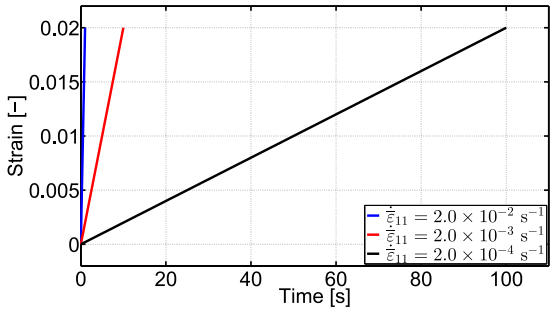

(a) Déformation appliquée ($\overline{\varepsilon}_{11}$) - temps

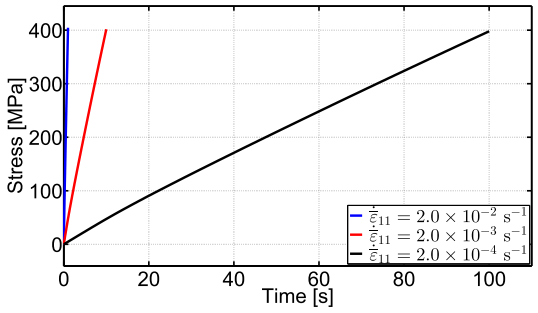

(b) Réponse en contrainte ($\overline{\sigma}_{11}$) - temps

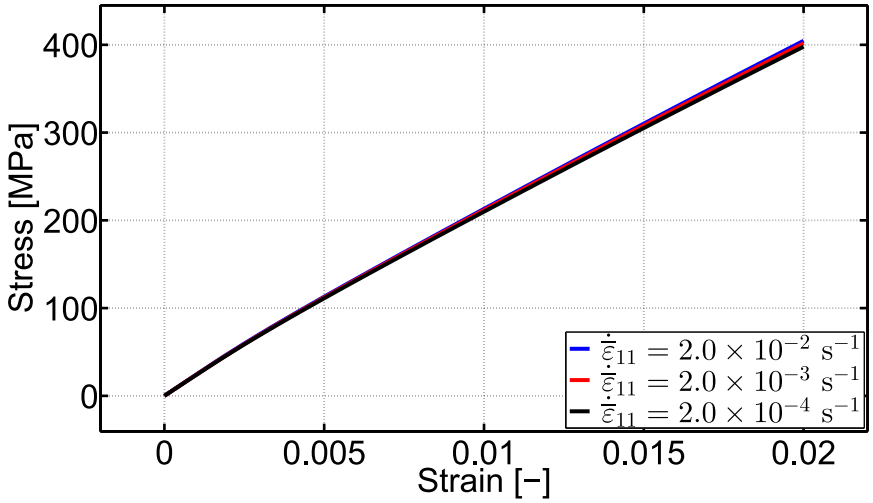

(c) Contrainte ($\overline{\sigma}_{11}$) - déformation ($\overline{\varepsilon}_{11}$)

Figure IV.17: Jeu de simulations 1: traction monotone sens chaîne.

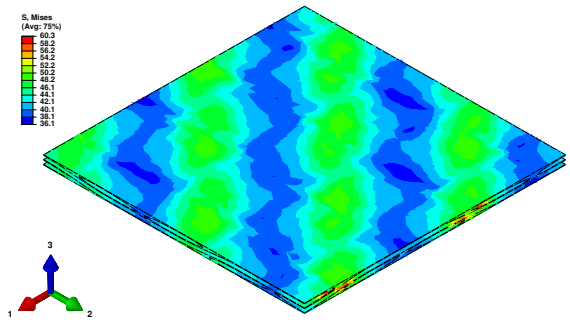

(a) Contrainte équivalente de Von Mises (eq($\boldsymbol{\sigma}$)) dans la matrice

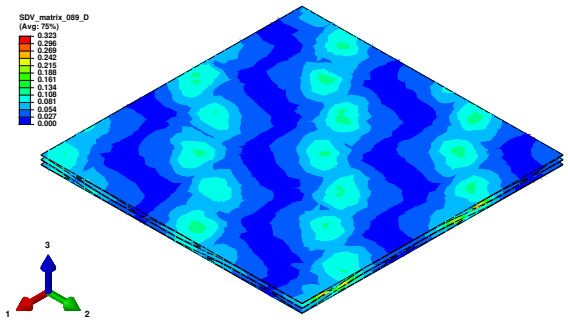

(b) Endommagement (D) dans la matrice

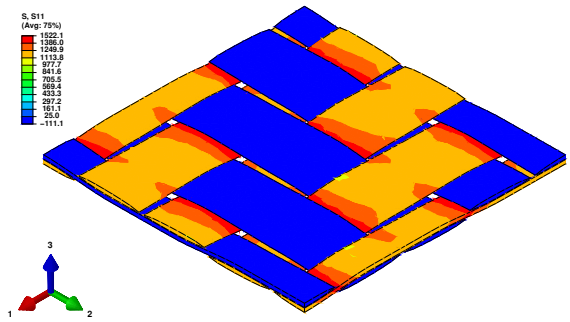

(c) Contrainte longitudinale (σ_{11}) dans les torons

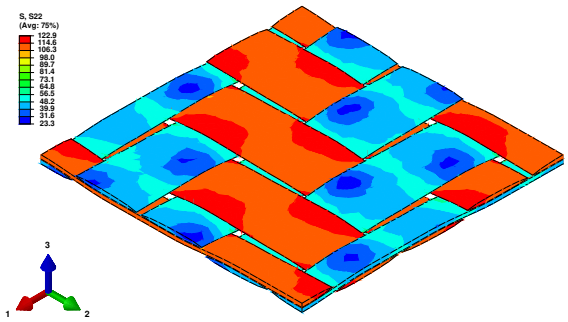

(d) Contrainte transversale (σ_{22}) dans les torons

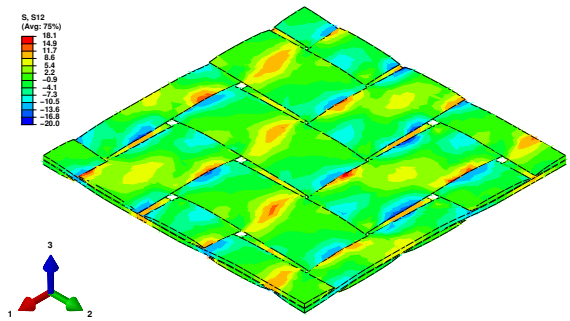

(e) Contrainte de cisaillement plan (σ_{12}) dans les torons

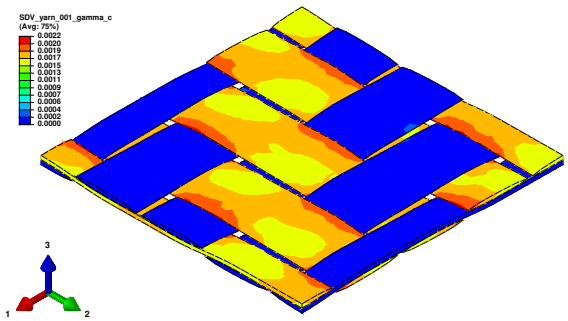

(f) Densité de microfissures (γ_c) dans les torons

Figure IV.18: Jeu de simulations 1: traction monotone sens chaîne, champs locaux à la fin de la simulation effectuée avec une vitesse de déformation de $\dot{\bar{\varepsilon}}_{11} = 2.0 \times 10^{-2}$ s^{-1}. Il est important de préciser que les contraintes locales dans les torons sont exprimées dans le repère local de chaque point matériel de toron (voir Figure I.10d).

Dans le jeu de simulation 2 (voir Figures IV.19 et IV.20), lorsque le composite est chargé en un cisaillement plan, les contraintes longitudinales et transversales restent presque nulles dans les torons (voir Figures IV.20c et IV.20d), qui ne sont alors chargés qu'en cisaillement (voir Figure IV.20e). Ceci entraîne une croissance rapide de la microfissuration et donc une réduction de la rigidité à la fois dans les torons de chaîne et de trame (voir Figure IV.20f). Ainsi, les efforts sont progressivement transférés vers la matrice où les contraintes se concentrent principalement entre les torons, là où l'endommagement matriciel se développe (voir Figures IV.20a et IV.20b). Notons que ces mécanismes de dégradation ont une influence significative sur la réponse macroscopique en cisaillement plan du composite, qui semble être davantage dominée par la matrice, avec un effet de vitesse bien visible (voir Figure IV.19c).

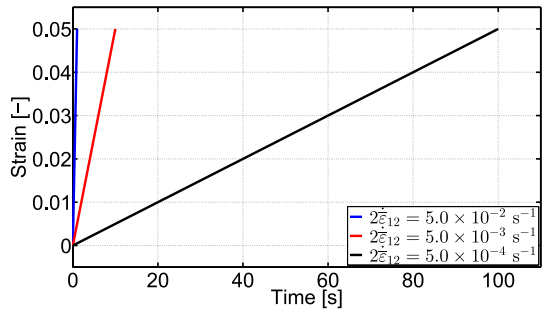

(a) Déformation appliquée ($2\bar{\varepsilon}_{12}$) - temps

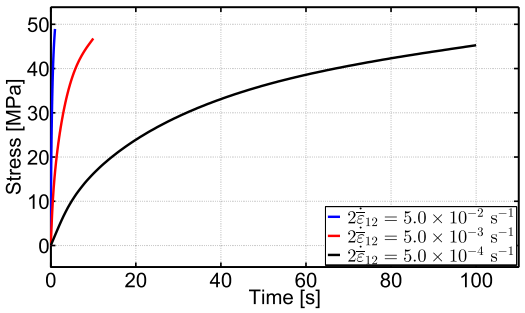

(b) Réponse en contrainte ($\bar{\sigma}_{12}$) - temps

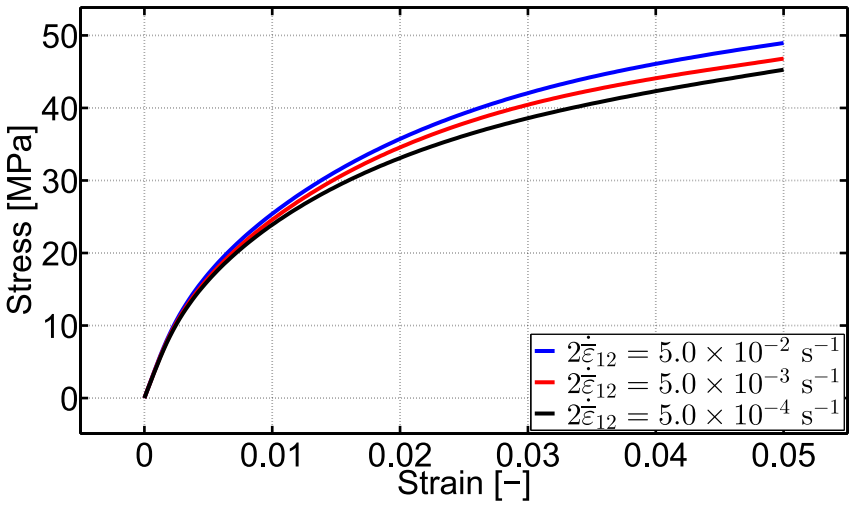

(c) Contrainte ($\bar{\sigma}_{12}$) - déformation ($2\bar{\varepsilon}_{12}$)

Figure IV.19: Jeu de simulations 2: cisaillement plan monotone.

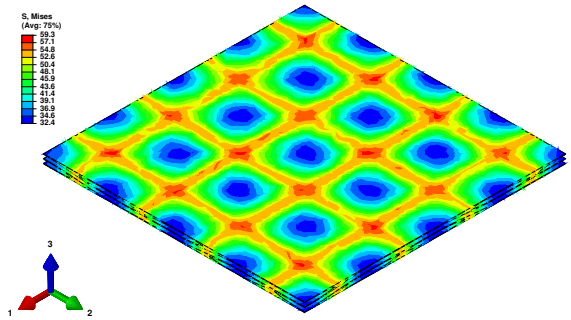

(a) Contrainte équivalente de Von Mises (eq($\boldsymbol{\sigma}$)) dans la matrice

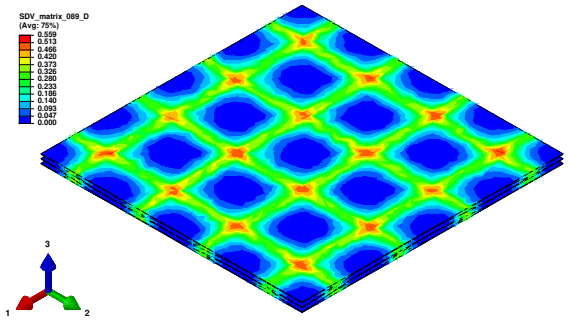

(b) Endommagement (D) dans la matrice

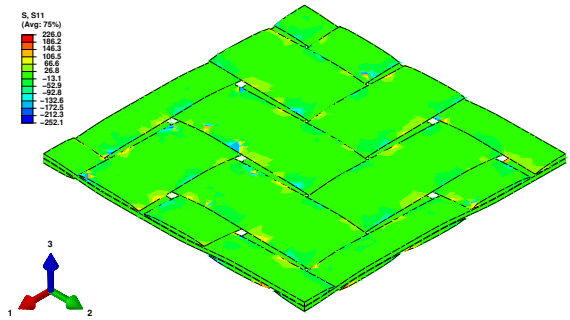

(c) Contrainte longitudinale (σ_{11}) dans les torons

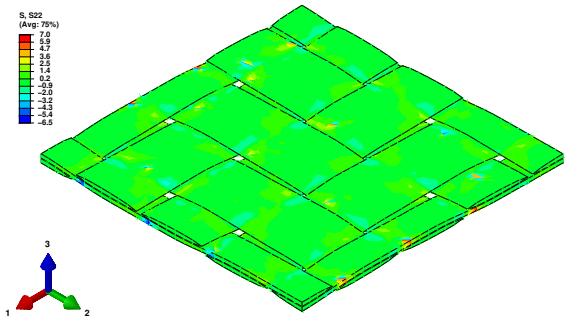

(d) Contrainte transversale (σ_{22}) dans les torons

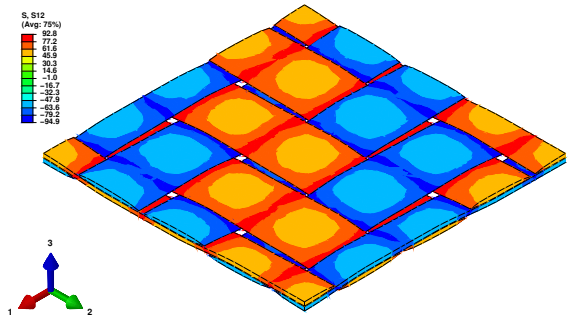

(e) Contrainte de cisaillement plan (σ_{12}) dans les torons

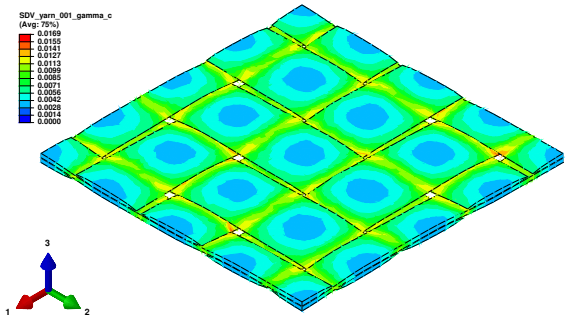

(f) Densité de microfissures (γ_c) dans les torons

Figure IV.20: Jeu de simulations 2: cisaillement plan monotone, champs locaux à la fin de la simulation effectuée avec une vitesse de déformation de $2\dot{\bar{\varepsilon}}_{12} = 5.0 \times 10^{-2}$ s^{-1}. Il est important de préciser que les contraintes locales dans les torons sont exprimées dans le repère local de chaque point matériel de toron (voir Figure I.10d).

4.2 Fluage et recouvrance

Dans les simulations 3 et 4 (voir Figures IV.21, IV.22, IV.23 et IV.24), pendant la phase de fluage, de même manière que pour la matrice seule (voir Section 5.1 du Chapitre II), la déformation macroscopique augmente sous l'action d'une contrainte macroscopique constante.

Au cours de cette période, le composite stocke et dissipe l'énergie ($\overline{\rho}\dot{\overline{\psi}} > 0$ and $\dot{\overline{\Phi}} > 0$). A l'étape suivante, le composite est déchargé et laissé libre de toute contrainte. Une partie de la déformation macroscopique se recouvre quasi instantanément, tandis qu'une autre partie ne se recouvre qu'après un certain temps, à la fin duquel une partie non recouvrable reste (voir Figures IV.21b et IV.23b). Pendant cette phase de recouvrance, l'énergie stockée est convertie en énergie dissipée (voir Figures IV.21e et IV.23e). La réponse macroscopique en fluage du composite est due au comportement dépendant du temps de la matrice, ainsi qu'aux interactions liées à la microstructure entre la matrice et les torons. Bien que le sous-modèle des torons soit indépendant du temps, on observe une augmentation de la microfissuration dans ce composant (voir Figures IV.22 et IV.24). En effet, lorsque la matrice flue et s'endommage localement, une partie de la charge qu'elle soutient est progressivement transférée aux torons. Ce qui conduit à une augmentation de la densité de micro-fissures dans les torons. On ajoutera, dans le cas de la traction sens chaîne, que le fluage macroscopique est très faible, contrairement au cisaillement plan. Ceci est dû au fait que, dans ce dernier cas, le comportement du composite est principalement dominé par celui de la matrice.

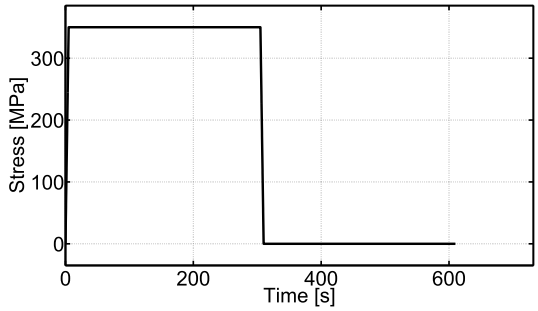

(a) Contrainte appliquée ($\overline{\sigma}_{11}$) - temps

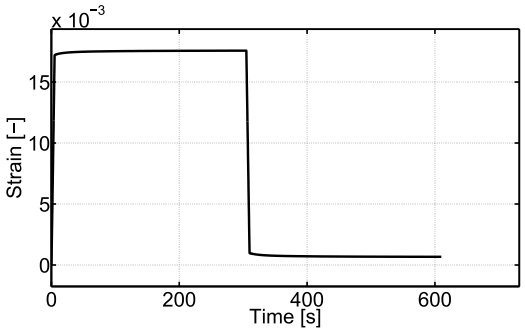

(b) Réponse en déformation ($\overline{\varepsilon}_{11}$) - temps

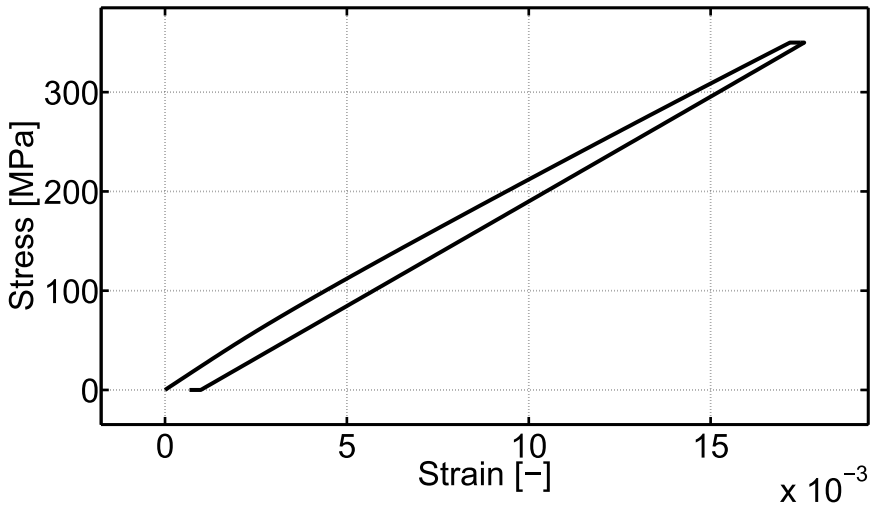

(c) Contrainte ($\overline{\sigma}_{11}$) - déformation ($\overline{\varepsilon}_{11}$)

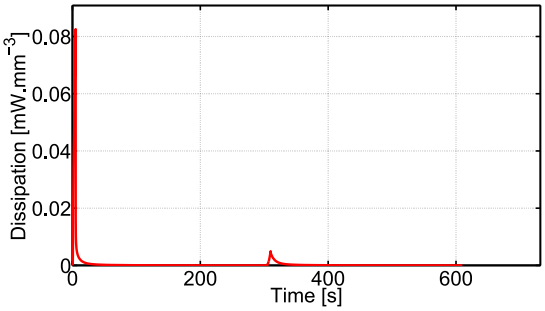

(d) Dissipation ($\dot{\overline{\Phi}}$) - temps

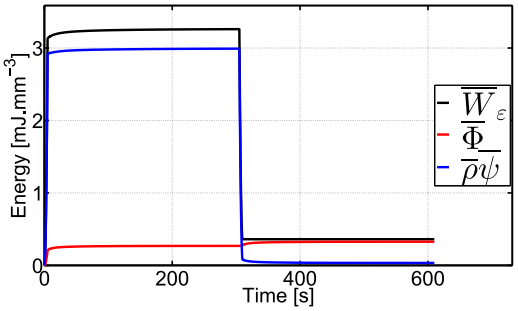

(e) Energie de déformation ($\overline{W}_\varepsilon$), énergie dissipée ($\overline{\rho\psi}$) et énergie stockée ($\overline{\Phi}$) - temps

Figure IV.21: Simulation 3: fluage et recouvrance en traction sens chaîne.

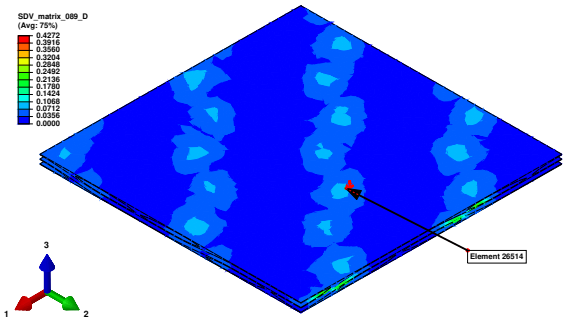

(a) Endommagement (D) dans la matrice à la fin de la phase de chargement ($t = 5$ s)

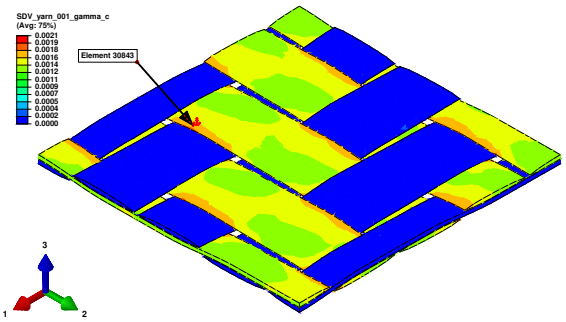

(b) Densité de microfissures (γ_c) dans les torons à la fin de la phase de chargement ($t = 5$ s)

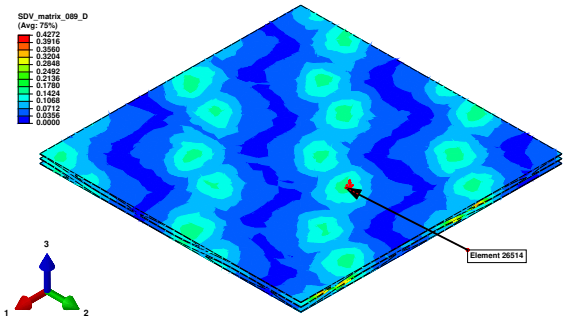

(c) Endommagement (D) dans la matrice à la fin de la phase de fluage ($t = 305$ s)

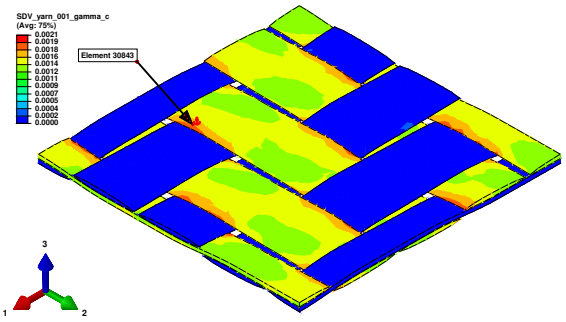

(d) Densité de microfissures (γ_c) dans les torons à la fin de la phase de fluage ($t = 305$ s)

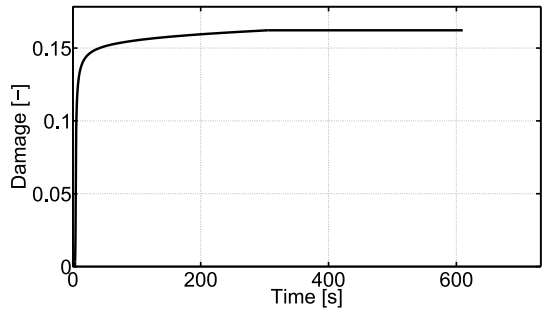

(e) Endommagement (D) dans la matrice, pour l'élément 26514 indiqué ci-dessus en Figures IV.22a et IV.22c

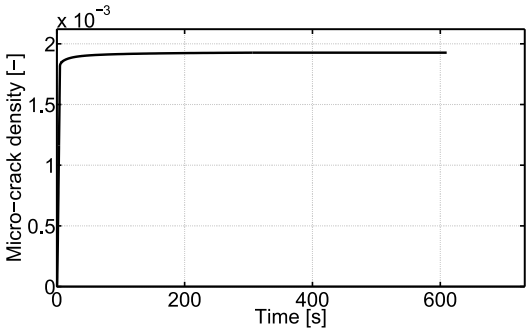

(f) Densité de microfissures (γ_c) dans les torons, pour l'élément 30843 indiqué ci-dessus en Figures IV.22b et IV.22d

Figure IV.22: Simulation 3: fluage et recouvrance en traction sens chaîne, champs locaux.

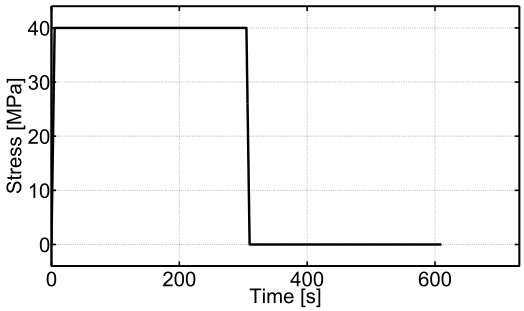

(a) Contrainte appliquée ($\overline{\sigma}_{12}$) - temps

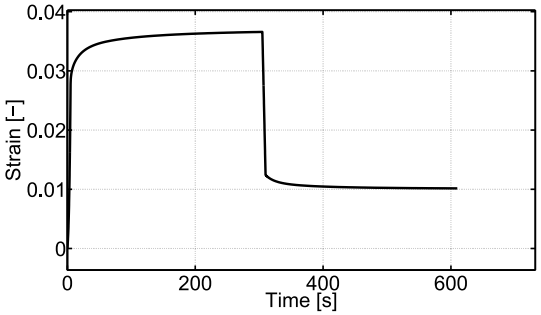

(b) Réponse en déformation ($2\overline{\varepsilon}_{12}$) - temps

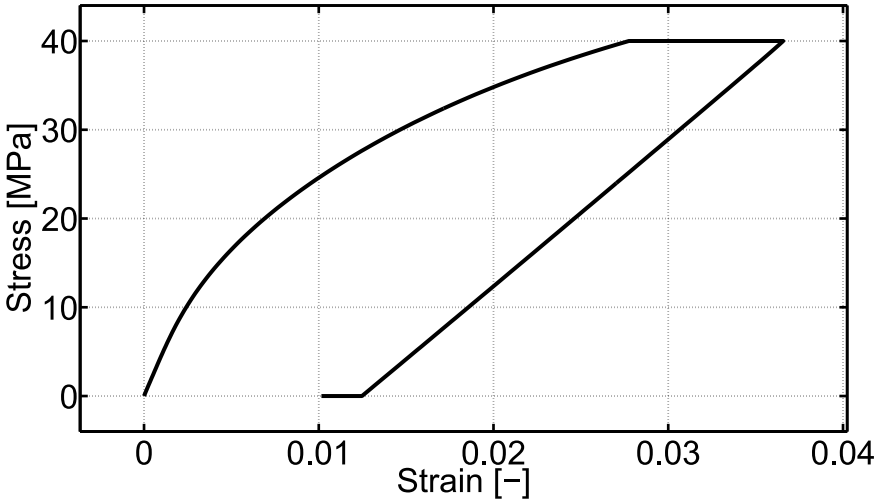

(c) Contrainte ($\overline{\sigma}_{12}$) - déformation ($2\overline{\varepsilon}_{12}$)

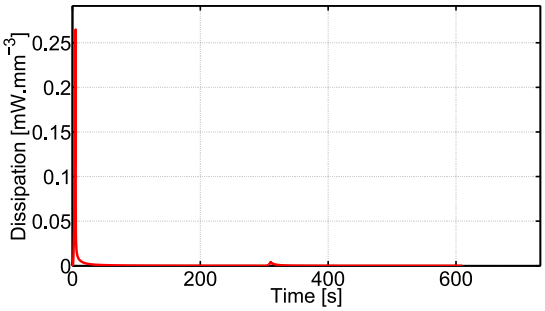

(d) Dissipation ($\dot{\overline{\Phi}}$) - temps

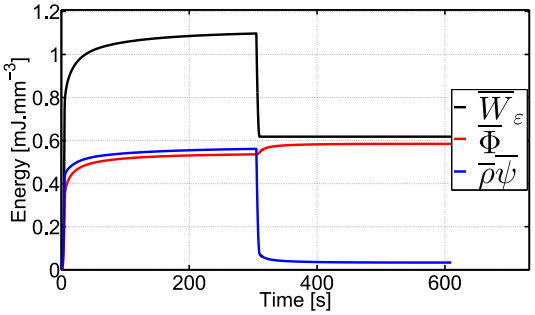

(e) Energie de déformation ($\overline{W}_\varepsilon$), énergie dissipée ($\overline{\rho\psi}$) et énérgie stockée ($\overline{\Phi}$) - temps

Figure IV.23: Simulation 4: fluage et recouvrance en cisaillement plan.

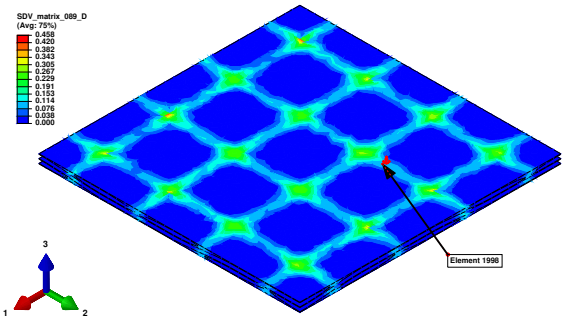

(a) Endommagement (D) dans la matrice à la fin de la phase de chargement ($t = 5$ s)

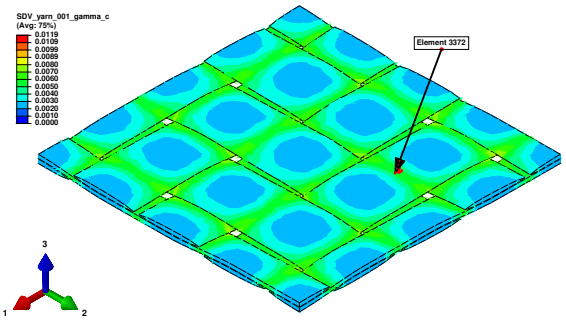

(b) Densité de microfissures (γ_c) dans les torons à la fin de la phase de chargement ($t = 5$ s)

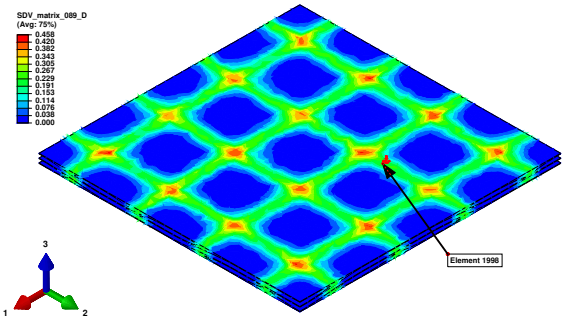

(c) Endommagement (D) dans la matrice à la fin de la phase de fluage ($t = 305$ s)

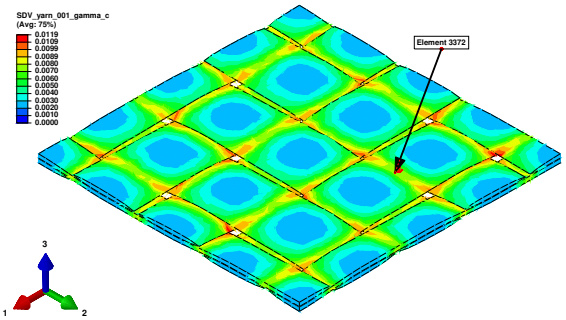

(d) Densité de microfissures (γ_c) dans les torons à la fin de la phase de fluage ($t = 305$ s)

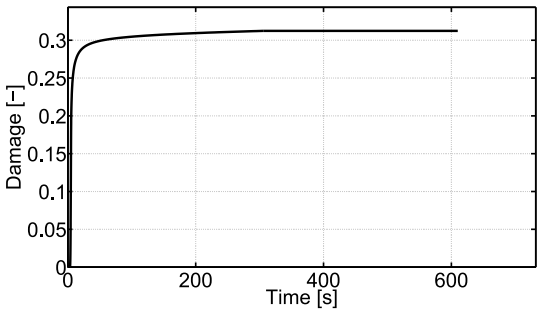

(e) Endommagement (D) dans la matrice, pour l'élément 1998 indiqué ci-dessus en Figures IV.24a et IV.24c

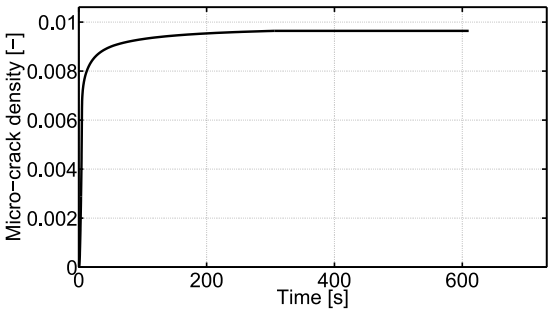

(f) Densité de microfissures (γ_c) dans les torons, pour l'élément 3372 indiqué ci-dessus en Figures IV.24b et IV.24d

Figure IV.24: Simulation 4: fluage et recouvrance en cisaillement plan, champs locaux.

4.3 Chargements cycliques

Dans les simulations 5 et 6 (voir Figures IV.25, IV.26, IV.27 et IV.28), sous chargement cyclique, le composite flue globalement, la déformation macroscopique augmente progressivement d'un cycle à l'autre sous l'action d'une contrainte macroscopique moyenne. Au fil des cycles répétés, l'endommagement s'accumule dans la matrice et s'accompagne de microfissuration intra-toron, en raison des interactions de microstructure. Ceci conduit à une réduction progressive de la rigidité du composite tout au long des cycles répétés et à une augmentation de la déformation rémanente, visible lors du déchargement. Comme déjà re-

marqué pour les simulations 3 et 4, et pour les mêmes raisons, ce phénomène est beaucoup plus important lorsque le composite est chargé en cisaillement plan. De plus, bien qu'elles soient difficilement visibles (surtout en tension de chaîne), des boucles d'hystérésis héritées de la viscoélasticité de la matrice (voir Section 5.1 du Chapitre II) peuvent être observées à l'échelle macroscopique, apportant une certaine quantité d'énergie dissipée à chaque cycle. Cette dissipation liée à la matrice représente, après un certain nombre de cycles, la plus grande partie de l'énergie totale dissipée par le composite.

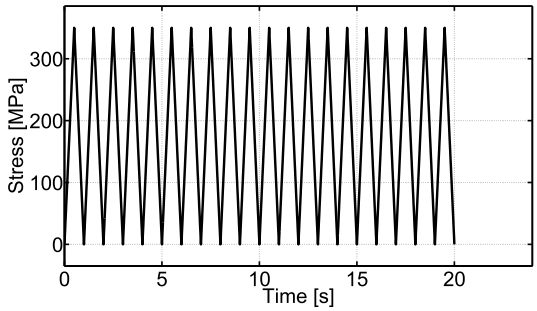

(a) Contrainte appliquée ($\overline{\sigma}_{11}$) - temps

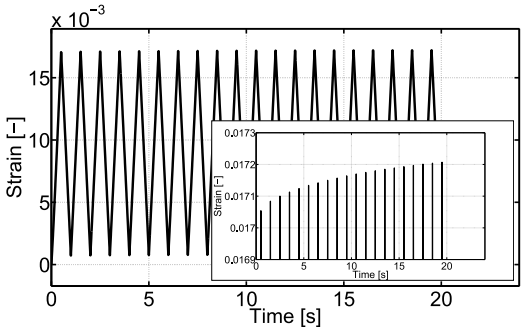

(b) Réponse en déformation ($\overline{\varepsilon}_{11}$) - temps

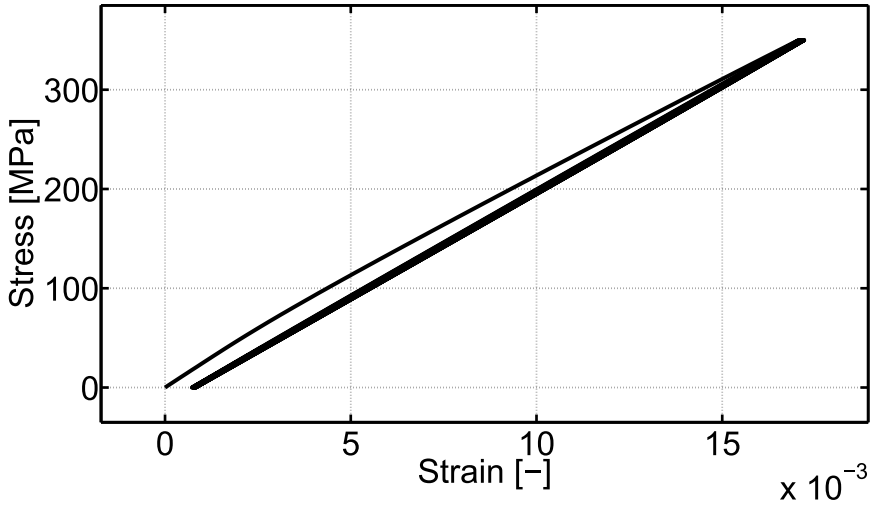

(c) Contrainte ($\overline{\sigma}_{11}$) - déformation ($\overline{\varepsilon}_{11}$)

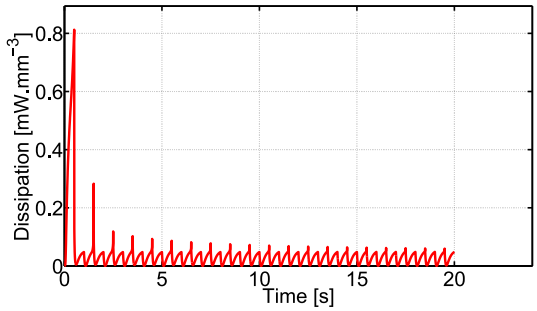

(d) Dissipation ($\dot{\overline{\Phi}}$) - temps

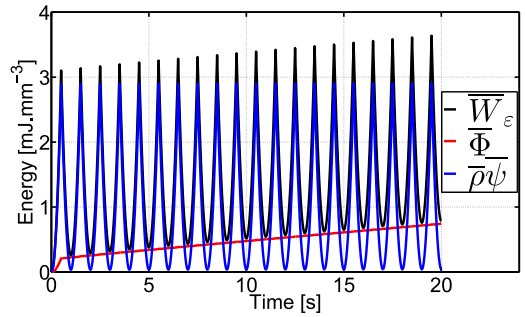

(e) Energie de déformation ($\overline{W}_{\varepsilon}$), énergie dissipée ($\overline{\rho\psi}$) et énergie stockée ($\overline{\Phi}$) - temps

Figure IV.25: Simulation 5: traction cyclique sens chaîne.

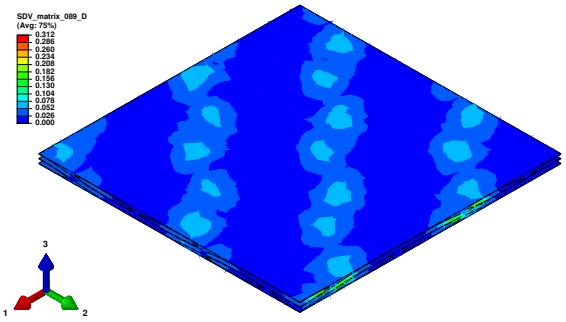

(a) Endommagement (D) dans la matrice à la fin du 1^{er} cycle ($t = 1$ s)

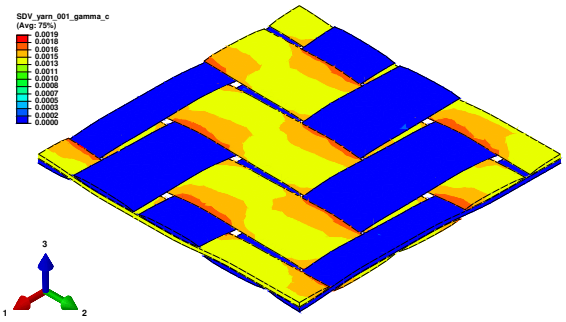

(b) Densité de microfissures (γ_c) dans les torons à la fin du 1^{er} cycle ($t = 1$ s)

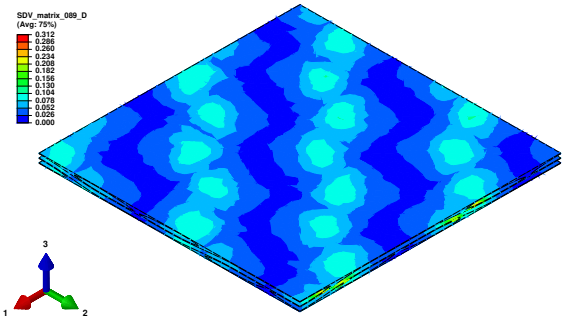

(c) Endommagement (D) dans la matrice à la fin du 10^{eme} cycle ($t = 10$ s)

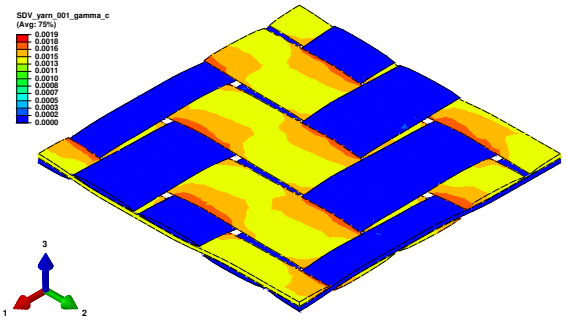

(d) Densité de microfissures (γ_c) dans les torons à la fin du 10^{eme} cycle ($t = 10$ s)

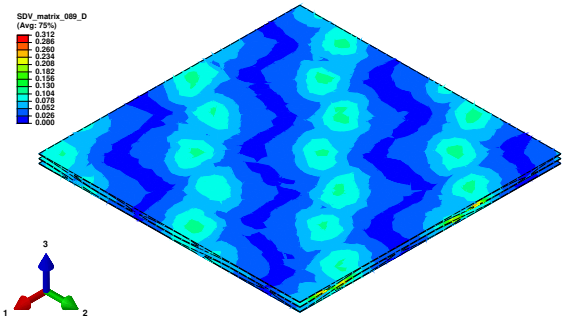

(e) Endommagement (D) dans la matrice à la fin du 20^{eme} cycle ($t = 20$ s)

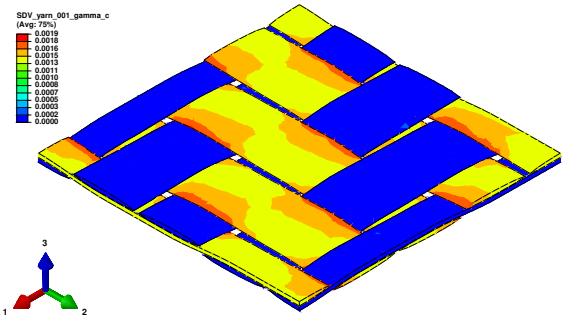

(f) Densité de microfissures (γ_c) dans les torons à la fin du 20^{eme} cycle ($t = 20$ s)

Figure IV.26: Simulation 5: traction cyclique sens chaîne, champs locaux.

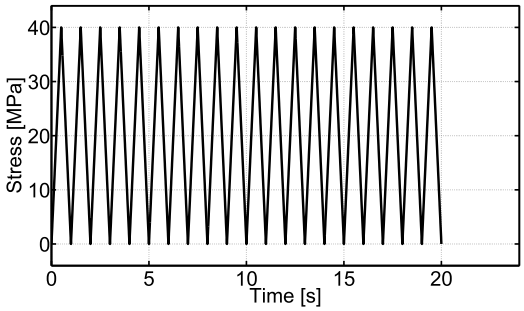

(a) Contrainte appliquée ($\overline{\sigma}_{12}$) - temps

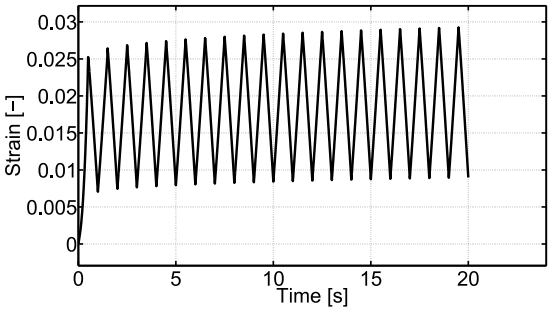

(b) Réponse en déformation ($2\overline{\varepsilon}_{12}$) - temps

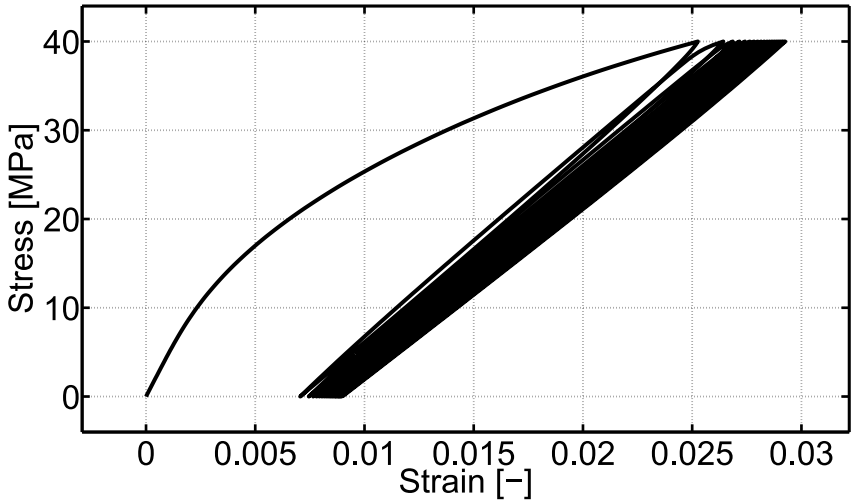

(c) Contrainte ($\overline{\sigma}_{12}$) - déformation ($2\overline{\varepsilon}_{12}$)

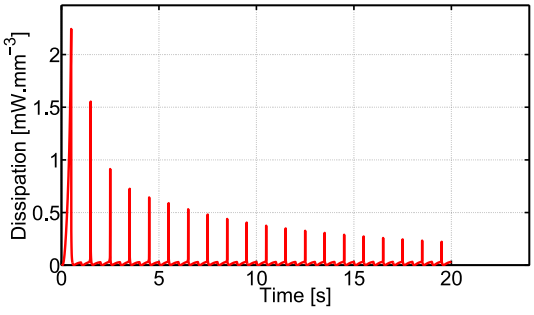

(d) Dissipation ($\dot{\overline{\Phi}}$) - temps

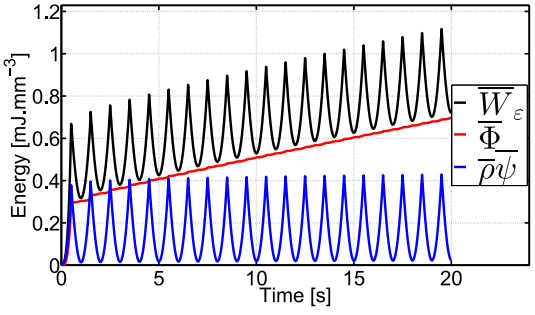

(e) Energie de déformation ($\overline{W}_\varepsilon$), énergie dissipée ($\overline{\rho\psi}$) et énergie stockée ($\overline{\Phi}$) - temps

Figure IV.27: Simulation 6: cisaillement plan cyclique.

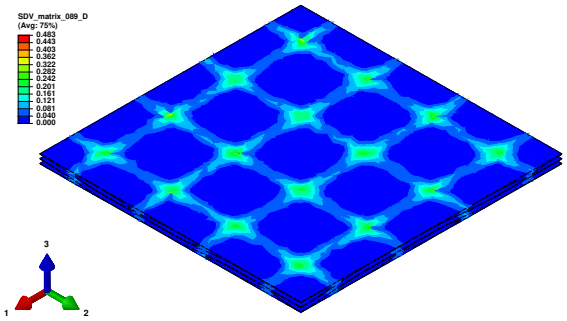

(a) Endommagement (D) dans la matrice à la fin du 1^{er} cycle ($t = 1$ s)

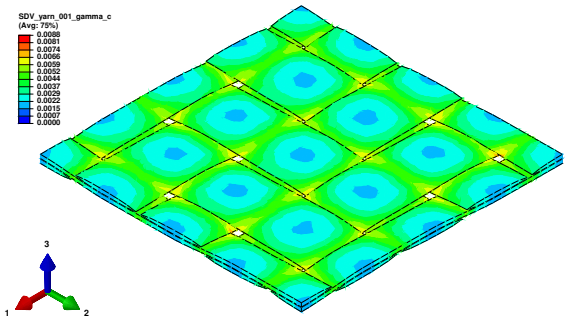

(b) Densité de microfissures (γ_c) dans les torons à la fin du 1^{er} cycle ($t = 1$ s)

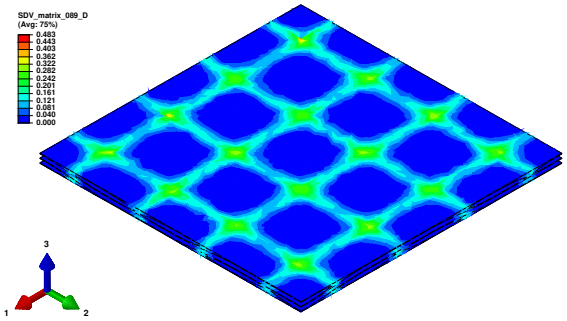

(c) Endommagement (D) dans la matrice à la fin du 10^{eme} cycle ($t = 10$ s)

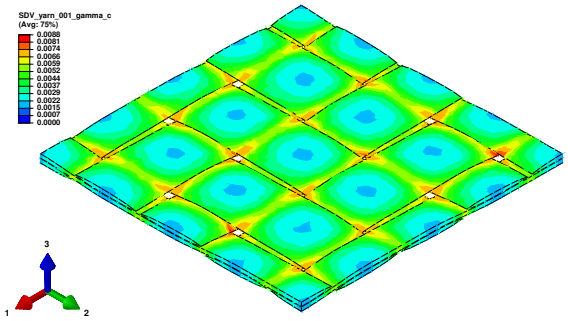

(d) Densité de microfissures (γ_c) dans les torons à la fin du 10^{eme} cycle ($t = 10$ s)

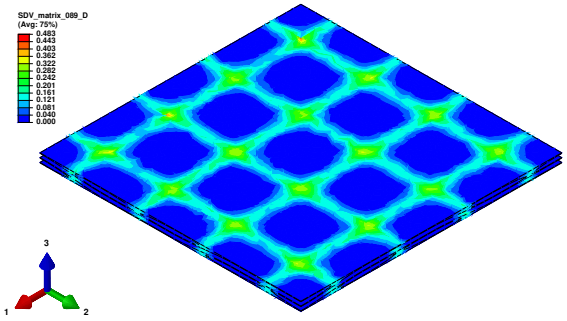

(e) Endommagement (D) dans la matrice à la fin du 20^{eme} cycle ($t = 20$ s)

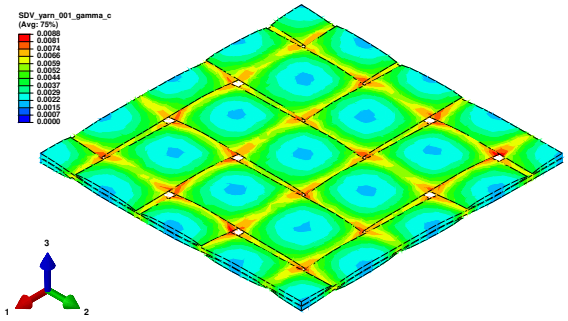

(f) Densité de microfissures (γ_c) dans les torons à la fin du 20^{eme} cycle ($t = 20$ s)

Figure IV.28: Simulation 6: cisaillement plan cyclique, champs locaux.

4.4 Chargements non proportionnels, traction sens chaîne et cisaillement plan combinés

Le jeu de simulation 7 (voir Figures IV.29, IV.30 et IV.31) met en évidence l'importance du chemin de chargement lorsque le composite est soumis à un état de contrainte combiné. Bien que les mêmes amplitudes de contrainte soient appliquées pour les chemins 1 et 2, on

peut remarquer que les amplitudes des réponses en déformation sont très différentes. La valeur maximale de la déformation $\overline{\varepsilon}_{11}$ obtenue pour le chemin 1 est légèrement supérieure que celle obtenue pour le chemin 2. En effet, pour le chemin 1, la contrainte $\overline{\sigma}_{11}$ a été maintenue plus longtemps que pour le chemin 2. Par conséquent, le composite a davantage eu le temps de fluer en traction sens chaîne. De même, la valeur maximale de la contrainte de cisaillement plan $2\overline{\varepsilon}_{12}$ résultant du chemin 2 est beaucoup plus grande que celle obtenue à partir du chemin 1. En effet, pour le chemin 2, la contrainte de cisaillement plan $\overline{\sigma}_{12}$ a été maintenue plus longtemps que pour le chemin 1. Par conséquent, le composite a davantage eu le temps de fluer en cisaillement plan. Néanmoins, la différence dans les amplitudes de déformation est beaucoup plus importante en cisaillement plan, car dans ce cas le comportement du composite est plus dominé par la matrice et davantage sujet au fluage. D'un point de vue énergétique (voir Figures IV.29f et IV.29g), le composite a dissipé plus d'énergie avec le chemin 1 qu'avec le chemin 2, alors que la quantité maximale d'énergie stockée est approximativement la même pour les deux chemins. Cependant, une plus grande partie de cette énergie stockée a été récupérée avec le chemin 2. Dans l'ensemble, le chemin de chargement 1 implique plus d'énergie de déformation que le chemin 2.

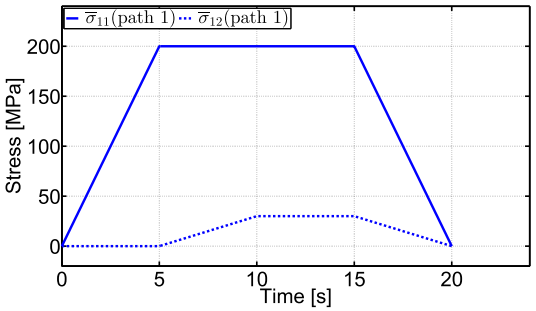

(a) Chemin 1: contraintes appliquées ($\overline{\sigma}_{11}$ et $\overline{\sigma}_{12}$) - temps

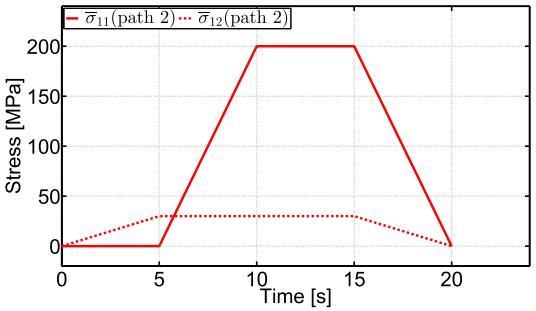

(b) Chemin 2: contraintes appliquées ($\overline{\sigma}_{11}$ et $\overline{\sigma}_{12}$) - temps

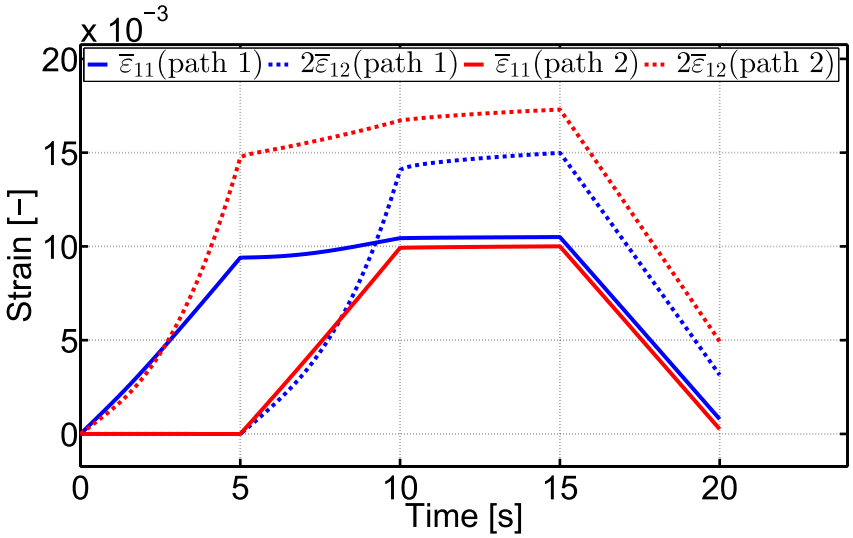

(c) chemins 1 et 2: réponses en déformation ($\overline{\varepsilon}_{11}$ et $2\overline{\varepsilon}_{12}$) - temps

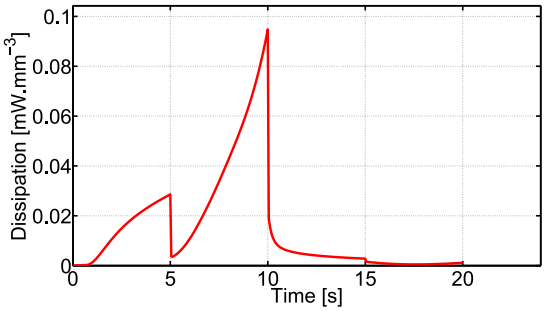

(d) Chemin 1: dissipation ($\dot{\overline{\Phi}}$) - temps

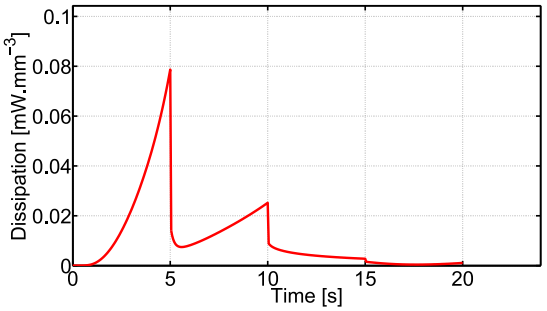

(e) Chemin 2: dissipation ($\dot{\overline{\Phi}}$) - temps

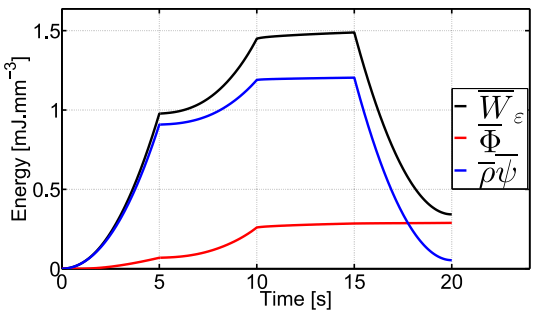

(f) Chemin 1: énergie de déformation ($\overline{W}_\varepsilon$), énergie dissipée ($\overline{\rho\psi}$) et énergie stockée ($\overline{\Phi}$) - temps

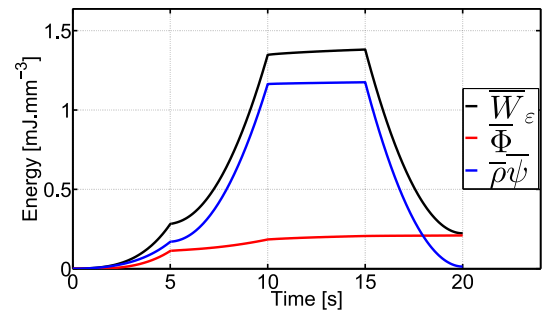

(g) Chemin 2: énergie de déformation ($\overline{W}_\varepsilon$), énergie dissipée ($\overline{\rho\psi}$) et énergie stockée ($\overline{\Phi}$) - temps

Figure IV.29: Jeu de simulations 7: traction sens chaîne et cisaillement plan combinés non proportionnellement.

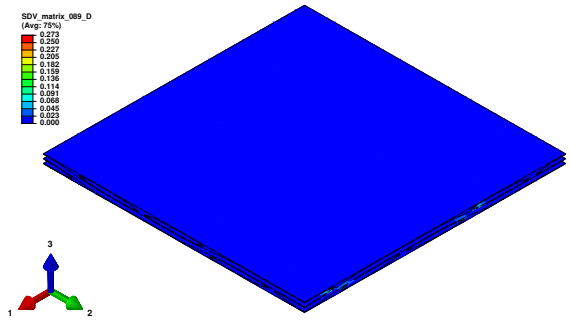

(a) Chemin 1: endommagement (D) dans la matrice à $t = 5$ s ($\overline{\sigma}_{11} = 200$ MPa and $\overline{\sigma}_{12} = 0$ MPa)

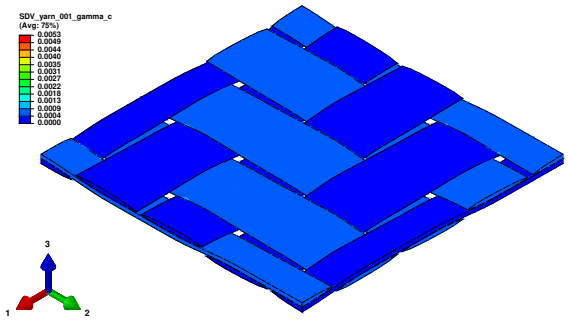

(b) Chemin 1: densité de microfissures (γ_c) dans les torons à $t = 5$ s ($\overline{\sigma}_{11} = 200$ MPa and $\overline{\sigma}_{12} = 0$ MPa)

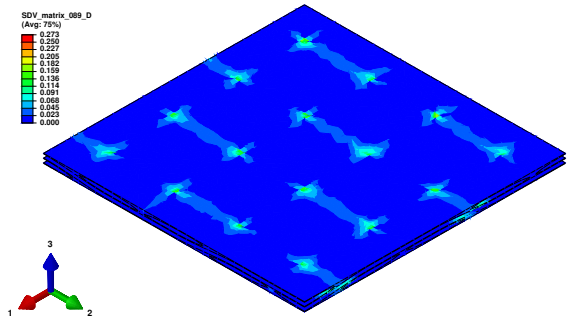

(c) Chemin 1: endommagement (D) dans la matrice à $t = 10$ s ($\overline{\sigma}_{11} = 200$ MPa and $\overline{\sigma}_{12} = 30$ MPa)

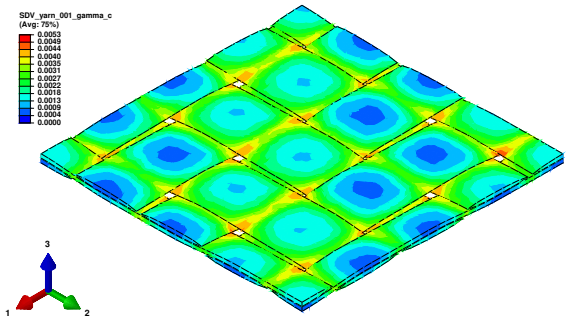

(d) Chemin 1: densité de microfissures (γ_c) dans les torons à $t = 10$ s ($\overline{\sigma}_{11} = 200$ MPa and $\overline{\sigma}_{12} = 30$ MPa)

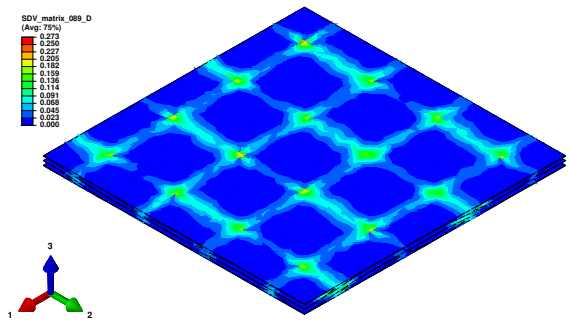

(e) Chemin 1: endommagement (D) dans la matrice à $t = 15$ s ($\overline{\sigma}_{11} = 200$ MPa and $\overline{\sigma}_{12} = 30$ MPa)

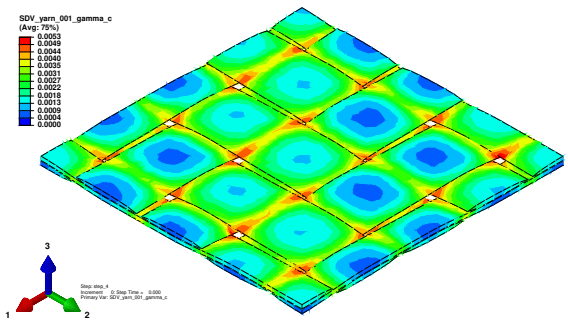

(f) Chemin 1: densité de microfissures (γ_c) dans les torons à $t = 15$ s ($\overline{\sigma}_{11} = 200$ MPa and $\overline{\sigma}_{12} = 30$ MPa)

Figure IV.30: Jeu de simulations 7: traction sens chaîne combinés non proportionnellement, champs locaux pour le chemin 1.

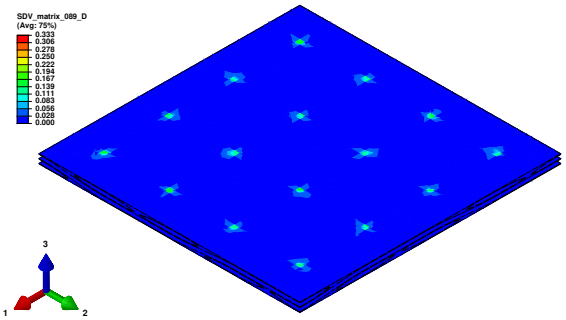

(a) Chemin 2: endommagement (D) dans la matrice à $t = 5$ s ($\overline{\sigma}_{11} = 0$ MPa and $\overline{\sigma}_{12} = 30$ MPa)

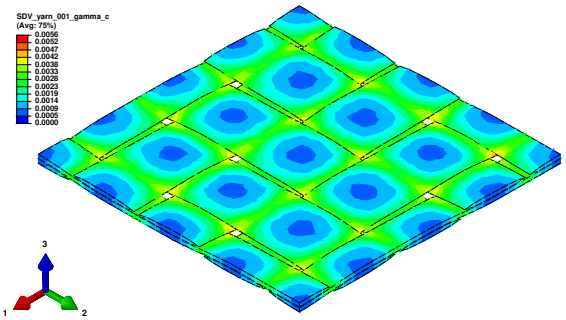

(b) Chemin 2: densité de microfissures (γ_c) dans les torons à $t = 5$ s ($\overline{\sigma}_{11} = 0$ MPa and $\overline{\sigma}_{12} = 30$ MPa)

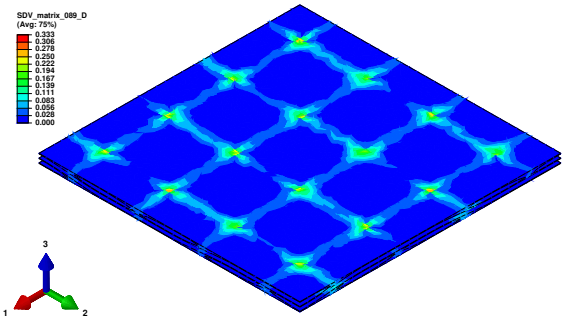

(c) Chemin 2: endommagement (D) dans la matrice à $t = 10$ s ($\overline{\sigma}_{11} = 200$ MPa and $\overline{\sigma}_{12} = 30$ MPa)

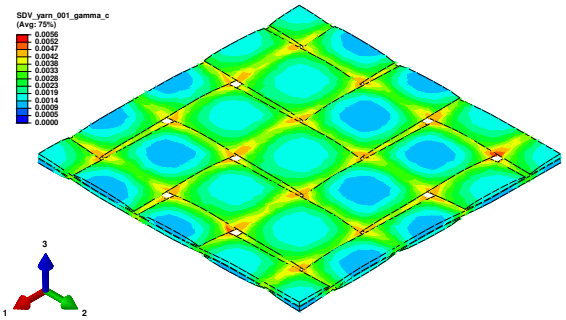

(d) Chemin 2: densité de microfissures (γ_c) dans les torons à $t = 10$ s ($\overline{\sigma}_{11} = 200$ MPa and $\overline{\sigma}_{12} = 30$ MPa)

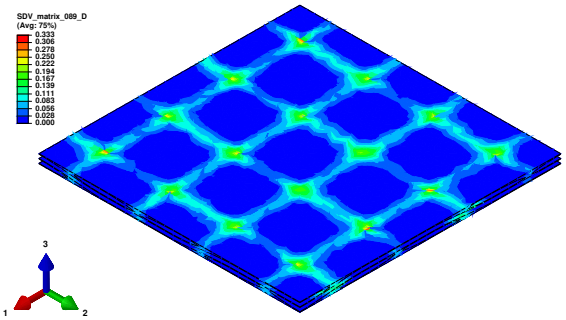

(e) Chemin 2: endommagement (D) dans la matrice à $t = 15$ s ($\overline{\sigma}_{11} = 200$ MPa and $\overline{\sigma}_{12} = 30$ MPa)

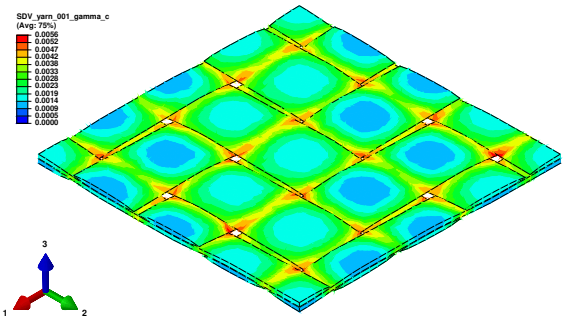

(f) Chemin 2: densité de microfissures (γ_c) dans les torons à $t = 15$ s ($\overline{\sigma}_{11} = 200$ MPa and $\overline{\sigma}_{12} = 30$ MPa)

Figure IV.31: Jeu de simulations 7: traction sens chaîne combinés non proportionnellement, champs locaux pour le chemin 2.

5 Conclusions

Dans ce dernier chapitre, un modèle multi-échelle pour les composites tissés à matrice thermoplastique a été mis en place à partir des modèles constitutifs locaux de la matrice et des torons, présentés dans les Chapitres II et III, respectivement. Ils sont assemblés à l'aide de l'approche de modélisation multi-échelle présentée au Chapitre I.

La cellule unitaire du composite étudié est générée à partir de données microstructurales obtenues par tomographie à rayons X. Les paramètres inconnus de la loi de compotement de torons sont identifiés à partir d'essais expérimentaux effectués sur des éprouvettes stratifiées $[0^o]_s$, $[\pm 15^o]_s$, $[\pm 30^o]_s$ et $[\pm 45^o]_s$ en conditions quasi-statiques. Par la suite, les prédictions du modèle multi-échelle sont comparées à d'autres essais où le composite est soumis à des chargements cycliques. Les bons accords entre les tendances prédites et les expériences démontrent les capacités du modèle multi-échelle à capter la réponse anisotrope du composite induite par la microstructure, ainsi que les effets dépendant du temps inhérents à la matrice thermoplastique, à savoir: l'accumulation de la déformation et l'endommagement sous chargement cyclique. Les prédictions sont assez précises pour les éprouvettes $[0^o]_s$ et $[\pm 15^o]_s$, alors qu'on observe certains écarts entre les réponses prédites et les résultats expériemtaux pour le $[\pm 30^o]_s$ et $[\pm 45^o]$, en particulier sous chargement cyclique. Cela met en évidence qu'il peut y avoir d'autres mécanismes d'endommagement (tels que de la décohésion à l'interface torons/matrice) impliqués lorsque le composite est chargé préférentiellement en cisaillement plan, et/ou que les torons présentent un comportement dépendant du temps (tel que la viscoélasticité). Ces aspects ne sont pas pris en compte dans le modèle multi-échelle actuel.

Des exemples supplémentaires sont proposés pour illustrer les capacités du modèle multi-échelles à réaliser des «essais virtuels», ainsi qu'à analyser l'influence des processus de déformation locaux sur le comportement macroscopique du composite. Ces simulations ont montré que, sous traction sens chaîne, les mécanismes d'endommagement locaux se produisent principalement dans les torons de trame et la matrice. Néanmoins, ces dégradations n'ont pas d'impact significatif sur la réponse macroscopique car la plus grande partie de la charge est portée par les torons de chaîne, qui présentent une réponse élastique et rigide dans leur direction longitudinale. À l'inverse, en cisaillement plan, la réponse macroscopique est beaucoup plus dominée par la matrice, les mécanismes d'endommagement locaux se produisent dans les torons de chaîne et de trame, conduisant à un transfert de charge assez rapide vers la matrice. Dans ce cas, les mécanismes de dégradation jouent un rôle significatif sur la réponse macroscopique du composite, où les effets dépendant du temps liés à la matrice sont clairement visibles. En outre, il convient de remarquer que ces effets dépendant du temps liés à la matrice interagissent à travers la microstructure avec les torons, dont le mécanisme d'endommagement est indépendant du temps. En plus de l'endommagement dans la matrice, ces interactions microstructurales créent une augmentation de la microfissuration intra-toron lorsque le composite est soumis à un niveau de contrainte constant ou cyclique. Pour terminer, le modèle multi-échelle permet d'analyser l'effet du chemin de chargement lorsque le composite est soumis à des états de contraintes combinés, mettant en évidence l'importance de ce dernier point.

General Conclusions and perspectives

Contents

1 General conclusions

Throughout this thesis, a multi-scale model is employed to describe the cyclic and time-dependent behaviour of thermoplastic-based woven composites. This model results from the assembly of the sub-models of the composite constituents through a fully integrated multi-scale modelling strategy (see Figure 1). The latter has the strong advantage to be entirely modular and applicable to any type of composites with periodic microstructure. Furthermore, this modularity enables the multi-scale model to be easily enhanced with even more advanced sub-models that might be developed in the future.

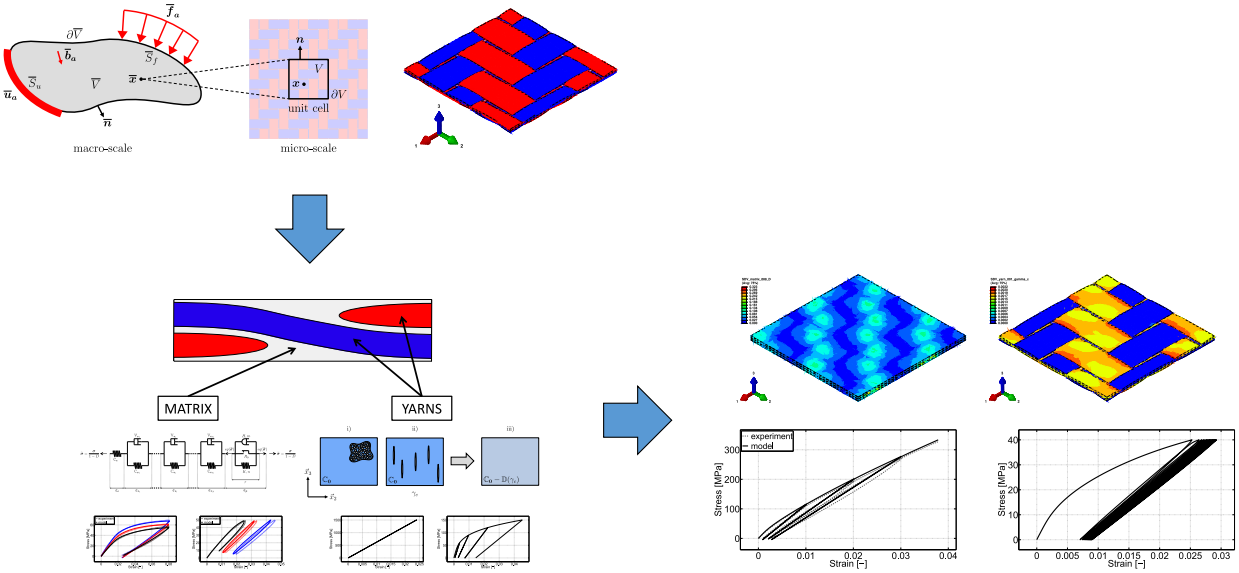

Figure 1: Fully integrated multi-scale modelling approach.

In Chapter I, a general framework of multi-scale modelling based on the concept of periodic homogenization has been introduced and applied to the particular case of woven composites through the use of the dedicated tool *TexGen*. The proposed approach allows to determine the macroscopic response of the composite through a FE simulation of the unit cell representative of the microstructure, where the local constitutive laws of each components are integrated, namely: the matrix and the yarns.

In Chapter II, a phenomenological multi-mechanisms constitutive model for thermoplastic polymers has been proposed to describe the behaviour the matrix phase within the composite. The constitutive equations are formulated through the framework of thermodynamics and account for viscoelasticity, viscoplasticity and ductile damage. This model is successfully identified for the polyamide 6-6 through a suitable experimental program including several types of tests, namely: monotonic, creep and cyclic tests. The good agreement between experimental and numerical results demonstrates the capabilities of the model to capture the mechanical response of thermoplastic polymers under various conditions and especially cyclic loading.

In Chapter III, a hybrid micromechanical-phenomenological constitutive model has been proposed to predict the behaviour of the yarn phase within the composite. The constitutive equations are formulated through the framework of thermodynamics and account for anisotropic damage and anelasticity, which are induced by the presence of a diffuse oriented micro-crack network in an initially transversely isotropic medium. The representation of

damage is obtained by a micromechanical description of a micro-cracked RVE, while the anelastic deformations are phenomenologically introduced through the new concept of damage induced anelasticity. The identification and the prediction capabilities have been validated from experimental data for flax-epoxy unidirectional composite, demonstrating that this model is well adapted to describe the transverse tension and the in-plane shear responses of such media.

Finally, in Chapter IV, the multi-scale model for thermoplastic-based woven composites is established the from the local constitutive models of the matrix and the yarns, presented in Chapters II and III, respectively. They are assembled together with the help of the multi-scale modelling approach presented in Chapter I. Overall, the tendencies predicted by the model are in good agreement with the experimental data. The model accuracy is reduced when the composite is preferentially loaded in in-plane shear. This emphasizes that, in this case, other damage mechanisms (such as debonding at yarn/matrix interface) and/or time-dependent features in the yarns (such as viscoelasticity) may be involved. Furthermore, the influence of the local damage mechanisms and deformation processes on the macroscopic response of the composite are analysed through several examples where the composite undergoes time-dependent deformations under monotonic loading, constant or cyclic stress levels and non-proportional multi-axial loading.

2 Perspectives

2.1 Integration of the microstructure variability

In this thesis, the proposed geometric description of the composite unit cell (see Section 3 in Chapter I) is an idealised representation of the woven microstructure. In reality, the geometry of the microstructure may experience some variability due to the manufacturing process. Thus, a better geometrical description of the unit cell could be eventually predicted through the simulation of the compaction and forming processes [162, 12, 70, 142].

2.2 Enhancement of the constitutive model of the yarns

It is recalled that the constitutive model considered for the yarn phase is time-independent and all the time-dependent effects arise from the matrix phase, as well as the microstructure interactions. In Section 3.3 of Chapter IV, it has been demonstrated that, in certain cases, the multi-scale model does not capture accurately the overall time-dependency (the hysteresis loops for example) and also the energy dissipated by the composite. This highlights the existence of other time-dependent deformation mechanisms related to the yarn phase, that have not been accounted for in the present modelling. To resolve this issue, viscoelastic mechanisms could be eventually added with the help of a coupled formulation [89, 92, 163]. Moreover, the evolution equations of the yarns could be also enhanced or/and modified in order to account for visco-damage [85, 10, 11, 176].

2.3 Integration of debonding and interface mechanisms

In Section 3.3 of Chapter IV, it has been shown that, when the composite is mainly loaded in in-plane shear, debonding mechanisms may be involved at the yarns/matrix interface.

These mechanisms are not accounted for in the proposed multi-scale model, but could eventually added by means of cohesive elements in the unit cell FE model [180, 45, 46, 35].

2.4 Virtual testing

As previously discussed in Section 1 of Chapter IV, the multi-scale modelling approach presented in this thesis is intended to be employed to generate a "virtual tests" database that would allow to identify a phenomenological model having an equivalent overall behaviour [65, 2]. Subsequently, this model could be utilized for large-scale structural applications, while keeping an acceptable computational cost.

2.5 FE^2 analyses

One of the major future challenges related to this type of multi-scale modelling is to connect the unit cell problem to a FE macroscopic model with the help of a FE^2 computational scheme. In such two-scales analyses, the macroscopic problem is incrementally solved by calling the microscopic problem at each time step and for each macroscopic integration point [61, 63, 62, 9, 182, 184, 183]. Currently, the computational cost involved in such a process is highly expensive and the dedicated numerical techniques are still under development, preventing its use in an industrial context.

2.6 Multi-scale fully-coupled thermomechanical analyses

The modelling approaches presented in this thesis assumes isothermal conditions. However, it has been demonstrated that, under cyclic loading, a significant increase of temperature arising from the dissipative mechanisms may likely occur, altering the mechanical properties of the composite (see Section 3.3 in Chapter IV). In order to account for this self-heating phenomenon, the present multi-scale model could be extended to fully-coupled thermomechanical analyses [32, 22, 33], where the mechanical and thermal problems are simultaneously solved. Such analyses require to write the local constitutive equations with a proper thermodynamical formalism [150, 151, 31, 197, 198] and to work with an energetically consistent multi-scale theory, similar to the periodic homogenization framework presented in Section 2 of Chapter I.

2.7 Model reduction techniques

With a view to perform multi-scale analyses over long periods of time and/or a large number of cycles within a reasonable computational time, it becomes of prime importance to implement dedicated numerical schemes for fatigue analysis involving complex thermomechanical behaviours. A first category of numerical schemes is dedicated to reduce the problem in terms of time integration. Among them it can be mentioned the cycle jump method [39], the temporal homogenization [72] or the LArge Time INcrement (LATIN) method [38]. In a second category, other more advanced numerical schemes allow to reduce the problem in terms of space and time [36, 94, 140, 23].

2.8 Fatigue criterion analyses and life-time estimation

Besides the model reduction techniques, fatigue analyses and life-time estimation require to establish an appropriate fatigue criterion. The latter might be based on both

microscopic and/or macroscopic fields. Additionally, energy balanced analyses could also be considered to establish such a criterion, as experimental investigations have shown that energetic quantities seem to be appropriate indicators to predict the failure of thermoplastic-based composites [100, 13, 156].

Appendix A

Details of the kinematic constraint equations

The setting up of periodic boundary conditions using the "constraint drivers" method requires first to identify the nodes located on the faces, the edges and the corner of the cell. For simplicity, the notation presented in Figure A.1 will be utilized:

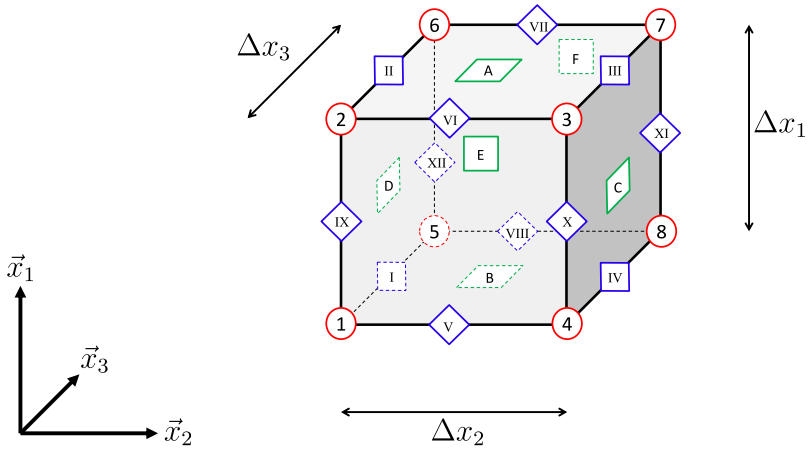

Figure A.1: Locations of the faces, the edges and the corners on a unit cell

1 Kinematic constraint equations for faces

From the equation (I.30), the relationship between nodes at the same relative position on the opposite faces can be written as follows:

$$\begin{cases} u_1^A - u_1^B - u_{11}^{cd}\ \Delta x_1 = 0 \\ u_2^A - u_2^B - u_{12}^{cd}\ \dfrac{1}{2}\Delta x_1 = 0 \\ u_3^A - u_3^B - u_{13}^{cd}\ \dfrac{1}{2}\Delta x_1 = 0 \end{cases}, \tag{A.1}$$

$$\begin{cases} u_1^C - u_1^D - u_{12}^{cd}\ \dfrac{1}{2}\Delta x_2 = 0 \\ u_2^C - u_2^D - u_{22}^{cd}\ \Delta x_2 = 0 \\ u_3^C - u_3^D - u_{23}^{cd}\ \dfrac{1}{2}\Delta x_2 = 0 \end{cases}, \tag{A.2}$$

$$\begin{cases} u_1^E - u_1^F - u_{13}^{cd}\ \dfrac{1}{2}\Delta x_3 = 0 \\ u_2^E - u_2^F - u_{23}^{cd}\ \dfrac{1}{2}\Delta x_3 = 0 \\ u_3^E - u_3^F - u_{33}^{cd}\ \Delta x_3 = 0 \end{cases}, \tag{A.3}$$

where faces A to F are shown in Figure A.2.

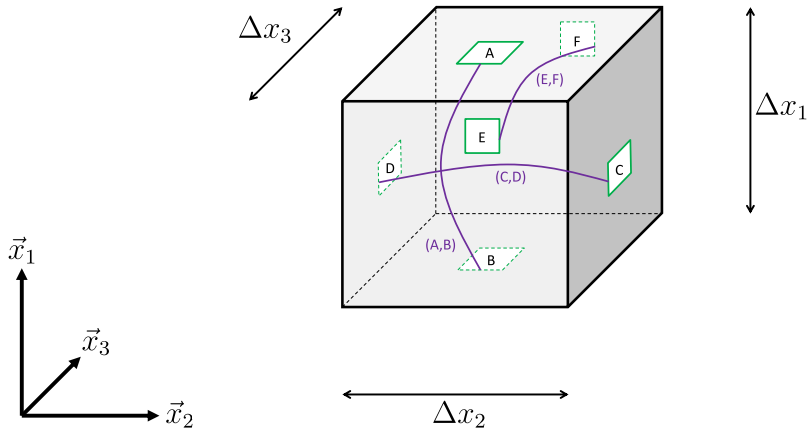

Figure A.2: Kinematic equations for the faces

2 Kinematic constraint equations for the 1^{st} group of edges

For a node located on an edge (that belongs to two faces in the same time), it is clear that two opposite nodes can be found at the same relative position. Then at first, from the equation (I.30), four equations can be deduced for each group of edges. For the first group the equations are initially given by:

$$\begin{cases} u_1^{II} - u_1^I - u_{11}^{cd}\ \Delta x_1 = 0 \\ u_2^{II} - u_2^I - u_{12}^{cd}\ \dfrac{1}{2}\Delta x_1 = 0 \\ u_3^{II} - u_3^I - u_{13}^{cd}\ \dfrac{1}{2}\Delta x_1 = 0 \end{cases}, \tag{A.4}$$

$$\begin{cases} u_1^{III} - u_1^{II} - u_{12}^{cd}\ \frac{1}{2}\Delta x_2 = 0 \\ u_2^{III} - u_2^{II} - u_{22}^{cd}\ \Delta x_2 = 0 \\ u_3^{III} - u_3^{II} - u_{23}^{cd}\ \frac{1}{2}\Delta x_2 = 0 \end{cases}, \tag{A.5}$$

$$\begin{cases} u_1^{III} - u_1^{IV} - u_{11}^{cd}\ \Delta x_1 = 0 \\ u_2^{III} - u_2^{IV} - u_{12}^{cd}\ \frac{1}{2}\Delta x_1 = 0 \\ u_3^{III} - u_3^{IV} - u_{13}^{cd}\ \frac{1}{2}\Delta x_1 = 0 \end{cases}, \tag{A.6}$$

$$\begin{cases} u_1^{IV} - u_1^{I} - u_{12}^{cd}\ \frac{1}{2}\Delta x_2 = 0 \\ u_2^{IV} - u_2^{I} - u_{22}^{cd}\ \Delta x_2 = 0 \\ u_3^{IV} - u_3^{I} - u_{23}^{cd}\ \frac{1}{2}\Delta x_2 = 0 \end{cases}, \tag{A.7}$$

where edges I to IV are shown in Figure A.3. However, if the equations are defined in this way, there will be a redundancy making the system over-constrained and likely unsolvable. Indeed, for instance, the edge III is both linked to the edges II and IV that are themselves linked to edge I. Thus, it will be preferable to replace the equations (A.5) and (A.6) by the equation (A.8) that can be obtain by either putting (A.4) into (A.5) or (A.7) into (A.6):

$$\begin{cases} u_1^{III} - u_1^{I} - u_{11}^{cd}\ \Delta x_1 - u_{12}^{cd}\ \frac{1}{2}\Delta x_2 = 0 \\ u_2^{III} - u_2^{I} - u_{12}^{cd}\ \frac{1}{2}\Delta x_1 - u_{22}^{cd}\ \Delta x_2 = 0 \\ u_3^{III} - u_3^{I} - u_{13}^{cd}\ \frac{1}{2}\Delta x_1 - u_{23}^{cd}\ \frac{1}{2}\Delta x_2 = 0 \end{cases}. \tag{A.8}$$

Finally, only the equations (A.4), (A.7) and (A.8) will be used for the first group of edges.

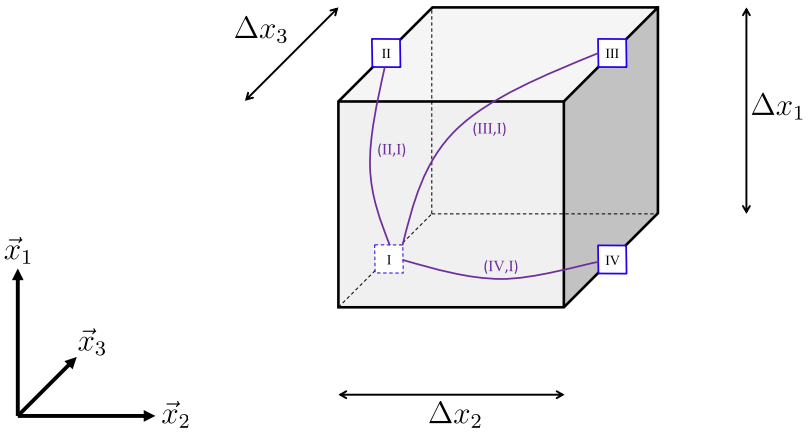

Figure A.3: Kinematic equations for the 1^{st} group of edges

3 Kinematic constraint equations for the 2^{nd} group of edges

In the same way, from (I.30), the equations of the second group of edge are given by:

$$\begin{cases} u_1^{VI} - u_1^{V} - u_{11}^{cd}\ \Delta x_1 = 0 \\ u_2^{VI} - u_2^{V} - u_{12}^{cd}\ \frac{1}{2}\Delta x_1 = 0 \\ u_3^{VI} - u_3^{V} - u_{13}^{cd}\ \frac{1}{2}\Delta x_1 = 0 \end{cases}, \tag{A.9}$$

$$\begin{cases} u_1^{VIII} - u_1^{V} - u_{13}^{cd}\ \frac{1}{2}\Delta x_3 = 0 \\ u_2^{VIII} - u_2^{V} - u_{23}^{cd}\ \frac{1}{2}\Delta x_3 = 0 \\ u_3^{VIII} - u_3^{V} - u_{33}^{cd}\ \Delta x_3 = 0 \end{cases}, \tag{A.10}$$

$$\begin{cases} u_1^{VII} - u_1^{V} - u_{11}^{cd}\ \Delta x_1 - u_{13}^{cd}\ \frac{1}{2}\Delta x_3 = 0 \\ u_2^{VII} - u_2^{V} - u_{12}^{cd}\ \frac{1}{2}\Delta x_1 - u_{23}^{cd}\ \frac{1}{2}\Delta x_3 = 0 \\ u_3^{VII} - u_3^{V} - u_{13}^{cd}\ \frac{1}{2}\Delta x_1 - u_{33}^{cd}\ \Delta x_3 = 0 \end{cases}, \tag{A.11}$$

where edges V to VIII are shown in Figure A.4.

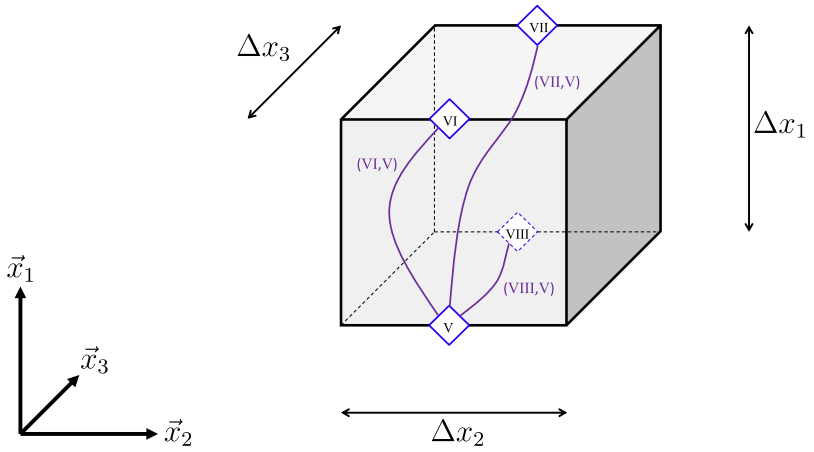

Figure A.4: Kinematic equations for the 2^{nd} group of edges

4 Kinematic constraint equations for the 3^{rd} group of edges

In the same way, from (I.30), the equations of the third group of edge are given by:

$$\begin{cases} u_1^X - u_1^{IX} - u_{12}^{cd}\ \dfrac{1}{2}\Delta x_2 = 0 \\ u_2^X - u_2^{IX} - u_{22}^{cd}\ \Delta x_2 = 0 \\ u_3^X - u_3^{IX} - u_{23}^{cd}\ \dfrac{1}{2}\Delta x_2 = 0 \end{cases}, \tag{A.12}$$

$$\begin{cases} u_1^{XII} - u_1^{IX} - u_{13}^{cd}\ \dfrac{1}{2}\Delta x_3 = 0 \\ u_2^{XII} - u_2^{IX} - u_{23}^{cd}\ \dfrac{1}{2}\Delta x_3 = 0 \\ u_3^{XII} - u_3^{IX} - u_{33}^{cd}\ \Delta x_3 = 0 \end{cases}, \tag{A.13}$$

$$\begin{cases} u_1^{XI} - u_1^{IX} - u_{12}^{cd}\ \dfrac{1}{2}\Delta x_2 - u_{13}^{cd}\ \dfrac{1}{2}\Delta x_3 = 0 \\ u_2^{XI} - u_2^{IX} - u_{22}^{cd}\ \Delta x_2 - u_{23}^{cd}\ \dfrac{1}{2}\Delta x_3 = 0 \\ u_3^{XI} - u_3^{IX} - u_{23}^{cd}\ \dfrac{1}{2}\Delta x_2 - u_{33}^{cd}\ \Delta x_3 = 0 \end{cases}, \tag{A.14}$$

where edges IX to XII are shown in Figure A.5.

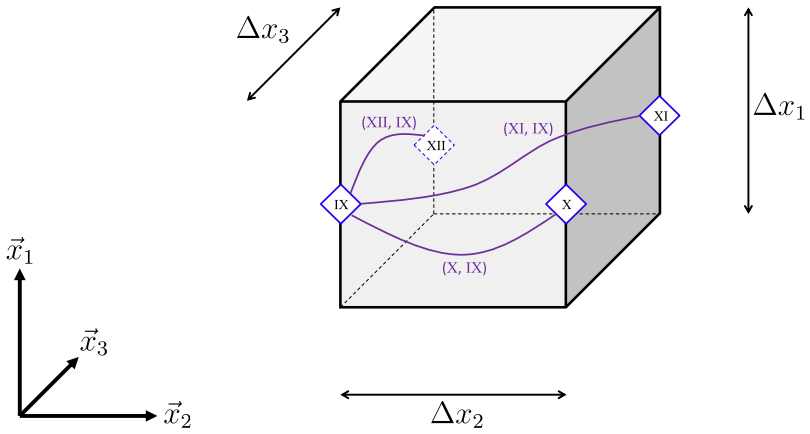

Figure A.5: Kinematic equations for the 3^{rd} group of edges

5 Kinematic constraint equations for corners

Following the same methods, from (I.30), the equations for the corners are given by:

$$\begin{cases} u_1^2 - u_1^1 - u_{11}^{cd}\ \Delta x_1 = 0 \\ u_2^2 - u_2^1 - u_{12}^{cd}\ \dfrac{1}{2}\Delta x_1 = 0 \\ u_3^2 - u_3^1 - u_{13}^{cd}\ \dfrac{1}{2}\Delta x_1 = 0 \end{cases}, \tag{A.15}$$

$$\begin{cases} u_1^4 - u_1^1 - u_{12}^{cd}\ \dfrac{1}{2}\Delta x_2 = 0 \\ u_2^4 - u_2^1 - u_{22}^{cd}\ \Delta x_2 = 0 \\ u_3^4 - u_3^1 - u_{23}^{cd}\ \dfrac{1}{2}\Delta x_2 = 0 \end{cases}, \tag{A.16}$$

$$\begin{cases} u_1^5 - u_1^1 - u_{13}^{cd}\ \dfrac{1}{2}\Delta x_3 = 0 \\ u_2^5 - u_2^1 - u_{23}^{cd}\ \dfrac{1}{2}\Delta x_3 = 0 \\ u_3^5 - u_3^1 - u_{33}^{cd}\ \Delta x_3 = 0 \end{cases}, \tag{A.17}$$

$$\begin{cases} u_1^3 - u_1^1 - u_{11}^{cd}\ \Delta x_1 - u_{12}^{cd}\ \dfrac{1}{2}\Delta x_2 = 0 \\ u_2^3 - u_2^1 - u_{12}^{cd}\ \dfrac{1}{2}\Delta x_1 - u_{22}^{cd}\ \Delta x_2 = 0 \\ u_3^3 - u_3^1 - u_{13}^{cd}\ \dfrac{1}{2}\Delta x_1 - u_{23}^{cd}\ \dfrac{1}{2}\Delta x_2 = 0 \end{cases}, \tag{A.18}$$

$$\begin{cases} u_1^6 - u_1^1 - u_{11}^{cd}\ \Delta x_1 - u_{13}^{cd}\ \dfrac{1}{2}\Delta x_3 = 0 \\ u_2^6 - u_2^1 - u_{12}^{cd}\ \dfrac{1}{2}\Delta x_1 - u_{23}^{cd}\ \dfrac{1}{2}\Delta x_3 = 0 \\ u_3^6 - u_3^1 - u_{13}^{cd}\ \dfrac{1}{2}\Delta x_1 - u_{33}^{cd}\ \Delta x_3 = 0 \end{cases}, \tag{A.19}$$

$$\begin{cases} u_1^8 - u_1^1 - u_{12}^{cd}\ \dfrac{1}{2}\Delta x_2 - u_{13}^{cd}\ \dfrac{1}{2}\Delta x_3 = 0 \\ u_2^8 - u_2^1 - u_{22}^{cd}\ \Delta x_2 - u_{23}^{cd}\ \dfrac{1}{2}\Delta x_3 = 0 \\ u_3^8 - u_3^1 - u_{23}^{cd}\ \dfrac{1}{2}\Delta x_2 - u_{33}^{cd}\ \Delta x_3 = 0 \end{cases}, \tag{A.20}$$

$$\begin{cases} u_1^7 - u_1^1 - u_{11}^{cd}\ \Delta x_1 - u_{12}^{cd}\ \dfrac{1}{2}\Delta x_2 - u_{13}^{cd}\ \dfrac{1}{2}\Delta x_3 = 0 \\ u_2^7 - u_2^1 - u_{12}^{cd}\ \dfrac{1}{2}\Delta x_1 - u_{22}^{cd}\ \Delta x_2 - u_{23}^{cd}\ \dfrac{1}{2}\Delta x_3 = 0 \\ u_3^7 - u_3^1 - u_{13}^{cd}\ \dfrac{1}{2}\Delta x_1 - u_{23}^{cd}\ \dfrac{1}{2}\Delta x_2 - u_{33}^{cd}\ \Delta x_3 = 0 \end{cases}, \tag{A.21}$$

where corners 1 to 8 are shown in Figure A.6.

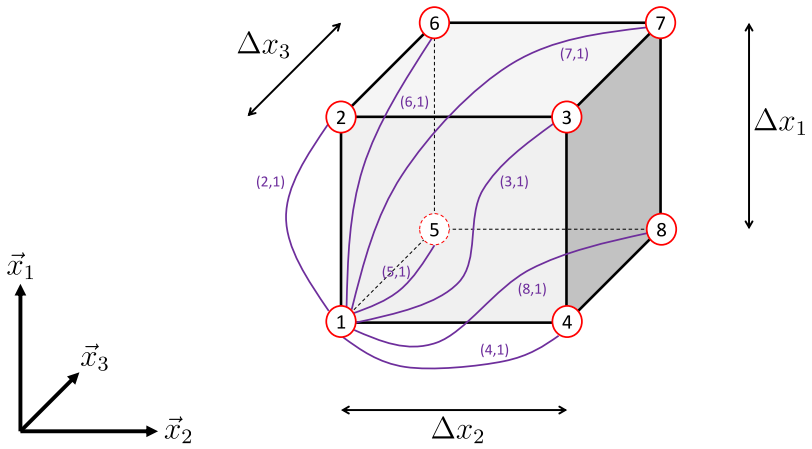

Figure A.6: Kinematic equations for the corners

Appendix B

Framework for thermodynamically-based constitutive modelling of homogeneous materials

The study of composite materials via micromechanics and multi-scale analyses requires a deep knowledge of the material response of each individual component that appears in the microstructure. In this purpose, the thermodynamic of irreversible processes [67, 68, 69, 109, 33] provides a rigorous framework to establish constitutive equations for homogeneous materials. This appendix presents a brief overview of this framework. Basics of thermodynamics for continuum media under the small perturbations assumption are introduced along with some helpful definitions for readers that are not familiar with these concepts.

Before starting with the framework of thermodynamics, it is necessary to introduce the following energetic quantities. The mechanical work of a material point is defined as the twice contracted product between the stress and the strain:

$$W = \boldsymbol{\sigma} : \boldsymbol{\varepsilon}, \tag{B.1}$$

written under its rate form, this gives:

$$\dot{W} = \dot{W}_\varepsilon + \dot{W}_\sigma \qquad \text{where} \qquad \dot{W}_\varepsilon = \boldsymbol{\sigma} : \dot{\boldsymbol{\varepsilon}} \qquad \text{and} \qquad \dot{W}_\sigma = \dot{\boldsymbol{\sigma}} : \boldsymbol{\varepsilon}. \tag{B.2}$$

W_ε and W_σ are the strain and complementary energies, respectively. As illustrated in Figure B.1, W_ε represents the area under the stress-strain curve, while by complementarity W_σ is the area above the stress-strain curve.

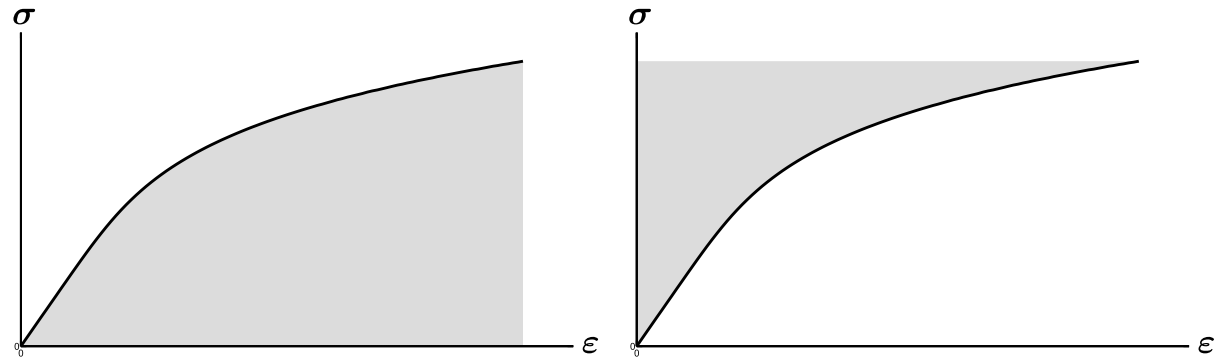

(a) Strain energy (area under the stress-strain curve): $W_\varepsilon(t) = \int_0^t \boldsymbol{\sigma}(\xi) : \frac{d\boldsymbol{\varepsilon}(\xi)}{d\xi} \; d\xi$

(b) Complementary energy (area above the stress-strain curve): $W_\sigma(t) = \int_0^t \frac{d\boldsymbol{\sigma}(\xi)}{d\xi} : \boldsymbol{\varepsilon}(\xi) \; d\xi$

Figure B.1: Schematic representation of the strain and complementary energies W_ε and W_σ, respectively.

1 Basics of thermodynamics

1.1 1^{st} and 2^{nd} laws of thermodynamics

The 1^{st} law of thermodynamics postulates that, in a material volume element, the rate of internal energy is equal to the sum of the power produced by the material itself and its deformation minus the power that leaves this material element through thermal conduction:

$$\rho \dot{e} = \omega + \dot{W}_\varepsilon - \mathrm{div}_{\boldsymbol{x}}(\boldsymbol{q}). \tag{B.3}$$

In the above equation ρ stands for the material density, e denotes the internal energy per unit of mass, ω is an eventual heat source (power per unit of volume) an $\boldsymbol{q}$ the heat flux (power per unit of surface).

The second law of thermodynamics is written under the form of an inequality expressing the irreversibility of the involved physical phenomena:

$$\rho \dot{s} + \mathrm{div}_{\boldsymbol{x}}\left(\frac{\boldsymbol{q}}{T}\right) - \frac{\omega}{T} \geq 0. \tag{B.4}$$

This principle introduces the notion of entropy, denoted by s (power per unit of mass per unit of temperature):

1.2 State variables and state potentials

To describe the energetic state of the material, it is necessary to express the internal energy e as a state function. The latter depends on the strain, the entropy and a set of internal state variables denoted by the symbols $\mathcal{V}_k$:

$$e = e(\boldsymbol{\varepsilon}, s, \mathcal{V}_k). \tag{B.5}$$

However, identifying a constitutive law in terms of entropy is not practical. Instead, it is more convenient to introduce alternative potentials through an appropriate transformation. In this purpose, either the Helmholtz or the Gibbs free energy potentials can be considered. They are respectively written as:

$$\psi(\boldsymbol{\varepsilon}, T, \mathcal{V}_k) = e - Ts, \tag{B.6}$$

$$\psi^*(\boldsymbol{\sigma}, T, \mathcal{V}_k) = e - Ts - \frac{W}{\rho}. \tag{B.7}$$

The Helmholtz potential considers the strain and the absolute temperature as observable (or external) state variables, while it is the stress and the absolute temperature for the Gibbs potential. It is worth noticing that observable state variables depict variables that can be controlled (during an experiment for example). In an opposite way, internal state variables cannot be controlled as they are only governed by specific evolution laws expressing their kinetics with regard to the observable state variables.

1.3 Clausius-Duhem inequality

The Clausius-Duhem inequality, establishes that the dissipation (rate of dissipated energy) must be always positive or null to ensure that the constitutive relation of a material is well thermodynamically allowable. This inequality is obtained by combining together the 1^{st} and 2^{nd} laws of thermodynamics in (B.3) and (B.4) with the Helmholtz free energy potentials (B.6). This gives:

$$\underbrace{\dot{W}_\varepsilon - \rho(\dot{\psi} + \dot{T}s)}_{\text{mechanical dissipation}} + \underbrace{\boldsymbol{q} \cdot \frac{-\mathbf{grad}_{\boldsymbol{x}}(T)}{T}}_{\text{thermal dissipation}} \geq 0. \tag{B.8}$$

If the Gibbs potential (B.7) is used instead of Helmholtz, the Clausius-Duhem inequity becomes:

$$\underbrace{-\dot{W}_\sigma - \rho(\dot{\psi}^* + \dot{T}s)}_{\text{mechanical dissipation}} + \underbrace{\boldsymbol{q} \cdot \frac{-\mathbf{grad}_{\boldsymbol{x}}(T)}{T}}_{\text{thermal dissipation}} \geq 0. \tag{B.9}$$

In both cases, two term can be clearly identified. The first one represents the mechanical dissipation associated with the evolution of the internal state variables, generally resulting in heat production from the material volume element. The second term depicts the thermal dissipation due to heat conduction. Let's remark that, the Fourier law implies that the thermal dissipation is itself positive or null:

$$\boldsymbol{q} \cdot \frac{-\mathbf{grad}_{\boldsymbol{x}}(T)}{T} \geq 0 \qquad \text{as} \qquad \boldsymbol{q} = -\boldsymbol{K} \cdot \mathbf{grad}_{\boldsymbol{x}}(T), \tag{B.10}$$

where $\boldsymbol{K}$ is the positive definite 2^{nd} order conductivity tensor. The strong form of the Clausius-Duhem inequality requires that the mechanical dissipation, henceforth denoted by $\dot{\Phi}$, is always positive or null. For the Helmholtz and Gibbs potentials, this respectively gives:

$$\dot{\Phi} = \dot{W}_\varepsilon - \rho(\dot{\psi} + \dot{T}s) \geq 0. \tag{B.11}$$

$$\dot{\Phi} = -\dot{W}_\sigma - \rho(\dot{\psi}^* + \dot{T}s) \geq 0. \tag{B.12}$$

1.4 State laws and associated variables

Written under their rate form, the Helmholtz and Gibbs potentials are respectively given by:

$$\dot{\psi} = \frac{\partial \psi}{\partial \boldsymbol{\varepsilon}} : \dot{\boldsymbol{\varepsilon}} + \frac{\partial \psi}{\partial T}\dot{T} + \sum_{k=1}^{N} \frac{\partial \psi}{\partial \mathcal{V}_k} * \dot{\mathcal{V}}_k, \tag{B.13}$$

$$\dot{\psi}^* = \frac{\partial \psi^*}{\partial \boldsymbol{\sigma}} : \dot{\boldsymbol{\sigma}} + \frac{\partial \psi^*}{\partial T}\dot{T} + \sum_{k=1}^{N} \frac{\partial \psi^*}{\partial \mathcal{V}_k} * \dot{\mathcal{V}}_k. \tag{B.14}$$

By introducing the expression of the Helmholtz free energy rate (B.13) in the Clausius-Duhem inequality in (B.11) the expression of the mechanical dissipation eventually becomes:

$$\dot{\Phi} = \left(\boldsymbol{\sigma} - \rho \frac{\partial \psi}{\partial \boldsymbol{\varepsilon}}\right) : \dot{\boldsymbol{\varepsilon}} - \rho \left(s + \frac{\partial \psi}{\partial T}\right)\dot{T} - \sum_{k=1}^{N} \rho \frac{\partial \psi}{\partial \mathcal{V}_k} * \dot{\mathcal{V}}_k \geq 0. \tag{B.15}$$

If the Gibbs potential is considered instead, (B.14) is introduced into (B.12), this gives:

$$\dot{\Phi} = -\left(\boldsymbol{\varepsilon} + \rho \frac{\partial \psi^*}{\partial \boldsymbol{\sigma}}\right) : \dot{\boldsymbol{\sigma}} - \rho \left(s + \frac{\partial \psi^*}{\partial T}\right)\dot{T} - \sum_{k=1}^{N} \rho \frac{\partial \psi^*}{\partial \mathcal{V}_k} * \dot{\mathcal{V}}_k \geq 0. \tag{B.16}$$

Under certain assumptions, a few terms of the above equations, (B.15) and (B.16), can be independently cancelled. Indeed, utilizing the Helmholtz potential, let's assume an isothermal strain state without any evolution in the internal state variables ($\dot{\boldsymbol{\varepsilon}} \neq \mathbf{0}$, $\dot{T} = 0$ and $\dot{\mathcal{V}}_k = 0$). Such a process implies that the stress is defined by:

$$\boldsymbol{\sigma} - \rho \frac{\partial \psi}{\partial \boldsymbol{\varepsilon}} = \mathbf{0} \quad \Leftrightarrow \quad \boldsymbol{\sigma} = \rho \frac{\partial \psi}{\partial \boldsymbol{\varepsilon}}. \tag{B.17}$$

Thereafter, if only the temperature is evolving ($\dot{\boldsymbol{\varepsilon}} = \mathbf{0}$, $\dot{T} \neq 0$ and $\dot{\mathcal{V}}_k = 0$), such a a thermomechanical state implies that the entropy is defined by:

$$s + \frac{\partial \psi}{\partial T} = 0 \quad \Leftrightarrow \quad s = -\frac{\partial \psi}{\partial T}. \tag{B.18}$$

If the Gibbs potential is utilized instead of Helmholtz, in the same idea, the strain is defined by assuming an isothermal stress state without any evolution in the internal state variables ($\dot{\boldsymbol{\sigma}} \neq \mathbf{0}$, $\dot{T} = 0$ and $\dot{\mathcal{V}}_k = 0$):

$$\boldsymbol{\varepsilon} + \rho \frac{\partial \psi^*}{\partial \boldsymbol{\sigma}} = \mathbf{0} \quad \Leftrightarrow \quad \boldsymbol{\varepsilon} = -\rho \frac{\partial \psi^*}{\partial \boldsymbol{\sigma}}, \tag{B.19}$$

and the entropy is obtained by assuming that only the temperature is evolving ($\dot{\boldsymbol{\sigma}} = \mathbf{0}$, $\dot{T} \neq 0$ and $\dot{\mathcal{V}}_k = 0$):

$$s + \frac{\partial \psi^*}{\partial T} = 0 \quad \Leftrightarrow \quad s = -\frac{\partial \psi^*}{\partial T}. \tag{B.20}$$

Additionally, the thermodynamical forces associated with the internal state variables are defined as:

$$\mathcal{A}_k = \rho \frac{\partial \psi}{\partial \mathcal{V}_k}, \qquad \mathcal{A}_k = \rho \frac{\partial \psi^*}{\partial \mathcal{V}_k}. \tag{B.21}$$

By introducing (B.17), (B.18) and (B.21) into (B.11) or (B.19), (B.20) and (B.21) into (B.12), the expression of the mechanical dissipation finally becomes:

$$\dot{\Phi} = -\sum_{k=1}^{N} \mathcal{A}_k * \dot{\mathcal{V}}_k \geq 0. \tag{B.22}$$

1.5 Evolution laws

In order to have a thermodynamically admissible process, the evolution of the internal state variables must be formulated in such a way that $\dot{\Phi} \geq 0$. To ensure this condition, it is convenient to derive the evolution law from a dissipation potential φ, expressed as scalar and convex function of the internal state variables rates. In the potential, the state variables may act themselves as parameters:

$$\varphi = \varphi(\dot{\mathcal{V}}_k; \boldsymbol{\varepsilon} \text{ or } \boldsymbol{\sigma}, T, \mathcal{V}_k), \qquad \mathcal{A}_k = -\frac{\partial \varphi}{\partial \dot{\mathcal{V}}_k}. \tag{B.23}$$

Generally, it is more convenient to directly express the evolution law in terms of internal state variable rates according to their corresponding thermodynamic forces. Thus, the Legendre-Fenchel transformation allows to define the dual dissipation potential φ^* related to φ. Thus φ^* is expressed as scalar and convex function of the thermodynamic forces, in which the state variables may act themselves as parameters. The evolution laws are then directly obtained by derivation of this dual potential:

$$\varphi^* = \varphi^*(\mathcal{A}_k; \boldsymbol{\varepsilon} \text{ or } \boldsymbol{\sigma}, T, \mathcal{V}_k), \qquad \dot{\mathcal{V}}_k = -\frac{\partial \varphi^*}{\partial \mathcal{A}_k}. \tag{B.24}$$

Another way to ensure $\dot{\Phi} \geq 0$, is to express the evolution by normality of an indicative convex function F of the thermodynamic forces, in which the state variables may act themselves as parameters.

$$F = F(\mathcal{A}_k; \boldsymbol{\varepsilon} \text{ or } \boldsymbol{\sigma}, T, \mathcal{V}_k), \qquad \dot{\mathcal{V}}_k = -\frac{\partial F}{\partial \mathcal{A}_k}\dot{\lambda}, \tag{B.25}$$

where λ is a Lagrange multiplier, that is deduced from the consistency of the activation condition of the considered mechanism, such as $\dot{\lambda} > 0$ if the mechanism is active or $\dot{\lambda} = 0$ if the mechanism is not active. Note that this last formalism (B.25) is particularly adapted for time-independent and/or non-associative mechanisms, while the utilization of a dissipation potential (B.23) or a dual potential (B.24) necessarily implies time-dependent and associative mechanisms.

1.6 Heat equation

The heat equation is obtained from the 1^{st} principle (B.3) in which the expression of the Helmholtz potential (B.6) is substituted. After proper calculation, this gives:

$$\rho c \dot{T} = -\mathrm{div}_{\boldsymbol{x}}(\boldsymbol{q}) + \omega \underbrace{\underbrace{-\sum_{k=1}^{N} \mathcal{A}_k * \dot{\mathcal{V}}_k}_{\dot{\Phi}\geq 0} + \underbrace{T\left(\frac{\partial \boldsymbol{\sigma}}{\partial T} : \dot{\boldsymbol{\varepsilon}} + \sum_{k=1}^{N} \frac{\partial \mathcal{A}_k}{\partial T} * \dot{\mathcal{V}}_k\right)}_{\dot{\Gamma}}}_{\omega_\varepsilon}. \tag{B.26}$$

Instead of Helmholtz, if the Gibbs potential (B.7) is introduced in (B.3), the heat equation becomes:

$$\rho c \dot{T} = -\mathrm{div}_{\boldsymbol{x}}(\boldsymbol{q}) + \omega \underbrace{\underbrace{-\sum_{k=1}^{N} \mathcal{A}_k * \dot{\mathcal{V}}_k}_{\dot{\Phi}\geq 0} + \underbrace{T\left(-\frac{\partial \boldsymbol{\varepsilon}}{\partial T} : \dot{\boldsymbol{\sigma}} + \sum_{k=1}^{N} \frac{\partial \mathcal{A}_k}{\partial T} * \dot{\mathcal{V}}_k\right)}_{\dot{\Gamma}}}_{\omega_\varepsilon}. \tag{B.27}$$

The term ω_ε represents the heat (power per unit of volume) induced by the mechanical work, and is composed of two terms: the mechanical dissipation $\dot{\Phi}$ and the thermomechanical coupling sources $\dot{\Gamma}$. In the left member in equations (B.26) and (B.27), c denotes the specific heat capacity defined by:

$$c = T\frac{\partial s}{\partial T}. \tag{B.28}$$

Rigorously, the specific heat capacity may depend on the state variables. However, in most of the cases, according to the considered model formulation, the heat capacity c is constant or approximated as a constant [1].

From equations (B.26) or (B.27), it is evident that the deformation of a material is usually accompanied by a change in temperature. Most of the times, the induced temperature variation remains small with regards to the service temperatures or/and the temperature sensitivity of the material. In these conditions, the heat generated by mechanical work can be reasonably neglected through an uncoupled thermomechanical analysis or a classical mechanical analysis assuming isothermal conditions. Nevertheless, there are a few cases where the heat induced by the mechanical work may lead to significant increase in temperature (self-heating phenomenon) that may alter the mechanical properties of the material itself. Such cases require to treat the mechanical and thermal problem simultaneously through a fully-coupled thermomechanical analysis.

2 Simplified framework for isothermal conditions

Under the isothermal assumption, all the temperature dependent terms of the state potential (Helmholtz or Gibbs) are constant. Hence, they can be removed from the problem that is only treated in terms of mechanical-related variables, as summarized in Tables B.1 and B.2.

Note that, in the study performed in this work, it is assumed that the heat induced by the mechanical work ω_ε does not lead to significant change in temperature so that it can be reasonably considered that the material stays at "constant temperature".

1. It should be mentioned that, depending on the considered state potential, the interpretation of the specific heat capacity is different. For the Helmholtz potential, c denotes the heat capacity at constant volume, whereas for the Gibbs potential, c denotes the heat capacity at constant pressure. Nevertheless, for solids, these definitions are practically the same.

State potential	Helmholtz $\rho\psi(\boldsymbol{\varepsilon}, \mathcal{V}_k)$	Gibbs $\rho\psi^*(\boldsymbol{\sigma}, \mathcal{V}_k)$
State laws	$\boldsymbol{\sigma} = \rho\dfrac{\partial\psi}{\partial\boldsymbol{\varepsilon}} \quad \mathcal{A}_k = \rho\dfrac{\partial\psi}{\partial\mathcal{V}_k}$	$\boldsymbol{\varepsilon} = -\rho\dfrac{\partial\psi^*}{\partial\boldsymbol{\sigma}} \quad \mathcal{A}_k = \rho\dfrac{\partial\psi^*}{\partial\mathcal{V}_k}$
Dissipation	$\dot{\Phi} = \dot{W}_\varepsilon - \rho\dot{\psi} \geq 0$	$\dot{\Phi} = -\dot{W}_\sigma - \rho\dot{\psi}^* \geq 0$
	$\dot{\Phi} = -\sum_{k=1}^{N} \mathcal{A}_k * \dot{\mathcal{V}}_k \geq 0$	

Table B.1: State laws obtained from the derivation of a state potential (Helmholtz or Gibbs) and expression of the dissipation.

Dissipation potential	Potential $\varphi(\dot{\mathcal{V}}_k; \boldsymbol{\varepsilon} \text{ or } \boldsymbol{\sigma}, \mathcal{V}_k)$	Dual potential $\varphi^*(\mathcal{A}_k; \boldsymbol{\varepsilon} \text{ or } \boldsymbol{\sigma}, \mathcal{V}_k)$	Indicative function $F(\mathcal{A}_k; \boldsymbol{\varepsilon} \text{ or } \boldsymbol{\sigma}, \mathcal{V}_k)$
Evolution laws	$\mathcal{A}_k = -\dfrac{\partial\varphi}{\partial\dot{\mathcal{V}}_k}$	$\dot{\mathcal{V}}_k = -\dfrac{\partial\varphi^*}{\partial\mathcal{A}_k}$	$\dot{\mathcal{V}}_k = -\dfrac{\partial F}{\partial\mathcal{A}_k}\dot{\lambda}$

Table B.2: Evolution laws obtained from the derivation of a dissipation potential or dual potential or by normality of an indicative function.

Appendix C

Assessment of the self-heating from an uncoupled "0D" thermal analysis

When performing a purely mechanical analysis, it may be interesting to evaluate if the isothermal conditions hold and if the self-heating is likely to occur. In this purpose, it is proposed to perform an uncoupled thermal analysis where the heat equation is separately solved after the mechanical problem. In such an uncoupled thermomechanical analysis, it is necessary to neglect the thermomechanical coupling sources ($\dot{\Gamma} = 0$). Therefore, in the absence of any other heat sources ($\omega = 0$), the heat is only induced by the mechanical dissipation $\dot{\Phi}$. In this context, the heat equation (B.26 or B.27) becomes:

$$\rho c \dot{T}(\boldsymbol{x}, t) = -\mathrm{div}_{\boldsymbol{x}}\big(\boldsymbol{q}(\boldsymbol{x}, t)\big) + \dot{\Phi}(\boldsymbol{x}, t) \qquad \text{where} \qquad \boldsymbol{q}(\boldsymbol{x}, t) = -\boldsymbol{K} \cdot \mathbf{grad}_{\boldsymbol{x}}\big(T(\boldsymbol{x}, t)\big). \quad \text{(C.1)}$$

In the above partial differential equation, $\dot{\Phi}$ is extracted from the mechanical problem and is subsequently utilized as an input of the thermal problem. In this manner, the variation of temperature induced by the mechanical dissipation is evaluated without accounting for its effect on the mechanical problem.

1 Uncoupled "0D" thermal analysis

Considering a body ideally subjected to uniform thermomechanical fields, one can write the heat equation (C.1) under its "0D" formalism [37, 20, 24, 13, 198]. Therefore, the thermal problem can be reduced to the following differential equation:

$$\rho c \left(\dot{T}(t) + \frac{T(t) - T_\infty}{\tau} \right) = \dot{\Phi}(t), \qquad \text{(C.2)}$$

where the characteristic time τ quantifies the heat losses of this body. They are assumed to be proportional to the difference between the current temperature $T(t)$ of the body and the equilibrium temperature T_∞.

When performing tensile tests, such a "0D" analysis is particularly convenient as it permits to focus on the thermomechanical response within the gauge length of a tensile specimen. In this area of interest, the thermomechanical fields can be considered as uniform.

2 Numerical resolution: Backward Euler time implicit algorithm

When considering the backward Euler time implicit method, it is convenient to write the governing equations under the form of residual functions that must satisfy a nullity condition. In the present case, the residual form of the heat equation C.2 gives:

$$\phi_T(\dot{T}, T) = \rho c\left(\dot{T} + \frac{T - T_\infty}{\tau}\right) - \dot{\Phi} = 0. \tag{C.3}$$

In order to initiate the computation, at each time step, the temperature is assumed not to evolve at first, such that: $\Delta T^{(n+1)(k=0)} = 0$. Once the residual ϕ_T is predicted, its nullity cannot be respected, then the temperature must be corrected in order to satisfy this condition. Accordingly, the temperature is updated at each iteration k by:

$$T^{(n+1)(k+1)} = T^{(n+1)(k)} + \delta T^{(n+1)(k)}, \tag{C.4}$$

where $\delta T^{(n+1)(k)}$ is obtained from the nullity condition of the residual ϕ_T:

$$\phi_T^{(n+1)(k)} + \delta\phi_T^{(n+1)(k)} = 0. \tag{C.5}$$

In the above equation, $\phi_T^{(n+1)(k)}$ is expressed by linearisation. This gives (all the quantities are taken at the increment $^{(n+1)(k)}$):

$$\begin{aligned}
\delta\phi_T &= \frac{\partial\phi_T}{\partial\dot{T}}\delta\dot{T} + \frac{\partial\phi_T}{\partial T}\delta T \\
&= \frac{\partial\phi_T}{\partial\dot{T}}\frac{1}{\Delta t}\delta T + \frac{\partial\phi_T}{\partial T}\delta T \\
&= \left(\frac{\partial\phi_T}{\partial\dot{T}}\frac{1}{\Delta t} + \frac{\partial\phi_T}{\partial T}\right)\delta T \\
&= K_{TT}\delta T \qquad \text{where} \qquad K_{TT} = \left(\frac{\partial\phi_T}{\partial\dot{T}}\frac{1}{\Delta t} + \frac{\partial\phi_T}{\partial T}\right) = \rho c\left(\frac{1}{\Delta t} + \frac{1}{\tau}\right).
\end{aligned} \tag{C.6}$$

Finally, by introducing (C.6) into (C.5), the unknown value of δT is computed from the known value of the residual ϕ_T. This gives:

$$\delta T^{(n+1)(k)} = \frac{-\phi_T^{(n+1)(k)}}{K_{TT}^{(n+1)(k)}}. \tag{C.7}$$

Once the temperature is updated, the residual ϕ_T is reassessed through the relationship (C.3). This correction procedure is iteratively repeated (k loop) until the convergence is reached [1], namely when $|\phi_T^{(n+1)(k+1)}| \leq 0 + \delta$.

3 Experimental evaluation of the heat losses

The heat losses can be determined by measuring the return to equilibrium occurring after a rapid elevation of temperature [20]. Indeed, at this stage, there is no heat generated

1. Normally, as the differential equation (C.2) is linear, it can be shown that only one correction is sufficient to reach the convergence. However, this scheme could also be applied if this differential equation was non-linear. In this case, several corrections would be likely required.

by the material ($\dot{\Phi} = 0$) and the heat equation given in (C.2) is reduced to:

$$\rho c\left(\dot{T}(t) + \frac{T(t) - T_\infty}{\tau}\right) = 0, \qquad \text{where} \qquad T(t=0) = T_0 > T_\infty \tag{C.8}$$

Thus, the analytical solution of the above differential equation gives:

$$T(t) = T_\infty + (T_0 - T_\infty)\exp\left(-\frac{t}{\tau}\right), \tag{C.9}$$

where the characteristic time τ can be easily identified, as illustrated on Figure C.1.

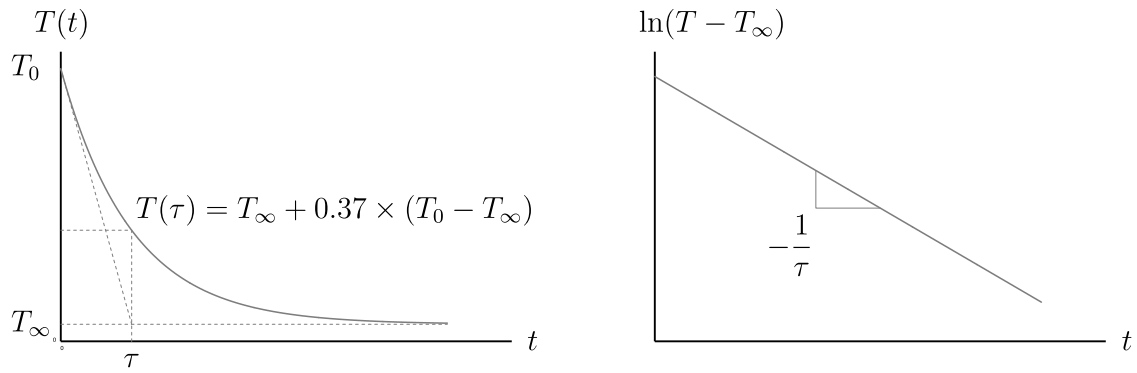

(a) Temperature (T) vs. time

(b) $\ln(T - T_\infty)$ vs. time

Figure C.1: Identification of the characteristic time τ.

Note that the characteristic time τ depends on the material thermal properties, the geometry of the considered body and the heat exchanges between this body and its surrounding medium (conduction and/or convection). If these parameters are likely to change, the characteristic time τ must be reassessed to account for the new configuration.

Appendix D

Linearisation of the constitutive equations of the matrix with the convex cutting plane method

It is recalled that, with the "convex cutting plane" form of the "return mapping algorithm" [179, 145, 178], a simplification is made regarding the linearisation of the flow equations. Indeed, the gradients of the flows are not considered. Thus, with regard to the proposed model, the linearisation of the flow equations (II.36) are given by:

$$\delta\boldsymbol{\varepsilon_p} = \frac{\boldsymbol{\Lambda}(\boldsymbol{\sigma})}{1-D}\delta r, \qquad \delta D = \frac{\Omega(Y)}{1-D}\delta r. \tag{D.1}$$

Considering this point, the linearisation of the residuals $\boldsymbol{\phi}_{\boldsymbol{v}_i}$ (II.40) and ϕ_r (II.41), and the stress (II.10) are expressed as follows:

$$\begin{aligned}
\delta\boldsymbol{\phi}_{\boldsymbol{v}_i} &= \frac{\partial\boldsymbol{\phi}_{\boldsymbol{v}_i}}{\partial\boldsymbol{\sigma}} : \delta\boldsymbol{\sigma} + \frac{\partial\boldsymbol{\phi}_{\boldsymbol{v}_i}}{\partial\boldsymbol{\varepsilon}_{\boldsymbol{v}_i}} : \delta\boldsymbol{\varepsilon}_{\boldsymbol{v}_i} + \frac{\partial\boldsymbol{\phi}_{\boldsymbol{v}_i}}{\partial\dot{\boldsymbol{\varepsilon}}_{\boldsymbol{v}_i}} : \delta\dot{\boldsymbol{\varepsilon}}_{\boldsymbol{v}_i} + \frac{\partial\boldsymbol{\phi}_{\boldsymbol{v}_i}}{\partial D}\delta D \\
&= \frac{\partial\boldsymbol{\phi}_{\boldsymbol{v}_i}}{\partial\boldsymbol{\sigma}} : \delta\boldsymbol{\sigma} + \frac{\partial\boldsymbol{\phi}_{\boldsymbol{v}_i}}{\partial\boldsymbol{\varepsilon}_{\boldsymbol{v}_i}} : \delta\boldsymbol{\varepsilon}_{\boldsymbol{v}_i} + \frac{\partial\boldsymbol{\phi}_{\boldsymbol{v}_i}}{\partial\dot{\boldsymbol{\varepsilon}}_{\boldsymbol{v}_i}}\frac{1}{\Delta t} : \delta\boldsymbol{\varepsilon}_{\boldsymbol{v}_i} + \frac{\partial\boldsymbol{\phi}_{\boldsymbol{v}_i}}{\partial D}\frac{\Omega(Y)}{1-D}\delta r \\
&= \frac{\partial\boldsymbol{\phi}_{\boldsymbol{v}_i}}{\partial\boldsymbol{\sigma}} : \delta\boldsymbol{\sigma} + \left(\frac{\partial\boldsymbol{\phi}_{\boldsymbol{v}_i}}{\partial\boldsymbol{\varepsilon}_{\boldsymbol{v}_i}} + \frac{\partial\boldsymbol{\phi}_{\boldsymbol{v}_i}}{\partial\dot{\boldsymbol{\varepsilon}}_{\boldsymbol{v}_i}}\frac{1}{\Delta t}\right) : \delta\boldsymbol{\varepsilon}_{\boldsymbol{v}_i} + \frac{\partial\boldsymbol{\phi}_{\boldsymbol{v}_i}}{\partial D}\frac{\Omega(Y)}{1-D}\delta r \\
&= \mathbb{A}_{\boldsymbol{v}_i\boldsymbol{\sigma}} : \delta\boldsymbol{\sigma} + \mathbb{A}_{\boldsymbol{v}_i\boldsymbol{v}_i} : \delta\boldsymbol{\varepsilon}_{\boldsymbol{v}_i} + \boldsymbol{A}_{\boldsymbol{v}_i\boldsymbol{r}}\delta r,
\end{aligned} \tag{D.2}$$

$$\begin{aligned}
\delta\phi_r &= \frac{\partial\phi_r}{\partial\boldsymbol{\sigma}} : \delta\boldsymbol{\sigma} + \frac{\partial\phi_r}{\partial r}\delta r + \frac{\partial\phi_r}{\partial\dot{r}}\delta\dot{r} + \frac{\partial\phi_r}{\partial D}\delta D \\
&= \frac{\partial\phi_r}{\partial\boldsymbol{\sigma}} : \delta\boldsymbol{\sigma} + \frac{\partial\phi_r}{\partial r}\delta r + \frac{\partial\phi_r}{\partial\dot{r}}\frac{1}{\Delta t}\delta r + \frac{\partial\phi_r}{\partial D}\frac{\Omega(Y)}{1-D}\delta r \\
&= \frac{\partial\phi_r}{\partial\boldsymbol{\sigma}} : \delta\boldsymbol{\sigma} + \left(\frac{\partial\phi_r}{\partial r} + \frac{\partial\phi_r}{\partial\dot{r}}\frac{1}{\Delta t} + \frac{\partial\phi_r}{\partial D}\frac{\Omega(Y)}{1-D}\right)\delta r \\
&= \boldsymbol{A}_{\boldsymbol{r}\boldsymbol{\sigma}} : \delta\boldsymbol{\sigma} + A_{rr}\delta r,
\end{aligned} \tag{D.3}$$

$$\begin{aligned}\delta\boldsymbol{\sigma} &= \frac{\partial\boldsymbol{\sigma}}{\partial\boldsymbol{\varepsilon}} : \delta\boldsymbol{\varepsilon} + \sum_{j=1}^{N} \frac{\partial\boldsymbol{\sigma}}{\partial\boldsymbol{\varepsilon}_{\boldsymbol{v}_j}} : \delta\boldsymbol{\varepsilon}_{\boldsymbol{v}_j} + \frac{\partial\boldsymbol{\sigma}}{\partial\boldsymbol{\varepsilon}_{\boldsymbol{p}}} : \delta\boldsymbol{\varepsilon}_{\boldsymbol{p}} + \frac{\partial\boldsymbol{\sigma}}{\partial D}\delta D \\ &= \frac{\partial\boldsymbol{\sigma}}{\partial\boldsymbol{\varepsilon}} : \delta\boldsymbol{\varepsilon} + \sum_{j=1}^{N} \frac{\partial\boldsymbol{\sigma}}{\partial\boldsymbol{\varepsilon}_{\boldsymbol{v}_j}} : \delta\boldsymbol{\varepsilon}_{\boldsymbol{v}_j} + \frac{\partial\boldsymbol{\sigma}}{\partial\boldsymbol{\varepsilon}_{\boldsymbol{p}}} : \frac{\boldsymbol{\Lambda}(\boldsymbol{\sigma})}{1-D}\delta r + \frac{\partial\boldsymbol{\sigma}}{\partial D}\frac{\Omega(Y)}{1-D}\delta r \\ &= \frac{\partial\boldsymbol{\sigma}}{\partial\boldsymbol{\varepsilon}} : \delta\boldsymbol{\varepsilon} + \sum_{j=1}^{N} \frac{\partial\boldsymbol{\sigma}}{\partial\boldsymbol{\varepsilon}_{\boldsymbol{v}_j}} : \delta\boldsymbol{\varepsilon}_{\boldsymbol{v}_j} + \left(\frac{\partial\boldsymbol{\sigma}}{\partial\boldsymbol{\varepsilon}_{\boldsymbol{p}}} : \frac{\boldsymbol{\Lambda}(\boldsymbol{\sigma})}{1-D} + \frac{\partial\boldsymbol{\sigma}}{\partial D}\frac{\Omega(Y)}{1-D}\right)\delta r \\ &= \mathbb{B}_{\boldsymbol{\sigma\varepsilon}} : \delta\boldsymbol{\varepsilon} + \sum_{j=1}^{N} \mathbb{B}_{\boldsymbol{\sigma v}_j} : \delta\boldsymbol{\varepsilon}_{\boldsymbol{v}_j} + \boldsymbol{B}_{\boldsymbol{\sigma r}}\delta r.\end{aligned} \tag{D.4}$$

where

$$\mathbb{A}_{\boldsymbol{v}_i\boldsymbol{\sigma}} = \frac{\partial\boldsymbol{\phi}_{\boldsymbol{v}_i}}{\partial\boldsymbol{\sigma}} = -\frac{\mathbb{V}_{\boldsymbol{v}_i}^{-1}}{1-D}, \tag{D.5}$$

$$\mathbb{A}_{\boldsymbol{v}_i\boldsymbol{v}_i} = \frac{\partial\boldsymbol{\phi}_{\boldsymbol{v}_i}}{\partial\boldsymbol{\varepsilon}_{\boldsymbol{v}_i}} + \frac{\partial\boldsymbol{\phi}_{\boldsymbol{v}_i}}{\partial\dot{\boldsymbol{\varepsilon}}_{\boldsymbol{v}_i}}\frac{1}{\Delta t} = \mathbb{V}_{\boldsymbol{v}_i}^{-1} : \mathbb{C}_{\boldsymbol{v}_i} + \frac{\mathbb{I}}{\Delta t}, \tag{D.6}$$

$$\boldsymbol{A}_{\boldsymbol{v}_i\boldsymbol{r}} = \frac{\partial\boldsymbol{\phi}_{\boldsymbol{v}_i}}{\partial D}\frac{\Omega(Y)}{1-D} = -\frac{\mathbb{V}_{\boldsymbol{v}_i}^{-1} : \boldsymbol{\sigma}\Omega(Y)}{(1-D)^3}. \tag{D.7}$$

$$\boldsymbol{A}_{\boldsymbol{r\sigma}} = \frac{\partial\phi_r}{\partial\boldsymbol{\sigma}} = -\frac{\partial Q^{-1}}{\partial f}\frac{\boldsymbol{\Lambda}(\boldsymbol{\sigma})}{1-D}, \tag{D.8}$$

$$A_{rr} = \frac{\partial\phi_r}{\partial r} + \frac{\partial\phi_r}{\partial\dot{r}}\frac{1}{\Delta t} + \frac{\partial\phi_r}{\partial D}\frac{\Omega(Y)}{1-D} = \frac{\partial Q^{-1}}{\partial f}\left(\frac{\partial R}{\partial r} - \frac{\mathrm{eq}(\boldsymbol{\sigma})\Omega(Y)}{(1-D)^3}\right) + \frac{1}{\Delta t}, \tag{D.9}$$

$$\mathbb{B}_{\boldsymbol{\sigma\varepsilon}} = \frac{\partial\boldsymbol{\sigma}}{\partial\boldsymbol{\varepsilon}} = (1-D)\mathbb{C}_{\boldsymbol{e}}, \tag{D.10}$$

$$\mathbb{B}_{\boldsymbol{\sigma v}_j} = \frac{\partial\boldsymbol{\sigma}}{\partial\boldsymbol{\varepsilon}_{\boldsymbol{v}_j}} = -(1-D)\mathbb{C}_{\boldsymbol{e}}, \tag{D.11}$$

$$\boldsymbol{B}_{\boldsymbol{\sigma r}} = \frac{\partial\boldsymbol{\sigma}}{\partial\boldsymbol{\varepsilon}_{\boldsymbol{p}}} : \frac{\boldsymbol{\Lambda}(\boldsymbol{\sigma})}{1-D} + \frac{\partial\boldsymbol{\sigma}}{\partial D}\frac{\Omega(Y)}{1-D} = -\mathbb{C}_{\boldsymbol{e}} : \left[\left(\boldsymbol{\varepsilon} - \sum_{i=1}^{N}\boldsymbol{\varepsilon}_{\boldsymbol{v}_i} - \boldsymbol{\varepsilon}_{\boldsymbol{p}}\right)\frac{\Omega(Y)}{1-D} + \boldsymbol{\Lambda}(\boldsymbol{\sigma})\right]. \tag{D.12}$$

Appendix E

Linearisation of the constitutive equations of the yarns with the convex cutting plane method

It is recalled that, with the "convex cutting plane" form of the "return mapping algorithm" [179, 145, 178], a simplification is made regarding the linearisation of the flow equations. Indeed, the gradients of the flows are not considered. Thus, with regard to the proposed model, the linearisation of the flow equation (III.26) is given by:

$$\delta\boldsymbol{\varepsilon_s} = \boldsymbol{\Lambda_s}(\boldsymbol{\sigma})\delta\gamma_c. \tag{E.1}$$

Considering this point, the linearisation of the residual ϕ_{γ_c} (III.27), the stress criterion H_c (III.19) and the stress (III.3) are expressed as follows:

$$\begin{aligned}\delta\phi_{\gamma_c} &= \frac{\partial\phi_{\gamma_c}}{\partial H_c}\delta H_c + \frac{\partial\phi_{\gamma_c}}{\partial\gamma_c}\delta\gamma_c \\ &= A_{\gamma_c H_c}\delta H_c + A_{\gamma_c\gamma_c}\delta\gamma_c,\end{aligned} \tag{E.2}$$

$$\begin{aligned}\delta H_c &= \frac{\partial H_c}{\partial\boldsymbol{\sigma_0}} : \delta\boldsymbol{\sigma_0} \quad \text{where from (III.13)} \quad \delta\boldsymbol{\sigma_0} = \frac{\partial\boldsymbol{\sigma_0}}{\partial\boldsymbol{\varepsilon}} : \delta\boldsymbol{\varepsilon} + \frac{\partial\boldsymbol{\sigma_0}}{\partial\boldsymbol{\varepsilon_s}} : \delta\boldsymbol{\varepsilon_s} + \frac{\partial\boldsymbol{\sigma_0}}{\partial\gamma_c}\delta\gamma_c \\ &= \frac{\partial H_c}{\partial\boldsymbol{\sigma_0}} : \left(\frac{\partial\boldsymbol{\sigma_0}}{\partial\boldsymbol{\varepsilon}} : \delta\boldsymbol{\varepsilon} + \frac{\partial\boldsymbol{\sigma_0}}{\partial\boldsymbol{\varepsilon_s}} : \boldsymbol{\Lambda_s}(\boldsymbol{\sigma})\delta\gamma_c + \frac{\partial\boldsymbol{\sigma_0}}{\partial\gamma_c}\delta\gamma_c\right) \\ &= \frac{\partial H_c}{\partial\boldsymbol{\sigma_0}} : \frac{\partial\boldsymbol{\sigma_0}}{\partial\boldsymbol{\varepsilon}} : \delta\boldsymbol{\varepsilon} + \frac{\partial H_c}{\partial\boldsymbol{\sigma_0}} : \left(\frac{\partial\boldsymbol{\sigma_0}}{\partial\boldsymbol{\varepsilon_s}} : \boldsymbol{\Lambda_s}(\boldsymbol{\sigma}) + \frac{\partial\boldsymbol{\sigma_0}}{\partial\gamma_c}\right)\delta\gamma_c \\ &= \boldsymbol{B_{H_c\varepsilon}} : \delta\boldsymbol{\varepsilon} + B_{H_c\gamma_c}\delta\gamma_c,\end{aligned} \tag{E.3}$$

$$\begin{aligned}\delta\boldsymbol{\sigma} &= \frac{\partial\boldsymbol{\sigma}}{\partial\boldsymbol{\varepsilon}} : \delta\boldsymbol{\varepsilon} + \frac{\partial\boldsymbol{\sigma}}{\partial\boldsymbol{\varepsilon_s}} : \delta\boldsymbol{\varepsilon_s} + \frac{\partial\boldsymbol{\sigma}}{\partial\gamma_c}\delta\gamma_c \\ &= \frac{\partial\boldsymbol{\sigma}}{\partial\boldsymbol{\varepsilon}} : \delta\boldsymbol{\varepsilon} + \frac{\partial\boldsymbol{\sigma}}{\partial\boldsymbol{\varepsilon_s}} : \boldsymbol{\Lambda_s}(\boldsymbol{\sigma})\delta\gamma_c + \frac{\partial\boldsymbol{\sigma}}{\partial\gamma_c}\delta\gamma_c \\ &= \frac{\partial\boldsymbol{\sigma}}{\partial\boldsymbol{\varepsilon}} : \delta\boldsymbol{\varepsilon} + \left(\frac{\partial\boldsymbol{\sigma}}{\partial\boldsymbol{\varepsilon_s}} : \boldsymbol{\Lambda_s}(\boldsymbol{\sigma}) + \frac{\partial\boldsymbol{\sigma}}{\partial\gamma_c}\right)\delta\gamma_c \\ &= \mathbb{B}_{\boldsymbol{\sigma\varepsilon}} : \delta\boldsymbol{\varepsilon} + \boldsymbol{B_{\sigma\gamma_c}}\delta\gamma_c,\end{aligned} \tag{E.4}$$

where

$$A_{\gamma_c H_c} = \frac{\partial\phi_{\gamma_c}}{\partial H_c} = \frac{\partial g(H_c)}{\partial H_c}, \tag{E.5}$$

$$A_{\gamma_c\gamma_c} = \frac{\partial \phi_{\gamma_c}}{\partial \gamma_c} = -1, \tag{E.6}$$

$$\boldsymbol{B_{H_c\varepsilon}} = \frac{\partial H_c}{\partial \boldsymbol{\sigma_0}} : \frac{\partial \boldsymbol{\sigma_0}}{\partial \boldsymbol{\varepsilon}} = \left(\frac{\mathbb{H} : \boldsymbol{\sigma_0}}{H_c}\right) : \mathbb{C}_\mathbf{0} : \mathbb{A}_\mathbf{0}(\gamma_c), \tag{E.7}$$

$$\begin{aligned} B_{H_c\gamma_c} &= \frac{\partial H_c}{\partial \boldsymbol{\sigma_0}} : \left(\frac{\partial \boldsymbol{\sigma_0}}{\partial \boldsymbol{\varepsilon_s}} : \boldsymbol{\Lambda_s}(\boldsymbol{\sigma}) + \frac{\partial \boldsymbol{\sigma_0}}{\partial \gamma_c}\right) \\ &= \left(\frac{\mathbb{H} : \boldsymbol{\sigma_0}}{H_c}\right) : \mathbb{C}_\mathbf{0} : \left(- \mathbb{A}_\mathbf{0}(\gamma_c) : \boldsymbol{\Lambda_s}(\boldsymbol{\sigma}) + \frac{\partial \mathbb{A}_\mathbf{0}(\gamma_c)}{\partial \gamma_c} : (\boldsymbol{\varepsilon} - \boldsymbol{\varepsilon_s})\right), \end{aligned} \tag{E.8}$$

$$\mathbb{B}_{\boldsymbol{\sigma\varepsilon}} = \frac{\partial \boldsymbol{\sigma}}{\partial \boldsymbol{\varepsilon}} = \mathbb{C}_\mathbf{0} - \mathbb{D}(\gamma_c), \tag{E.9}$$

$$\boldsymbol{B_{\sigma\gamma_c}} = \frac{\partial \boldsymbol{\sigma}}{\partial \boldsymbol{\varepsilon_s}} : \boldsymbol{\Lambda_s}(\boldsymbol{\sigma}) + \frac{\partial \boldsymbol{\sigma}}{\partial \gamma_c} = -[\mathbb{C}_\mathbf{0} - \mathbb{D}(\gamma_c)] : \boldsymbol{\Lambda_s}(\boldsymbol{\sigma}) - \frac{\partial \mathbb{D}(\gamma_c)}{\partial \gamma_c} : (\boldsymbol{\varepsilon} - \boldsymbol{\varepsilon_s}), \tag{E.10}$$

and

$$\frac{\partial \mathbb{D}(\gamma_c)}{\partial \gamma_c} = \mathbb{C}_\mathbf{0} : \mathbb{T}_\boldsymbol{c} : \left(\mathbb{A}_\mathbf{0}(\gamma_c) + \gamma_c \frac{\partial \mathbb{A}_\mathbf{0}(\gamma_c)}{\partial \gamma_c}\right), \tag{E.11}$$

$$\frac{\partial \mathbb{A}_\mathbf{0}(\gamma_c)}{\partial \gamma_c} = -\mathbb{A}_\mathbf{0}(\gamma_c) : (\mathbb{T}_\boldsymbol{c} - \mathbb{I}) : \mathbb{A}_\mathbf{0}(\gamma_c). \tag{E.12}$$

Appendix F

Evaluation of the Eshelby tensor

For a general anisotropic medium surrounding an ellipsoidal inclusion, the Eshelby tensor [59] is given by a surface integral, parametrized on the surface of the unit sphere [139]. The components S_{Eijkl} of the Eshelby tensor $\mathbb{S}_{\boldsymbol{E}}$ are given by:

$$S_{Eijkl} = \frac{1}{8\pi} C_{0mnkl} \int_{-1}^{+1} \int_{0}^{2\pi} \Big(G_{imjn}(\omega, \zeta_3) + G_{jmin}(\omega, \zeta_3) \Big) \, d\omega \, d\zeta_3, \tag{F.1}$$

where

$$\begin{gathered} G_{ijkl} = \frac{\bar{\zeta}_k \bar{\zeta}_l N_{ij}}{D}, \\ \bar{\zeta}_i = \frac{\zeta_i}{a_i}, \quad \zeta_1 = \sqrt{1-\zeta_3^2}\cos(\omega), \quad \zeta_2 = \sqrt{1-\zeta_3^2}\sin(\omega), \quad \zeta_3 = \zeta_3, \\ D = \epsilon_{mnl} K_{m1} K_{n2} K_{l3}, \quad N_{ij} = \frac{1}{2} \epsilon_{ikl} \epsilon_{jmn} K_{km} K_{ln}, \quad K_{ik} = C_{0ijkl} \bar{\zeta}_j \bar{\zeta}_l. \end{gathered} \tag{F.2}$$

C_{0ijkl} are the components of the stiffness tensor of the infinite medium $\mathbb{C}_{\mathbf{0}}$, while a_1, a_2 and a_3 are the three principal axes of the ellipsoid (Figure III.3). They are expressed in a rectangular Cartesian coordinate system. ω is an angular position and ζ_3 is the longitudinal coordinate. ϵ_{ijk} are the components of the 3^{rd} order permutation tensor expressed by:

$$\epsilon_{ijk} = \begin{cases} 0 & \text{if } i=j,\ i=k,\ j=k \\ 1 & \text{if } (i,j,k) \in \{(1,2,3),(2,3,1),(3,1,2)\} \\ -1 & \text{if } (i,j,k) \in \{(1,3,2),(3,2,1),(2,1,3)\} \end{cases}. \tag{F.3}$$

When the infinite medium is isotropic or transversally isotropic, an analytical solution exists for (F.1). For all the other cases, no explicit formulas have been developed. Thus, the components of $\mathbb{S}_{\boldsymbol{E}}$ must be evaluated numerically. As proposed by [66], this numerical evaluation can be performed using the following Gaussian quadrature formula:

$$S_{Eijkl} = \frac{1}{8\pi} C_{0mnkl} \sum_{p=1}^{M} \sum_{q=1}^{N} \Big(G_{imjn}(\omega_q, \zeta_{3_p}) + G_{jmin}(\omega_q, \zeta_{3_p}) \Big) W_{pq}, \tag{F.4}$$

where M and N are the number of points used for the integration over ζ_3 and ω, W_{pq} are the Gaussian weights. More details about the determination of the Gaussian points and weights can be found in [194].

Appendix G

Behaviour of the yarns

1 Initial stiffness

The initial stiffness of the yarns is first evaluated by mean of periodic homogenization (see Section 2.1.6 in Chapter I). The homogenization is performed using a cubic unit cell representing a unidirectional medium. The latter is idealised by a periodic hexagonal arrangement (see Figure G.1) with a fibre volume fraction of 85%. This value was evaluated from experimental observations (see Section 2 in Chapter IV). It should be mentioning that, if the individual components are isotropic, a unit cell with a hexagonal arrangement is supposed to provide a transversely isotropic homogenized stiffness tensor.

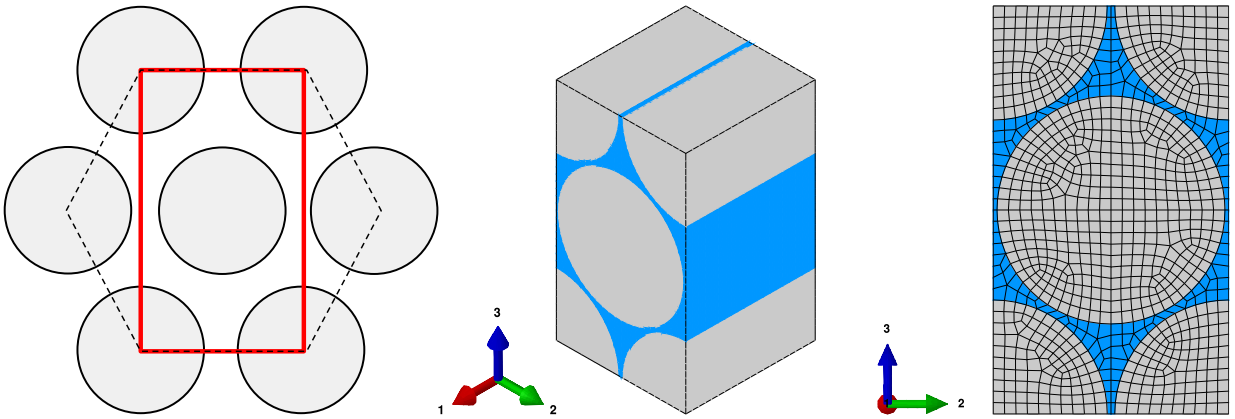

(a) Hexagonal arrangment (b) Unit cell (c) Mesh of the unit cell

Figure G.1: Unit cell of an unidirectional medium with a hexagonal arrangement and a fibre volume fraction of 85%.

The elastic properties of the constituents, namely: the matrix and the fibres, are listed in Table G.1. For the fibres, typical data of E-glass were taken from [6]. For the matrix, since the polyamide 6-6 is a time-dependent material (see Chapter II), an average modulus is considered. The latter is obtained from the initial slopes taken on several monotonic tensile tests performed at several strain rates (see Figure II.5). Note that the standard value of 0.3 is utilized for the Poisson ratio of the matrix.

Constituent	Parameter	value	unit
Matrix (isotropic)	E	2074	MPa
	ν	0.3	-
Fibres (isotropic)	E	72400	MPa
	ν	0.22	-

Table G.1: Elastic properties of the yarns constituents, namely: the matrix and the fibres. For the fibres, typical data of E-glass were taken from [6]. For the matrix, since the polyamide 6-6 is a time-dependent material, an average modulus is obtained from the initial slopes taken on several monotonic tensile tests performed at several strain rates (see Figure II.5).

The initial stiffness tensor of the yarns is recovered through the strain driven approach (see Section 2.1.6 in Chapter I). Thus, according to the relationship (I.24), each term of the stiffness tensor are recovered from the stresses resulting from the the six unitary strain states (I.23). With the help of the Voigt notation, this gives the following stiffness tensor:

$$\mathbb{C}_{\mathbf{0}} = \begin{pmatrix} 65822 & 7041 & 7041 & 0 & 0 & 0 \\ & 23947 & 6971 & 0 & 0 & 0 \\ & & 23947 & 0 & 0 & 0 \\ & & & 8661 & 0 & 0 \\ & & & & 8661 & 0 \\ \text{sym.} & & & & & 8488 \end{pmatrix} \text{ MPa.} \tag{G.1}$$

As expected, the computed stiffness tensor is well transversely isotropic [1], since $C_{0_{2222}} = C_{0_{3333}}$, $C_{0_{1122}} = C_{0_{1133}}$, $C_{0_{1212}} = C_{0_{1313}}$ and $C_{0_{2323}} = \frac{1}{2}(C_{0_{2222}} - C_{0_{2233}}) = \frac{1}{2}(C_{0_{3333}} - C_{0_{2233}})$.

2 Stiffness reduction

Let's recall that the stiffness reduction tensor $\mathbb{D}(\gamma_c)$ is calculated from the initial stiffness tensor $\mathbb{C}_{\mathbf{0}}$ along with a chosen configuration of void inclusions, in the present case: "crossing micro-cracks along $\vec{x}_1$" (see Figure III.4a and Table III.2). Figures G.2 and G.3 shows the non-null term of $\mathbb{D}(\gamma_c)$ obtained with the initial stiffness previously computed in G.1.

1. Note that the computed terms of $\mathbb{C}_{\mathbf{0}}$ were slightly modified so that the latter is perfectly transversely isotropic. Indeed, due to numerical approximations, a small deviation of a few MPa may be observed.

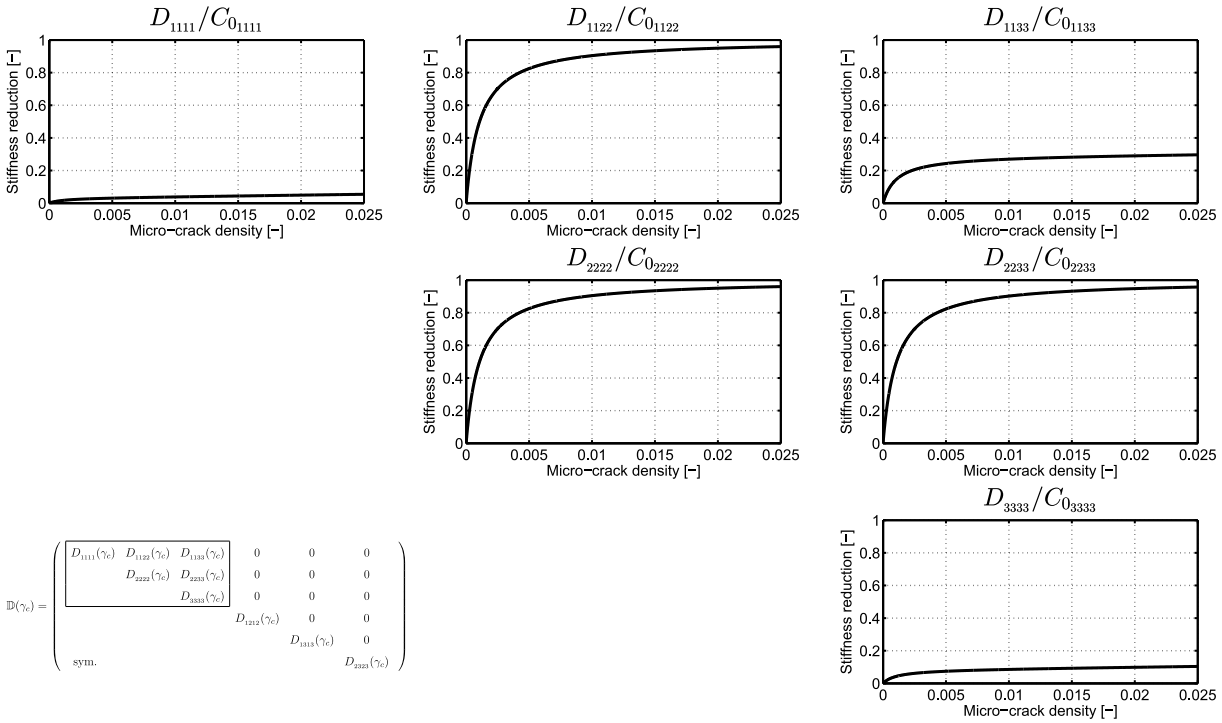

Figure G.2: Relative non-null components of the stiffness reduction tensor (upper left quadrant).

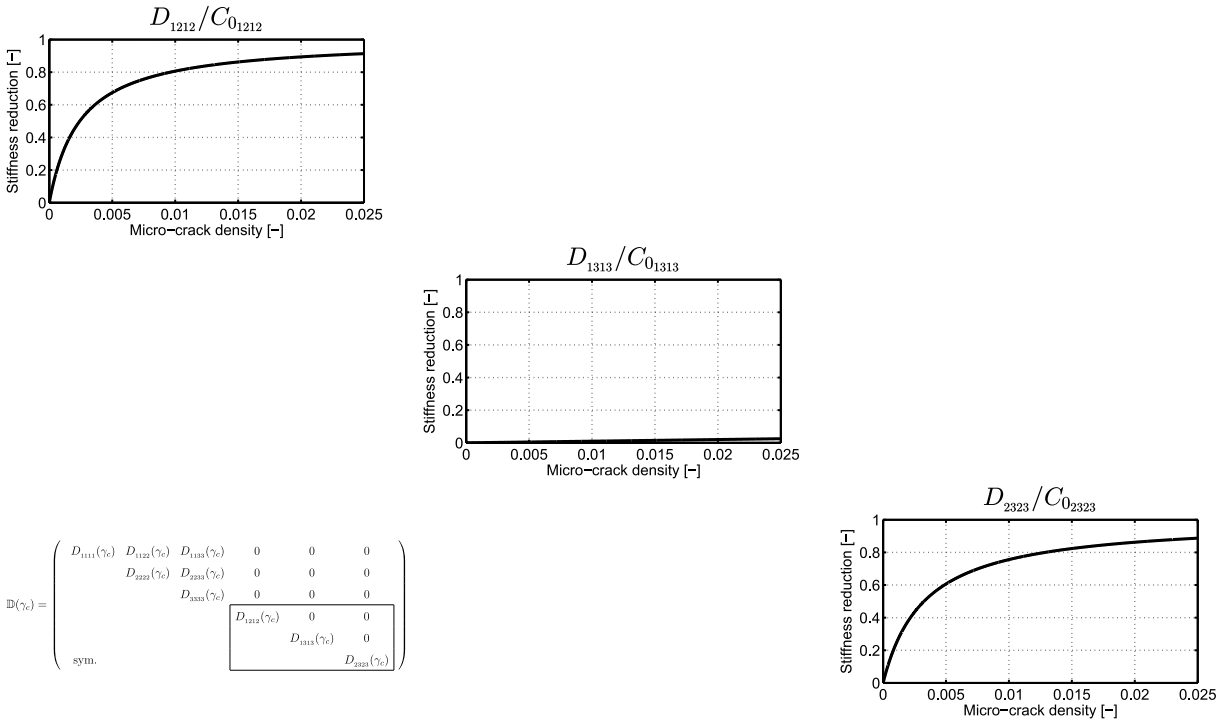

Figure G.3: Relative non-null components of the stiffness reduction tensor (lower right quadrant).

3 Mechanical response of the yarns

The parameters of the yarns, listed in Table IV.3, were identified from the macroscopic response of the whole woven composite (see Section 3 in Chapter IV). In order to visualize how the yarn phase would behave if this component was removed from the woven composite and tested apart, basic simulations carried out on a single yarn material point are presented. In these simulations, the material is repeatedly loaded and unloaded at progressively increasing maximum stress levels in longitudinal and transverse tension as well as in in-plane shear (see Figures G.4a, G.4b and G.4c, respectively).

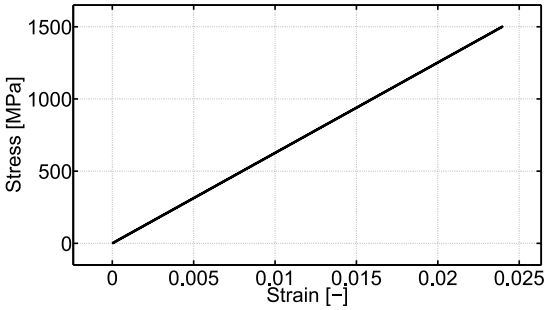

(a) Stress (σ_{11}) vs. strain (ε_{11})

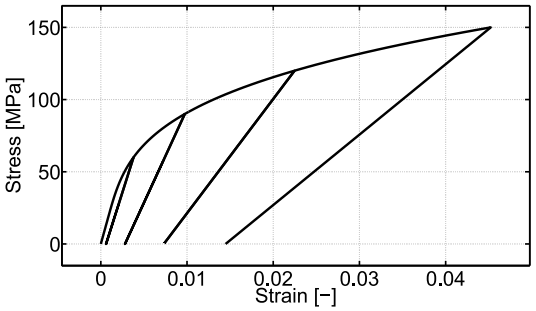

(b) Stress (σ_{22}) vs. strain (ε_{22})

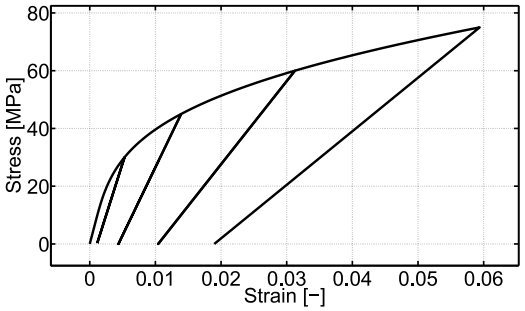

(c) Stress (σ_{12}) vs. strain ($2\varepsilon_{12}$)

Figure G.4: Behaviour of the yarns (see parameters in Table IV.3): in longitudinal tension (a), transverse tension (b) and in-plane shear (c).

Bibliography

[1] Y. Abdin, A. Jain, I. Verpoest, and S.-V. Lomov. Mean-field based micro-mechanical modelling of short wavy fiber reinforced composites. *Composites: Part A*, 91:472–483, 2016.

[2] N. Achour. *Modélisation Multi-échelles et analyse expérimentale du comportement de composites à matrice thermoplastique renforcée en fibres de verre sous sollicitations dynamiques modérées*. PhD thesis, Arts et Métiers ParisTech, 2017.

[3] N. Achour, G. Chatzigeorgiou, F. Meraghni, Y. Chemisky, and J. Fitoussi. Implicit implementation and consistent tangent modulus of a viscoplastic model for polymers. *International Journal of Mechanical Sciences*, 103:297–305, 2015.

[4] W. Albouy. *De la contribution de la visco-élasto-plasticité au comportement en fatigue des composites à matrice thermoplastique et thermodurcissable*. PhD thesis, INSA Rouen, 2013.

[5] O. Allix, P. Ladevèze, and E. Vittecoq. Modelling and identification of the mechanical behaviour of composite laminates in compression. *Composites Science and Technology*, 51:35–42, 1994.

[6] M.-F. Arif. *Damage mechanisms is short glass fiber reinforced polyamide-66 under quasi-static and fatigue loading: Effect of relative humidity and injection molding induced microstructure*. PhD thesis, Arts et Métiers Paristech, 2014.

[7] M.-F. Arif, F. Meraghni, Y. Chemisky, N. Despringre, and G. Robert. In situ damage mechanisms investigation of PA66/GF30 composite: Effect of relative humidity. *Composites: Part B*, 58:487–495, 2014.

[8] E.-M. Arruda, M.-C. Boyce, and R. Jayachandran. Effects of strain rate, temperature and thermomechanical coupling on the finite strain deformation of glassy polymers. *Mechanics of Materials*, 19:193–212, 1995.

[9] T. Asada and N. Ohno. Fully implicit formulation of elastoplastic homogenization problem for two-scale analysis. *International Journal of Solids and Structures*, 44:7261–7275, 2007.

[10] A. Asadi and J. Raghavan. Influence of time-dependent damage on creep of multidirectional polymer composite laminates. *Composites: Part B*, 42:489–498, 2011.

[11] A. Asadi and J. Raghavan. Model for prediction of simultaneous time-dependent damage evolution in multiple plies of multidirectional polymer composite laminates and its influence on creep. *Composites: Part B*, 79:359–373, 2015.

[12] P. Badel, S. Gautier, E. Vidal-Sallé, and P. Boisse. Rate constitutive equations for computational analyses of textile composite reinforcement mechanical behaviour during forming. *Composites: Part A*, 40:997–1007, 2009.

[13] A. Benaarbia. *Analyse énergétique du comportement thermomécanique du PA6.6 chargé de fibres de verre*. PhD thesis, Université Montpellier II, 2014.

[14] A. Benaarbia, A. Chrysochoos, and G. Robert. Kinetics of stored and dissipated energies associated with cyclic loadings of dry polyamide 6.6 specimens. *Polymer Testing*, 34:155–167, 2014.

[15] A. Benaarbia, A. Chrysochoos, and G. Robert. Thermomechanical behavior of PA6.6 composites subjected to low cycle fatigue. *Composites: Part B*, 76:52–64, 2015.

[16] Y. Benveniste. A new approach to the application of Mori-Tanaka's theory in composite materials. *Mechanics of Materials*, 6:147–157, 1987.

[17] Y. Benveniste, G.-J. Dvorak, and T. Chen. Stress fields in composites with coated inclusions. *Mechanics of Materials*, 7:305–317, 1989.

[18] Y. Benveniste, G.-J. Dvorak, and T. Chen. On diagonal and elastic symmetry of the approximate effective stiffness tensor of heterogeneous media. *Journal of the Mechanics and Physics of Solids*, 39(7):927–946, 1991.

[19] Y. Benveniste, G.-J. Dvorak, and T. Chen. On effective properties of composites with coated cylindrically orthotropic fibers. *Mechanics of Materials*, 12:289–297, 1991.

[20] B. Berthel. *Mesures thermographiques de champs de dissipation accompagnant la fatigue à grand nombre de cycles des aciers*. PhD thesis, Université Montpellier II, 2007.

[21] J.-M. Berthelot. *Matériaux composite comportement mécanique et analyse des structures*. Tech & Doc, 3 edition, 1999.

[22] R. Berthelsen, R. Denzer, P. Oppermann, and A. Menzel. Computational homogenisation for thermoviscoplasticity: application to thermally sprayed coatings. *Computational Mechanics*, 60:739–766, 2017.

[23] M. Bhattacharyya, A. Fau, U. Nackenhorst, D. Néron, and P. Ladevèze. A model reduction technique in space and time for fatigue simulation. In *Multiscale Modeling of Heterogeneous Structures*, pages 183–203. Springer, 2018.

[24] A. Blanche. *Effets dissipatifs en fatigue à grand et très grand nombre de cycles*. PhD thesis, Université Montpellier II, 2012.

[25] M.-L. Boubakar, F. Trivaudey, D. Perreux, and L. Vang. A meso-macro finite element modelling of laminate structures - Part I: time-independent behaviour. *Composite Structures*, 58:271–286, 2002.

[26] M.-L. Boubakar, L. Vang, F. Trivaudey, and D. Perreux. A meso-macro finite element modelling of laminate structures Part II: time-dependent behaviour. *Composite Structures*, 60:275–305, 2003.

[27] L. Brassart, L. Stainier, I. Doghri, and L. Delannay. Homogenization of elasto-(visco) plastic composites based on an incremental variational principle. *International Journal of Plasticity*, 86:86–112, 2012.

[28] J.-L. Chaboche. Damage induced anisotropy: on the difficulties associated with the active/passive unilateral condition. *International Journal of Damage Mechanics*, 1(2):148–171, 1992.

[29] J.-L. Chaboche, P. Kanouté, and A. Roos. On the capabilities of mean-field approaches for the description of plasticity in metal matrix composites. *International Journal of Plasticity*, 21:1409–1434, 2005.

[30] N. Charalambakis, G. Chatzigeorgiou, Y. Chemisky, and F. Meraghni. Mathematical homogenization of inelastic dissipative materials: a survey and recent progress. *Continuum Mechanics and Thermodynamics*, 30:1–51, 2017.

[31] D. Chatziathanasiou, Y. Chemisky, G. Chatzigeorgiou, and F. Meraghni. Modeling of coupled phase transformation and reorientation in shape memory alloys under non-proportional thermomechanical loading. *International Journal of Plasticity*, 82:192–224, 2016.

[32] G. Chatzigeorgiou, N. Charalambakis, Y. Chemisky, and F. Meraghni. Periodic homogenization for fully coupled thermomechanical modeling of dissipative generalized standard materials. *International Journal of Plasticity*, 81:18–39, 2016.

[33] G. Chatzigeorgiou, N. Charalambakis, Y. Chemisky, and F. Meraghni. *Thermomechanical Behavior of Dissipative Composite Materials*. Elsevier, 2018.

[34] G. Chatzigeorgiou, Y. Chemisky, and F. Meraghni. Computational micro to macro transitions for shape memory alloy composites using periodic homogenization. *Smart Materials and Structures*, 24, 2015.

[35] G. Chatzigeorgiou, F. Meraghni, and A. Javili. Generalized interfacial energy and size effects in composites. *Journal of Mechanics and Physics of Solids*, 106:257–282, 2017.

[36] F. Chinesta, A. Ammar, and E. Cueto. Proper generalized decomposition of multiscale models. *Numerical Methods in Engineering*, 83(8-9):1114–1132, 2009.

[37] A. Chrysochoos and H. Louche. An infrared image processing to analyse the calorific effects accompanying strain localisation. *International Journal of Engineering Science*, 38:1759–1788, 2000.

[38] J.-Y. Cognard and P. Ladevèze. A large time increment approach for cyclic viscoplasticity. *International Journal of Plasticity*, 9:141–157, 1993.

[39] D. Cojocaru and A.-M. Karlsson. A simple numerical method of cycle jumps for cyclically loaded structures. *International Journal of Fatigue*, 28:1677–1689, 2006.

[40] G. Couégnat. *Approche multiéchelle du comportement mécanique de matériaux composites à renfort tissé*. PhD thesis, Université Bordeaux I, 2008.

[41] L. Delannay, I. Doghri, and O. Pierard. Prediction of tension-compression cycles in multiphase steel using a modified incremental mean-field model. *International Journal of Solids and Structures*, 44:7291–7306, 2007.

[42] K. Derrien, J. Fitoussi, G. Guo, and D. Batiste. Prediction of the effective damage properties and failure properties of nonlinear anisotropic discontinuous reinforced composites. *Computer Methods in Applied Mechanics and Engineering*, 185:93–107, 2000.

[43] R. Desmorat. Décomposition de Kelvin et concept de contraintes effectives multiples pour les matériaux anisotropes. *Comptes Rendus Mécanique*, 337:733–738, 2009.

[44] R. Desmorat, F. Gatuingt, and F. Ragueneau. Nonlocal anisotropic damage model and related computational aspects for quasi-brittle materials. *Engineering Fracture Mechanics*, 74:1539–1560, 2007.

[45] N. Despringre. *Analyse et modélisation des mécanismes d'endommagement et de déformation en fatigue multiaxiale de matériaux composites : polyamide renforcé par des fibres courtes*. PhD thesis, Arts et Métiers ParisTech, 2015.

[46] N. Despringre, Y. Chemisky, K. Bonnay, and F. Meraghni. Micromechanical modeling of damage and load transfer in particulate composites with partially debonded interface. *Composite Structures*, 155:77–88, 2016.

[47] F. Detrez, S. Cantournet, and R. Seguela. Plasticity/damage coupling in semicrystalline polymers prior to yielding: Micromechanisms and damage law identification. *Polymer*, 52:1998–2008, 2011.

[48] B.-J. Dimitrijevic and K. Hackl. A method for gradient enhancement of continuum damage models. *Technische Mechanik*, 28(1):43–52, 2008.

[49] I. Doghri and A. Ouaar. Homogenization of two-phase elasto-plastic composite materials and structures Study of tangent operators, cyclic plasticity and numerical algorithms. *International Journal of Solids and Structures*, 40:1681–1712, 2003.

[50] A.-D Drosdov. Cyclic thermo-viscoplasticity of high density polyethylene. *International Journal of Solids and Structures*, 47:1592–1602, 2010.

[51] A.-D Drosdov. Cyclic viscoplasticity of semicrystalline polymers. *Mechanics Research Communications*, 37:28–31, 2010.

[52] A.-D Drosdov and J.-deC. Christiansen. Cyclic viscoplasticity of solid polymers: The effects of strain rate and amplitude of deformation. *Polymer*, 48:3003–3012, 2007.

[53] A.-D Drosdov, J.-deC. Christiansen, R. Klitkou, and C.-G. Potamiche. Viscoelasticity and viscoplasticity of polypropylene/polyethylene blends. *International Journal of Solids and Structures*, 47:2498–2507, 2010.

[54] A.-D Drosdov, R. Klitkou, and J.-deC. Christiansen. Cyclic viscoplasticity of semicrystalline polymers with finite deformations. *Mechanics of Materials*, 56:53–64, 2013.

[55] A.-D Drosdov, C.-G. Sanporean, and J.-deC. Christiansen. Mechanical response of HEMA gel under cyclic deformation: Viscoplasticity and swelling-induced recovery. *International Journal of Solids and Structures*, 52:220–234, 2015.

[56] Y. Duan, A. Saigal, R. Greif, and M.-A. Zimmerman. A Uniform Phenomenological Constitutive Model for Glassy and Semicrystalline Polymers. *Polymer Engineering & Science*, 41:1322–1328, 2001.

[57] Y. Duan, A. Saigal, R. Greif, and M.-A. Zimmerman. Impact Behavior and Modeling of Engineering Polymers. *Polymer Engineering & Science*, 43:112–124, 2003.

[58] M. Ekh, A. Menzel, K. Runesson, and P. Steinmann. Anisotropic damage with the MCR effect coupled to plasticity. *International Journal of Engineering Science*, 41:1535–1551, 2003.

[59] J.-D. Eshelby. The determination of the elastic field of an ellipsoidal inclusion, and related problems. *Proceedings of the Royal Society of London A*, 241(1226):376–396, 1957.

[60] N. Feld, F. Coussa, and B. Delattre. A novel approach for the strain rate dependent modelling of woven composites. *Composite Structures*, 192:568–576, 2018.

[61] F. Feyel. Multiscale FE2 elastoviscoplastic analysis of composite structures. *Computational Materials Science*, 16:344–354, 1999.

[62] F. Feyel. A multilevel finite element method (FE2) to describe the response of highly non-linear structures using generalized continua. *Computer Methods in Applied Mechanics and Engineering*, 192:3233–3244, 2003.

[63] F. Feyel and J.-L. Chaboche. FE2 multiscale approach for modelling the elastoviscoplastic behaviour of long fibre SiC/Ti composite materials. *Computer Methods in Applied Mechanics and Engineering*, 183:309–330, 2000.

[64] E.-K. Gamstedt and B.-A. Sjögren. Micromechanisms in tension-compression fatigue of composite laminates containing transverse plies. *Composites Science and Technology*, 59:167–178, 1999.

[65] D. Garoz, F.-A. Gilabert, R.-D.-B. Sevenois, S.-W.-Spronk Spronk, and W. Van Paepegem. Material parameter identification of the elementary ply damage mesomodel using virtual micro-mechanical tests of a carbon fiber epoxy system. *Composite Structures*, 181:391–404, 2017.

[66] A.-C. Gavazzi and D.-C. Lagoudas. On the numerical evaluation of Eshelby's tensor and its application to elastoplastic fibrous composites. *Computational Mechanics*, 7:13–19, 1990.

[67] P. Germain. *Cours de mécanique des milieux continus, Tome I: Théorie générale.* Masson, Paris, 1973.

[68] P. Germain. Sur certaines définitions liées à l'énérgie en mécanique de solides. *International Journal of Engineering Science*, 20(2):245–259, 1982.

[69] P. Germain, Q.-S. Nguyen, and P. Suquet. Continuum thermodynamics. *Journal of Applied Mechanics*, 50:1010–1020, 1983.

[70] G. Grail. *Approche multimodèle pour la conception de structures composites à renfort tissé.* PhD thesis, Université d'Orléans, 2013.

[71] A.-L. Gurson. Continuum Theory of Ductile Rupture by Void Nucleation and Growth: Part I. Yield Criteria and Flow Rules for Porous Ductile Media. *Journal of Engineering Materials and Technology*, 99:2–15, 1977.

[72] S. Haouala and I. Doghri. Modeling and algorithms for two-scale time homogenization of viscoelastic-viscoplastic solids under large numbers of cycles. *International Journal of Plasticity*, 70:98–125, 2015.

[73] Z. Hashin. Failure Criteria for Unidirectional Fiber Composites. *Journal of Applied Mechanics*, 47(2):329–334, 1980.

[74] Z. Hashin and A. Rotem. A Fatigue Failure Criterion for Fibre Reinforced Materials. *Journal of Composite Materials*, 7:448–464, 1973.

[75] W. He, Y.-F. Wu, Y. Xu, and T.-T. Fu. A thermodynamically consistent nonlocal damage model for concrete materials with unilateral effects. *Computer Methods in Applied Mechanics and Engineering*, 297:371–391, 2015.

[76] R. Hill. A theory of the yielding and plastic flow of anisotropic metals. *Proceedings of the Royal Society of London A*, 193(1033):281–297, 1948.

[77] R. Hill. A self-consistent mechanics of composite materials. *Journal of the Mechanics and Physics of Solids*, 13:213–22, 1965.

[78] R. Hill. The essential structure of constitutive laws for metal composites and polycrystals. *Journal of Materials Science and Engineering*, 15(2):79–95, 1967.

[79] C. Hochard, P.-A. Aubourg, and J.-P. Charles. Modelling of the mechanical behaviour of woven-fabric CFRP laminates up to failure. *Composites Science and Technology*, 61:221–230, 2001.

[80] C. Hochard, J. Payan, and C. Bordreuil. A progressive first ply failure model for woven ply CFRP laminates under static and fatigue loads. *International Journal of Fatigue*, 28:1270–1276, 2006.

[81] C. Hochard and Y. Thollon. A generalized damage model for woven ply laminates under static and fatigue loading conditions. *International Journal of Fatigue*, 32:158–165, 2010.

[82] O. Hoffman. The Brittle Strength of Orthotropic Materials. *Journal of Composite Materials*, 1:200–206, 1967.

[83] J. Huang and D.-V. Griffiths. Return mapping algorithms and stress predictors for failure analysis in geomechanics. *Journal of Engineering Mechanics*, 135(4):276–284, 2009.

[84] A.-P. Karafillis and M.-C. Boyce. A general anisotropic yield criterion using bounds and transformation weighting tensor. *Journal of the Mechanics and Physics of Solids*, 41(12):1959–1886, 1993.

[85] M. Kawai, Y. Masuko, and T. Sagawa. Off-axis tensile creep rupture of unidirectional CFRP laminates at elevated temperature. *Composites: Part A*, 37:257–269, 2006.

[86] A.-S. Khan, O. Lopez-Pamies, and R. Kazmi. Thermo-mechanical large deformation response and constitutive modeling of viscoelastic polymers over a wide range of strain rates and temperatures. *International Journal of Plasticity*, 22:581–601, 2006.

[87] B. Kiefer, T. Waffenschmidt, L. Sprave, and A. Menzel. A gradient-enhanced damage model coupled to plasticity-multi-surface formulation and algorithmic concepts. *International Journal of Damage Mechanics*, 2017.

[88] A. Krairi. *Multiscale modeling of the damage and failure of homogeneous and short-fiber reinforced thermoplastics under monotonic and fatigue loadings*. PhD thesis, Université catholique de Louvain, 2015.

[89] A. Krairi and I. Doghri. A thermodynamically-based constitutive model, for thermoplastic polymers coupling viscoelasticity viscoplasticity and ductile damage. *International Journal of Plasticity*, 60:163–181, 2014.

[90] A. Krairi, I. Doghri, and G. Robert. Multiscale high cycle fatigue models for neat and short fiber reinforced thermoplastic polymers. *International Journal of Fatigue*, 92:179–192, 2016.

[91] A. Krasnobrizha. *Modelisation des mechanismes d'hysteresis des composites tissés a l'aide d'un modèle collaboratif elasto-plastique endommageable à derivees fractionnaires*. PhD thesis, Ecole Centrale de Nantes, 2015.

[92] A. Krasnobrizha, P. Rozycki, L. Gornet, and P. Cosson. Hysteresis behaviour modelling of woven composite using a collaborative elastoplastic damage model with fractional derivatives. *Composite Structures*, 158:101–111, 2016.

[93] P. Ladevèze. A damage computational method for composite structures. *Computers & Structures*, 44:79–87, 1992.

[94] P. Ladevèze. On reduced models in nonlinear solid mechanics. *European Journal of Mechanics - A/Solids*, 60:227–237, 2016.

[95] P. Ladevèze and E. Le Dantec. Damage modelling of the elementary ply for laminated composites. *Composites Science and Technology*, 43:257–267, 1992.

[96] D.-C. Lagoudas, A.-C. Gavazzi, and H. Nigam. Elastoplastic behavior of metal matrix composites based on incremental plasticity and the Mori-Tanaka averaging scheme. *Computational Mechanics*, 8:193–203, 1991.

[97] R.-S. Lakes. *Viscoelastic Solids*. CRC Press, 1999.

[98] J. Läufer, V. Becker, and W. Wagner. Gradient enhancement of a transversely isotropic continuum damage model. *Composite Structures*, 181:138–144, 2017.

[99] A. Launay, M.-H. Maitournam, Y. Marco, and I. Raoult. Multiaxial fatigue models for short glass fiber reinforced polyamide – Part I: Nonlinear anisotropic constitutive behavior for cyclic response. *International Journal of Fatigue*, 47:382–389, 2013.

[100] A. Launay, M.-H. Maitournam, Y. Marco, and I. Raoult. Multiaxial fatigue models for short glass fibre reinforced polyamide. Part II: Fatigue life estimation. *International Journal of Fatigue*, 47:2013, 2013.

[101] A. Launay, M.-H. Maitournam, Y. Marco, I. Raoult, and F. Szmytka. Cyclic behaviour of short glass fibre reinforced polyamide: Experimental study and constitutive equations. *International Journal of Plasticity*, 27:1267–1293, 2011.

[102] A. Launay, Y. Marco, M.-H. Maitournam, and I. Raoult. Modelling the influence of temperature and relative humidity on the time-dependent mechanical behaviour of a short glass fibre reinforced polyamide. *Mechanics of Materials*, 56:1–10, 2013.

[103] W.-B. Lawrimore II, D.-K. Francis, J.-L Bouvard, Y. Hammi, and M.-F. Horstemeyer. A mesomechanics parametric finite element study of damage growth and coalescence in polymers using an Elastoviscoelastic-Viscoplastic internal state variable model. *Mechanics of Materials*, 96:83–95, 2016.

[104] N. Laws and J.-R. Brockenbrough. The effect of micro-crack systems on the loss of stiffness of brittle solids. *International Journal of Solids and Structures*, 23:1247–1268, 1987.

[105] N. Laws, G.-J. Dvorak, and M. Hejazi. Stiffness changes in unidirectional composites caused by crack systems. *Mechanics of Materials*, 2:123–137, 1983.

[106] E. Le Dantec. *Contribution à la modélisation du comportement mécanique des composites stratifiés*. PhD thesis, Université Paris VI, 1989.

[107] H.-K. Lee and S.-H. Pyo. Micromechanics-based elastic damage modeling of particulate composites with weakened interfaces. *International Journal of Solids and Structures*, 44:8390–8406, 2007.

[108] J. Lemaitre. Coupled elasto-plasticity and damage constitutive equations. *Computer Methods in Applied Mechanics and Engineering*, 51:31–49, 1985.

[109] J. Lemaitre and J.-L. Chaboche. *Mechanics of solid materials*. Cambridge University Press, 1990.

[110] J. Lemaitre and R. Desmorat. *Engineering damage mechanics : ductile, creep, fatigue and brittle failure*. Springer, 2005.

[111] K. Levenberg. A method for the solution of certain non-linear problem in least squares. *Quarterly of Applied Mathematics*, 2:164–168, 1944.

[112] S. Li. On the unit cell for micromechanical analysis of fibre-reinforced composites. *Proceedings of the Royal Society of London A*, 455(1983):815–838, 1999.

[113] S. Li. General unit cells for micromechanical analyses of unidirectional composites. *Composites: Part A*, 32:815–826, 2001.

[114] S. Li and A. Wongsto. Unit cells for micromechanical analyses of particle-reinforced composites. *Mechanics of Materials*, 36:543–572, 2004.

[115] H. Lin, L.-P. Brown, and A.-C. Long. Modelling and Simulating Textile Structures Using TexGen. *Advanced Materials Research*, 331:44–47, 2011.

[116] S.-V. Lomov, A.-V. Gusakov, G. Huysmans, A. Prodromou, and I. Verpoest. Textile geometry preprocessor for meso-mechanical models of woven composites. *Composites Science and Technology*, 60:2083–2095, 2000.

[117] S.-V. Lomov, G. Huysmans, Y. Luo, R.-S. Parnas, A. Prodromou, I. Verpoest, and F.-R. Phelan. Textile composites: modelling strategies. *Composites: Part A*, 32:1379–1394, 2001.

[118] S.-V. Lomov, D.-S. Ivanov, I. Verpoest, M. Zako, T. Kurashiki, H. Nakai, and S. Hirosawa. Meso-FE modelling of textile composites: Road map, data flow and algorithms. *Composites Science and Technology*, 67:1870–1891, 2007.

[119] Z. Mahboob, Y. Chemisky, F. Meraghni, and H. Bougherara. Mesoscale modelling of tensile response and damage evolution in natural fibre reinforced laminates. *Composites: Part B*, 119:168–183, 2017.

[120] A. Malpot. *Etude du comportement en fatigue d'un composite à matrice polyamide renforcé d'un tissu de fibres de verre pour application automobile*. PhD thesis, ENSMA Poitiers, 2016.

[121] A. Malpot, F. Touchard, and S. Bergamo. Effect of relative humidity on mechanical properties of a woven thermoplastic composite for automotive application. *Polymer Testing*, 48:160–168, 2015.

[122] A. Malpot, F. Touchard, and S. Bergamo. Influence of moisture on the fatigue behaviour of a woven thermoplastic composite used for automotive application. *Materials & Design*, 98:12–19, 2016.

[123] A. Malpot, F. Touchard, and S. Bergamo. An investigation of the influence of moisture on fatigue damage mechanisms in a woven glass-fibre-reinforced PA66 composite using acoustic emission and infrared thermography. *Composites: Part B*, 130:11–20, 2017.

[124] L. Marcin. *Modélisation du comporetement, de l'endommagement et de la rupture de matériaux composites à renforts tissés pour le dimentionnement robuste de structures*. PhD thesis, Université Bordeaux I, 2010.

[125] D.W. Marquardt. An algorithm for least-squares estimation of nonlinear parameters. *Journal of the Society for Industrial and Applied Mathematics*, 11(2):431–441, 1963.

[126] A. Maurel-Pantel, E Baquet, J Bikard, J.-L Bouvard, and N. Billon. A thermo-mechanical large deformation constitutive model for polymers based on material network description: Application to a semi-crystalline polyamide 66. *International Journal of Plasticity*, 67:102–126, 2015.

[127] F. Meraghni and M.-L. Benzeggagh. Micromechanical modelling of matrix degradation in randomly oriented discontinuous-fibre composites. *Composites Science and Technology*, 55:171–186, 1995.

[128] F. Meraghni, C.-J. Blakeman, and M.-L. Benzeggagh. Effect of interfacial decohesion on stiffness reduction in a random discontinuous-fibre composite containing matrix microcracks. *Composites Science and Technology*, 56:541–555, 1996.

[129] F. Meraghni, Y. Chemisky, B. Piotrowski, R. Echchorfi, N. Bourgeois, and E. Patoor. Parameter identification of a thermodynamic model for superelastic shape memory alloys using analytical calculation of the sensitivity matrix. *European Journal of Mechanics - A/Solids*, 45:226–237, 2014.

[130] F. Meraghni, F. Desrumaux, and M.-L. Benzeggagh. Implementation of a constitutive micromechanical model for damage analysis in glass mat reinforced composite structures. *Composites Science and Technology*, 62:2087–2097, 2002.

[131] F. Meraghni, H. Nouri, N. Bourgeois, C. Czarnota, and P. Lory. Parameters identification of fatigue damage model for short glass fiber reinforced polyamide (PA6-GF30) using digital image correlation. *Procedia Engineering*, 10:2110–2116, 2011.

[132] M.-H.-H Meuwissen, C.-W.-J Oomens, F.-P.-T. Baaijens, R. Petterson, and J.-D. Janssen. Determination of the elasto-plastic properties of aluminium using a mixed numerical-experimental method. *Journal of Materials Processing Technology*, 75:204–211, 1998.

[133] J.-C. Michel, H. Moulinec, and P. Suquet. Effective properties of composite materials with periodic microstructure: a computational approach. *Computer Methods in Applied Mechanics and Engineering*, 172:109–143, 1999.

[134] B. Miled, I. Doghri, L. Brassart, and L. Delannay. Micromechanical modeling of coupled viscoelastic-viscoplastic composites based on an incrementally affine formulation. *International Journal of Solids and Structures*, 50:1755–1769, 2013.

[135] B. Miled, I. Doghri, and L. Delannay. Coupled viscoelastic-viscoplastic modeling of homogeneous and isotropic polymers: Numerical algorithm and analytical solutions. *Computer Methods in Applied Mechanics and Engineering*, 200:3381–3394, 2011.

[136] S. Moreau, A. Chrysochoos, J.-M. Muracciole, and B. Wattrisse. Analysis of thermoelastic effects accompanying the deformation of PMMA and PC polymers. *Comptes Rendus Mécanique*, 333:648–653, 2005.

[137] T. Mori and K. Tanaka. Average stress in matrix and average elastic energy of materials with misfitting inclusions. *Acta Metallurgica*, 21:571–574, 1973.

[138] A. Muliana. Nonlinear viscoelastic-degradation model for polymeric based materials. *International Journal of Solids and Structures*, 51:122–132, 2014.

[139] T. Mura. *Micromechanics of defects in solids*. Martinus Nijhoff publishers, 2 edition, 1987.

[140] M.-A. Nasri. *Réduction dimensionnelle pour la simulation de la fatigue des métaux*. PhD thesis, Arts et Métiers ParisTech, 2017.

[141] S. Nemat-Nasser and M. Hori. *Micromechanics: Overall Properties of Heterogeneous Materials*. North Holland, 2nd edition, 1999.

[142] Q.-T. Nguyen, E. Vidal-Sallé, P. Boisse, C.-H. Park, A Saouab, J. Bréard, and G. Hivet. Mesoscopic scale analyses of textile composite reinforcement compaction. *Composites: Part B*, 44:231–241, 2013.

[143] H. Nouri. *Modélisation et identification de lois de comportement avec endommagement en fatigue polycyclique de matériaux composites à matrice thermoplastique*. PhD thesis, Arts et Métiers ParisTech, 2009.

[144] H. Nouri, F. Meraghni, and P. Lory. Fatigue damage model for injection-molded short glass fibre reinforced thermoplastics. *International Journal of Fatigue*, 31:934–942, 2009.

[145] M. Ortiz and J.-C. Simo. An analysis of a new class of integration algorithms for elasto-plastic constitutive relations. *International Journal for Numerical Methods in Engineering*, 23:353–366, 1986.

[146] V.-G. Oshmyan, S.-A. Patlazhan, and Y. Remond. The Effect of Structural Changes and Nonlinear Character of Plastic Flow on Low Strains in Semicrystalline Polymers. *Polymer Science*, 47:346–351, 2005.

[147] V.-G. Oshmyan, S.-A. Patlazhan, and Y. Remond. Principles of Structural-Mechanical Modeling of Polymers and Composites. *Polymer Science*, 48:1004–1013, 2006.

[148] N.-S. Ottosen and M. Ristinmaa. Failure and initial yield criteria. In *The Mechanics of Constitutive Modeling*, chapter 8, pages 145–193. Elsevier, 2005.

[149] N.-S. Ottosen and M. Ristinmaa. Introduction to time-dependent material behavior. In *The Mechanics of Constitutive Modeling*, chapter 14, pages 357–378. Elsevier, 2005.

[150] C. Ovalle Rodas, F. Zaïri, and M. Naït-Abdelaziz. A finite strain thermo-viscoelastic constitutive model to describe the self-heating in elastomeric materials during low-cycle fatigue. *Journal of the Mechanics and Physics of Solids*, 64:396–410, 2014.

[151] C. Ovalle Rodas, F. Zaïri, M. Naït-Abdelaziz, and P. Charrier. A thermo-visco-hyperelastic model for the heat build-up during low-cycle fatigue of filled rubbers: Formulation, implementation and experimental verification. *International Journal of Plasticity*, 79:217–236, 2016.

[152] J. Payan. *Etude du comportement de composites stratifiés sous chargement statique et de fatigue*. PhD thesis, Université Aix-Marseille II, 2004.

[153] J. Payan and C. Hochard. Damage modelling of laminated carbon epoxy composites under static and fatigue loadings. *International Journal of Fatigue*, 24:299–306, 2002.

[154] D. Perreux and D. Lazuardi. The effect of residual stress on the non-linear behaviour of composite laminates Part II. Layer, laminate non-linear models and the effect of stress on the model parameters residual. *Composites Science and Technology*, 61:177–190, 2001.

[155] D. Perreux and C. Oytana. Continuum damage mechanics for microcracked composites. *Composites Engineering*, 3:115–122, 1993.

[156] C. Peyrac, T. Jollivet, N. Leray, F. Lefebvre, O. Westphal, and L. Gornet. Self-Heating Method for Fatigue Limit Determination on Thermoplastic Composites. *Procedia Engineering*, 133:129–135, 2015.

[157] O. Pierard and I. Doghri. An enhanced affine formulation and the corresponding numerical algorithms for the mean-field homogenization of elasto-viscoplastic composites. *International Journal of Plasticity*, 22:131–157, 2006.

[158] O. Pierard, C. Friebel, and I. Doghri. Mean-field homogenization of multi-phase thermo-elastic composites a general framework and its validation. *Composites Science and Technology*, 64:1587–1603, 2004.

[159] O. Pierard, C. Gonzalez, J. Segurado, J. Llorca, and I. Doghri. Micromechanics of elasto-plastic materials reinforced with ellipsoidal inclusions. *International Journal of Solids and Structures*, 44:6945–6962, 2007.

[160] O. Pierard, J. Llorca, J. Segurado, and I. Doghri. Micromechanics of particle-reinforced elasto-viscoplastic composites: Finite element simulations versus affine homogenization. *International Journal of Plasticity*, 23:1041–1060, 2007.

[161] P. Ponte Castañeda and J.-R. Willis. The effect of spacial distribution on the effective behavior of composite materials and cracked media. *Journal of the Mechanics and Physics of Solids*, 43(12):1919–1951, 1995.

[162] P. Potluri and T.-V Sagar. Compaction modelling of textile preforms for composite structures. *Composite Structures*, 86:177–185, 2008.

[163] F. Praud, G. Chatzigeorgiou, J. Bikard, and F. Meraghni. Phenomenological multi-mechanisms constitutive modelling for thermoplastic polymers, implicit implementation and experimental validation. *Mechanics of Materials*, 114:9–29, 2017.

[164] F. Praud, G. Chatzigeorgiou, Y. Chemisky, and F. Meraghni. Micromechanical modelling of viscoelastic-viscoplastic-damage behaviour for polyamide woven fabric composites under cyclic loading. In *European Conference on Composite Materials ECCM17*, Munich, Germany, 2016.

[165] F. Praud, G. Chatzigeorgiou, Y. Chemisky, and F. Meraghni. Hybrid micromechanical-phenomenological modelling of anisotropic damage and anelasticity induced by micro-cracks in unidirectional composites. *Composite Structures*, 182:223–236, 2017.

[166] F. Praud, G. Chatzigeorgiou, Y. Chemisky, and F. Meraghni. Modélisation multi-échelle des composites tissés à matrice thermoplastique sous chargements cycliques non proportionnels. In *Journées Nationales sur les Composites JNC20*, Champs sur Marne, France, 2017.

[167] A. Puck and W. Schneider. On failure mechanisms and failure criteria of filament-wound glass-fibre/resin composites. *Plastics and Polymers*, 37:33–43, 1969.

[168] A. Puck and H. Schürmann. Failure analysis of FRP laminates by means of physically based phenomenological models. *Composites Science and Technology*, 58:1045–1067, 1998.

[169] M. Qi, A. Giraud, J.-B. Colliat, and J.-F. Shao. A numerical damage model for initially anisotropic materials. *International Journal of Solids and Structures*, 100-101:245–256, 2016.

[170] M.-A. Qidwai, D.-J. Hartl, and D.-C. Lagoudas. Numerical implementation of an SMA thermomechanical constitutive model using return mapping algorithms. In *Shape Memory Alloys: Modeling and Engineering Applications*, chapter 4, pages 189–231. Springer, 2008.

[171] M.-A. Qidwai and D.-C. Lagoudas. Numerical implementation of a shape memory alloy thermomechanical constitutive model using return mapping algorithms. *International Journal for Numerical Methods in Engineering*, 47:1123–1168, 2000.

[172] J. Qu and M. Cherkaoui. *Fundamentals of micromechanics of solids*. Wiley, 2006.

[173] E. Sanchez-Palencia. Comportement local et macroscopique d'un type de milieux physiques hétérogènes. *International Journal of Engineering Science*, 12(4):331–351, 1974.

[174] R.-A. Schapery. On the characterization of nonlinear viscoelastic materials. *Polymer Engineering & Science*, 9(4):295–310, 1969.

[175] F.-J. Schirmaier, J. Weiland, L. Kärger, and F. Henning. A new efficient and reliable algorithm to determine the fracture angle. *Composites Science and Technology*, 100:19–25, 2014.

[176] H. Shahsavari, R. Naghdabadi, M. Baghani, and S. Sohrabpour. A viscoelastic-viscoplastic constitutive model considering damage evolution for time dependent materials: Application to asphalt mixes. *International Journal of Damage Mechanics*, 25(7):921–942, 2016.

[177] M. Sherburn. *Geometric and mechanical modelling of textiles*. PhD thesis, University of Nottingham, 2007.

[178] J.-C. Simo and T.-J.-R. Hughes. *Computational inelasticity*. Springer, 1998.

[179] J.-C. Simo and M. Ortiz. A unified approach to finite deformation elastoplastic analysis based on the use of hyperelastic constitutive equations. *Computer Methods in Applied Mechanics and Engineering*, 49(2):221–245, 1985.

[180] D.-W. Spring and G.-H. Paulino. A growing library of three-dimensional cohesive elements for use in ABAQUS. *Engineering Fracture Mechanics*, 126:190–216, 2014.

[181] P. Suquet. Elements of homogenization for inelastic solid mechanics. *Lecture Notes in Physics*, 272:193–278, 1987.

[182] A. Tchalla, S. Belouettar, A. Makradi, and H. Zahrouni. An ABAQUS toolbox for multiscale finite element computation. *Composites: Part B*, 52:323–333, 2013.

[183] E. Tikarrouchine, G. Chatzigeorgiou, F. Praud, B. Piotrowski, Y. Chemisky, and F. Meraghni. Three-dimensional FE2 method for the simulation of non-linear, rate-dependent response of composite structures. *Composite Structures*, 193:165–179, 2018.

[184] E. Tikarrouchine, F. Praud, G. Chatzigeorgiou, B. Piotrowski, Y. Chemisky, and F. Meraghni. Modélisation multi-échelle non-linéaire par homogénéisation périodique et analyses par EF2: application aux composites à matrice élastoviscoplastique endommageable. In *Journées Nationales sur les Composites JNC20*, Champs sur Marne, France, 2017.

[185] S. Tsai and E. Wu. A general theory of strength for anisotropic materials. *Journal of Composite Materials*, 5:58–80, 1971.

[186] P. Vannucci. General anisotropic elasticity. In *Anisotropic Elasticity*, chapter 2, pages 19–73. Springer, 2018.

[187] D. Vasiukov, S. Panier, and A. Hachemi. Non-linear material modeling of fiber-reinforced polymers based on coupled viscoelasticity-viscoplasticity with anisotropic continuous damage mechanics. *Composite Structures*, 132:527–535, 2015.

[188] I. Verpoest and S.-V. Lomov. Virtual textile composites software WiseTex: Integration with micro-mechanical, permeability and structural analysis. *Composites Science and Technology*, 65:2563–2574, 2005.

[189] B. Vieille, W. Albouy, and L. Taleb. Viscoelastic viscoplastic model for aeronautical thermoplastic laminates at high temperature: Validation on high stress gradient structures. *Composites: Part B*, 90:278–286, 2016.

[190] G.-Z. Voyiadjis and A. Samadi-Dooki. Constitutive modeling of large inelastic deformation of amorphous polymers: Free volume and shear transformation zone dynamics. *Journal of Applied Physics*, 119(22):225104, 2016.

[191] T. Waffenschmidt, C. Polindara, A. Menzel, and S. Blanco. A gradient-enhanced large-deformation continuum damage model for fibre-reinforced materials. *Computer Methods in Applied Mechanics and Engineering*, 268:801–842, 2014.

[192] W. Weibull. A statistical distribution function of wide applicability. *Journal of Applied Mechanics*, 18:293–297, 1951.

[193] J. Wiegand, N. Petrinic, and B. Elliott. An algorithm for determination of the fracture angle for the three-dimensional Puck matrix failure criterion for UD composites. *Composites Science and Technology*, 68:2511–2517, 2008.

[194] H. William. *Numerical recipes in Fortran: The art of scientific computing*. Cambridge University Press, New York, 1989.

[195] L. Wu, L. Adam, I. Doghri, and L. Noels. An incremental-secant mean-field homogenization method with second statistical moments for elasto-visco-plastic composite materials. *Mechanics of Materials*, 114:180–200, 2017.

[196] L. Wu, L. Noels, L. Adam, and I. Doghri. A combined incremental-secant mean-field homogenization scheme with per-phase residual strains for elasto-plastic composites. *International Journal of Plasticity*, 51:80–102, 2013.

[197] C. Yu, G. Kang, and K. Chen. A hygro-thermo-mechanical coupled cyclic constitutive model for polymers with considering glass transition. *International Journal of Plasticity*, 89:29–65, 2017.

[198] C. Yu, G. Kang, K. Chen, and F Lu. A thermo-mechanically coupled nonlinear viscoelastic-viscoplastic cyclic constitutive model for polymeric materials. *Mechanics of Materials*, 105:1–15, 2017.

[199] F. Zaïri, M. Naït-Abdelaziz, J.-M. Gloaguen, A. Bouaziz, and J.-M. Lefebvre. Micromechanical modelling and simulation of chopped random fiber reinforced polymer composites with progressive debonding damage. *International Journal of Solids and Structures*, 45:5220–5236, 2008.

[200] P. Zerbe, B. Schneider, E. Moosbrugger, and M. Kaliske. A viscoelastic-viscoplastic-damage model for creep and recovery of a semicrystalline thermoplastic. *International Journal of Solids and Structures*, 110-111:340–350, 2017.

[201] Q.-Z. Zhu, J.-F. Shao, and D. Kondo. A micromechanics-based thermodynamic formulation of isotropic damage with unilateral and friction effects. *European Journal of Mechanics - A/Solids*, 30:316–325, 2011.

[202] J. Zouhaier, F. Meraghni, J. Fitoussi, and D. Batiste. Multi-scales modelling of dynamic behaviour for discontinuous fibre SMC composites. *Composites Science and Technology*, 69:97–103, 2009.

Multi-scale modelling of thermoplastic-based woven composites, cyclic and time-dependent behaviour

Abstract: In this thesis, a multi-scale model established from the concept of periodic homogenization is utilized to study the cyclic and time-dependent response of thermoplastic-based woven composites. With the proposed approach, the macroscopic behaviour of the composite is determined from a finite element simulation of the representative unit cell of the periodic microstructure, where the local constitutive behaviours of the components are directly integrated, namely: the matrix and the yarns. The local response of the thermoplastic matrix is described by a phenomenological multi-mechanisms constitutive model accounting for viscoelasticity, viscoplasticity and ductile damage. For the yarns, a hybrid micromechanical-phenomenological constitutive model is considered. The latter accounts for anisotropic damage and anelasticity induced by the presence of a diffuse micro-crack network through the micromechanical description of a micro-cracked representative volume element. The capabilities of the multi-scale model are validated by comparing the numerical predictions with experimental data. The capabilities of the model are also illustrated through several examples where the composite undergoes time-dependent deformations under monotonic loading, constant or cyclic stress levels and non-proportional multiaxial loading. Furthermore, the multi-scale model is also employed to analyse the influence of the local deformation processes on the macroscopic response of the composite.

Keywords: Woven composites, Thermoplastic matrices, Constitutive modelling, Multi-scale modelling, Periodic homogenization, Cyclic loading

Modélisation multi-échelle des composites tissés à matrice thermoplastique, comportement cyclique et dépendance au temps

Résumé: Dans ce travail de thèse, une modélisation multi-échelle est mise en place à partir du concept d'homogénéisation périodique pour étudier le comportement cyclique et dépendant du temps des composites tissés à matrice thermoplastique. Avec l'approche proposée, le comportement macroscopique du composite est déterminé à partir d'une simulation éléments finis effectuée sur une cellule unitaire représentative de la microstructure périodique, où les lois de comportement des constituants sont directement intégrées, à savoir: la matrice et les torons. La réponse locale de la matrice est décrite par une loi de comportement phénoménologique multi-mécanismes intégrant viscoélasticité, viscoplasticité et endommagement ductile. Pour les torons, une loi de comportement hybride micromécanique-phénoménologique est considérée. Cette dernière prend en compte l'endommagement anisotrope et l'anélasticité induite par la présence d'un réseau diffus de microfissures à travers une description micromécanique d'un volume élémentaire représentatif contenant des microfissures. Les capacités du modèle multi-échelles sont validées en comparant les prédictions numériques aux essais expérimentaux. Les capacités du modèle sont également illustrées à travers plusieurs exemples où le composite subit des déformations dépendantes du temps lors de chargements monotones, de chargements à amplitude constante ou cyclique et encore lors de chargement multiaxiaux non proportionnels. En outre, le modèle multi-échelle est aussi utilisé pour analyser l'influence des mécanismes de déformation locaux sur la réponse macroscopique du composite.

Mots clés: Composites tissés, Matrices thermoplastiques, Lois de comportement, Modélisation multi-échelle, Homogénéisation périodique, Chargements cycliques

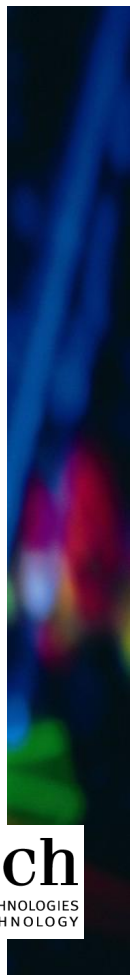

ARTS ET MÉTIERS ParisTech

ParisTech
INSTITUT DES SCIENCES ET TECHNOLOGIES
PARIS INSTITUTE OF TECHNOLOGY